Science

CUCKOO COEVOLUTION
Host matching drives lineage divergence p. 1030

THE SHAW PRIZE
邵逸夫獎

SHAW LAUREATES 2024

The Shaw Prize honours individuals, regardless of race, nationality, gender and religious belief, who have recently achieved significant breakthroughs in academic and scientific research or applications and whose works have resulted in a positive and profound impact on humankind.

SHRINIVAS R KULKARNI	SWEE LAY THEIN	STUART ORKIN	PETER SARNAK
Astronomy	Life Science and Medicine	Life Science and Medicine	Mathematical Sciences

The Prize in Astronomy

For his ground-breaking discoveries about millisecond pulsars, gamma-ray bursts, supernovae, and other variable or transient astronomical objects. His contributions to time-domain astronomy culminated in the conception, construction and leadership of the Palomar Transient Factory and its successor, the Zwicky Transient Facility, which have revolutionised our understanding of the time-variable optical sky.

The Prize in Life Science & Medicine

For their discovery of the genetic and molecular mechanisms underlying the fetal-to-adult hemoglobin switch, making possible a revolutionary and highly effective genome-editing therapy for sickle cell anemia and β thalassemia, devastating blood diseases that affect millions of people worldwide.

The Prize in Mathematical Sciences

For his development of the arithmetic theory of thin groups and the affine sieve, by bringing together number theory, analysis, combinatorics, dynamics, geometry and spectral theory.

PREMIO INTERNAZIONALE
Lombardia è Ricerca

"LOMBARDY IS RESEARCH"
INTERNATIONAL AWARD

Celebrating Excellence in Life Sciences that Forge New Frontiers in Medicine, Science, and Engineering for a Sustainable Future

THE PRIZE 1 MILLION EURO

The Prize, funded by **Lombardy Region** (Italy), is a prestigious recognition that celebrates outstanding achievements across Life Sciences and groundbreaking advancements in the areas of Medicine, Engineering, and Science, which have the potential **to improve significantly the quality of life and well-being of all**.

The Prize may be assigned to researchers from all over the world. **The winners are visionaries** who are redefining the boundaries of knowledge and technology, focusing on enhancing the quality of life for all.

THE TOPIC LIFE SCIENCES

- Personalized Medicine and development of innovative models of care, therapy, and prevention
- Technological advancements in different Engineering and Science disciplines
- Sustainability, environmental and social advancement
- Research in Science that transcends traditional boundaries

SUBMIT A NOMINATION: THE DEADLINE IS JULY 15, 2024

Use the following link **to submit your nomination for some of your esteemed colleagues** who may deserve the Prize

www.openinnovation.regione.lombardia.it/en/edition-2024

Also, feel free to share the link with your colleagues. **They may nominate you as a potential winner as well.**

For informations and Regulations

Fondazione VERONESI

Regione Lombardia

Celebrating 50 years of Passion for Science.

We all share a passion for science. Curiosity inspires us. The research community's quest to find answers to pressing global issues, such as improving human health, addressing food shortages, and combating climate change, is what drives us.

NEB was created by scientists for scientists, and we prioritize the advancement of science, stewardship of the environment, and giving back to the world around us. Since our establishment in 1974, we have remained committed to developing high quality, innovative products that not only empower your research but also our own. Our profits have always funded an extensive research program, which we believe is critical for staying connected to our customers and helping to drive scientific breakthroughs.

As we reflect on the last 50 years and look toward the future, we are excited to support your research and help you address these complex challenges.

We hope that by working together, we can shape the science of tomorrow.

Thank you for your continued trust and support. Find out how you can help us celebrate 50 years by visiting **www.neb.com/NEBturns50**

CONTENTS

950
A quantum processor that does chemistry

CONTENTS

An artificial skin that shares our ability to sense texture, shape, and stiffness

RESEARCH

ON THE COVER

Bronze-cuckoos are brood parasites that are reared by host birds, such as this superb fairy-wren. Hosts reject foreign nestlings, which has selected for mimicry of host nestlings by cuckoos. When a cuckoo species exploits several host species, selection

for mimicry of different hosts drives genetic divergence of cuckoos into distinct lineages. This research shows how species interactions can contribute to speciation. See page 1030. *Photo: Mark Lethlean*

PHOTO: YIHUI ZHANG/TSINGHUA UNIVERSITY

Bridging two views of autism

Last week, *Science*, *Science Advances*, and *Science Translational Medicine* published an extensive set of papers from the PsychENCODE Consortium, a multi-institutional collaboration whose aim is to study the genetics of neuropsychiatric disorders such as bipolar disorder, autism spectrum disorder, and schizophrenia. The papers, collectively called PsychENCODE2, apply advances in single-cell and multi-omic technologies to postmortem brain tissue to elucidate factors that may help explain and develop treatments for neuropsychiatric conditions. The new insights gained from these considerable data will hopefully inspire new ways in which the clinical community can find common ground with researchers, something that is not always guaranteed in the contentious mental health field.

In autism, perhaps more than any other such condition, there is great tension between the researchers focused on the mechanisms and potential treatments of autism as a disease and the neurodiversity community that views autism as a difference to be accommodated, not a disease to be cured. As an autistic person and a journal editor, I live in both worlds and talk to folks on both sides. It is unlikely that many of the most passionate adherents to either model will overcome their disagreements anytime soon. The neurodiversity community, which believes that it is a biological fact that people experience and interact with the world around them in many different ways, views a disease model as disrespectful to the humanity of autistic individuals, whereas the medical model community is motivated by a desire to end suffering for autistic patients—especially those who require lifelong support—and their families. I take great inspiration from both camps: the exceptional neuroscience, on one hand, and the compassion and strength of the autism community, on the other. I'm also an optimist who is always looking for common ground, which does exist if you look for it.

Perhaps most notably, the continued development of a solid biological explanation for autism helps dispel early notions, propagated most prominently by psychiatrist Leo Kanner in the 1940s, that autism was a result of toxic parenting, not a biological difference, and that autism was a very narrow category applying only to individuals with considerable impairment. Kanner also claimed to have been the first to describe autism instead of the physician Hans Asperger, who had a broader vision for autism similar to the idea of the autism spectrum we consider today. Yet, Asperger referred patients to Nazi eugenics programs, which is partly why Asperger's syndrome is no longer used as a diagnostic term for autistic individuals. Given this fraught background, it's no wonder that there has always been tension in the field. Laura Klinger, executive director of the University of North Carolina's TEACCH program that is rooted in the neurodiversity approach, agrees that establishing the biological basis of autism should not come with controversy. "Understanding how people become neurodiverse is an important research question," she said.

> "...establishing the biological basis of autism should not come with controversy."

Complicating matters, placement on the autism spectrum is often accompanied by other conditions, such as anxiety, depression, epilepsy, and gastrointestinal problems. Klinger and neuroscientist Simon Baron-Cohen, who leads the Autism Research Centre at the University of Cambridge, both told me that although autistic people may push back on the idea that there are biomarkers for autism, rejecting the notion that it is a disease that should be treated, more insight into the coexisting conditions may be welcomed. A PsychENCODE2 study suggests that further research may lead to the ability to categorize autism into subtypes that occur along with these other diagnoses. Klinger's own research centers on therapy for anxiety, depression, and cognitive decline in autistic adults. "If there was something in the genetics that would allow me to be more personalized in my therapy," she said, "that would be a great advance." Such progress would help Klinger and other clinicians know when to prioritize treating autism with therapy or treating the coexisting conditions with pharmaceutical approaches.

More work lies ahead for better understanding the biological details of mental illness. At the same time, acceptance and support for individuals with mental health conditions and neurodevelopmental disabilities will hopefully continue to grow. Tension between how to respond to these two trends will persist, but the scientific community can work to find ways in which both are mutually reinforcing.

–H. Holden Thorp

H. Holden Thorp
Editor-in-Chief,
Science journals.
hthorp@aaas.org

NEWS

IN BRIEF

Edited by
Jeffrey Brainard

South Korean President Yoon Suk Yeol (second from left) inspects a planned orbital laboratory.

SPACE SCIENCE

South Korea launches its own NASA

In a sign of its growing ambitions in technology, South Korea this week formally launched a national agency to boost the nation's commercial and scientific capabilities in space. Goals of the new Korea AeroSpace Administration (KASA) include landing robotic spacecraft on the Moon by 2032 and Mars by 2045. Modeled on the United States's NASA, KASA will take charge of space-related programs previously scattered across the government. A government plan calls for roughly doubling its spending level on space activities as of 2022 to 1.5 trillion won ($1.1 billion) by 2027. Much of that funding would go to developing rockets, satellites, and other technologies with commercial applications. This year, about 6% of South Korea's space budget, or about $45 million, will go to science and exploration. But that level of funding is expected to increase, and the government has recruited John Lee, a Korean American and former NASA executive, to be KASA deputy administrator in charge of missions and R&D. Projects under development include a space telescope with a 3.5-meter mirror.

NIH aide pressed on emails

POLITICS | Last week brought more bad news for scientists connected to a nonprofit U.S. research organization, the EcoHealth Alliance, which some critics allege helped spark the COVID-19 pandemic with risky virus studies. A congressional panel grilled David Morens, a top scientific adviser to former National Institute of Allergy and Infectious Diseases (NIAID) Director Anthony Fauci, about email exchanges the witness had with his longtime friend Peter Daszak, EcoHealth's embattled president. Both Republicans and Democrats on the panel suggested the adviser tried to evade public records laws and offered inappropriate help to EcoHealth's leader. Morens was put on administrative leave last year after it became public that he used personal email accounts to correspond with Daszak, as well as other researchers, about the 2020 suspension of a controversial NIAID grant to EcoHealth and its subsequent reinstatement. The hearing was the latest in a series by the House of Representatives's Select Subcommittee on the Coronavirus Pandemic. In a separate action, federal officials informed Daszak last week they want to bar him personally—not just his organization—from receiving federal funding.

African ancestry and the brain

DIVERSITY | A groundbreaking project studying how genes and African ancestry influence brain functions and disorders has yielded its first results. A research team identified 2570 genes in the brain whose expression is affected by ancestry and found that they account for about one-third of the genetic risk of developing brain conditions such as ischemic stroke and Alzheimer's disease—disorders more likely to strike Black people than white people. In *Nature Neuroscience* last week, the researchers reported studying samples of 151 post-mortem brains, a subset of more than 700 donated by families of Black people for the project. The African Ancestry Neuroscience Research Initiative—which partners a neuroscience institute and a historically Black university, both in Baltimore—aims to correct the historical exclusion of Black people in studies of brain disease, in which they made up less than 5% of subjects. Given the history of racism in medical research, project leaders sought support from Baltimore's Black community through meetings organized by historically Black churches. (Read an interview with two of the new study's leaders at https://scim.ag/QABrainAncestry.)

Bacterium builds a DNA defense

BIOLOGY | A bacterium, *Klebsiella pneumoniae*, fends off viruses using a novel mechanism—it creates new genes, a research team has found. Scientists had known some bacteria respond to viral infection by activating enzymes called reverse transcriptases, which create strands of DNA from RNA. So-called jumping genes use the same enzymes to move their genetic sequences within their genome, but it wasn't clear what role the generated DNA strands play in the infected cells. Now, researchers have found that they encode a cellular process that stops the bacterium from dividing, trapping the virus so it can't go on to infect other cells, the team reported last week in a preprint posted on bioRxiv.

U.K. graduate visas survive

IMMIGRATION | The U.K. government has eased its "crackdown" on student visas, announcing last week it will spare a class of visas that allows immigrant graduate students to remain in the country for 2 years after earning their degrees. U.K. Prime Minister Rishi Sunak had previously threatened to scrap these visas as part of an ongoing campaign to reduce immigration. Now, following a report

Studies of Kanzi, a bonobo, have documented his extensive linguistic and cognitive skills.

ANIMAL COGNITION

Can AI chat with animals? A competition is open

A competition announced this week plans to reward researchers for making progress toward using artificial intelligence or other methods to enable humans and animals to share meaningful dialogue—with an eventual prize of up to $10 million for mastering the task. The Coller Dolittle Challenge for Interspecies Two-Way Communication (Doctor Dolittle was the famed fictional veterinarian who talked to animals) aims to harness a growing base of research on interpreting nonhuman species' vocalizations, such as bat chirps and whale songs. Each year for the next 5 years, the competition's sponsors plan to award $100,000 to the team making the most progress toward two-way communication based entirely on the animal's own language. The first to achieve it would get $10 million in equity or $500,000 in cash. The competition is sponsored by the Jeremy Coller Foundation, whose interests include ending intensive animal agriculture.

from an immigration policy advisory panel that found no abuse of the graduate visas, Sunak's Conservative government announced it will retain the category but keep it "under review." However, it may make other changes, such as penalizing higher education bodies if students they sponsor for a visa later fail their visa applications. Universities have argued against new restrictions, saying their finances will suffer if the government reduces the number of high-paying international students, many of whom study science. Conservatives may have little time to implement the proposals; they have announced a July election that the party is expected to lose.

Early peanut allergy dosing lasts

BIOMEDICINE | Giving peanut products to babies and preschoolers provides them protection against developing a peanut allergy that persists at least into early adolescence, a study reported last week. All of the 508 children in the study had participated in an earlier project in which some had consumed peanut products from birth until age 5, while others did not. That study found that the first group had a much lower chance of becoming allergic to peanuts by kindergarten, as the early exposure helped train their immune system to tolerate the peanut protein. In the follow-up study, published in *NEJM Evidence*, the research team found this benefit persisted as the children grew up, regardless of whether they kept eating peanuts. By about age 13, only 4% given peanuts in early life developed the allergy compared with 15% of those from the avoidance group. (Some who had avoided consuming peanuts while young and became allergic nevertheless had become peanut-tolerant by adolescence.)
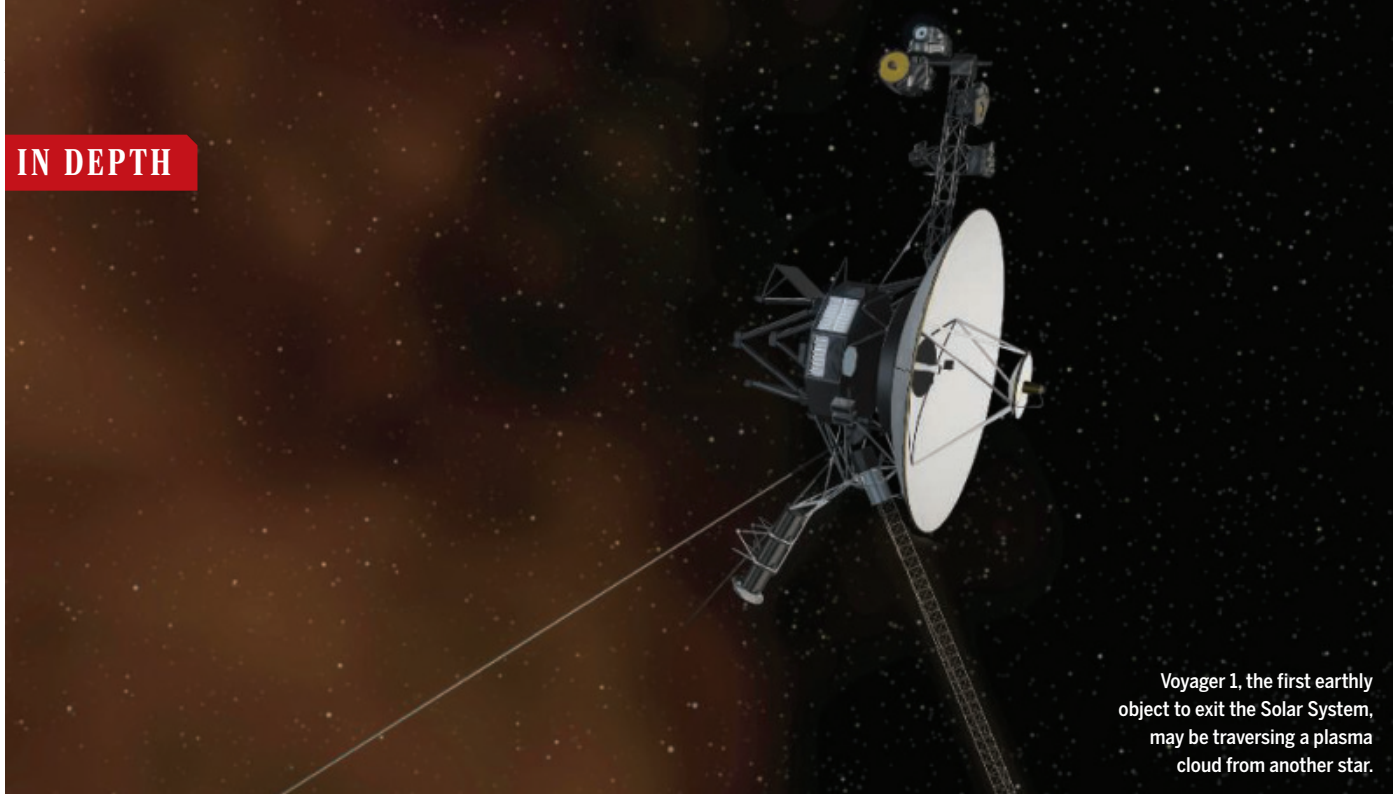
Voyager 1, the first earthly object to exit the Solar System, may be traversing a plasma cloud from another star.

SPACE PHYSICS

Voyager 1 science resumes after interstellar crisis

Before a computer crash, venerable NASA probe entered mysterious new region of space

By **Collin Blinder**

It was the ultimate remote IT service, spanning 24 billion kilometers of space to fix an antiquated, hobbled computer built in the 1970s. Voyager 1, one of the celebrated twin spacecraft now exploring interstellar space, has finally resumed beaming science data back to Earth after a 6-month communications blackout, NASA announced this week. After a corrupted chip rendered Voyager 1's transmissions unintelligible in November 2023, engineers nursed the spacecraft back to health. It began transmitting engineering data and then, on 17 May, science data for two of its four remaining instruments.

"It was a nail biter," says Jamie Rankin, an astrophysicist at Princeton University and Voyager's deputy project scientist. Even after securing engineering data "it wasn't clear whether or not we'd get science data back," she says, adding that her team is both "excited and relieved." NASA will attempt to resuscitate Voyager 1's other two instruments in the coming weeks.

Voyagers 1 and 2 have faced other close calls during their 47-year journey through the outer Solar System and beyond, but Voyager 1's communications crisis was unprecedented, says Alan Cummings, a physicist at the California Institute of Technology (Caltech) and a 51-year Voyager mission veteran. "This is the longest time we've been without data."

Prior to the interruption, Voyager 1 had been traversing a mysterious new region of interstellar space—perhaps an enormous swell of pressure or a cloud of ancient plasma—and scientists are eager to resume the investigation.

The Voyagers launched in 1977 and sent back the first detailed images beyond Mars, capturing Jupiter's Great Red Spot, the startling sight of volcanoes on the jovian moon Io, and the cerulean storms in Neptune's atmosphere. Their mission complete, the probes continued toward the edge of the heliosphere—a bubble of plasma, inflated by the Sun, that surrounds the Solar System. Voyager 1 exited the heliosphere in 2012, the first earthly object to reach interstellar space. Voyager 2 followed in 2018.

With only 6 years of power remaining in their electric generators, which run off the heat from decaying plutonium, time is running short for the spacecraft. Mission managers have shut off six of Voyager 1's 10 original instruments. Now that the spacecraft is outside the Sun's protective bubble, its electronics are also vulnerable to strikes from galactic cosmic rays, charged particles accelerated to ultrahigh energies by supernovae and other cosmic engines.

That's what NASA thinks might have happened last November, when Voyager 1 suddenly started to transmit a string of nonsensical binary code. An emergency team of engineers tried to pinpoint the issue, sending a few cautious commands at a time and waiting 45 hours for a reply from the probe, nearly a light-day away. To understand the system, they had to sift through half a century of documentation written by engineers who had mostly retired or passed away.

The team finally traced the problem to one dead memory chip, which stored code necessary for communications. The engineers redistributed the chip's function across the computer's remaining memory—first the commands necessary for engineering data and then, after careful consideration, those needed for science data. "It wasn't clear at first that it would all fit," Rankin says.

Before the breakdown, Voyager 1 had been investigating a mystery. In 2020 Voyager 1's magnetometer registered an abrupt jump in the intensity of the magnetic fields embedded in the tenuous interstellar plasma while its plasma detector measured a rise in plasma density. Similar anomalies had been seen before, but the observations returned to baseline levels after a period of months.

Researchers believe those transient jumps were generated when surges of plasma streaming outward from the Sun smashed against the boundary of the heliosphere, creating swells that reverberated through interstellar space, compressing interstellar plasmas and intensifying their magnetic fields. "The source is like a piston," says Adam Szabo, an astrophysicist at NASA's Goddard Space Flight Center and principal investigator for the magnetometer.

The anomalies that began in 2020, however, did not abate, leading some mission scientists to question whether they originated with the Sun at all. Szabo thinks they could indicate that Voyager 1 has entered a cloud of ancient interstellar plasma carrying the higher magnetic field of whatever star or star-forming region spat it out. Now, scientists are eager to see whether the two instruments—the ones now returning data—are still recording heightened field intensities and plasma densities after 6 months of silence. That could suggest Voyager 1 is still cruising through the cloud, Szabo says, and "truly make it a huge area."

Szabo's theory is just one of several that could explain the observations. Some scientists believe the new region is still just a pressure wave of solar origin, albeit one of unprecedented size. Others think these observations hint that Voyager 1 still hasn't completely left the heliosphere.

Settling the matter won't be easy. Stella Ocker, a postdoctoral fellow at Caltech and the Carnegie Observatories, says astronomers are good at observing things far off or inside our solar bubble, but struggle to see what's in between. "It is surprisingly difficult to observe the interstellar medium that is just outside of our heliosphere." The Voyager spacecraft are sort of "on the border of astro- and space physics," adds Chika Onubogu, a Ph.D. astronomy student at Boston University and a member of the NASA-funded SHIELD collaboration, which studies the heliosphere.

Even so, Voyager scientists say the ambiguous data are precious. It will be decades before a new interstellar science mission provides another "opportunity to initiate such fundamentally important and novel lines of research," says Kostas Dialynas, an astrophysicist at the Academy of Athens and a co-investigator on one of Voyager 1's energetic particle instruments.

For now, scientists are celebrating Voyager 1's reawakening. The "Voyagers are traveling in completely uncharted territories," Dialynas says. "We have no idea what lies ahead." ∎

Collin Blinder is a science journalist based in Pasadena, California.

BIOMEDICINE

Drug development blossoms for rare, fatal bone disease

Five drugs are now approved or in trials for genetic condition that triggers misplaced bone growth

By **Mitch Leslie**

Rare diseases often get the cold shoulder from drug developers, and fibrodysplasia ossificans progressiva (FOP), an infamous genetic condition that makes bone sprout where it shouldn't, is one of the rarest. It can inflict terrible pain and disability and is ultimately fatal, but only affects some 8000 people around the world.

Yet at least 13 companies are chasing therapies for FOP, and all this effort has started to pay off. Last year, the U.S. Food and Drug Administration approved the first drug to treat the disease, palovarotene. Four others are in trials, including a compound described this week in *Science Translational Medicine* that stymies the defective protein behind the disease.

Thanks to this progress, scientists and doctors say, a suite of drugs could soon be available to treat the fatal condition. They're likely to be costly because the market is so small; palovarotene runs $624,000 per year in the United States. But the compounds may stop progression of the disease and could even allow surgeons to remove out-of-place bone without exacerbating the illness. "I hope we can turn a catastrophic disease into an inconvenience," says Frederick Kaplan, an orthopedic surgeon at the University of Pennsylvania (UPenn) Perelman School of Medicine who has been studying FOP for more than 30 years.

Kaplan and other researchers suggest one reason drug developers have focused on FOP is the cruelty of the disease, which is triggered by a mutation in a gene crucial to bone growth. Children with FOP usually seem fine at birth, but as they get older bone starts to form in their muscles, tendons, and ligaments. The frequent falls and bruises of childhood can spark these spates of bone development, as can surgery and even injections—forcing patients to skip vaccinations.

As the disease progresses, the superfluous bone can contort the body and lock up joints, making it difficult to walk and eat. Patients are usually in wheelchairs by age 30 and die in their 50s, often because the excess bone hampers breathing. After seeing the suffering, "researchers feel obligated to do something," says developmental biologist Maurizio Pacifici of the Children's Hospital of Philadelphia, whose lab identified palovarotene as a potential FOP treatment.

Researchers also hope the disease will provide insights into how to treat more common conditions in which bone formation goes awry. For example, people without FOP sometimes accumulate mis-

A scan of a young girl with fibrodysplasia ossificans progressiva shows inappropriate bone growth from her pelvis and an upper femur.

placed bone after burns, blast injuries, and hip replacements, or when they develop heart disease.

Not that long ago it wasn't even clear the disease was genetic, says Eileen Shore, a geneticist and cell biologist also at UPenn, which is the epicenter for studies of the disease. "We couldn't get pharma [companies] interested," she recalls.

But when she, Kaplan, and their col-

leagues identified the faulty gene behind FOP in 2006, "that changed everything," Shore says. The disease results from mutations in the gene for ALK2, a surface protein on many kinds of cells, including certain stem cells. Researchers don't fully understand the disease mechanism, but the abnormal ALK2s are overactive. They may dispatch messages that cause stem cells to specialize, triggering skeletal eruptions at the wrong time and place.

That molecular pathway revealed possible drug targets. Instead of taking aim at ALK2, Pacifici and his colleagues decided to interdict the pathway farther downstream by activating a molecule that blocks formation of cartilage, bone's precursor. The researchers tested several related molecules, including palovarotene, which had the advantage of already being in clinical trials for another condition. A 2016 study showed that the drug curbs new bone buildup in mice genetically engineered to mimic FOP.

Palovarotene seems to do the same in people. In a phase 3 trial reported last year, patients who received the drug accrued 60% less new bone per year than patients in a separate study who received no therapy.

As the first approved targeted treatment for FOP, palovarotene became a landmark. But it has several drawbacks besides its cost. It doesn't stop the disease. Moreover, young children can't take it for fear it will stunt their growth, so it isn't used to combat the early stages of the illness, Kaplan says. "The battleground in FOP is children."

So far, only four countries—the U.S., Canada, Australia, and the United Arab Emirates—have approved palovarotene, which is made by the French pharma company Ipsen. "It's exciting that there is a drug, but the reality is we can do better with targeted treatments," says endocrinologist Marc Wein of Massachusetts General Hospital, who is not involved in developing the drug.

Researchers at the pharmaceutical company Regeneron have devised a monoclonal antibody, garetosmab, that may overcome some of palovarotene's limitations but has brought some new concerns. In 2015, researchers at the company and an independent group in Japan discovered that the faulty version of ALK2 becomes overactive when it is stimulated by a protein called activin A, to which normal ALK2 doesn't respond. Garetosmab clamps onto activin A, blocking the abnormal stimulation.

A phase 2 trial of garetosmab in 44 patients with FOP, published in 2023 in *Na-*

ture Medicine, showed that although 41% of one patient subgroup sprouted additional bone lesions during 7 months on a placebo, only 5% did after they began receiving garetosmab. Regeneron recently began recruiting patients for a phase 3 trial to further test the drug's effectiveness—and safety.

The latter is a major issue as five patients died in the garetosmab phase 2 trial. "We looked under every stone we could to understand what happened to these patients," says Dushyanth Srinivasan, medical director of the garetosmab program at Regeneron. Participants in the trial were ill, and in the end, the consensus was that the drug did not cause the deaths, he says. But Kaplan, who was a co-author on the *Nature Medicine* paper, says the safety of garetosmab remains a concern. Activin A performs a variety of jobs in the body, so blocking it may lead to side effects.

Three other drugs in clinical trials take aim at ALK2 itself. The protein is a kinase, an enzyme that turns other proteins on or off by affixing phosphate molecules to them, and the new compounds jam its active site. One, developed by Alison Davis, then a lead biologist at Blueprint Medicines, and colleagues, halted formation of new bone in mice with an FOP-like condition, the researchers report this week in *Science Translational Medicine*. Now owned by Ipsen and dubbed fidrisertib, the drug is already in a phase 2 trial. The other two ALK2 inhibitors are also in phase 2 trials.

> ## "I hope we can turn a catastrophic disease into an inconvenience."
>
> **Frederick Kaplan**,
> University of Pennsylvania Perelman School of Medicine

Although the kinase inhibitors are promising, blocking ALK2 could also trigger side effects, notes medical geneticist Toshifumi Yokota of the University of Alberta. (FOP patients still have one normal gene for the protein.) He has helped start a company to probe whether oligonucleotides, short strands made of the building blocks of RNA or DNA, can inhibit the protein more selectively.

Even if the new drugs only stop the disease rather than reversing it, they could be a major help. Surgeons hesitate to cut away excess bone in patients with FOP because the tissue trauma spurs yet more bone formation. "If we could prevent reformation of bone after surgical removal, that would be a coup," Pacifici says.

This surge in drug development is encouraging for patients with FOP, Wein says. But he adds that it should also be heartening for patients with other rare illnesses, who should think, "if they can do it for FOP, they can do it for my disease." ∎

Mysterious sea urchin plague is spreading rapidly

Pathogen that kills victims within days leaps from Caribbean to Red Sea

By **Sean Cummings**

When Omri Bronstein began to trace the advance of a mysterious sea urchin plague down the Gulf of Aqaba in early 2023, he was ahead of the tide. Starting in late 2022, urchins had been dying en masse at the gulf's northern terminus near Aqaba, Jordan. When Bronstein's team began sampling in February 150 kilometers to the south, along Egypt's Sinai Peninsula, all still appeared well. But in late April, the outbreak caught up to his team, overtaking them as they worked. Within days, every urchin in the area was dead.

"It's surreal and horrific," says Bronstein, a marine biologist at Tel Aviv University. "You swim through piles of dead sea urchins that until days ago were significant components of the reef."

The deadly wave, which may soon threaten these spiny, slow-moving invertebrates globally, appears to have begun half a world away. In early 2022, the first reports of mass urchin mortality, in a species called *Diadema antillarum*, came from the Caribbean Sea. Investigators pinned it on a single-celled pathogen from a family of organisms never before known to kill urchins. Now, as Bronstein and his colleagues reported last week in *Current Biology*, the same pathogen is killing other urchin species in the Gulf of Aqaba and beyond, suggesting the disease is spreading around the world at astonishing speed.

The consequences of a widespread urchin die-off for marine ecosystems could be dire, biologists say. Without these key herbivores, corals can become smothered by overgrowths of algae that block out the sunlight they need to survive. "[Sea urchins] help keep these environments' health up to par. When they're removed, downstream effects can be quite costly,"

Dead sea urchins began washing ashore on Réunion Island in the western Indian Ocean last year.

says Collin Closek, a marine scientist at Stanford University who was not involved in the research.

When the disease first broke out in the Caribbean, "we were scratching our heads," says Ian Hewson, an oceanographer at Cornell University who has studied diseases in sea stars and other marine animals. Genetic analyses of diseased urchins didn't yield any obvious viral or bacterial pathogens. But after Hewson and his colleagues turned their attention to other microorganisms, they identified the culprit: a scuticociliate, a single-celled animal with hairlike appendages called cilia and a track record of causing diseases in sharks, fishes, and crustaceans. "To the best of our knowledge, ciliates have never been observed in association with urchin diseases elsewhere," Hewson and his colleagues wrote in a *Science Advances* paper published last year. The team noted that it wasn't clear whether the pathogen was new to the region, or if it had been there previously and was somehow "influenced by prevailing conditions to cause mass mortality."

Meanwhile, the problem continued to spread. By July 2022, urchins began turning up dead off the coast of Greece. Within 4 months, the die-off spanned 1000 kilometers of coastline in the eastern Mediterranean Sea. The event bore marked similarities to the one in the Caribbean, researchers reported last year in *Royal Society Open Science*: "Progression of the symptoms seem to be rapid, leading to death within two days," the team wrote.

In the Mediterranean, the affected urchin—*Diadema setosum*—is an invasive species. But the authors of that study, including Bronstein, warned that the problem could soon move to the Red Sea, where *D. setosum* is native and a significant player in reef ecosystems.

Bronstein readied himself to track any spread. He was soon swept up in a sprint of underwater surveys and sampling of urchin remains. After its initial appearance in Jordan, the outbreak tore south down the Gulf of Aqaba into the Red Sea and beyond, reaching Oman by April 2023. By July of that year, it had leaped all the way to Réunion Island in the western Indian Ocean.

The culprit behind the Mediterranean outbreak was never confirmed, in part because the team didn't collect urchins for autopsy. Hewson says it was a challenge for his team in the Caribbean. The spiny black creatures become largely immobile once infected, leaving them vulnerable to predators. Those not eaten waste away: Tissues erode, spines drop off. Within days, only the ball of a skeleton remains—and that, too, rapidly crumbles away, leaving little time to gather specimens to analyze for a cause of death.

But in the Red Sea, Bronstein's team was able to identify the same scuticociliate seen in the Caribbean. They also documented mass die-offs not just in *Diadema* urchins, but also in the closely related genus *Echinothrix*. "That makes it a multi-host pathogen. If it's a generalist, it's more dangerous," says Drew Harvell, a marine ecologist at Cornell who was not involved in the research.

Hewson wasn't shocked that the same pathogen was the culprit, "but the speed at which it went [to the Red Sea] was a surprise." The continuing rapid expansion into the western Indian Ocean has stoked fears that it could soon reach Australia and the Great Barrier Reef. The Caribbean offers a preview of the possible result: Forty years before the 2022 outbreak, a still-unknown disease leveled the region's urchins. Deprived of a primary herbivore, the reefs succumbed to algal overgrowth and never fully recovered. Since the more recent urchin die-off, anecdotal reports suggest algae have grown denser in the region again, Hewson says, although he isn't aware of any scientific studies documenting that.

If the same ecosystem shift were to occur around the world, the impacts to both reefs and the coastal communities that depend on them for livelihood could be massive, especially given the stress many reef ecosystems already face from overfishing and bleaching because of rising sea temperatures. "Urchins are critical components of benthic ecosystems, and there are pretty tight tipping points: We don't want too many or too few," Harvell says.

Slowing the spread of the pathogen requires knowing how it travels. Although experts aren't sure, one explanation is that it hitches rides on ship traffic. There's no way it could have made it from the Caribbean to the Red Sea on its own, Hewson says. And after the outbreak was reported near Aqaba, one of its next stops was at a port in Egypt that receives ships from that Jordanian city.

If ship traffic is to blame, testing ballast water could become one containment strategy. "The best way to manage a pathogen in the ocean is to keep it from getting in the ocean," Harvell says.

In case the outbreak continues to spread out of control, Bronstein calls for maintaining urchins in captivity—quarantined, without seawater circulating directly from the ocean—in hopes of reintroducing the animals to affected habitats after the disease is gone. "This is something that we have to do now," he says. "The window of opportunity is closing rapidly." ∎

SCIENCE POLICY

Research faces cuts as Dutch shift to the right

New coalition to scrap science and innovation funds, roll back environmental measures

By **Martin Enserink**

The far right's stunning victory in the Netherlands's parliamentary elections last fall will upset far more than the country's immigration policies. An agreement by the four parties aiming to form a new government, presented on 16 May, also calls for cuts in science and innovation funding, rollbacks of environment and climate policies, and restrictions on the influx of foreign students.

Scientists and their advocates are dismayed. "As a country we're falling further behind if we implement these cuts," Marcel Levi, chair of a broad group of institutes and companies known as the Knowledge

The plan endorsed by the four parties, a crucial step in forming a new government, includes harsh anti-immigration measures. It calls for cutting taxes, investing in housing, and bolstering support for farmers.

But it would scrap the final two rounds—together worth €6.8 billion—of the National Growth Fund, a 5-year scheme launched in 2021 to boost innovation and economic growth by disbursing a total of €20 billion to consortia of research organizations and companies. The fund's first three rounds supported dozens of projects, for example to boost the biotech sector, make the steel industry greener, and innovate in education. The cut is "shocking, because it will hurt the country's potential for innovation," says chemist and 2016 Nobel Prize winner

Geert Wilders (left), head of the far-right Party for Freedom, is in negotiations to form a new Dutch government.

Coalition, said in a statement. Jouke de Vries, interim chair of Universities of the Netherlands, called the cuts "a blow to our students and employees, who are already under enormous pressure."

The nationalist, populist Party for Freedom, led by Geert Wilders, won 23% of the vote in the November 2023 House elections, putting Wilders—once a fringe figure who proposed a "head rag tax" on women wearing headscarves—close to the center of power. Since then, he has been in contentious and often chaotic negotiations to form a government with three other parties, including the center-right party led by outgoing Prime Minister Mark Rutte, which saw its electoral share shrink to 15%.

Ben Feringa of the University of Groningen, who sits on the fund's advisory council. "It's not a very smart strategy if you think about the problems we have to solve as a society."

The agreement also puts an end to the so-called Sector Plans, a scheme launched in 2023 that spends €200 million annually to reduce academic workloads, provide jobs at universities and academic medical centers, and structure the division of labor between institutes. And the parties agreed to cut €150 million annually from a roughly €500 million fund to advance basic research.

Both those schemes were introduced by Robbert Dijkgraaf, a physicist and former head of the Institute for Advanced Study in Princeton, New Jersey, who became science

minister in 2022 and enjoyed broad support from the academic community. "It pains my heart to see that plans are being made to roll back many of these investments," Dijkgraaf said in Parliament on 21 May. "It feels as if we were at the head of the peloton, and now are hitting the brakes."

The new coalition has also vowed to slow a recent influx of foreign students, which has exacerbated housing shortages and triggered complaints about the second-class position of Dutch in higher education. The coalition wants more courses taught in Dutch instead of English, a cap on the number of foreign students, and higher tuition fees for people from outside the European Union. Those measures threaten "the international character" of Dutch higher education, de Vries said in his statement. "That has major consequences for the availability of talent for science and the labor market."

Another sharp turn comes in environmental policy. Animal waste from Dutch farms emits high levels of nitrogen compounds that violate EU rules and harm the country's ecosystems. Past government plans to tackle the issue have triggered massive protests by farmers and the rise of a new party, the Farmer-Citizen Movement, that is part of the new coalition. The four parties want to relax limits on farms' nitrogen emissions and seek exemptions from EU manure and nitrogen rules—a plan observers say is unlikely to succeed. And they will scrap a €20 billion fund to make agriculture more sustainable by buying out farmers.

In his election platform, Wilders called for putting all climate policies and agreements "through the shredder." That won't happen: The governing agreement leaves the country's climate goals in place, but they will become harder to achieve because a proposed carbon dioxide tax for industry and a plan to speed up the introduction of heat pumps in homes have been abandoned.

Wilders's future governing partners don't want him to become prime minister. His first choice for that job, molecular biologist and former science minister Ronald Plasterk, withdrew from consideration on 20 May after a media frenzy erupted over his alleged role in a patent dispute involving a cancer vaccine company he co-founded. (Plasterk denies wrongdoing.) On 28 May, Wilders instead proposed top civil servant Dick Schoof as the new prime minister. ∎

Cancer clinical trials are key to research, but may not improve survival for participants.

BIOMEDICINE

Joining a cancer trial doesn't improve survival odds

New study questions often-implied benefit for participants

By **Jennifer Couzin-Frankel**

Cancer researchers, doctors, and patients widely view clinical trials as a boon to participants—a chance to advance medicine while possibly gaining access to experimental treatment that could be lifesaving. Even when assigned to the placebo group, patients are told they'll benefit from rigorous care. But how much do they actually gain by signing on?

A study out last week suggests that although there may be pluses to trial participation, improved survival isn't one of them. Researchers analyzed 39 publications that compared people in cancer trials with patients who were not enrolled and found participants had no survival advantage. A second study, out in April, suggests cancer trial participants randomized to get the experimental treatment see a small benefit—but at the cost of more severe side effects.

Those findings run counter to how clinical trials are sometimes promoted, says Jonathan Kimmelman, a bioethicist at McGill University who led the recent studies. Consent documents and educational materials for patients "oftentimes describe closer monitoring, greater attention as one of the benefits of trial participation," he says. But without evidence that these improve outcomes, "I don't think that language is serving patients well."

Distilling the benefits of trials for patients "is really complicated," says Tove Godskesen, a professor of nursing and a bioethicist at Nord and Uppsala universities who led an earlier study with similar conclusions.

In an analysis in *JAMA* on 20 May, Kimmelman, his Ph.D. student Renata Iskander, and their colleagues analyzed studies spanning cancer types, including breast cancer, melanoma, and brain cancer; some included multiple comparisons of participants and nonparticipants in different trials. In most of the studies, the patients got the same or very similar treatment. For example, one looked at men with prostate cancer treated with radiation either inside or outside a trial. This made it possible to isolate what's called the "participation effect"—whether simply being in a trial confers advantages, setting aside any effect of the experimental treatment.

About half the comparisons suggested trial participants survived longer. But Kimmelman's team found factors that risked muddying those results. For example, if trial participants were younger than those in the comparison cohort a study might show a survival difference that wasn't from the trial itself. And cancer trials often exclude patients with other serious illnesses, which again could create an apparent survival advantage for participants. After adjusting for these and other issues, the team found no survival benefit from the access to top-notch care that trial participants are said to enjoy.

The second study from Kimmelman's group addressed another question: Do patients in trials benefit if they get the experimental treatment? That research, published on 30 April in the *Annals of Internal Medicine*, covered 128 trials of treatments for solid tumors, and found that those randomized to get the experimental strategy did have a small survival edge: about five extra weeks, on average. They also had a higher risk of serious side effects. The survival advantage is statistically significant, Kimmelman says, "but that number needs to be considered against the fact that you have elevated risks."

Kimmelman worries potential overselling of trial benefits isn't limited to cancer. In 2019 his group published a paper about neurological trials, reporting no medical benefit from being assigned to get an experimental treatment versus a placebo.

Other studies echo Kimmelman's recent findings. Godskesen led a group that analyzed nine studies comparing cancer trial participants and nonparticipants and in 2020 reported no clear health benefit to being in a trial. And yet interviews with 57 doctors and nurses at two university hospitals in Denmark and Sweden revealed a rosier view of trials. "You get better results, whatever study you participate in," one physician said.

An article that accompanies the new *JAMA* paper cites a similar message in guidelines from the National Comprehensive Cancer Network (NCCN), a nonprofit alliance of U.S. cancer centers. "NCCN believes that the best management of any patient with cancer is in a clinical trial," they state. That suggestion "cannot withstand critical scrutiny," say the authors of the article, David Shalowitz, a gynecologic oncologist and bioethicist at the West Michigan Cancer Center, and Franklin Miller, an ethicist at Weill Cornell Medicine.

Wui-Jin Koh, NCCN's chief medical officer, told *Science* that in part because the *JAMA* paper reanalyzes existing studies rather than gathering new data, "it does not definitively prove that there is no benefit, and certainly does not suggest poorer outcomes with clinical trial participation."

Godskesen hopes the recent findings don't undercut the importance of trials or dampen participation. Doctors and researchers have long lamented that only about 3% of U.S. adults with cancer join a trial. Godskesen notes that participants may benefit in various ways. Her interviews suggest some patients are pleased to have a direct telephone number for a research nurse, for example. "They said that the whole family felt taken care of."

Clinical trials may also improve disparities in care, Shalowitz notes, because "they're so tightly controlled with regard to how treatment proceeds that there is less room … to treat patients differently."

But although joining a trial can be rewarding, patients "give up a fair amount to drive the process of development forward," Kimmelman says, and they should have a clear understanding of the potential benefits. As for how to explain his finding that a cancer trial doesn't confer a survival benefit over competent care outside of one, "I guess the question is, 'Why should it?'" ∎

NEUROSCIENCE

Theory of sleep as a brain cleanser challenged

Mouse study contradicts landmark finding, but some question its methodology

By **Sara Reardon**

We all need sleep, but no one really knows why. For the past 10 years, a prevailing theory has been that sleep washes waste and toxins from the brain via a series of tiny channels called the glymphatic system. Sleep problems can disrupt this process, the theory's proponents say, perhaps raising the risk of Alzheimer's disease and other brain disorders.

Mouse experiments have seemed to support the idea. But in recent years, several groups of scientists have challenged some aspects of the theory. Now, a new study has found that the mouse brain clears small dye molecules more efficiently while the animal is awake than when it is asleep or under anesthesia. A glymphatic system might still cleanse the brain, the authors say, but sleep actually slows this cleansing down.

Other researchers are stumped as to how to explain the opposing results, and several declined to comment on the record for fear of entering a heated debate. A few see the new findings as a serious blow to the sleep clearance theory, but others say the new paper's methods are too different from those of the earlier work to credibly challenge it. "When you criticize a concept that has been there for some time, then your design should be even better," says Per Kristian Eide of the University of Oslo.

In the original mouse experiments, neuroscientist Maiken Nedergaard at the University of Rochester and her team injected a dye into the cisterna magna, a fluid-filled pocket at the back of the neck, which sits just outside the brain and supplies it with cerebrospinal fluid (CSF). They used a two-photon microscope to measure the influx of the dye to the brain and its spread through the organ. The influx increased when mice were asleep or under anesthesia compared with when they were awake, allowing the dye to penetrate through the brain. That led the researchers to conclude that more fluid was flowing through the brain and draining into blood or lymphatic vessels during sleep. Nedergaard proposed that this efflux relied on the pumping of fluid through tiny glymphatic vessels between neurons, which her team had identified in an earlier study.

Nicholas Franks, an anesthesia researcher at Imperial College London and senior author of the new paper, didn't set out to disprove this popular hypothesis. "I really liked this sort of theory of sleep … as a basic housekeeping mechanism that keeps the brain healthy and fully functional," he says. But he questioned whether the influx of dye was a reliable proxy for efflux, which could only be measured directly by tracking every blood or lymphatic vessel or potential exit point from the brain.
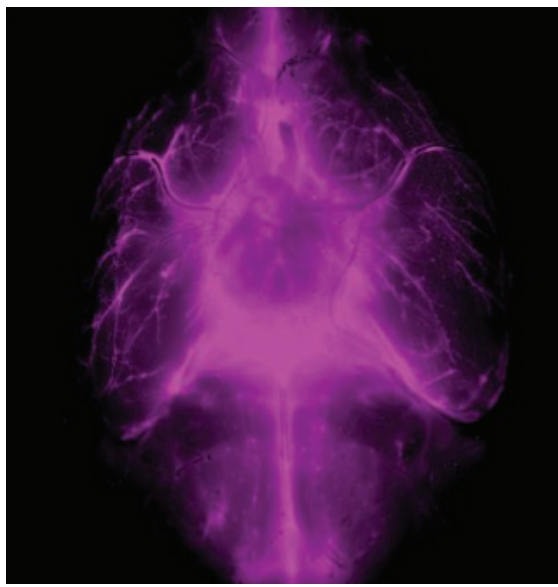
A system of fluid-filled channels is thought to help flush the brain.

He likens the brain to a leaky bucket, where the water level is the amount of dye that penetrates it. That level will rise when water is poured into the bucket faster—if the brain pulls more CSF in during sleep. But it will also rise if the hole at the bottom shrinks—if efflux slows. And it's difficult to distinguish the two.

Franks's team used a different technique, also indirect, to infer flow. They injected dye directly into mice's brains via portals through their skulls and measured its concentration with a sensor in another part of the brain away from the injection site. The sensor revealed far less dye when the mice were awake than when they were asleep or anesthetized, suggesting the molecules were leaving the brain more quickly, the team reported on 13 May in *Nature Neuroscience*.

"I think they did a very good job," says Erik Bakker, a circulation expert at Amsterdam University Medical Center. Steven Proulx, a vascular expert at the University of Bern, calls the new study's approach "very clever." Proulx found something similar in 2018: that tracer dyes injected into the cisterna magna entered the systemic blood more quickly in awake mice than anesthetized ones.

But Nedergaard says the new study doesn't seriously challenge her results. "You can't just come in and do something that's completely different and say all the old data is wrong," she says. "I'm actually shocked that this paper was published." Nedergaard is writing a letter to *Nature Neuroscience* detailing her many concerns. One is that the dye was pumped in at the same rate during wake and sleep, which she argues could lead to spurious results. Her research has found neurons shrink during sleep—a claim others have challenged—which could lower pressure in the brain and affect how quickly dye flows through it.

Her main concern, shared by others, is that inserting the dye portal damaged the brain—the glymphatic system is delicate and could easily collapse. (Franks's team waited a week after surgery before injecting dye to allow potential injuries to heal, he notes.) Eide adds that the team didn't measure dye in the cortex, which is where most glymphatic clearance occurs.

Bakker says the brain may have multiple waste clearing mechanisms. Small molecules such as dyes might exit through different means from large ones such as the Alzheimer's-linked protein beta amyloid.

Nedergaard's group is working on a rodent model that produces waste products that can be precisely traced as they leave the brain. Meanwhile, Franks's team plans to investigate how different-size molecules behave in the brain and what mechanisms might pump waste-bearing fluid through the organ in the first place.

Challenging a popular theory about something as basic as sleep is difficult, he says. "It's got such a firm rooting in the zeitgeist." ∎

eppendorf
& Science

PRIZE FOR NEURO BIOLOGY

**2023 Winner
Marissa Scavuzzo, Ph.D.
Case Western Reserve
University School of
Medicine, Cleveland, USA**

**For research on glial
cells in the gut**

Application Deadline
June 15, 2024

Call for Entries 2024

Eppendorf & Science Prize for Neurobiology
The annual Eppendorf & Science Prize for Neurobiology is an international prize which honors young scientists for outstanding neurobiological research based on methods of molecular, cellular, systems, or organismic biology. If you are 35 years of age or younger and doing great research, now is the time to submit an entry for this prize.

It's easy to apply! Write a 1,000-word essay and tell the world about your work.

eppendorf.com/prize

As the winner, you could be next to receive
> Prize money of US$25,000
> Publication of your work in *Science*
> Full support to attend the Prize Ceremony held in conjunction with the Annual Meeting of the Society for Neuroscience in the USA
> 10-year AAAS membership and online subscription to *Science*
> Complimentary products worth US$1,000 from Eppendorf
> An invitation to visit Eppendorf in Hamburg, Germany

eppendorf   **Science**
AAAS

FEATURES

COMPOUND INTEREST

Practical uses for quantum computers are emerging in chemistry, promising to speed the development of materials, catalysts, and drugs

By **Robert F. Service**, in Broomfield, Colorado

In Quantinuum's H2 chip, ions hovering above a tiny, central "racetrack" can compute molecular structures.

The core of this quantum computer looks familiar enough: a silicon chip the size of a stamp. But the resemblance to your laptop ends there. The chip, cocooned within a vacuum chamber and cooled nearly to absolute zero, is patterned with 198 gold electrodes, arranged like an oval racetrack.

Above the racetrack, a handful of ytterbium ions are trapped and levitated by a train of electrical, radiofrequency, and laser pulses. Subsequent manipulations impart specific amounts of energy to the ions and coax them to interact with one another to carry out a sequence of logical operations. A final burst of laser pulses nudges each ion to either fluoresce or not—a flash of binary code that detectors read out as the computation's solution.

Last year, researchers here at Quantinuum, a quantum computing startup, used a chip with eight ytterbium ions to compute the precise arrangement of a hydrogen molecule's two electrons in their most stable state, out of myriad possible configurations. In and of itself, that computational feat is barely worth noting; a typical laptop can manage it in seconds. But it marked the first demonstration of an advanced quantum simulation that's ex-pected to perform better—and take on more complex molecules—as quantum computers grow more powerful.

The achievement shows how quantum computers are tentatively moving from the realm of mere promise to tackling real-world challenges. Quantinuum is one of many companies that believes applications in chemistry—particularly the hunt for novel drugs and catalysts—will be among the very first practical tasks for these new machines. They are ideally suited for predicting the structure and behavior of molecules, researchers say, because both the machines and the molecules are ruled by the counter-
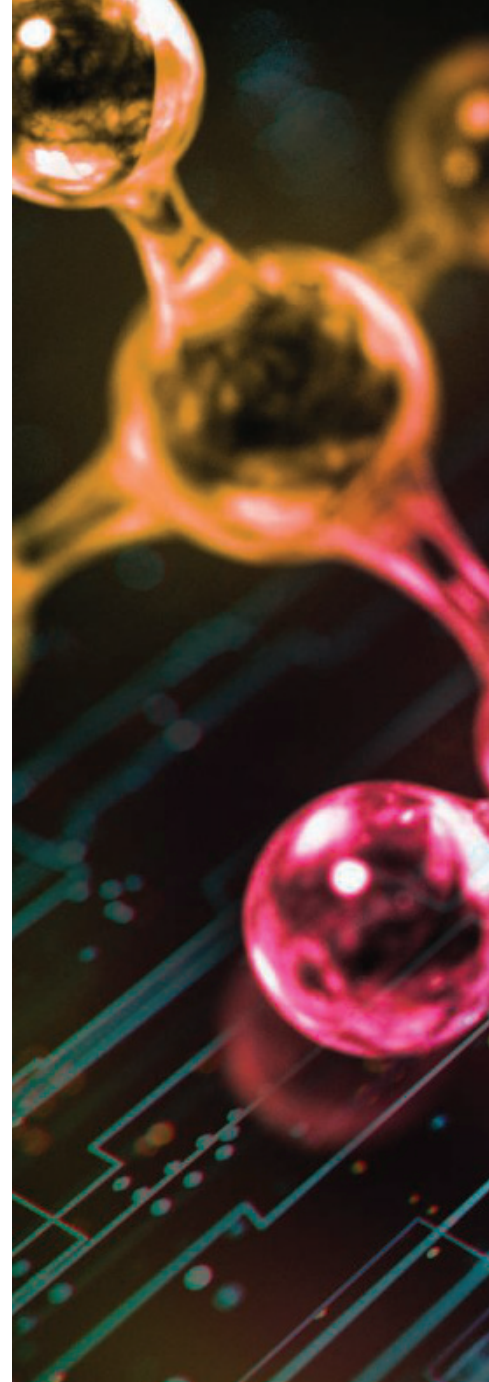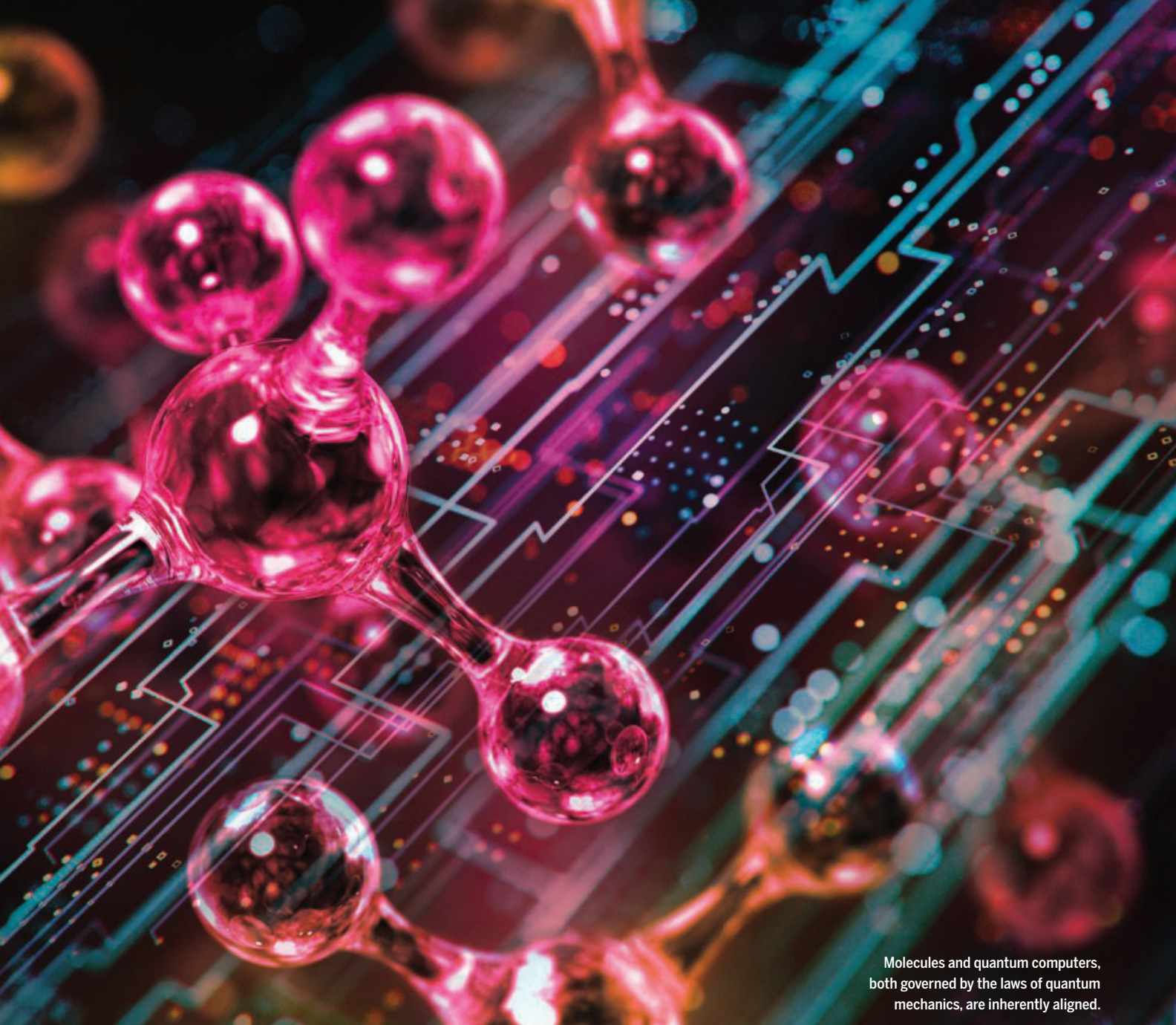
Molecules and quantum computers, both governed by the laws of quantum mechanics, are inherently aligned.

intuitive laws of quantum mechanics.

"We are currently using chemistry problems to advance quantum computing instead of using quantum computing to advance chemistry," says Quantinuum's head of strategy, Chad Edwards. "But there will be a tipping point," where those roles will be reversed. "There has been a clear speedup in the past year," agrees quantum physicist Louis-Paul Henry at PASQAL, a quantum computing startup based in Paris that is also focusing on chemistry. "More and more people are talking about applications and taking a look at harder problems relevant for real world uses."

Already, quantum computers are helping researchers zoom in on reaction pathways in fuel cell catalysts, simulate the infinitesimally brief interactions of light and matter, and reveal druggable pockets in proteins. Ashley Montanaro, a co-founder of Phasecraft, a quantum computing company, says today's quantum computers are almost good enough to make discoveries beyond the reach of classical systems. "It's a lot closer than people previously thought."

WHERE STANDARD computers manipulate bits of data as either 0s and 1s, quantum computers rely on "qubits," which can encode data

as a 0, a 1, or any combination of the two states in a simultaneous "superposition." In the case of Quantinuum's computer, the qubits are the electrons in the ytterbium ions, which can hover in a superposition of two different energy levels. During a computation, multiple qubits are "entangled" so their energy states influence one another, making it possible to evaluate all their possible interactions simultaneously.

Quantinuum founder Ilyas Khan likens a classical computation to a mouse navigating a maze, taking one random turn after another in a trial-and-error search for the correct path through. A quantum computer, he says,

has a bird's-eye view of the same maze, which makes it easier to see the optimum pathway all at once. And verifying the solution is as easy as testing the molecular structure or behavior revealed by the quantum computer. "You know you're at the end because you've got the piece of cheese," Khan says. Linking together even a few hundred qubits should enable fantastically complex calculations.

The challenge is that qubits are fragile: The slightest jostle by an air particle, a modicum of heat, or even a stray cosmic ray can upset a qubit's superposition state, creating an error that throws off the result. Researchers minimize these influences by chilling qubits and isolating them from their environment. They also build in redundancy. Even though today's quantum computers may link up dozens or hundreds of qubits, only a fraction of them perform logical operations, whereas the rest correct errors.

Even so, the machines are getting more powerful. Last year, IBM unveiled a computer with 1121 qubits based on tiny superconducting circuits, up from a 127-qubit version released in 2021. Atom Computing, a California startup, went one better, last year presenting a 1180-qubit computer that relies on the spins of neutral ytterbium atoms.

Others are striving for improved accuracy. In December 2023, researchers at Harvard University, working with a 280-qubit computer from QuEra, another neutral atom startup, reported that reduced error rates in their system enabled them to encode up to 48 logical qubits and faithfully carry out hundreds of operations before the quantum house of cards collapsed, a major improvement over prior setups. And last month, Quantinuum scientists reported that a new Microsoft algorithm dramatically improved their ability to detect and correct errors in their latest 32-qubit ion chip. "The hardware advances are [coming] fast enough that they could soon impact the number of applications achievable," says Prineha Narang, a quantum computing expert at the University of California, Los Angeles.

MANY RESEARCHERS expect those applications to emerge from chemistry. The properties of chemical compounds and materials are governed by the making and breaking of chemical bonds, the motion of electrons, and magnetic behaviors—all of which are dictated by quantum mechanics. Researchers can deduce the behavior of a molecule by solving its Schrödinger equation, which in part describes the probabilistic, wavelike behavior of electrons and their interactions with atomic nuclei, based on inputs such as electron energy levels and chemical bond lengths.

Classical computers have managed the calculation for molecules as large as penta-
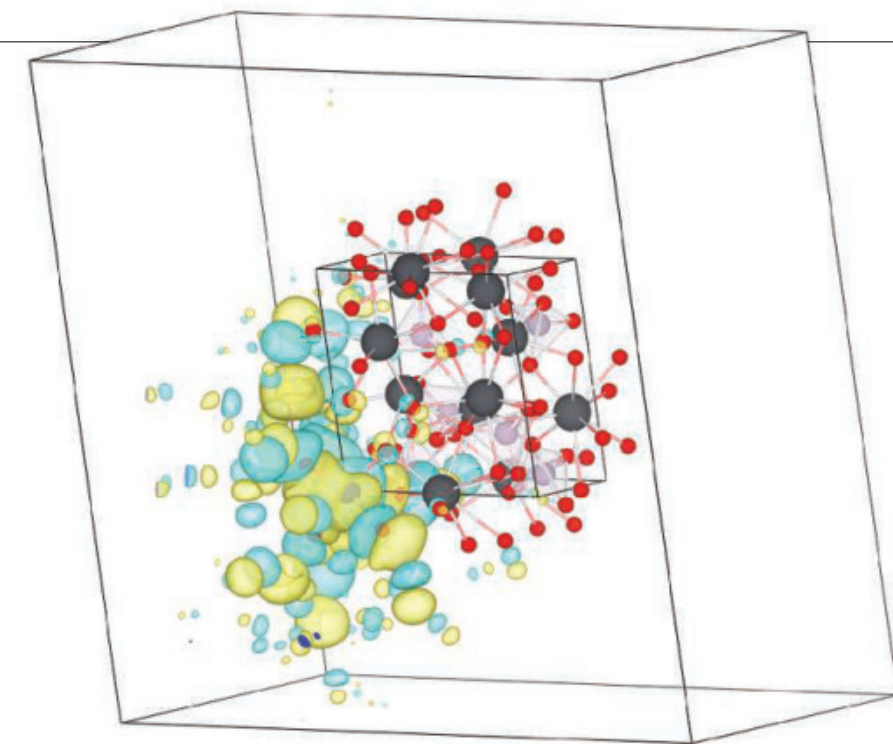
Researchers at Phasecraft depicted what a quantum computer would need to simulate the behavior of electrons (yellow and blue) around atoms in a proposed superconductor (red and gray).

cene, a chain of five hydrocarbon rings with 22 electrons in "pi" covalent bonds, which govern the molecule's shape and reactivity. But the classical calculation relies on approximations, and for larger molecules inevitable errors compound, throwing off the results. Quantum computers, by contrast, need not use these fudge factors, and instead can directly map the interactions between electrons and nuclei onto qubits, using actual quantum systems to represent their kin. "There is an inherent alignment between quantum systems and quantum computing," Edwards says.

Another reason chemistry is a good match for quantum computing is that the problems can often be narrowly constrained, putting them within reach of the small quantum computers available today. A researcher may only need to focus on the interaction of a handful of electrons to understand how a drug molecule binds to its protein target. "The best problem for a quantum computer has a small problem size," with many possible outcomes, says Brian Bilodeau, chief operating officer of Microsoft's quantum group.

Given the still-modest capabilities of today's quantum computers, researchers aren't asking them to do all the computational lifting by themselves. Instead, most scientists pursue hybrid approaches that marry quantum and classical processors. "The reality is it will be a hybrid world," Bilodeau says.

Today's most popular hybrid, an algorithm known as a variational quantum eigensolver (VQE), uses classical computers to approximate a molecule's stable ground state, the lowest energy configuration that is key to its structure and how it interacts with neighbors. Then a quantum computer takes over to find the ground state's precise solution. But today's error-prone quantum computers typically struggle with VQEs. The largest VQE simulation came in 2020, when Google researchers modeled the behavior of the 12 electrons in a molecular chain of 12 hydrogen atoms. That approaches but still falls short of the classically modeled pentacene and its 22 pi electrons.

But new and improved hybrid algorithms are gaining momentum. In 2022, Google scientists unveiled one that could compute ground states for up to 120 interacting electrons in substances such as molecular nitrogen and solid diamond. The algorithm used a classical computer to explore random variations in the electron interactions, and a quantum computer to guide the classical system to a precise result. But it did not achieve enough accuracy for the researchers to claim a quantum advantage over classical approaches.

CHEMISTS ARE NOW pushing these hybrid setups toward the discovery of new materials and catalysts, and even understanding mysterious light-driven reactions. In a January report in *Nature Communications*, researchers at Phasecraft described yet another hybrid algorithm that harnesses a quantum computer to simulate the structure and electronic behavior of crystalline materials, whose repeating structures make them easier

to model. In one such analysis, Phasecraft researchers found that their new algorithm should require 1 million–fold fewer computational steps than existing VQEs to accurately model strontium vanadate, a promising new battery electrode material. Although quantum computers are not yet good enough for Phasecraft to apply the algorithm, it could in theory reveal ways to tweak strontium vanadate's structure and improve batteries.

The reaction surfaces of catalysts, which speed up chemical reactions, are another target for this early work. In a July 2023 preprint on arXiv, Quantinuum researchers reported using a hybrid setup to explore the chemical reactivity of platinum-based catalysts, which are commonly used in fuel cells to generate electricity by converting hydrogen and oxygen into water. Platinum is expensive and rare, so researchers would love to ramp up its catalytic speed, allowing fuel cells to use less of the metal, or better yet replace it altogether with a cheaper substance.

To do so they need to understand how the platinum works—how oxygen and hydrogen adsorb to the catalyst, how they transfer electrons and protons through intermediate compounds, and how they finally react to form water molecules, which then dissociate from the catalyst. The computations have proved too tall a task for classical computers alone. So, researchers led by Quantinuum quantum chemist David Muñoz Ramo improved the accuracy of their simulations. First they used classical computers to model how molecules adsorb and desorb from catalyst particles; then they applied their quantum computer to identify the most likely reaction pathway of the electrons and protons involved. Although the approach hasn't yet discovered new fuel cell catalysts, Muñoz Ramo says the results of such simulations should only grow more powerful as quantum computing hardware improves.

Quantum algorithms also enable researchers to investigate basic questions in chemistry. Last year, for example, quantum researchers simulated how light and matter interact, a process central to vision and photosynthesis. They targeted a photochemical reaction in which molecules absorb energy from photons and transfer it to a neighbor. The energy transfer occurs in mere femtoseconds, or quadrillionths (10^{15}) of a second, too fast to observe. Classical computers can simulate how multiple photons interact, but only a few at a time, because of the computational intensity.

So, Ting Rei Tan, a physicist at the University of Sydney, and colleagues used a trapped ion quantum computer to simulate how a single quantum "wave packet" of energy moves between neighboring molecules. That effectively slowed the process down 100 billion–fold and made it possible to simulate one of the events. With a more powerful quantum computer, the team should be able to model more of the reactions and surpass the classical technique. "We are approaching a quantum advantage," Tan says.

IN THE NEAR TERM, quantum computing could have its biggest impact in drug development. Today, developing a new drug takes an average of 12 years and costs more than $2 billion. Drug companies are looking for any advantage they can get in finding the next blockbuster, Edwards says. Already, Roche, Pfizer, Merck, Biogen, and other industry giants have formed early partnerships with

> ## "Once quantum computing capabilities improve, it will become an integral part of drug discovery."
>
> **Petrina Kamya**,
> Insilico Medicine Canada

quantum computing companies, hoping the new technology will accelerate discovery. "I'm absolutely convinced that it is coming," says Mark Fingerhuth, who heads R&D for drug developer ProteinQure.

Some of those partnerships are starting to generate early results. In September 2023, researchers at PASQAL and Qubit Pharmaceuticals posted a preprint describing a hybrid approach to tracking the water molecules that surround proteins, which can indicate the locations of drug-binding pockets. The researchers first narrowed the problem by using a classical algorithm to track the density of water molecules in and around a liver protein called major urinary protein-1 (MUP-1), which belongs to a class of proteins that has been considered undruggable. They then used PASQAL's quantum computer to pin down the specific location of water molecules in potential drug-binding pockets of MUP-1, setting the stage for using the same approach to identify druggable targets for proteins involved in diseases.

Meanwhile, in May 2023, researchers at Gero, another drug development company, reported in *Scientific Reports* that they used a quantum computer to more realistically simulate the electronic properties of likely drug targets, such as the distribution of positive and negative charges across molecules and the arrangement of weak chemical bonds called Van der Waals forces between neighboring atoms. They fed those constraints to artificial intelligence (AI) software running on classical computers, which came up with more than 2300 druglike molecules that could take aim at those targets. Although the results are just a proof of concept, Gero scientists noted how their quantum-AI hybrid showed its promise by homing in on chemical structures common to the best medicines. "If you solve the hard part with a quantum computer the other part becomes easy with classical AI," says Gero CEO Peter Fedichev.

A sharper picture of interactions between potential drug molecules and their protein targets is also the goal for drug developer Insilico Medicine. Insilico researchers reported in February that their hybrid algorithm, running on IBM's 16-qubit quantum computer, could help find new inhibitors of a cell-signaling protein called KRAS that's commonly mutated in cancers. After the algorithm had designed and ranked 1 million different potential KRAS inhibitors, the researchers synthesized 15 of the most promising candidates. Cell-based tests showed two of those compounds worked well, setting the stage for further testing.

Finding novel medicines isn't the only goal. Researchers at PASQAL also hope to forecast which drug candidates will fail. Even when would-be drugs excel in lab studies, many trigger toxic side effects when tested in people. Weeding out toxic drugs before human trials could save companies millions of dollars. In an initial attempt, Henry and his PASQAL colleagues used their 32-qubit computer to predict the toxicity of 286 compounds by modeling their structure in high resolution and comparing them with 349 compounds known to cause cancer in mice. In an April 2023 paper in *Physical Review A*, they reported that their quantum algorithm gave results comparable to the best classical alternatives. "We are solving a real problem with a real biochemistry data set," says Loïc Henriet, PASQAL's chief technology officer.

The early work is just a taste of what may come with bigger and better machines. Google and IBM have road maps suggesting scientists will soon have hundreds of thousands of qubits at their disposal. And Quantinuum says it's close to releasing a new quantum chip, trading in the racetrack for a larger 2D grid that can handle more of their high-fidelity ion qubits. Chemists have high hopes. "We think there is a lot of work to be done in this way to accelerate chemistry and drug discovery," Bilodeau says. "We are just at the inflection point."

The field of quantum computing itself stands to benefit, as researchers in other fields see that the exotic technology has down-to-earth payoffs. "Once quantum computing capabilities improve, it will become an integral part of drug discovery," says Petrina Kamya, president of Insilico Medicine Canada. "It's here to stay." ∎

INSIGHTS

POLICY FORUM

CLIMATE POLICY

No new fossil fuel projects: The norm we need

A social-moral norm against new fossil fuel projects has strong potential to contribute to achieving global climate goals

By **Fergus Green**[1], **Olivier Bois von Kursk**[2], **Greg Muttitt**[2,3], **Steve Pye**[3]

G
lobal production and use of fossil fuels continue to expand, making the goals of the Paris Agreement ever more difficult to achieve. Echoing calls made by climate advocates for years, the groundbreaking decision at the United Nations (UN) climate meeting in late 2023 (COP28) calls on parties "to contribute to…transitioning away from fossil fuels in energy systems." The normative case for ultimately phasing out fossil fuels is strong, and in some cases, it is feasible to phase out projects before the end of their economic life. However, the movement should focus on a more feasible, yet crucial, step on the road to fossil fuel phaseout: stopping fossil fuel expansion. Proponents of ambitious climate action should direct policy and advocacy efforts toward building a global "No New Fossil" norm, encompassing exploration for and development of new fossil fuel extraction sites, and permitting and construction of new, large-scale fossil fuel–consuming infrastructure.

We make the case for this norm in three steps. First, we show that no new fossil fuel projects are needed in a 1.5°C world: Existing fossil fuel capital stock is sufficient to meet energy demand in representative scenarios aligned with the Paris Agreement target of limiting global warming to 1.5°C. Second, we explain why preventing new fossil fuel projects is, generally, more economically, politically, and legally feasible than closing existing projects. The first two claims together justify a third, normative claim: that new fossil fuel projects ought not be permitted. It is this third claim that, we argue, ought

[1]Department of Political Science, University College London (UCL), London, UK. [2]International Institute for Sustainable Development, Geneva, Switzerland. [3]UCL Energy Institute, London, UK. Email: fergus.green@ucl.ac.uk

Pipe is laid during construction of a natural gas pipeline in Texas, USA.

found that no new fossil fuel extraction projects are needed in its Net Zero Emissions by 2050 (NZE) scenario (*1*). However, as a single scenario, this provides a limited guide for policy. Here, we assess a range of 1.5°C scenarios compiled for the Intergovernmental Panel on Climate Change's (IPCC's) Sixth Assessment Report (AR6) (*2*), by comparing them with data on capacity of existing projects, and we find that the IEA's conclusion is warranted. In addition to analyzing oil and gas extraction projects [coal extraction is excluded owing to data limitations; see supplementary materials (SM) for discussion], we go beyond the IEA to also assess the largest consuming segments, coal and gas power generation (see the figure).

Forecast data on existing and planned oil and gas production levels are derived using the Rystad Energy UCube, whereas forecasted capacity levels from gas and coal plants are derived from Global Energy Monitor datasets. The scenarios that we assess are the C1 scenarios (limiting warming to 1.5°C with low or no overshoot) reviewed in the IPCC's AR6 (*2*), including only those scenarios that do not exceed IPCC feasibility and sustainability thresholds on carbon sequestration (see SM). Such thresholds effectively exclude scenarios dependent on high levels of carbon sequestration technologies, such as carbon dioxide removal (CDR), which are unproven at scale and which, if they failed to materialize, would pose serious risks to the achievability of the Paris Agreement's temperature goals. For comparison, we also show the IEA's NZE scenario (*1*). Additional scenarios are considered in the SM.

Demand for oil and gas in the scenarios could be met from fields already in production or under development (see the figure). These findings are consistent with the IEA's conclusions based on the NZE scenario (*2*) and follow similarly from the vast majority of major credible 1.5°C scenarios (*3*) (see SM). Coal production needs are even lower in both presented scenarios, declining by over 90% by 2040 (see SM). There is far too much coal-fired power generation capacity already in existence relative to 1.5°C-consistent capacity, which plummets over the coming decade in the analyzed scenarios (see the figure). Adding those new coal plants that are under construction or at an earlier stage of planning would only widen this gap. Finally, existing and under-construction gas power infrastructure is sufficient to meet projected demand under most scenarios.

Regional disaggregation of scenarios' data shows that the only exceptions to the general conclusion that no new capacity is required are due to minor discrepancies in gas power capacity and modeled demand in India and Sub-Saharan Africa. However, shifts in market conditions for renewables have now effectively priced out gas in India, while African governments have economic and political incentives to avoid risks of stranded fossil fuel assets. In any case, new gas power plants could not be justified within the analyzed 1.5°C scenarios if the availability of CDR did not materialize to the extent that relevant scenarios rely on it to counterbalance fossil fuel emissions, or if the highly ambitious pace of coal power phaseout in these model projections cannot be achieved (see SM).

Our analysis considers the energy production over time that is associated with a given set of infrastructure and compares this to mitigation scenarios. An alternative analytical approach would compare fossil fuel reserves or cumulative lifetime production with carbon budgets. Applying the latter approach, the IPCC, in its AR6, indicated that continuing to operate existing fossil fuel–consuming infrastructure at current levels would, by itself, generate enough carbon dioxide emissions to exhaust the remaining 1.5°C carbon budget (*2*). Research since the AR6 reaches the same conclusion for fossil fuel–extracting infrastructure (*4*).

In short, existing fossil fuel infrastructure is sufficient to meet energy demand in the vast majority of scenarios consistent with the 1.5°C objective. In theory, the same outcome could be achieved with more new projects coming online if these are offset by retiring more existing infrastructure before the end of its economic life. However, the economic, political, and legal considerations that we adduce in the next section show that this strategy would be misguided.

POLITICAL ECONOMY OF NEW VERSUS EXISTING PROJECTS
In this section, we synthesize evidence from economics, political science, and law that explains why it is, generally, more feasible to restrict new fossil fuel projects than to close existing projects early. The evidence provided is widely accepted in each field but in our view has been insufficiently appreciated in the debate over fossil fuels and climate change.

For firms, a future fossil fuel project represents an investment prospect, which is weighed against the returns that could be obtained from alternative investments. But once construction has begun and capital sunk, the proponent's economic interests

to form the substantive content of the new norm that we propose. We draw on norm diffusion theory from the field of international relations to argue that efforts to stop fossil fuel expansion are conducive to the generation and spread of such a norm. By contrast, initiatives targeting a full fossil fuel phaseout (which do not differentiate between new and existing projects) are less conducive to norm-building. We conclude by explaining how the institutionalization of a No New Fossil norm would make it easier to phase down fossil fuels and ultimately achieve the goals of the Paris Agreement.

NO NEW FOSSIL FUEL PROJECTS IN A 1.5°C WORLD
Existing fossil fuel capital stock is sufficient to meet energy demands implied by representative 1.5°C scenarios; arguments for new projects assume that governments will not meet their shared climate goals. The International Energy Agency (IEA) has

lie in continuing to operate that project for as long as possible, so long as the product can be sold at a price greater than the marginal operating cost (even if that price is less than required to recoup the capital invested, because ongoing production will reduce losses). This economic dimension of "infrastructure lock-in" is a key reason why climate mitigation costs are higher in scenarios where mitigation is delayed than in those where it begins immediately (5).

To protect their sunk investments, firms tend to lobby more intensely against environmental regulations that diminish the value of their existing assets than they do against regulations that would diminish the value of hypothetical future investments, in which their capital is not yet sunk. Similarly, trade unions work mainly to support the interests of their members, and so lobby harder to protect their members' existing jobs than for hypothetical future jobs from new projects. Moreover, publics often oppose new developments for multiple reasons (see below) but are generally more likely to tolerate operational projects, especially where they generate local economic benefits. Because of these political pressures, legislators that support environmental regulation find it politically easier to enact more stringent regulations on new entrants (here, proponents of new fossil fuel projects in a given market) than on incumbents (6).

There are often also legal barriers to governments enacting regulations that decrease the value of existing investments. Most notably, foreign investors in fossil fuel projects can often avail themselves of strong protections against regulatory reforms that reduce expected profits, and can enforce these claims in private tribunals for investor-state dispute settlement, under international trade and investment treaties (7). By contrast, decisions to approve or reject a new project are not legally constrained in this way.

It is, therefore, generally more economically, politically, and legally feasible to stop new fossil fuel projects than to close existing capacity early.

A "NO NEW FOSSIL" NORM

The analysis in the preceding two sections justifies a normative claim: that new fossil fuel projects ought not be permitted. But how can this be achieved? We argue that state and nonstate proponents of ambitious climate action should engage in policy and advocacy aimed at diffusing and institutionalizing a social-moral norm against new fossil fuel projects.

A social-moral norm is a standard of appropriate behavior that is expected of

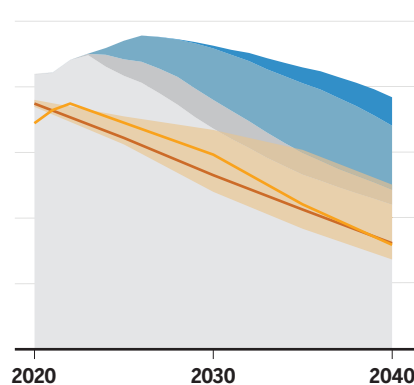## Forecasted global demand, extraction, and generation

Graphs reflect forecasted global primary energy production from gas and oil (panels 1 and 2) and capacity of unabated coal and gas power plants (panels 3 and 4) compared with energy demand based on IEA NZE and Selected IPCC 1.5°C scenarios (n = 26). See supplementary materials.
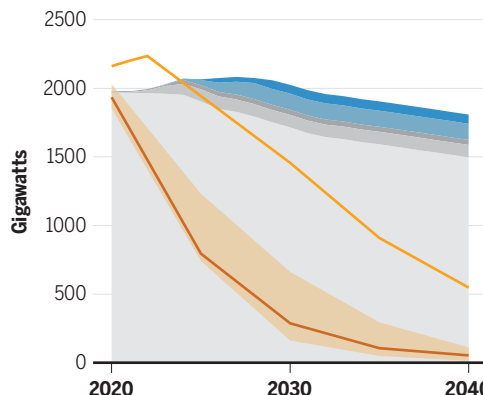

1 Gas extraction
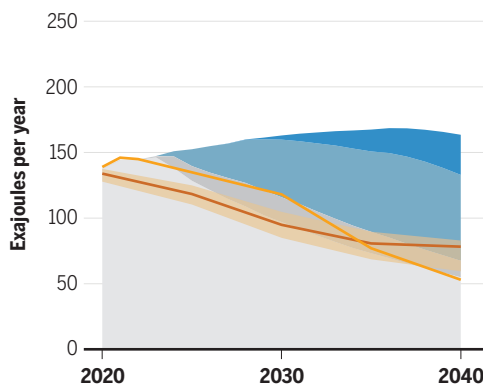
2 Oil extraction

- New exploration
- New field
- Field under development
- Producing fields
- Selected IPCC 1.5°C pathways including interquartile range
- IEA NZE 2023

3 Unabated coal power generation capacity

4 Unabated gas power generation capacity
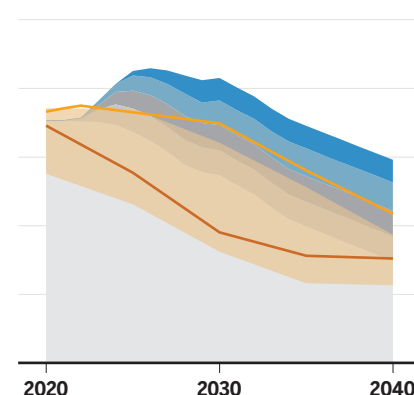
- Announced
- Pre-permit
- Permitted
- In construction
- Operating
- Selected IPCC 1.5°C pathways including interquartile range
- IEA NZE 2023

IEA, International Energy Agency; IPCC, Intergovernmental Panel on Climate Change; NZE, Net Zero Emissions.

an agent with a particular identity (8). Historical processes of social-moral norm change, though not perfectly analogous, are instructive for climate action to restrict fossil fuels, because they show how activities that were once profitable for powerful firms or geostrategically valuable for powerful states—such as trading in slaves or testing nuclear weapons—can become taboo (9). Committed groups of people, often acting through civil society organizations, generated these shifts by highlighting the harms these practices caused and mobilizing elite supporters and mass social movements to pressure governments to ban them. Ultimately, states institutionalized these new norms by enshrining bans in international treaties and domestic laws (8).

Elements of a No New Fossil norm are

already emerging. Member governments of the Beyond Oil and Gas Alliance (BOGA) have agreed to stop issuing new oil and gas exploration and production licenses, and Powering Past Coal Alliance (PPCA) members have agreed to a moratorium on new coal power stations without operational carbon capture and storage. In the Clean Energy Transition Partnership agreed at COP26, governments and financial institutions agreed to stop providing international public finance for fossil fuels (which largely affects new projects). And the UN secretary-general has repeatedly called on countries to stop new fossil fuel projects (10).

We argue that proponents of ambitious climate action should build on these nascent efforts by mobilizing for a No New Fossil norm. Specifically, we urge govern-

ments to announce that they will no longer permit new fossil fuel exploration, production, or power generation projects (including expansions of existing projects) and to take whatever legislative or administrative action is necessary to give effect to such a policy. Ideally, such action would take the form of a legislated ban, which would send a clear signal about the inappropriateness of new fossil fuel projects and would apply to successor administrations (*11*). Additional measures, including restrictions on finance and on subsidies to new projects, and measures to enable a just transition away from fossil fuels, would complement and facilitate such bans. Elite proponents of climate action outside of government, such as opposition politicians, senior officials from international organizations, leaders from civil society, and the wider climate movement, should advocate such government action. Both state and nonstate proponents should also seek to build the No New Fossil norm through international "soft law" instruments, such as COP decisions and declarations in other intergovernmental forums.

The fossil fuel industry and large fossil fuel–consuming and –producing states will inevitably continue to resist such initiatives. But there are good reasons to think that concerted action could build a No New Fossil norm that diffuses widely. First, the norm's framing is conducive to such diffusion: Norms are most resonant when they are framed in terms of simple demands for powerful actors to cease or ban harmful activities (*8*). Second, the focus on new projects structures the interest group contest in a way that reduces the power asymmetry between pro- and anti-fossil fuel forces. Because new fossil fuel projects cause multiple types of harms—not only through climate change but also through adverse local environmental, health, and social impacts—calls to stop such projects provide a focal point around which opponents with different grievances can mobilize (*9*). Meanwhile, the fossil fuel industry's alliances are more limited in respect of new projects for the reasons outlined in the previous section.

As more states adopt the No New Fossil norm, "holdout" states (those that continue to enable new fossil fuel projects) will face intensifying political pressure from other countries, and (in those countries with robust civil and political freedoms) from domestic civil society, to conform to the norm (*9*). Such pressure would push holdout governments to the international negotiating table seeking international concessions for committing to stop new projects and/or reciprocal commitments from other states (to address concerns about cross-border consumption or production "leakage").

Such concessions and reciprocal commitments could ultimately be provided for in a multilateral treaty prohibiting new projects (*12*). A treaty would also facilitate the emerging norm's institutionalization and its equitable implementation—for instance, by providing for finance and technology support for poorer nations, ensuring that all people have access to clean energy sources for decent living standards (*1, 12, 13*). A promising near-term building block toward such a treaty is a "club" arrangement (like BOGA and PPCA), involving a nonbinding agreement among a coalition of like-minded states and nonstate actors, which would aim to enlist larger fossil fuel producer and consumer states through persuasion, socialization, and incentives (*9, 12*). That the PPCA's membership has expanded to include Germany and the United States proves this logic has merit. Nor is the logic limited to the Global North. For instance, President Petro of Colombia, a substantial producer of oil and coal, has committed to stop fossil fuel expansion and transition away from existing production, signing up to both the PPCA and BOGA (and in the latter case, receiving financial support from the BOGA Fund).

Any such international cooperative arrangement would depend on states building mutual trust and confidence amid an increasingly fragmented global order. A historically successful strategy for doing so involves adopting commitments that are quickly and easily verifiable by third parties and increasing their ambition as performance is verified and trust is built (*14*). In this respect, a No New Fossil norm has two further advantages relative to a full phaseout. First, a commitment to cease or ban something creates an expectation of immediate policy action, for which the leaders making the commitment can be held accountable. This contrasts favorably with long-term targets to reduce greenhouse gas emissions or phase out fossil fuels, because leaders can all too easily "commit" to such targets rhetorically, safe in the knowledge that someone else will be in charge when the performance falls due. Second, because issuing fossil fuel licenses, permits, and other consents involves public processes, and because building fossil fuel infrastructure has a large physical footprint, compliance with a No New Fossil norm can readily be monitored and verified by third parties, such as journalists, nongovernmental organizations, and other states (*15*).

Ultimately, states will need to largely or entirely phase out fossil fuels. By building the necessary trust and confidence, successful cooperative efforts to stop new projects would make this more ambitious endeavor easier. Additionally, the successful institutionalization of a No New Fossil norm would substantially weaken the fossil fuel industry: An industry that is not expanding is an industry in decline, and declining industries find it harder to attract finance and win political favor. In short, efforts to construct a No New Fossil norm have great potential to be a major step on the path to achieving the goals of the Paris Agreement. ∎

REFERENCES AND NOTES

1. IEA, "Net Zero Roadmap: A Global Pathway to Keep the 1.5°C Goal in Reach, 2023 Update" (2023); https://www.iea.org/reports/net-zero-roadmap-a-global-pathway-to-keep-the-15-0c-goal-in-reach.
2. IPCC, "Sixth assessment report: Working Group III: Mitigation of climate change" (2022); https://www.ipcc.ch/report/ar6/wg3/.
3. O. Bois von Kursk, G. Muttitt, A. Picciariello, L. Dufour, "Navigating Energy Transitions: Mapping the Road to 1.5°C" (International Institute for Sustainable Development, 2022); https://www.iisd.org/publications/report/navigating-energy-transitions.
4. K. Trout *et al.*, *Environ. Res. Lett.* **17**, 064010 (2022).
5. K. C. Seto *et al.*, *Annu. Rev. Environ. Resour.* **41**, 425 (2016).
6. N. O. Keohane, R. L. Revesz, R. N. Stavins, *Harvard Environ. Law Rev.* **22**, 313 (1998).
7. K. Tienhaara, R. Thrasher, B. A. Simmons, K. P. Gallagher, *Science* **376**, 701 (2022).
8. M. Finnemore, K. Sikkink, *Int. Organ.* **52**, 887 (1998).
9. F. Green, *Clim. Change* **150**, 103 (2018).
10. U. N. Secretary General, "Secretary-General's video message for press conference to launch the Synthesis Report of the Intergovernmental Panel on Climate Change" (Interlaken, Switzerland, 20 March 2023); https://www.un.org/sg/en/content/sg/statement/2023-03-20/secretary-generals-video-message-for-press-conference-launch-the-synthesis-report-of-the-intergovernmental-panel-climate-change.
11. F. Green, *Nat. Clim. Chang.* **8**, 449 (2018).
12. H. van Asselt, P. Newell, *Glob. Environ. Polit.* **22**, 28 (2022).
13. Civil Society Equity Review, "An Equitable Phase Out of Fossil Fuel Extraction" (Civil Society Equity Review Coalition, 2023); https://www.equityreview.org/extraction-equity-2023.
14. R. Greenspan Bell, M. S. Ziegler, B. Blechman, B. Finlay, T. Cottier, "Building International Climate Cooperation: Lessons from the Weapons and Trade Regimes for Achieving International Climate Goals," R. Greenspan Bell, M. S. Ziegler, Eds. (World Resources Institute, 2012); https://www.wri.org/research/building-international-climate-cooperation.
15. F. Green, D. Kuch, *Glob. Environ. Polit.* **22**, 48 (2022).

CHEMISTRY

Breaking down microdroplet chemistry

Charged microdroplets accelerate mineral disintegration

By **R. Graham Cooks** and **Dylan T. Holden**

Charged microdroplets are commonly observed in clouds, sea spray, and other natural aerosols. The chemistry that occurs at the air-water interface of these droplets is often distinct from that observed in bulk solution, which is of considerable interest because chemical reactions can be accelerated at this boundary (1, 2). This may have implications for environmental processes such as the weathering of rocks, which contributes to soil formation. On page 1012 of this issue, Spoorthi et al. (3) report that micrometer-scale mineral particles can rapidly break down into nanoparticles when in charged aqueous microdroplets (see the figure). This points to a potential role for atmospheric water droplets in the natural disintegration of minerals.

To examine material degradation, Spoorthi et al. borrowed methodology used to accelerate bond-forming chemical reactions. By spraying an aqueous suspension of microparticles of natural minerals, the authors produced nanoparticles of minerals in high yield. Specifically, Spoorthi et al. used an electrospray device to emit a jet of liquid droplets (by applying high voltage) containing mineral particles of natural quartz, ruby, or synthetic alumina that ranged in size from 1 to 5 μm in diameter. The authors observed the production of nanoparticles that were 5 to 10 nm in diameter. Moreover, the fragmentation occurred in approximately 10 ms.

Such material degradation and chemical synthesis experiments are united by the extremes of chemical reactivity that occur at the air-water interface, where reagents are partially solvated (4). Whether formed through nebulization, splashing from a surface, or other means, microdroplet populations will include droplets with nonzero net charges. The small radius of curvature in a microdroplet produces a very strong electric field (5) that can support a double layer of electric charge at the air-water interface. The change in geometry (radius of curvature)

converts a two-dimensional air-water interface with limited electric field into a sphere with an electric field of a strength approaching the order of chemical bond energies (3 to 4.5 eV/Å). Coulombic fission (the splitting of charged microdroplets due to excess charge overcoming the surface tension) and evaporative processes further increase the surface area, reduce the radius of curvature, and augment the surface electric field of the droplet.

The unusual chemical nature of the air-water interface results in much remarkable chemistry. For example, amino acids in water undergo dehydration to form peptides in this environment (6), whereas bulk water simply solvates amino acids. The superacidic interface activates amino acids and removes water to yield peptides. In addition to such acid-base reactions, redox chemistry results from the formation of strong oxidants and reductants from water at the interface. For example, a high hydronium ion (H_3O^+) concentration at the interface derived from fleetingly charged surface water molecules ($H_2O^{+\bullet}/H_2O^{-\bullet}$) coexists with oxidative species such as hydrogen peroxide (H_2O_2) and OH•. These redox species enable a variety of spontaneous chemical trans-
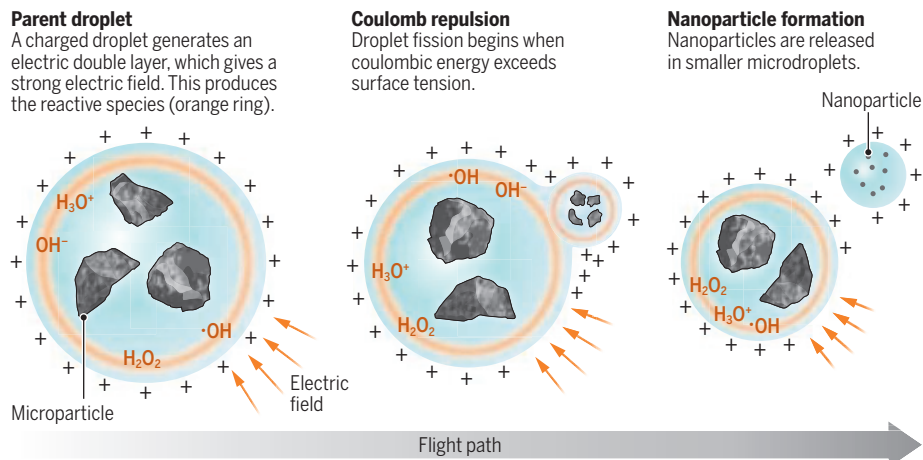
formations, including carbon-oxygen (C-O) bond cleavage in phosphonates, which yields the corresponding phosphonic acid (7), and in the Baeyer-Villiger oxidation of aryl ketones to give esters (8). These considerations thereby enable simultaneous acid-base and oxidation-reduction chemistry in a single population of droplets (7).

Through their study, Spoorthi et al. have added natural weathering to a list of processes in which accelerated interfacial microdroplet reactions play an important role. Other processes include those in the atmosphere, both natural and anthropogenic, the latter typified by pollution that involves nitrate photochemistry (9). A substantial number of accelerated catalyst-free microdroplet reactions form the basis for chemical syntheses that generate a variety of small molecules (10), including the facile and high-throughput functionalization of drugs. This latter approach can be scaled up so that microdroplet reactions produce substantial small-molecule products. Prebiotic chemistry, including peptide and nucleotide formation, is another process that is accelerated at the microdroplet air-water interface (11).

The millisecond timescale of quartz degradation reported by Spoorthi et al. matches the known microsecond-to-millisecond timescale for accelerated bond-formation and bond-cleavage chemical reactions in microdroplets (1). This reinforces the conclusion that the chemical basis for accelerated weathering lies in the powerful acidic and hydrolytic nature of the air-water interface. The authors further suggest a role for the superacid interface in inducing slippage at crystal plane boundaries in quartz and ruby fragmentation. Their simulations show that individual protons inserted into the slip configuration mineral

Department of Chemistry, Purdue University, West Lafayette, IN, USA. Email: cooks@purdue.edu

Micro-to-nano transitions in minerals at the air-water interface

Reactions that promote mineral disintegration are accelerated at the air-water interface of microdoplets. Key reactive species are the result of the effects of a high electric field at the surface of the water droplets.

Parent droplet
A charged droplet generates an electric double layer, which gives a strong electric field. This produces the reactive species (orange ring).

Coulomb repulsion
Droplet fission begins when coulombic energy exceeds surface tension.

Nanoparticle formation
Nanoparticles are released in smaller microdroplets.

Flight path

GRAPHIC: K. HOLOSKI/SCIENCE

matrices induce substantial structural deformations. The inclusion of multiple local protons results in the formation of small silicate fragments or a "chipping away" of the minerals. Microdroplets splashing onto mineral particles also results in surface roughening.

The interface may also facilitate the oxidization of silyl ethers to produce silicates during quartz fragmentation. This mechanism is supported by parallels in accelerated microdroplet reactions with silicate silicon-oxygen (Si-O) bond cleavage and oxidation in C-O chemistry (7, 8). As for the nature of the oxidizing agent at air-water interfaces, the role of the water radical cation (12) has been implicated in C-O bond cleavages, carbon-hydrogen (C-H) bond activation, and other oxidation reactions. Spoorthi et al. provide computational support for the hypothesis that $H_2O^{+\bullet}$ may facilitate mineral degradation by abstracting electrons from silica.

Other processes may rely on accelerated reactions at the air-water interface of microdroplets. For example, evidence supports a role in accelerating enzymatic reactions, such as peptide proteolysis by trypsin (13). This raises the question of whether intracellular reactions might also be accelerated because air-water interfaces with a small radius of curvature are associated with local changes in the hydrophilicity of amino acids near active sites of enzymes. This argument is especially relevant given the role of electric fields on enzyme reaction rates (14). Another question is whether it is possible that inverted droplets—air droplets in aqueous solution—might also show accelerated reactions. Such microdroplets are formed during bubble injection from breaking waves. Accelerated reactions occur at electrode surfaces (15) and raise questions about whether redox reactions and electrodeposition might be used to improve battery performance and whether the microparticle-to-nanoparticle transformations demonstrated by Spoorthi et al. might also play a useful role here. ∎

REFERENCES AND NOTES

1. Z. Wei et al., Annu. Rev. Phys. Chem. 71, 31 (2020).
2. D. Ben-Amotz, Science 376, 800 (2022).
3. B. K. Spoorthi et al., Science 384, 1012 (2024).
4. X. Yan et al., Angew. Chem. Int. Ed. 55, 12960 (2016).
5. H. Hao et al., Nat. Commun. 13, 280 (2022).
6. D. T. Holden et al., Proc. Natl. Acad. Sci. U.S.A. 119, e2212642119 (2022).
7. L. Qiu, R. G. Cooks, Angew. Chem. Int. Ed. 134, e202210765 (2022).
8. D. Gao et al., Chem. Sci. 10, 10974 (2019).
9. P. Kim et al., J. Phys. Chem. Lett. 14, 10677 (2023).
10. Y. Meng et al., J. Am. Chem. Soc. 35, 19202 (2023).
11. I. Nam et al., Proc. Natl. Acad. Sci. U.S.A. 115, 36 (2018).
12. L. Qiu, R. G. Cooks, Angew. Chem. Int. Ed. 136, e202400118 (2024).
13. X. Zhong et al., Nat. Commun. 11, 1049 (2020).
14. C. Zheng et al., Nat. Chem. 15, 1715 (2023).
15. K. J. Vannoy et al., Proc. Natl. Acad. Sci. U.S.A. 118, e2025726118 (2021).

SOCIAL SCIENCE

A broader view of misinformation reveals potential for intervention

Misleading claims from credible sources can be more damaging than blatant falsehoods

By **Sander van der Linden** and **Yara Kyrychenko**

Misinformation is viewed as a threat to science, public health, and democracies worldwide (1). Experts define misinformation as content that is false or misleading, such that it contains some facts but is otherwise manipulative (2, 3). Yet, the importance of this distinction has remained unquantified. On pages 978 and 979 of this issue, Allen et al. (4) and Baribi-Bartov et al. (5), respectively, report on the impact of misinformation on social media. Allen et al. find that Facebook content not flagged as misinformation but still expressing misleading views on vaccinations had a much bigger effect on vaccination intentions compared with outright falsehoods because of its greater reach. Baribi-Bartov et al. investigate who is responsible for spreading misinformation about voting on X (previously Twitter), identifying highly networked citizens ("supersharers") who supply about a quarter of the fake news received by their followers. These findings highlight new ways to intervene in misinformation propagation.

The global spread of misinformation can have deleterious consequences for society, including election denial and vaccine hesitancy (1, 2, 6). Yet, some scholars have criticized such claims, noting that quantitative evidence of the causal impact of misinformation—and those who spread it—is often lacking and limited to self-reported data or laboratory conditions that may not generalize to the real world (7). Although this is a valid concern, it would neither be ethical nor feasible to randomly assign half the population to misinformation about vaccines or elections to determine whether that changes vaccine uptake or election outcomes. The tobacco industry weaponized the lack of direct causal evidence for the impact of smoking on lung cancer by manipulating public opinion and casting doubt on the negative health consequences of smoking, even though plenty of other good evidence was available to inform action (8). It is therefore important to have realistic expectations for standards of evidence.

Allen et al. combine high-powered controlled experiments with machine learning and social media data on roughly 2.7 billion vaccine-related URL views on Facebook during the rollout of the first COVID-19 vaccine at the start of 2021. Contrary to claims that misinformation does not affect choices (7), the causal estimates reported by Allen et al. suggest that exposure to a single piece of vaccine misinformation reduced vaccination intentions by ~1.5 percentage points. Particularly noteworthy is that when predicting how big an impact misinformation exerts on vaccination intentions, what mattered most was not the veracity of the article but rather the extent to which the article claimed that vaccines were harmful to people's health. A key example of such true-but-misleading content is the following headline from the *Chicago Tribune*: "A 'healthy' doctor died two weeks after getting a COVID-19 vaccine; CDC is investigating why." This headline is misleading because the framing falsely implies causation where there is only correlation (i.e., there was no evidence that the vaccine had anything to do with the death of the doctor). Nonetheless, this headline was viewed by nearly 55 million people on Facebook, which is more than six times the exposure of all fact-checked misinformation combined.

In the final step, Allen et al. assign weight to the treatment (i.e., persuasion) effect (estimated with a machine learning classifier) by looking at the number of exposures for each URL on the platform. To accomplish this, they obtained 13,206 URLs about COVID-19 vaccines on Facebook in 2021. By differentiating URLs flagged as misinformation by fact-checkers from those not flagged but still hesitancy inducing, the authors compared the impact of false versus misleading information. About 98% of the total 500 million URL views came from misleading content rather than content that was fact-checked as false. When taking the product of exposure and treatment

Department of Psychology, Downing Site, University of Cambridge, Cambridge, UK.
Email: sander.vanderlinden@psychol.cam.ac.uk

The impact of fake and misleading information on social media

Misleading information makes up a much larger proportion of misinformation than fact-checked fake news and has a higher impact on society because more people get exposed to it, potentially through supersharers. Interventions to reduce the public's susceptibility to misleading techniques and the reach of supersharers could lower the impact of misinformation. Darker nodes represent fake and misleading news supersharers, and lighter nodes represent members of the public exposed to fake or misleading news.
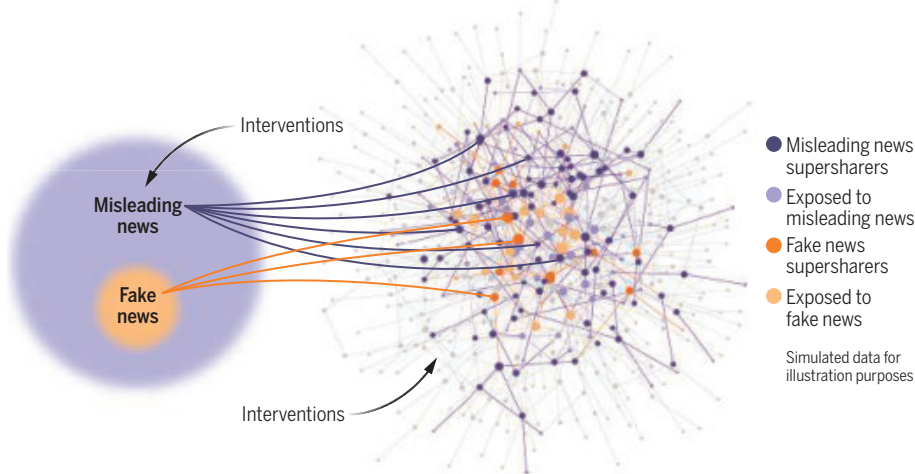
impact, the authors estimate that vaccine-skeptical content not flagged by fact-checkers reduced vaccination intentions by 2.8 percentage points relative to just 0.05 percentage points for blatant falsehoods. In other words, the negative impact of misleading content on the intention to receive a COVID-19 vaccine was 46 times that of content flagged as misinformation. Considering the 233 million Facebook users, preventing exposure to this type of content would have resulted in at least 3 million more vaccinated Americans.

One important caveat is that intentions do not always translate into behavior, but the above predictions account for this by assuming that the impact of misinformation on actual vaccination rates is about 60% of the effect on the intention to get vaccinated, which is consistent with estimates of the intention-behavior gap (9). Moreover, these estimates do not include visual misinformation or content shared on other social media platforms and thus likely represent a lower bound for the true impact of misinformation.

The findings from Allen et al. do not address who is spreading most of the misinformation, which is important to understand because supersharers undermine democratic representation by flooding the online space with false information. Baribi-Bartov et al. profile 2107 registered US voters (0.3% of the total panel of 664,391 voters matched to active Twitter users) who were responsible for 80% of misinformation shared on X during the 2020 US presidential election. One of the key insights from their study is that these supersharers receive more engagement than regular users and are highly connected, ranking in the 86th percentile of network influence. The authors also mapped the content that users in the panel are exposed to based on their following, which revealed that supersharers supply nearly 25% of the misinformation available to their followers. In terms of their profile, supersharers had a higher likelihood of being (female) Republican, white, and older (average of 58.2 years of age). Although consistent with other preliminary work in the context of US elections (10), this profile is unlikely to be universal and thus may not generalize to other contexts.

An important difference between the two studies is that whereas Allen et al. draw attention to misleading news from mainstream sources, Baribi-Bartov et al. focus on the narrower class of fake news websites. An important area for future research would therefore be to consider supersharers of misleading information, regardless of the source (see the figure). For example, the Chicago Tribune headline was published by a mainstream high-quality source but was heavily pushed by anti-vaccination groups on Facebook (11), who could be supersharers and responsible for a substantial portion of the traffic. These results also broadly align with other recent work that identified 52 US physicians on social media as supersharers of COVID-19 misinformation (12). Baribi-Bartov et al. do not speculate on motives, but related work finds that supersharers are diverse, including political pundits, media personalities, contrarians, and antivaxxers with personal, financial, and political motives for spreading untrustworthy content (10).

Although research studies often define misinformation as a set of stimuli that have been fact-checked as true or false (3, 13), the most persuasive forms of misinformation are likely misleading claims published by mainstream sources subsequently pushed by well-networked supersharers. This has considerable ramifications for designing interventions to counter misinformation, most of which are focused on blatant falsehoods (13). One option is to suppress, flag, or moderate content, given that supersharers represent a tiny fraction of the population but have the potential to cause outsized harm. The downside is that such an approach often raises concerns about free speech. Another option is psychological inoculation or pre-bunking (14), which specifically targets manipulation techniques often present in true-but-misleading content, such as polarization, fearmongering, and false dichotomies. Inoculation preemptively exposes users to a weakened dose of the tactic to prevent full-scale manipulation and has been scaled on social media to millions of users. For example, short videos alerting users to false dichotomies and decontextualization have been implemented as YouTube advertisements (15) before people are exposed to potential misinformation. Social media companies could identify supersharers and inoculate them and their networks against such manipulation techniques. ∎

REFERENCES AND NOTES

1. S. Lewandowsky et al., Curr. Opin. Psychol. **54**, 101711 (2023).
2. S. van der Linden et al., "Using Psychological Science to Understand and Fight Health Misinformation: An APA Consensus Statement" (American Psychological Association, 2023); https://www.apa.org/pubs/reports/misinformation-consensus-statement.pdf.
3. C. S. Traberg, Nature **606**, 653 (2022).
4. J. Allen, D. J. Watts, D. G. Rand, Science **384**, eadk3451 (2024).
5. S. Baribi-Bartov, B. Swire-Thompson, N. Grinberg, Science **384**, 979 (2024).
6. G. Pennycook, D. G. Rand, HKS Misinform. Rev. 10.37016/mr-2020-51 (2021).
7. S. Altay, M. Berriche, A. Acerbi, Soc. Media Soc. **9**, 20563051221150412 (2023).
8. U. K. H. Ecker et al., PsyArXiv 10.31234/osf.io/8a6cj (2024).
9. T. L. Webb, P. Sheeran, Psychol. Bull. **132**, 249 (2006).
10. M. R. DeVerna et al., https://arxiv.org/abs/2207.09524 (2024).
11. J. Benton, "Facebook sent a ton of traffic to a Chicago Tribune Story. So why is everyone mad at them?" (Neiman Lab, 2021); https://www.niemanlab.org/2021/08/facebook-sent-a-ton-of-traffic-to-a-chicago-tribune-story-so-why-is-everyone-mad-at-them/.
12. S. Sule et al., JAMA Netw. Open **6**, e2328928 (2023).
13. S. van der Linden, Nat. Med. **28**, 460 (2022).
14. C. Lu et al., J. Med. Internet Res. **25**, e49255 (2023).
15. J. Roozenbeek et al., Sci. Adv. **8**, eabo6254 (2022).

CANCER

Germline variants alter immune surveillance

Germline-derived epitopes shape tumor development through immunoediting

By **Nicola Waddell** *and* **Venkateswar Addala**

The formation of tumors is complex and multifaceted, involving cancer cell–intrinsic and –extrinsic factors. An important influence on tumorigenesis is the immune system, by which immune surveillance (and subsequent elimination) provides a selective pressure that causes the evolution of tumor cells to evade detection (immunoediting). Cancer immunoediting involves three phases: immunosurveillance to eliminate tumor cells; the coexistence of tumor and immune cells through equilibrium; and immune evasion, in which tumor cells escape immune control (*1*). Tumor-specific neoantigens, formed as a result of somatic mutations that arise in cancer cells (*2*), are an important component of immunosurveillance because they can determine the immunogenicity of a cell and thus whether it is recognized by T cells to elicit an immune response. On page 975 of this issue, Houlahan *et al.* (*3*) report that epitopes derived from germline variants contribute to human breast cancer formation by modulating immunoediting.

The germline genome can influence tumorigenesis in a number of ways. The variants within an individual's genome can influence their lifetime risk of tumor development. For example, rare pathogenic germline variants in cancer-susceptibility genes are linked to an increased risk of cancer. Moreover, loci associated with various types of cancer have been identified by genome-wide association studies (*4*) and have enabled the development of polygenic risk scores, which summarize the estimated effect of multiple germline variants to provide numerical indicators of disease risk. Additionally, genetic determinants of cancer risk have been associated with the acquisition of somatic mutations during tumor development through, for example, increasing the propensity for mutational processes that result in patterns of somatic mutations known as mutation signatures (*5*). A notable example from breast cancer is the presence of deleterious germline variants in the DNA damage response genes *BRCA1* or *BRCA2* being associated with the development of somatic mutation signatures that are associated with deficient homologous recombination (a DNA repair pathway in which BRCA1 and BRCA2 function) (*6*). Moreover, germline variants in the melanocortin 1 receptor (*MC1R*) gene—which is linked to cutaneous melanoma risk, freckling, and sun sensitivity—influence somatic mutation burden and the prevalence of ultraviolet (UV) radiation–associated mutation signatures (*7*).

During tumor development, the acquisition of somatic oncogenic mutations is also influenced by the germline genome in a variety of cancer types. Cancer-associated germline genomic patterns, which are similar to somatic mutation signatures but estimated from information about the sequence context of germline variants, have been implicated in the selection of somatic mutations in specific genes (*8*). Moreover, germline variants in certain genes have been linked to the presence of somatic mutations in other genes; for example, germline variants in RNA binding fox-1 homolog 1 (*RBFOX1*) have been linked to an increased risk of acquiring oncogenic somatic mutations in the splicing factor 3b subunit 1 (*SF3B1*) gene. These genes encode RNA binding proteins involved in splicing, and when variants in *RBFOX1* and somatic mutation in *SF3B1* co-occur, they drive tumorigenesis by altering the splicing of several genes that contribute to cellular proliferation and metabolism (*9*). Additionally, germline variants within the 19p13.3 locus, which contains the G protein subunit α11 (*GNA11*) gene, have been linked to an increased likelihood of somatic loss-of-function mutations in the tumor suppressor gene phosphatase and tensin homolog (*PTEN*). This is thought to occur through an increase of *GNA11* expression, leading to an increase in mammalian target of rapamycin (mTOR) signaling, which is magnified when *PTEN* is lost, resulting in the promotion of tumor growth (*9*).

An emerging role for the germline genome is in influencing the immune system (*10*). For example, a high variation of human leukocyte antigen genotypes within the germline results in a diverse set of major histocompatibility complex molecules that present antigen. This diversity has been linked to the presentation of a wide range of neoantigen-derived peptides, T cell activation, and cancer cell elimination (*10*) and is associated with a lower risk of developing certain cancers (*11*) and a better patient response to immune checkpoint blockade (ICB) (*12*), which relies on reactivating T cells to cancer cells. Furthermore, germline

Germline variants and immunoediting in tumor development

Cells that amplify an oncogene with a high germline epitope burden (GEB) are more likely to be eliminated by the immune system than those that amplify oncogenes with a low GEB (top). Some cells with a high GEB can develop an immune-suppressive or immune-evasive phenotype, which allows them to escape immunosurveillance (bottom).
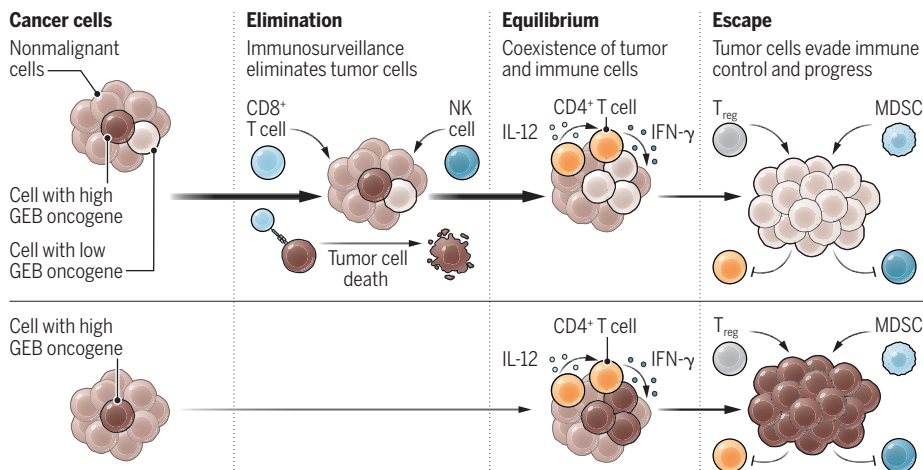
IFN-γ, interferon-γ; IL-12, interleukin 12; MDSC, myeloid-derived suppressor cell; NK, natural killer; T$_{reg}$, regulatory T cell.

Cancer Program, QIMR Berghofer Medical Research Institute, Brisbane, QLD, Australia. Email: nic.waddell@qimrberghofer.edu.au

GRAPHIC: A. MASTIN/*SCIENCE*

variants in certain loci are proposed to be associated with immune cell composition in the tumor microenvironment (13) and patient response to ICB treatment (14). However, how the germline genome alters the immune system to influence the selection of somatic mutations and type of tumors that occur is not clear.

Houlahan et al. analyzed genome sequence data from 4918 human primary breast cancers to propose that the germline genome alters cancer immunoediting, which results in a preference for certain breast cancer subtypes to arise in individuals. They showed that germline variants present in proto-oncogenes could produce immunogenic (detectable by immune system) epitopes and that the germline epitope burden (GEB), or number of immunogenic germline epitopes in a gene, may influence immunoediting. The authors determined GEB in the *ERBB2* oncogene, which encodes HER2, by identifying the number of germline variants that altered protein sequence and were predicted epitopes. They found that patients with high GEB in *ERBB2* were less likely to develop HER2$^+$ breast cancer. A similar finding was seen for other genes recurrently amplified in breast cancer, in which high GEB selected against amplification. This phenomenon is postulated to occur because amplification, resulting in increased expression, of a gene with high GEB would increase the number of epitopes and therefore enhance immuno-surveillance and elimination. Consequently, alternative oncogenic pathways through low-GEB oncogenes are more likely to occur (see the figure).

However, it was noted that cancer cells with high GEB can occur. These tumors had enrichment of macrophages and lower lymphocyte infiltration in the microenvironment, suggesting that they develop immune escape. These tumors were more aggressive, and high GEB was associated with decreased overall survival within 5 years. Moreover, the study observed higher GEB in HER2$^+$ ER$^-$ (estrogen receptor) metastatic tumors as compared with primary tumors, highlighting potential tumor adaptation mechanisms related to immune microenvironment modulation.

The focus of the study by Houlahan et al. was GEB within oncogenes whose expression had been increased through amplification. Oncogene activation through increased gene expression occurs in many cancer types and can arise through mechanisms that do not require amplification, which suggests that the findings are relevant beyond amplification. This includes changes to the regulation of gene expression through promoter hijacking, mutations within regulatory regions, or epigenetic changes. Furthermore,

it is likely that the findings will generalize beyond breast cancer to other cancer types. Therefore, this work has broad implications for germline-mediated immunoediting in tumor development and underscores its contribution to heterogeneity within a tumor.

The study by Houlahan et al. was possible owing to large multicenter sequencing initiatives that generate and share sequence data from cohorts of cancer patients. However, many of these datasets lack population diversity and predominantly represent individuals of European descent (15). Cancer incidence and mortality may differ between individuals of different ethnicity, and it is important that research is representative of the entire population it is intended to benefit. Therefore, future studies in diverse cohorts are needed to evaluate the generalizability of germline epitope-mediated immunoediting across populations.

The role of the germline genome in tumorigenesis highlights that tumor development is not a random process of DNA replication errors but has probabilistic boundaries imposed by an individual's genome. Germline-mediated immunoediting is likely to occur in precancerous cells, influencing tumor development. Further work could explore whether individuals whose genome is composed of genes with high GEB may have an innate resistance to certain cancers. Additionally, future analysis of longitudinal cancer samples taken before and after treatment will reveal the role of germline epitopes in the response to treatment and risk of relapse. Together, this may inform personalized immunotherapy in the form of epitope-derived vaccines—in which vaccines are designed on the basis of the epitopes from high-GEB genes—and provide insight on the most effective therapeutic interventions. ∎

REFERENCES AND NOTES

1. G. P. Dunn et al., *Nat. Immunol.* **3**, 991 (2002).
2. V. Addala et al., *Nat. Rev. Clin. Oncol.* **21**, 28 (2024).
3. K. E. Houlahan et al., *Science* **384**, eadh8697 (2024).
4. J. S. Varghese, D. F. Easton, *Curr. Opin. Genet. Dev.* **20**, 201 (2010).
5. L. B. Alexandrov et al., *Nature* **500**, 415 (2013).
6. S. Nik-Zainal et al., *Cell* **149**, 979 (2012).
7. C. D. Robles-Espinoza et al., *Nat. Commun.* **7**, 12064 (2016).
8. X. Xu et al., *Sci. Adv.* **6**, eaba4905 (2020).
9. H. Carter et al., *Cancer Discov.* **7**, 410 (2017).
10. D. S. Chen, I. Mellman, *Nature* **541**, 321 (2017).
11. Q. L. Wang et al., *EBioMedicine* **92**, 104588 (2023).
12. D. Chowell et al., *Science* **359**, 582 (2018).
13. R. W. Sayaman et al., *Immunity* **54**, 367 (2021).
14. M. Pagadala et al., *Nat. Commun.* **14**, 2744 (2023).
15. S. Fatumo et al., *Nat. Med.* **28**, 243 (2022).

MATERIALS SCIENCE

Living bioelectronics resolve inflammation

Coupling skin bacteria and electronics opens paths to adaptive treatment of inflammation

By **Peder S. Olofsson**

Although inflammation is an integral part of animal physiology and promotes homeostasis, unrestrained inflammation is linked to numerous diseases (1, 2). Recent advances have improved outcomes in several inflammatory diseases—for example, the introduction of anti-cytokine therapy to treat rheumatoid arthritis (3). However, side effects and therapy failure remain common. Medicines that adapt to individual needs to promote homeostasis would be highly desirable but will require concurrent reporting of treatment response to monitor efficacy. One interesting approach has been to combine microbes with electronic sensors in therapeutic devices that provide real-time signal readouts (4). On page 1023 of this issue, Shi et al. (5) describe the integration of bacterial and electronics components into a platform for studying and treating an inflammatory skin disease in mice. This amalgamation of living and synthetic components is a notable advance toward medical devices that enable real-time digital updates and potentially adaptive treatment of nonresolving inflammation.

Inflammation plays key roles in mammalian antimicrobial defenses and wound healing, comprising mechanisms that eradicate pathogens, clear debris, and facilitate restoration and recovery. It is a dynamic process that continually adapts to the changing needs of the tissue and organism and must be properly resolved when the threat is gone. Nonresolving inflammation is an important contributor to the development of prevalent diseases, including

Laboratory of Immunobiology, Division of Cardiovascular Medicine, Department of Medicine, Solna, Karolinska Institutet, Stockholm, Sweden. Email: peder.olofsson@ki.se

atherosclerotic cardiovascular disease, autoimmune diseases, obesity, failed recovery from severe infections, and certain cancers (*2*). Controlling inflammation is therefore a key challenge in medicine. In contrast to the innate systems that regulate homeostasis, pharmaceutical drugs are often optimized to target specific molecular mechanisms of disease but lack intrinsic adaptability and commonly affect a range of tissues, causing unwanted side effects.

In animals, many physiological functions are regulated by multiple opposing signals that promote homeostasis while adapting to changes in the environment. During inflammation, sensors for danger that are found on nearly every cell in the body can become activated by pathogen-associated molecular patterns, provoking a multilayered response involving tissue-resident cells and immune, cardiovascular, endocrine, and nervous systems. For example, when bacteria invade mouse skin and activate an inflammatory response, peripheral nerves also sense the bacterial components and simultaneously signal to attenuate the response (*6*), and activation of select neural circuits can accelerate the resolution of inflammation (*7*, *8*). Thus, multiple sensors trigger opposing signals, providing a measured response that promotes survival, healing, and homeostasis in the face of a wide variety of challenges.

Coevolution with microbes has shaped human physiology, and the resident microbiome contributes positively to many aspects of human health—for example, in the gastrointestinal tract and on the skin (*9*). Accordingly, live microbes are gaining increased attention as potentially attractive therapeutic agents (*10*–*12*). However, the development of microbe-based technologies that mimic innate homeostatic regulation and enable both sustained treatment and disease monitoring in one device has proven challenging (*4*). Even beneficial microbes can cause infections under certain conditions, becoming opportunistic pathogens. As such, for many therapeutic uses, bacteria may need to be confined in an environment that supports their viability, permits host-microbe interactions through secreted factors, and is biocompatible with the treatment target.

Shi *et al.* sought to harness the known beneficial effects of *Staphylococcus epidermidis* on skin health (*13*) to treat psoriasis, a disease associated with chronic, excessive inflammation of the skin (*14*). To achieve this, they developed "active biointegrated living electronics," which encapsulated *S. epidermidis* bacteria in a hydrogel matrix that was then integrated with an electronic array to combine treatment and continuous monitoring of disease activity in a single device.

Application of the device on the skin in

Regulation of homeostasis by closed-loop systems

In animals, homeostatic reflexes regulate physiology in a wide range of situations, including in inflammation. For example, distinct nerves measure aspects of tissue physiology and elicit reflex responses that convey control signals to the tissue on a molecular level, ultimately promoting homeostasis. Integration of living bacteria, physiological monitoring, and treatment delivery in a biocompatible and safe device provides a potential platform for combining synthetic biology and electronics to mimic the closed-loop properties of innate homeostatic regulation and ultimately progress toward the development of adaptive medicine.
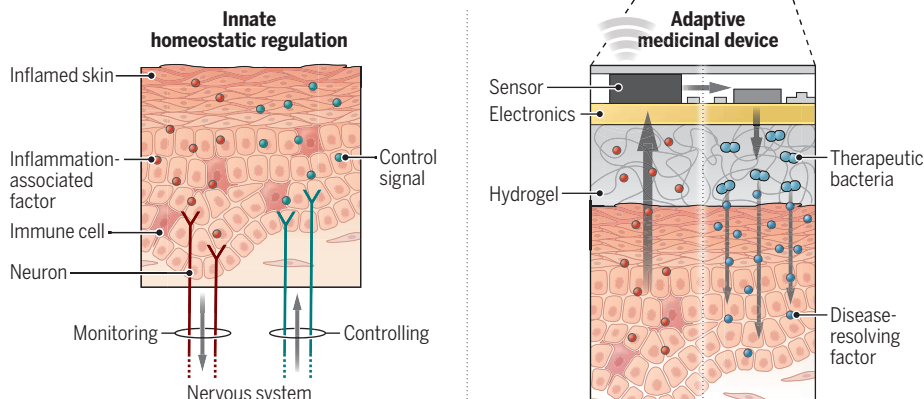
a mouse model of psoriasis significantly attenuated the disease, both at and beyond the immediate device-tissue interface. The treatment effect was in part mediated by *S. epidermidis*–derived lipoteichoic acid, a toll-like receptor 2 (TLR2) ligand, and was completely absent in TLR2-deficient mice. However, the mechanistic details remain to be fully defined, and it is likely that multiple properties of the device, in addition to factors released from the bacteria, contributed to the resolution of psoriasis.

The device uses mechanical, chemical, and electrical properties that combine to encapsulate, immobilize, and support bacteria while allowing concurrent delivery of treatment and feedback on the evolving disease state. With its tissue-mimicking, malleable, and adhesive features, the technology enables recording of electrophysiological signals on the skin surface, together with measurement of humidity and temperature. These measures provided qualitative information on disease activity, enabling intrinsic and convenient monitoring of treatment progress.

The approach used by Shi *et al.* has the potential to facilitate longer-term mechanistic studies of bidirectional interactions of microbes and tissues. It also holds promise for synthetic biology applications, exploring how devices that integrate engineered microbes might be used to both synthesize and release disease-resolving factors and support fine-tuning of treatment. The technology is an interesting advance toward the development of adaptive bioelectronic medicines. Integration of simultaneous therapy delivery using living cells and sensor-based monitoring of physiology is a step on the path to creating devices that exhibit closed-loop regulation, with adjustment of therapy to optimize the balance of therapeutic benefits and unwanted effects, reminiscent of the innate homeostatic regulation (see the figure).

It will be important to further study the underlying biological mechanisms and whether the approach is applicable beyond experimental psoriasis and practical to develop for use in human skin diseases. Ultimately, well-contained integration of discrete engineered microbes with electronics may constitute a feasible way to mimic important aspects of innate homeostatic regulation and realize adaptive medicines. ∎

REFERENCES AND NOTES
1. R. Medzhitov, *Science* **374**, 1070 (2021).
2. C. Nathan, *Immunity* **55**, 592 (2022).
3. G. Schett, I. B. McInnes, M. F. Neurath, *N. Engl. J. Med.* **385**, 628 (2021).
4. Y. Lyu *et al.*, *Matter* **7**, 1440 (2024).
5. J. Shi *et al.*, *Science* **384**, 1023 (2024).
6. I. M. Chiu *et al.*, *Nature* **501**, 52 (2013).
7. V. A. Pavlov, K. J. Tracey, *Neuron* **110**, 3627 (2022).
8. A. S. Caravaca *et al.*, *Proc. Natl. Acad. Sci. U.S.A.* **119**, e2023285119 (2022).
9. E. A. Grice, J. A. Segre, *Nat. Rev. Microbiol.* **9**, 244 (2011).
10. J. Hahn *et al.*, *Nat. Rev. Bioeng.* **2**, 120 (2024).
11. A. Cubillos-Ruiz *et al.*, *Nat. Rev. Drug Discov.* **20**, 941 (2021).
12. T. Nakatsuji *et al.*, *Nat. Med.* **27**, 700 (2021).
13. M. M. Severn, A. R. Horswill, *Nat. Rev. Microbiol.* **21**, 97 (2023).
14. F. O. Nestle, D. H. Kaplan, J. Barker, *N. Engl. J. Med.* **361**, 496 (2009).

GRAPHIC: N. BURGESS/*SCIENCE*

OCEANS

The future of the ocean

A journalist probes the challenges facing the global commons

By **Helen Czerski**

The high seas are vast and distant, often seen as the poster child for mysterious, wild, and lawless places. But we no longer have the luxury of ignoring them, because they are now also the site of one of the last great battles over the concept of "the global commons." Olive Heffernan's new book, *The High Seas: Greed, Power and the Battle for the Unclaimed Ocean*, surveys the many and varied fronts in this war, tells their histories, and draws the battle lines that will determine whether the ocean's future is to become spoils divided up between the victors or a genuinely shared benefit to all humankind. The book serves as a valuable wake-up call, setting out why we are at a critical point in "the blue acceleration" as well as the considerable risks of responding to the complexity of these challenges with either apathy or inaction.

Every chapter in the book explores a different topic, with the more obvious ones such as illegal fishing, deep-sea mining, and plastic pollution balanced by those that get far less press. This latter category in-

The High Seas
Olive Heffernan
Greystone Books, 2024.
368 pp.

cludes how we manage the ocean's genetic resources, the dumping of space waste as it falls out of orbit, and the rapidly expanding field of marine carbon dioxide removal. Heffernan's years as a science journalist have given her direct access to many of the people and locations at the heart of the issues, enriching the book with firsthand descriptions and personal reflections. The book is a well-researched exploration of the issues rather than an academic analysis; it sets out questions but does not prescribe specific answers.

The strongest and most valuable parts of the book are the stories it contains about the people and situations that led us to where we are now. Heffernan writes, for example, about the diplomat Arvid Pardo, who persuaded the United Nations to declare the high-seas seabed to be common heritage in 1970; about the serendipitous early discoveries of useful medicines derived from sea creatures; and about the consequences of one highly controversial estimate of the number of fish in the ocean's twilight zone. There are also some shocking revelations hidden in the details, for example, that more than half of high-seas fishing trips—which cause vast and tragic damage to many nontarget species—would be unprofitable without government subsidies.

The reviewer is at the Department of Mechanical Engineering, University College London, London, UK. Email: h.czerski@ucl.ac.uk

A scientist examines coral at an independent research institution in Summerland Key, Florida, in 2023.

This is a very readable introduction to an extremely complex topic, and it is commendably broad in its ambition, but Heffernan occasionally indulges a journalist's tendency to lead with the most extreme number bandied about on a given topic in ways that may frustrate professional scientists. She writes, for example, that electro-geochemistry in the ocean "could absorb somewhere between 100 billion and 1 trillion tons of CO_2 each year" (the only statistic provided, although it is clearly labeled as speculative). These statistics may be a consequence of a reliance on long-form magazine and news articles—rather than the primary literature—as data sources.

This book is not the place to find a detailed technical critique of the various ocean schemes that people are developing, selling, or trying to prevent. The activities described are all out there in the real world now, and whether they have a chance of achieving their aims or not, they still pose a lot of questions. Heffernan's achievement is to humanize the topic and to shift readers' perspective from framing the ocean's challenges as a dispassionate set of technical problems to a landscape of conflicting ideas, motivations, and incentives requiring global thinking to prevent the worst outcomes.

The most interesting sections of the book cover the ethical questions posed by new technologies, such as who should have access to and benefit from gene sequences collected from the high seas and what exactly "misappropriation" means in this context. I would also like to have learned more about the idea, touched on near the end, that closing the high seas to fishing completely would drastically reduce global inequality from fishing by increasing the catches within national exclusive economic zones more evenly.

By the end of the book, it is hard to argue with Heffernan's contention, set out at the start, that "today's unclaimed ocean is under siege." Not only is interest in using the ocean growing, the mixture of existing rule books and the lack of enforcement also provides an oceanscape ripe for short-term exploitation and long-term loss. The biggest risk comes from invisibility, and the unspoken point of this work is that if more of us knew about what is happening on the high seas, we would have a much better chance of choosing a healthier trajectory. This book is a valuable and welcome addition to the urgent debate about the ocean's future. ∎

PHOTO: CHANDAN KHANNA/AFP VIA GETTY IMAGES

MARINE BIOACOUSTICS

Hearing the seas

Rich underwater soundscapes await those who listen closely

**Sing Like Fish:
How Sound Rules Life
Under Water**
Amorina Kingdon
Crown, 2024. 336 pp.

By **Aaron N. Rice**

With increasing attention on the world's oceans, there is a growing appreciation of the importance of sound for aquatic organisms and a recognition of how human-generated noise may have adverse effects on these habitats (*1*). The field of marine bioacoustics now goes well beyond the classic example of singing male humpback whales (*2*), spanning how many thousands of marine species produce and perceive sounds.

Sing Like Fish: How Sound Rules Life Under Water by journalist Amorina Kingdon interweaves an inquisitive and poetic science writer's impressions of marine bioacoustics with a combination of interviews with current practitioners in the field and a history of the discipline's development. Kingdon provides overviews of how sound behaves and is measured underwater, how underwater organisms differ from those on land in how they detect and communicate with sound, and the increasing impacts of human noise on those organisms. The book presents an engaging and nontechnical description of the intersection of oceanography, physical acoustics, animal behavior, and noise pollution and includes delightful anecdotes about the happenstance discoveries that have led to key technologies and principles in the field as well as the more personal aspects of being a practicing scientist.

Much of the modern technology used for the study of sounds in the oceans originated in anti-submarine warfare conducted by the British Royal Navy and US Navy in World Wars I and II. Foundational biological discoveries quickly emerged from these technologies once they became accessible in civilian domains, highlighting the critical interrelationship between biology and technology that enables the field of marine bioacoustics today.

A subtle theme that develops over the course of the book is how siloed information constrained the development of bioacoustic science—something not always appreciated or apparent today. Despite descriptions of fish sounds by Aristotle and Pliny the Elder in classical antiquity and investigations of fish vocal anatomy in the 19th century, William Tavolga—one of the founders of modern marine bioacoustics—once asserted that "fish don't make sounds, and they can't hear." In many ways, our increased awareness of the ubiquity of underwater animal sound production comes from improved communication and dissemination of science across an ever-increasing and -diversifying group of scientists.

One unfortunate shortcoming of this book is that there are a number of awkwardly worded, misleading, and incorrect statements. For example, referring to cusk-eels (order Ophidiiformes), Kingdon says that they are "eel-shaped but are fish." (Eels are in fact a group of ray-finned fishes.) Later, she writes that "scientists have studied marine mammals' hearing in more detail than other animals," but scientists have little empirical data on hearing in toothed whales and have established no physiological measure of hearing abilities in baleen whales. There have, however, been thousands of peer-reviewed publications on hearing in fishes. And despite mentioning the importance of traditional ecological knowledge, she fails to describe how Indigenous and artisanal fishers around the world have long listened to underwater sounds made by fish and whales without modern Western technologies.

The book's chapters also frequently jump around in time, an approach that can be disorienting. In the span of just six pages, for example, a chapter on quieting the ocean travels from present-day recordings in Victoria, British Columbia, to Gordon Wenz's presentation on ambient acoustic noise in the ocean at a 1963 symposium, to the ocean quieting that followed 9/11, to the "anthropause" during the COVID-19 pandemic, to Bernie Krause's nature-recording efforts in 1968.
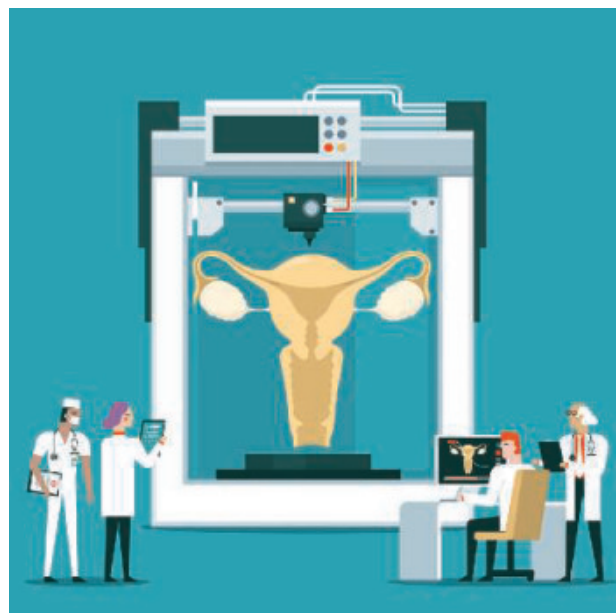
Sing Like Fish is nonetheless a compelling, nontechnical natural history text that a wide audience will appreciate. Even acousticians will likely enjoy many of the delightful personal details Kingdon shares about senior bioacousticians and pivotal figures in the field. With the importance and ubiquity of sound in the ocean, this approachable text helps bring attention to what was once an esoteric subdiscipline of marine biology and presents it with the importance and fascination it deserves. ∎

REFERENCES AND NOTES
1. C. M. Duarte *et al.*, *Science* **371**, eaba4658 (2021).
2. R. S. Payne, S. McVay, *Science* **173**, 585 (1971).

The reviewer is at the K. Lisa Yang Center for Conservation Bioacoustics, Cornell Lab of Ornithology, Cornell University, Ithaca, NY, USA, and the Department of Public and Ecosystem Health, Cornell University, Ithaca, NY, USA. Email: arice@cornell.edu

A FUTURE TO LOOK FORWARD TO

PODCAST

Eve: The Disobedient Future of Birth
Claire Horn
House of Anansi Press, 2023. 224 pp.

Like incubators for premature infants and in vitro fertilization, artificial wombs may one day join our reproductive technology toolkit. How should we think about and prepare for this possibility? This week on the *Science* podcast, legal scholar Claire Horn explores the implications of ectogenesis—reproduction outside the body—including what such technologies could mean for gender equality and reproductive rights.
https://bit.ly/3y9MELb

ILLUSTRATION: SORBETTO/ISTOCKPHOTO/ADAPTED BY N. BURGESS/*SCIENCE*

A great egret hunts in a stand of American lotus in Alabama's Mobile-Tensaw River Delta, which has been called "America's Amazon."

Edited by **Jennifer Sills**

Safely manage Alabama's Mobile-Tensaw Delta

The Mobile-Tensaw River Delta, dubbed "America's Amazon," has experienced substantial degradation as a result of logging, land use changes, hydrologic alterations, and pollution (1). In January, Alabama Power committed to remediating some of the waste produced by its coal-burning power plant on the delta (2), and conservation measures are in place in most of the delta's lowland areas. However, substantial portions of the highlands and privately owned regions remain unprotected, and threats to the region are intensifying.

Between 2001 and 2019, the urban areas in the Mobile-Tensaw River Delta expanded from 563.3 km² to 642.7 km², predominantly at the expense of forested areas, which decreased by about 7% (3). About 34.9 km² of this urban expansion occurred in regions previously covered by deciduous, evergreen, or mixed forests. Some protected areas have been affected by these changes, indicating a need to reevaluate and strengthen current protection measures.

Sea level rise and increased rainfall runoff associated with climate change (3) threaten the delta's low-lying areas with increased flooding, pollution, and salinity intrusion, which affect sensitive forested wetlands. Predictions based on present rates of sea level rise alone suggest substantial habitat transformations by 2100, with the conversion of forested wetlands to marsh or open water (4).

Industrial practices in the delta have created a legacy of pollution (5). Some areas have been designated US Environmental Protection Agency Superfund sites, indicating that they are among the most contaminated locations in the country (6). There is also widespread pollution by heavy metals and polyaromatic hydrocarbons (7), likely from industrial and shipping activities associated with the Port of Mobile.

Since the 1950s, the Barry Steam Plant, managed by Alabama Power, has stored about 17 million m³ of toxic coal ash—the by-product of coal burning—in a lagoon on the banks of the Mobile River (8). In response to tightening federal regulations and a decade of debate with stakeholders about the potential for contaminants to leak from the pond into the delta (9), Alabama Power now plans to excavate much of the toxic slurry at the Barry ponds and to build a coal-ash recycling facility that will use the ash to make concrete (2). This is a positive step but will not protect the delta in the absence of other action.

Conservation programs should include public-private partnerships and incentives for private landowners given that more than 94% of the forest land in Alabama is privately owned (10). Substantial investments from federal, state, and local governments are essential. Conservation efforts should aim to understand the delta's ecosystems and their responses to environmental changes and then implement targeted conservation strategies. Strategies that have been underway for decades in large aquatic ecosystems, such as the Florida Everglades (11) and the San Francisco Bay Delta (12), could serve as a template for effective management of Alabama's Mobile-Tensaw River Delta.

Gabriel de Oliveira[1,2]*, John Lehrter[1,2], Sean Powers[1,2], Guilherme Mataveli[3,4], Celso Santos[5]

[1]Stokes School of Marine and Environmental Sciences, University of South Alabama, Mobile, AL 36688, USA. [2]Dauphin Island Sea Lab, Dauphin Island, AL 36528, USA. [3]Earth Observation and Geoinformatics Division, National Institute for Space Research, Sao Jose dos Campos, SP 12227-010, Brazil. [4]School of Environmental Sciences, Tyndall Centre for Climate Change Research, University of East Anglia, Norwich NR4 7TJ, UK. [5]Department of Civil and Environmental Engineering, Federal University of Paraiba, João Pessoa, PB 58051-900, Brazil.
*Corresponding author.
Email: deoliveira@southalabama.edu

REFERENCES AND NOTES

1. B. Raines, *Saving America's Amazon: The Threat to Our Nation's Most Biodiverse River System* (NewSouth Books, 2018).
2. M. Renkl, "We might be one step closer to saving America's Amazon," *New York Times*, 5 February 2024.
3. G. de Oliveira, S. R. Schultze, G. Mataveli, "Fauna, flora, and land cover changes over the last two decades in the Mobile-Tensaw River Delta" (JagWorks@USA, Technical Report, 2024); https://jagworks.southalabama.edu/earthsci-techreports/1.
4. L. Geselbracht *et al*., "Modeling and abating the impacts of sea level rise on five significant estuarine systems in the Gulf of Mexico" (The Nature Conservancy, project no. MX-95463410-2, 2013).
5. Mobile Bay National Estuary Program, "Legacy contaminants" (2020); https://www.mobilebaynep.com/the_issues/legacy-contaminants.
6. US Environmental Protection Agency, "Search for Superfund sites where you live" (2023); https://www.epa.gov/superfund/search-superfund-sites-where-you-live.
7. R. B. J. Peachey, *Mar. Pollut. Bull.* **46**, 1365 (2003).
8. I. Chapman, "Gambling 'America's Amazon,'" *CNN*, 5 December 2021.
9. Alabama Power, "Alabama Power, Eco Material plan expected to recycle millions of tons of coal ash for beneficial use" (2024); https://www.alabamapower.com/press-releases/2024/alabama-power--eco-material-plan-to-recycle-tons-of-coal-ash.html.
10. A. J. Hartsell, J. A. Cooper, *Alabama's Forests, 2010* (US Department of Agriculture, Forest Service, Southern Research Station, 2013).
11. F. H. Sklar *et al*., *Front. Ecol. Environ.* **3**, 161 (2005).
12. M. Nagarkar, K. Raulund-Rasmussen, *Ecol. Soc.* **21**, 43 (2016).

PHOTO: BEN RAINES/SAVING AMERICA'S AMAZON

China's road slopes need long-term protection

Large-scale road construction in China's mountainous regions has led to many exposed road slopes. Bare road slope patches, stripped of soil and vegetation, have resulted in severe landscape fragmentation and destructive effects on surrounding habitats (1, 2). They are also potentially dangerous to humans. In April, the slope of a section of the Yinkun Expressway roadbed collapsed, blocking the road with about 4000 m³ of debris (3). China needs long-term strategies to stabilize and restore road slopes.

Slope leveling, artificial soil, and soil reinforcement mesh installation and maintenance can provide short-term protection for the ecosystems around road slopes (4). Leveling slopes can clear the protruding dangerous rocks on the slope, fill the depressed pits, and improve stability. Artificial soils contain seeds and substances, such as straw, bonding, and water-retention agents, that promote vegetation growth. Soil reinforcement meshes installed on road slope surfaces can reduce soil erosion rates and prevent damage caused by precipitation, machinery, and organisms.

However, buried reinforcement meshes in road slope soils undergo corrosion, limiting the strength of the mesh and compromising its effectiveness (5). The use of galvanized iron wire meshes can limit this corrosion for 5 years after installation, but weight loss rates of the soil reinforcement meshes can reach 96% 11 years after installation (6). When soil reinforcement meshes fail, soil erosion resumes, potentially leading to landslides, mudslides, and further ecological degradation (7). China must plan to regularly replace soil reinforcements before they corrode.

China should also invest in research and development of anticorrosive materials, anticorrosive coatings, and other anticorrosive technologies that could increase the life spans of soil reinforcement mesh (8, 9). Ideally, China should support research and development of technology that can replace soil reinforcement meshes with better road slope ecological protection measures. For example, "fish-scale" pits and hole grooves are variations of depressions or holes made at regular intervals on a slope. The holes catch water, sending it deeper into the soil and facilitating vegetation. In the case of overflow, they prevent water from running directly down the slope, decreasing the likelihood of landslides. These strategies are still under investigation, but if they could be implemented successfully, corrosion would no longer threaten the long-term stability of road slopes (10, 11).

Shenghao Ai[1], Zongyang Liu[2], Xiaoyan Ai[2], Yi Pan[1], Yingwei Ai[2]*

[1]Chengdu Institute of Organic Chemistry, Chinese Academy of Sciences, Chengdu 610213, China. [2]Key Laboratory of Bio-resources and Eco-environment, Ministry of Education, College of Life Sciences, State Key Laboratory of Hydraulics and Mountain River Engineering, Sichuan University, Chengdu 610065, China.
*Corresponding author. Email: aiyw99@sohu.com

REFERENCES AND NOTES

1. W. F. Laurance, A. Balmford, *Nature* **495**, 308 (2013).
2. J. R. Miller *et al.*, *Landsc. Ecol.* **11**, 115 (1996).
3. S. X. Shen, M. Cui, "Alert! Mountain collapse disrupts traffic on Yunnan roads!" *Spring City Evening News*, 30 April 2024; https://m.thepaper.cn/newsDetail_forward_27225704 [in Chinese].
4. W. Zhang *et al.*, *J. Environ. Manag.* **211**, 287 (2018).
5. X. Li *et al.*, *Nature* **527**, 441 (2015).
6. J. Chen *et al.*, *Sci. Total Environ.* **671**, 41 (2019).
7. B. Liu *et al.*, *Eng. Geol.* **293**, 106295 (2021).
8. M. Mebrahtom *et al.*, *Sci. Rep.* **14**, 8818 (2024).
9. C. Wang *et al.*, *Thin-Walled Struct.* **159**, 107281 (2021).
10. Z. Song *et al.*, *Eng. Geol.* **287**, 106114 (2021).
11. H. Zhang *et al.*, *J. Soil Water Conserv.* **36**, 156 (2022).

10.1126/science.adp5259

Militancy facilitates polio spread in Pakistan

Pakistan remains one of the last polio-endemic countries (1). The Pakistani government, along with its global partners, has successfully expanded vaccine coverage in conflict-affected and high-risk regions (2). However, militant attacks on polio vaccination teams, particularly by the Tehrik-e Taliban Pakistan, have reached unprecedented levels in the past 2 years (3–5). Pakistan and the global community must ensure the safety of vaccination workers.

The increase in militant activities substantially hinders polio vaccination efforts (6). As a result of polio vaccination team casualties, polio vaccination coverage and rates have declined, and the incidence of polio cases and environmental detection of the virus in Pakistan have increased (7). In 2021, only 1 polio case was reported in Pakistan, compared with 20 cases in 2022 and 6 cases in 2023 (8). In 2023, 80 environmental samples positive for polio were found (8), and positive samples were detected in 10 major Pakistani cities in the first 2 months of 2024 (9).

Given the global polio resurgence in the United States, Europe, and Africa, the setbacks in Pakistan's eradication efforts are a substantial concern (10). Immediate, collaborative actions are needed to protect vaccination teams. The government of Pakistan should increase the health budget—currently at 2.8% of the total development budget and 0.05% of gross domestic product (11)—and devote the additional funds to overcoming the challenges faced by health workers. Protection efforts should include engaging influential religious leaders, gaining community trust, combating extremist ideologies, and forging international partnerships. The government should also foster relationships between the health department, international organizations, and local communities. By harnessing local knowledge and awareness, vaccination teams can work together with communities to ensure safe and effective vaccination efforts. To provide additional security and assess progress, Pakistan should use real-time monitoring systems (12) to track the location of vaccination teams. Ensuring safe passage for vaccination teams will allow better vaccination coverage and, in turn, bring Pakistan closer to eradicating polio.

Tauheed Ullah Khan[1] and Shahid Ahmad[2]*

[1]Guangdong Key Laboratory of Animal Conservation and Resource Utilization, Guangdong Public Laboratory of Wild Animal Conservation and Utilization, Institute of Zoology, Guangdong Academy of Sciences, Guangzhou 510260, China. [2]Hainan University School of Ecology and Environment, Hainan 570228, China.
*Corresponding author. Email: bjfu1870@gmail.com

REFERENCES AND NOTES

1. World Health Organization (WHO), "Poliomyelitis" (2023); https://www.who.int/news-room/fact-sheets/detail/poliomyelitis.
2. M. A. Habib *et al.*, *Lancet Glob. Health* **5**, e593 (2017).
3. A. Khan, "2023 ends with 70% increase in militant attacks, 81% rise in deaths: PICSS Report" (Pakistan Institute for Conflict and Security Studies, 2024); https://www.picss.net/featured/2023-ends-with-70-increase-in-militant-attacks-81-rise-in-deaths-picss-report/.
4. A. Khan, "Pakistani Taliban claims responsibility for bomb that killed 6 police guarding anti-polio campaign," *AP News*, 8 January 2024.
5. A. Hussain, "Blast in Pakistan kills five police officers during polio vaccination drive," *Al Jazeera*, 8 January 2024.
6. A. Gul, "Deadly Bomb Hits Pakistan Polio Protection Police Team Near Afghan Border," *VOA News*, 8 January 2024.
7. A. A. Verma, M. P. Jimenez, R. H. Tangermann, S. V. Subramanian, F. Razak, *Proc. Natl. Acad. Sci. U.S.A.* **115**, 1593 (2018).
8. WHO, "Statement following the Thirty-seventh Meeting of the IHR Emergency Committee for Polio" (2023); https://www.who.int/news/item/22-12-2023-statement-following-the-thirty-seventh-meeting-of-the-ihr-emergency-committee-for-polio.
9. J. Khan, "Polio virus found in 10 biggest cities of Pakistan: Sources," *ARY News*, 12 March 2024.
10. "Why is polio making a comeback?" *Al Jazeera*, 30 August 2022.
11. J. Saeed, "Analyzing Health Budget 2023 in Context of Wellbeing of People" (Sustainable Development Policy Institute, 2023); https://sdpi.org/analyzing-health-budget-2023-in-context-of-wellbeing-of-people/news_detail.
12. B. Wahid, B. Kumari, K. M. Saifullah, M. Idrees, *Asia Pac. J. Public Health* **35**, 183 (2023).

10.1126/science.adp5269

AAAS NEWS & NOTES

Top row: Sudip Parikh, AAAS chief executive officer and publisher of the *Science* family of journals; award donor Mani L. Bhaumik; Stig Piras, deputy chief of mission at the Danish embassy. Bottom row: award winners Richard DiMarchi and Lotte Bjerre Knudsen.

Winning researchers unlocked GLP-1 drugs for obesity

Award recognizes individuals whose work best underpins the *Science* Breakthrough of the Year

By **Meagan Phelan**

A class of obesity-fighting drugs—the first to deliver significant weight loss without many adverse effects—may never have been delivered to patients if not for two problem-solvers. These individuals questioned the prevailing thinking about glucagon-like peptide-1 (GLP-1) medications, a peptide-based injectable developed to treat diabetes. They didn't waver in their belief that these treatments could also combat obesity with unprecedented force.

For their role in ensuring that GLP-1 receptor agonist medications were developed beyond diabetes, the Mani L. Bhaumik Breakthrough of the Year Award was awarded to Lotte Bjerre Knudsen, chief scientific advisor in research and early development at Novo Nordisk, and Richard DiMarchi, Distinguished Professor of Biochemistry and Gill Chair in Biomolecular Sciences at Indiana University, during a ceremony at AAAS headquarters on April 26.

Bjerre Knudsen figured out how to make the peptide underlying this drug class—an otherwise ephemeral substance—last long enough in the body to be a medication. DiMarchi transformed thinking about the hormones this class of therapies should mimic, a critical part of their efficacy. Both stayed strong in the face of critics who doubted obesity was a disease at all.

RECOGNIZING INDIVIDUAL RESEARCHERS

Recognizing the people behind such significant scientific developments is a central philosophy for donor Mani L. Bhaumik, PhD—a physicist with myriad contributions to the development of high-powered lasers—as well as for AAAS and the *Science* family of journals.

"Thinking outside the box is critical to scientific innovation," said

Bhaumik. "I'm delighted to see this year's recognition go to people whose tenacity kept this work—which stands to benefit us all—advancing to the finish line. We are lucky to be alive when results so conducive to our evolution are happening."

The Mani L. Bhaumik Breakthrough of the Year Award was established in 2022 with a $11.4 million pledge from Bhaumik—the largest in AAAS's history. The award supports a $250,000 cash prize annually for up to three scientists or researchers whose work best underpins the *Science* Breakthrough of the Year, the journal's choice of the top research advance of the year. In 2023, *Science* named the development of GLP-1 agonists to treat obesity—and their efficacy at blunting obesity-associated health problems—as its latest *Breakthrough*.

To select the winners, *Science* journals' editor-in-chief, Holden Thorp, convened a committee. "We were all excited about the clinical trials for obesity and associated health problems that were already happening or coming up," said Thorp, "but our committee had a difficult task, looking back at many who'd contributed to the success we're seeing now, to decide who to recognize."

"What the committee ultimately wanted to award," said committee member Eric Topol, a professor in the department of molecular medicine and an executive vice president at Scripps Research Institute, "was the impetus to switch over to obesity, because that was a very striking change from how GLP-1 medications were envisioned. If it wasn't for these two, we might only have this drug class for diabetes."

GLP-1 RECEPTOR AGONISTS: "CORNERED" FOR DIABETES

The work to study GLP-1 for diabetes, and later for weight loss, reaches back decades.

In the 1970s, scientists looking to lower blood glucose were

studying how peptides could help regulate glucose after food intake. They wanted to dial up insulin production.

At first, the endeavor didn't yield results. But then in 1983, scientists described the insulin-stimulating hormone GLP-1, and companies including Novo Nordisk and Eli Lilly dove in on converting GLP-1 agonists. Various companies thought they could reproduce the effect of GLP-1 by making smaller molecules that activate the pancreas's GLP-1 receptors. In the years that followed, Novo Nordisk, Eli Lilly, and other companies worked to convert GLP-1 receptor "agonists" into diabetes drugs.

The first such drug—an iteration of GLP-1 derived from a Gila monster—was approved for people with type 2 diabetes in 2005, and the first version based on human GLP-1 was approved for type 2 diabetes treatment in 2010.

But biases about weight loss and the classification of obesity meant more hurdles before the drugs were approved to fight weight issues.

"Obesity wasn't viewed as a disease," said selection committee member John Buse, the Verne S. Caviness Distinguished Professor of Medicine at the University of North Carolina School of Medicine. "Obesity was viewed as a failure of character," Buse said, as a flaw of willpower.

For some individuals, however, acts of will alone—diet or exercise—do not entirely address obesity, which is defined as a body mass index of at least 30. Additionally, not everyone who is considered overweight or obese by medical standards has other health concerns, though many patients still face bias and stigma from their medical providers. But for individuals with obesity-related health conditions such as type 2 diabetes or heart disease, GLP-1 drugs can impact more than weight.

"These GLP-1 medications are so validating for people who have known for such a long time that willpower alone won't help," said committee member Katherine Saunders, assistant professor of clinical medicine at Weill Cornell Medicine and cofounder of Intellihealth, a company democratizing access to medical obesity treatment. "The drugs are clearly working on pathways that are dysregulated."

Knowing obesity wasn't in people's sights when GLP-1 drugs were first developed, the prize committee members investigated the pivot.

The committee decided to focus on the earliest patents for these drugs for fighting obesity specifically. DiMarchi and Bjerre Knudsen were the first authors on two pivotal patents—filed in the 1990s—that ultimately led to the drugs' use for this purpose.

Bjerre Knudsen had been thinking about pursuing significant weight loss with these drugs since she noticed the literature around weight changes in treated animals, including in papers in 1995 and 1996. She and her colleagues at Novo Nordisk made an observation as they screened early diabetes drugs in mice. GLP-1 receptor agonists didn't just increase insulin secretion—they also made the mice eat less.

This appetite-diminishing effect was intriguing.

But some people, including leadership at Bjerre Knudsen's company, had trouble comprehending that one molecule could do more than one thing. The drug is either for diabetes or for weight loss, colleagues told her, even after clear evidence emerged of a weight loss effect.

"It was as if GLP-1s got cornered for diabetes," Bjerre Knudsen said.

INNOVATING TO ATTACK OBSTACLES

GLP-1s are peptides, meaning they have a relatively larger molecular size. This makes designing oral versions—like pills—difficult. The drugs had to be injected, which many thought would deter potential patients.

Bjerre Knudsen said that an even greater challenge with GLP-1s—

including for diabetes—was that these peptides degrade quickly once they enter the body, meaning their helpful effects don't last for long.

This problem was so significant that it almost led Novo Nordisk to shutter its GLP-1 work.

But Bjerre Knudsen believed that the hormone could become a medicine. She conceived of three different options to keep the peptide from being degraded: find a way to protect it, wipe out what destroys it, or make it more stable. Bjerre Knudsen ultimately focused on the first approach and created a fatty acid–based technique that bound the peptide-based drugs to a carrier in the blood, albumin, that protected them from enzyme attackers and prevented elimination from the kidneys.

"That was a very elegant solution," said DiMarchi.

With Bjerre Knudsen's help, Novo Nordisk developed a GLP-1–based drug called liraglutide, which entered clinical testing in 2000 as an injectable to treat diabetes. In 2010, it was approved by the FDA as Victoza to treat type 2 diabetes. In 2014, it was approved as Saxenda for weight loss, averaging a reduction of about 8% of overall body mass—slightly more than what other drugs with older mechanisms of action were achieving, but without side effects preventing chronic use.

The next-generation molecule from Novo Nordisk, semaglutide—approved for type 2 diabetes in 2017 and for obesity in 2021—showed 17 to 18% weight loss in clinical trials.

FINDING THE "MASTER KEY"

Across the Atlantic, DiMarchi had bumped into hurdles as well in his work to make GLP-1–based drugs to address obesity. While at Eli Lilly, DiMarchi began collaborating with internationally recognized clinical diabetes researcher Suad Efendic, who was studying GLP-1s in patients with type 2 diabetes. DiMarchi helped to synthesize GLP-1s for Efendic's trials, which showed something important: Patients lost more weight through use of GLP-1s than with insulin alone.

In 2003, DiMarchi joined the faculty at Indiana University, where he embarked on what would become a decades-long collaboration with German physician and scientist Matthias Tschöp. The two researchers started with a list of gut hormones to target for obesity drugs, ultimately picking glucagon. Glucagon works in the opposite direction of insulin—helping to release glucose into the blood when levels are too low, which can happen sometimes for diabetic patients.

DiMarchi had been working to develop a better synthetic glucagon to help patients recover faster during hypoglycemic attacks. Up to that point, glucagon came in a kit as a powder that had to be dissolved and then injected, all by someone struggling with life-altering low blood sugar. "You really needed something like an epinephrine pen," DiMarchi said.

He and his team developed multiple aqueously soluble and physically stable analogs of glucagon. And then something interesting happened when Tschöp infused one of the glucagons into obese animals: The mice lost weight — and by a provocative mechanism. The animals burned energy—but they were not burning it efficiently.

He remembers the impressions of leaders in the field when they saw the results. "'You're going the wrong way,' they told me. 'Glucagon will be dangerous by increasing blood glucose.'"

But DiMarchi believed glucagon could be used to generate a futile cycle that decreased body weight by increasing energy use. He wanted to know if this weight loss effect from stimulating glucagon receptors could be integrated with the appetite-suppressing effect of GLP-1—a single, safe molecule for unprecedented weight loss.

Working with grad students, he found that they could in fact design a single hormone that could stimulate both the glucagon and GLP-1 receptors. "It was as if we had a master key opening two doors as effectively as one," he said.

DiMarchi and Tschöp continued to explore other combinations, next focusing on glucose-dependent insulinotropic polypeptide, or GIP—another controversial hormone. Like GLP-1, GIP is a gut hormone that triggers insulin secretion. But to date, drug candidates based on GIP had not worked. Some experiments even showed that infusing GIP had no effect in patients with type 2 diabetes.

But work from Denmark inspired his team to think differently. That research had shown that GIP increased insulin after first improving the blood sugar of diabetics for a few weeks. "We envisioned GLP-1 as the first stage of the rocket to improve glycemic control, and then GIP would be able to function," DiMarchi said.

This led DiMarchi to combine GLP-1 and GIP into a single molecule that could "see" both receptors. "When we put such a dual-action molecule into rodents, it was phenomenally effective for weight loss," he said. This inspired the development of the drug tirzepatide, marketed by Eli Lilly as Mounjaro for diabetes and as Zepbound for obesity, which resulted in weight loss of up to 20%.

His team's third step—adding in glucagon—made the drugs even more powerful.

Today, a drug candidate called retatrutide, based on this triple-agonist approach being developed by Eli Lilly, has shown a 24% mean decrease in weight over 48 weeks of study.

DiMarchi noted how Bjerre Knudsen inspired him from afar as she continued her own work. In Denmark, Bjerre Knudsen had made progress convincing leadership at Novo Nordisk to pursue weight loss specifically, with GLP-1s. Bjerre Knudsen's colleagues Jesper Lau and Thomas Kruse led the invention of semaglutide, while Bjerre Knudsen went on to publish numerous papers studying the mechanism of these medicines as it relates to obesity, cardiovascular disease, kidney disease, and oral absorption.

Today, semaglutide is marketed as Ozempic for type 2 diabetes and Wegovy for obesity.

LEARNING FROM OUR WINNERS

The scientists who have contributed to GLP-1 medications' success are many, a reality Bjerre Knudsen and DiMarchi are the first to convey. But the guiding lights provided by Bjerre Knudsen and DiMarchi are indisputable.

"This story goes to show how fundamental science they were doing is so important," said Buse. "If people had stopped what they were doing 30 years ago, we would not be here."

"A lot of people didn't believe it," said Bjerre Knudsen about GLP-1s. "They didn't believe this class of drugs would be good for diabetes, but it was good. They didn't believe it would be good for weight loss, but it was good. They didn't believe it would provide any cardiovascular benefits, but it did. And that's why leadership in all companies needs to make sure that everyone thrives...because no one knows who has the next really good idea."

Science Podcasts

AAAS

Hear the stories behind
the latest news and research
from *Science*.

LISTEN & SUBSCRIBE

NEW EPISODES EVERY THURSDAY

RESEARCH

IN *SCIENCE* JOURNALS

Edited by **Michael Funk**

OCEAN CIRCULATION
As the world warms

Will ice mass loss from the Greenland Ice Sheet caused by climate warming disrupt large-scale ocean circulation? Zhou *et al.* reconstructed iceberg production rates during the massive calving episodes of the last glacial period, called Heinrich events, when icebergs did affect ocean circulation. The authors found that present-day Greenland Ice Sheet calving rates are as high as during some of those events. However, because melting is causing the Greenland Ice Sheet to recede from the coasts of Greenland, where icebergs originate, its iceberg discharge should not persist long enough to cause major disruption of the Atlantic overturning circulation by itself. —Jesse Smith   *Science* p. 983, 10.1126/science.adh8369

Icebergs off the coast of Greenland surrounding a research vessel

BIOMATERIALS
Mimicking the human sense of touch

Merkel cells and Ruffini endings, which reside at the bottom of the epidermis and within the dermis of human skin, respectively, can perceive external forces and the strain of the skin. Liu *et al*. designed, fabricated, and used artificial intelligence–guided signal processing to develop an electronic skin that mimics human mechanosensation. The three-dimensional configuration of pressure and strain sensors and a heterogeneous encapsulation strategy enabled the differentiation of normal or shear forces and induced strain. The authors demonstrated the application of this electronic skin by measuring the freshness of foods such as fruits, cake, and bread through touch-sensitive detection of changes in modulus. —Marc S. Lavine

Science p. 987, 10.1126/science.adk5556

NANOMATERIALS
Solution growth of perovskite nanowires

A templating method enables the growth of two-dimensional metal-halide perovskite nanowires that exhibit polarized photoluminescence and enable low-loss waveguiding. Shao *et al*. grew nanowires of $(BrCA3)_2PbBr_4$, where BrCA3 is 2-(2-bromo-5-carboxyphenoxy) ethan-1-aminium. The carboxylic acid group of BrCA3 inhibited the growth of all crystal facets except [110], which led to one-directional growth. The nanowires also achieved efficient light amplification, with a threshold of less than 20 microjoules per square centimeter. —Phil Szuromi

Science p. 1000, 10.1126/science.adl0920

EVOLUTION
A filter not a burst

Mammals have drawn particular research attention because of their huge level of morphological variation. Until recently, most believed that the dinosaur decline at the end of the Cretaceous opened niches for mammals to fill, resulting in a burst of speciation. Quintero *et al*. developed a model that integrated phylogenetics and fossils to estimate diversification rates across all mammalian lineages and concluded that mammalian speciation rates were high well before the Cretaceous–Paleogene boundary. Rather than leading to a burst of diversification, the major environmental changes during the time filtered out more slowly speciating mammalian lineages,

leading to domination of the group by those that speciated more rapidly. —Sacha Vignieri

Science p. 1007, 10.1126/science.adj2793

METALLURGY
Going with the flow in the cold

Low-temperature structural materials are important for applications such as the transportation and storage of liquified natural gas. Wang *et al.* developed a high-strength steel with attractive ductility even at liquid nitrogen temperatures. The steel contains iron, manganese, aluminum, nickel, and carbon and forms a very strong matrix with zones of local ordering and nanoprecipitates. The high strength is due to solid solution strengthening, and this strengthening effect is high enough that the normally brittle nanoparticles will shear instead and accommodate deformation. This allows the high-strength steel to resist brittle fracture better than other low-temperature structural materials. —Brent Grocholski

Science p. 1017, 10.1126/science.ado2919

IMMUNE MEMORY
Immune memory

Heart failure is often associated with recurrence and the development of comorbidities, but the mechanisms driving multimorbidity in patients with heart failure are not fully understood. Using a mouse model of heart failure, Nakayama *et al.* found that transplantation of bone marrow from these mice spontaneously resulted in cardiac dysfunction in recipient mice. Mice transplanted with heart failure–experienced bone marrow were also more vulnerable to kidney and skeletal muscle injury. Heart failure reprogrammed hematopoietic stem cell differentiation and altered tissue macrophage homeostasis. These findings demonstrate that the bone marrow can carry an innate immune memory of cardiac stress that may exacerbate heart failure

and predispose other organs to pathology. —Claire Olingy

Sci. Immunol. (2024) 10.1126/sciimmunol.ade3814

EVOLUTION
Virulence speeds up speciation

Coevolution has often been studied in systems such as infectious disease, where hosts and parasites have very different generation times and other life history traits. By contrast, Langmore *et al.* studied several virulent species of cuckoos, brood parasite birds that kick host young out of the nest after hatching, thus placing a high selective pressure on their hosts to recognize the imposters. Using modeling, the authors found that particularly virulent species had higher speciation rates than less virulent ones. They also looked at the DNA and morphology of bronze-cuckoos, finding that assortative mating was occurring between those that targeted the same hosts. This study elucidates speciation dynamics in this coevolving system. —Corinne Simonti

Science p. 1030, 10.1126/science.adj3210

BIOMIMETICS
Tracking with avian-inspired vision

The eyes of certain bird species contain a deep central fovea that can magnify a target object for motion tracking, as well as four cone types corresponding to red, blue, green, and ultraviolet light. Inspired by these avian eyes, Park *et al.* developed an artificial vision system for foveated and multispectral imaging. The system is composed of an artificial Gaussian-shaped fovea that can magnify and focus an object similarly to a zoom lens and a vertically stacked perovskite photodetector array that can detect multiple wavelengths of light without filters. This vision system is particularly promising in uncrewed aerial vehicles for detecting target objects and their motion. —Melisa Yashinski

Sci. Robot. (2024) 10.1126/scirobotics.adk6903

EVOLUTION
A genome in flux

Despite being closely related to vertebrates, the tiny marine tunicate *Oikopleura dioica* has the smallest nonparasitic animal genome known to date. Plessy *et al.* assembled genomes of this animal collected from several locations in Japan, Spain, and Norway. They found that the *O. dioica* genomes are highly scrambled as a result of thousands of chromosomal rearrangements. The recombination rate observed is 10-fold greater than that of other sea squirts, nematodes, fruit flies, and mammals. Tunicates from different locations cannot be distinguished by morphology, although they cannot hybridize. It appears that during evolution, reshuffling in the ancestral *Oikopleura* genome produced different configurations without fundamentally affecting morphology, physiology, and ecology. —Di Jiang

Genome Res. (2024)   10.1101/gr.278295.123
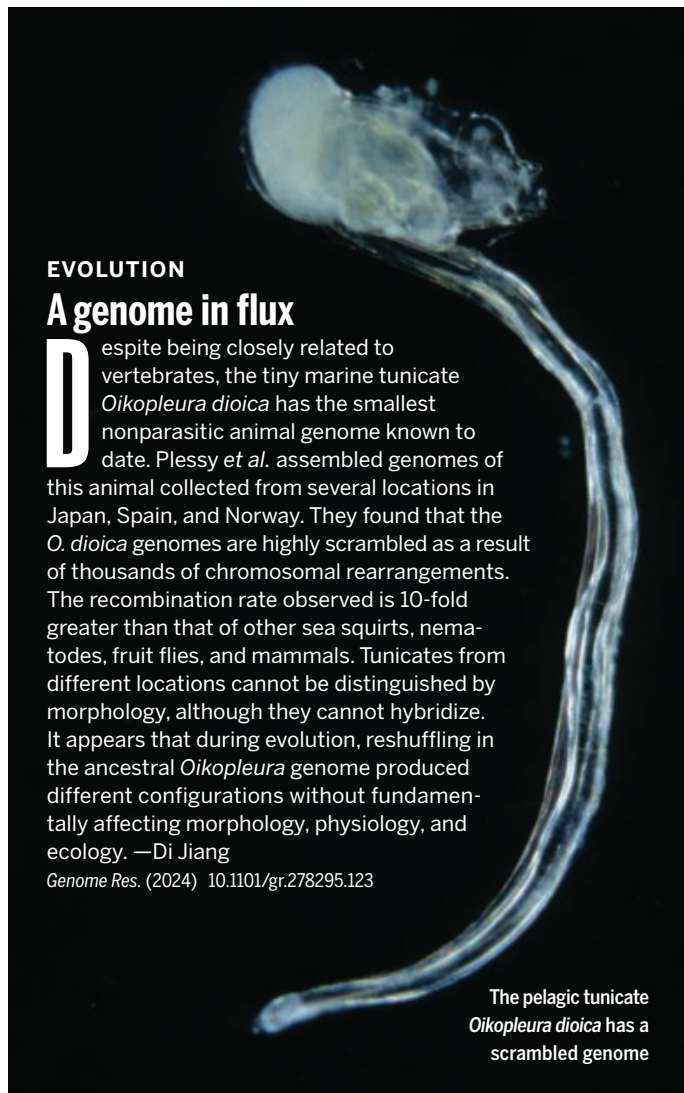
The pelagic tunicate *Oikopleura dioica* has a scrambled genome

BIOMATERIALS
Reducing harm from prolonged intubation

Intubation is a procedure in which endotracheal tubes are placed in a patient's airway to enable the delivery of air, anesthesia, or medications while also protecting the lungs by preventing contamination with blood or gastric contents. However, long-term intubation can cause injury to the mucosal epithelium due to inflammation or fibrosis. Miar *et al.* developed a hydrogel based on a polyethylene glycol acrylate matrix embedded with electrospun polycaprolactone fibers as a coating for the endotracheal tubes. The coating is used for the release of dexamethasone and small interfering RNA, which act to hinder inflammation and fibrosis. In a swine model, the coated tubes restored mechanical function of the vocal folds and maintained epithelial thickness over a 14-day intubation period. —Marc S. Lavine

Biomaterials (2024) 10.1016/j.biomaterials.2024.122602

INTERNET WELL-BEING
More good than harm?

The advent of the internet has forever changed the world and how rapidly people share information, but has this done more harm than good for human well-being

MICROBIOLOGY

What does a worm smell like?

Sight, smell, and taste in animals rely on molecular receptors, primarily G protein–coupled receptors (GPCRs), to sense light or chemical stimuli. Fungi also have a panoply of GPRCs that can sense diverse stimuli. Kuo *et al.* studied a nematode-trapping fungus and identified two distinct GPCR families that are involved in sensing prey. One group of GPCRs responded to specific pheromones produced by the nematode, triggering signaling pathways leading to trap development. The ligand for the other group of receptors remains unknown, but deletion of the receptor prevents trap formation. —Michael Funk   *Nat. Microbiol.* (2024) 10.1038/s41564-024-01679-w

Some nematode-trapping fungi use special molecular receptors to sense their prey and develop their traps.

---

globally? In an analysis of nearly 2.5 million people in 168 countries from 2006 to 2021, Vuorre and Przybylski looked at internet access and eight indicators of well-being, including life satisfaction, community well-being, and physical and emotional well-being. The authors found that in 85% of cases, internet connectivity was associated with better well-being around the world. Although recent research on this hotly debated topic has focused on the harms of social media or cyberbullying among younger generations, this study indicates that the potential impact of internet use changes across the life course. —Ekeoma Uzogara

Technol. Mind Behav. (2024) 10.1037/tmb0000127

METABOLISM

How now, brown fat?

The metabolism of branched-chain amino acids (BCAAs) in brown fat may have beneficial effects on metabolic health. Brown fat increases energy expenditure for thermogenesis and can thus decrease body weight, particularly in rodents. In humans, however, the beneficial effects of brown fat are independent of body weight. Verkerke *et al.* found that BCAAs in mouse brown adipocytes provide nitrogen to mitochondria to make glutathione and nonessential amino acids. Loss of the mitochondrial BCAA carrier in brown adipocytes caused insulin resistance but did not change energy expenditure, and obesity impaired BCAA metabolism. —L. Bryan Ray

Cell (2024) 10.1016/j.cell.2024.03.030

MIGRATION

Creatures of habitat

A major challenge for migrating birds is the loss of habitat along their migration routes. If important stopover sites become unavailable for refueling, then migrant birds become even more vulnerable and their conservation problematic. Lisovski *et al.* have attempted to forecast optimal migratory routes up to the year 2060 for five shorebird species that migrate between East Asia and Australasia, a region that has seen rapid coastal habitat change. By comparison with historical data, it seems that smaller species that need to stop more often can modify their routes and buffer habitat deterioration. However, larger species that make fewer stops tend to stick to their traditional routes and stopovers and thus suffer more from the loss of suitable habitat. The authors' model could help in planning conservation strategies to accommodate the needs of these different species. —Caroline Ash

Proc. Natl. Acad. Sci. U.S.A. (2024) 10.1073/pnas.2311146121

SEA LEVEL RISE

Not much help

As climate warms, mass loss from the Antarctic Ice Sheet is accelerating from a combination of faster melting and more rapid dynamic ice loss, speeding up its contribution to sea level rise. At the same time, however, snow accumulation is increasing because warmer air holds more moisture, thus offsetting mass loss. How important is this increase in snow accumulation in terms of mitigating sea level rise? Eswaran *et al.* reconstructed Antarctic snow accumulation from 1801 to 2000 CE, finding that mass accumulation rates increased only modestly over the 20th century, resulting in one-tenth the sea level rise mitigation that has been reported in other estimates. Most of that effect is due to a stronger snow accumulation trend since around 1970. —Jesse Smith

Geophys. Res. Lett. (2024) 10.1029/2023GL106991

PHOTO: BIOPHOTO ASSOCIATES/SCIENCE SOURCE

CANCER

Germline-mediated immunoediting sculpts breast cancer subtypes and metastatic proclivity

Kathleen E. Houlahan, Aziz Khan, Noah F. Greenwald, Cristina Sotomayor Vivas, Robert B. West, Michael Angelo, Christina Curtis*

INTRODUCTION: Cancer is defined by a set of abnormal biological capacities, termed the "hallmarks of cancer," which can be acquired by hijacking various cellular processes. As a result, tumors with the same clinical characteristics can vary dramatically across individuals, and these distinct molecular vulnerabilities can have important prognostic and therapeutic implications. Oncogenic alterations are acquired within the context of an individual's inherited DNA—known as the germline genome—which differ across individuals at millions of polymorphic sites. It remains poorly understood how inherited variants impact the evolution of a tumor. The most compelling example is that deleterious germline variants in *BRCA1* and, to a lesser extent, *BRCA2*, are preferentially associated with the development of triple negative breast cancer and estrogen receptor (ER)–positive (ER+) breast cancer, respectively, implying that germline variants modulate specific subtypes of disease. The mechanistic basis for this preference is incompletely characterized. Various lines of evidence suggest that avoidance of the adaptive immune system determines which somatic mutations per-

sist within a tumor. It remains less clear how germline differences influence immunoediting. Generally, germline variants have not been considered a source of immunogenic epitopes because cytotoxic response should be dampened by central and peripheral tolerance. However, nonmutated immunogenic epitopes have been identified in genes such as *ERBB2* in breast and ovarian cancer and H4 histone in prostate cancer, among others, suggesting that germline variants may play a role in immunosurveillance.

RATIONALE: We sought to investigate whether germline variants sculpt somatic evolution by mediating immunoediting. Specifically, we hypothesized that the burden of germline-derived epitopes in recurrently amplified driver genes may select against somatic gene amplification. This is because amplification of a gene with a high burden of germline-derived epitopes would increase epitope availability, likelihood of epitope presentation, and immune-mediated cell death. Thus, somatic amplification of the gene would come at a fitness cost in cells with a high burden of germline-derived epitopes.

Instead, a tumor may favor an alternative oncogenic pathway with lower fitness costs.

RESULTS: We leveraged paired tumor and normal sequencing data from 4918 primary and 611 metastatic breast cancer patients, as well as somatic genomic profiles from 341 patients with ductal carcinoma in situ (DCIS), and evaluated the relationship between germline-derived epitope burden (GEB) and subtype commitment, defined by the acquisition of focal oncogenic amplifications. As proof of concept, we identified two immunogenic peptides derived from the germline sequence of human epidermal growth factor receptor 2 (HER2; peptides GP2 and E75) and hypothesized that the ability to present either peptide would be negatively associated with developing HER2+ breast cancer. We discovered that individuals who possess MHC class I alleles that can bind and present GP2 or E75 are less likely to develop HER2+ breast cancer than other breast cancer subtypes. In addition to GP2 and E75, we found that individuals with a high GEB in *ERBB2*, encoding HER2, are less likely to develop HER2+ breast cancer. The same negative association was observed for three recurrent amplicons observed in distinct ER+ breast cancers, which are characterized by high risk of relapse. Negative associations were robust to the definition of subtype, binding affinity threshold, and the algorithm to predict binding affinity. Tumors that overcame immune-mediated negative selection were more aggressive and exhibited microenvironments depleted of lymphocytes. In DCIS, before immune escape, high GEB was negatively associated with invasive breast cancer recurrence, suggesting that GEB is protective in the preinvasive setting.

CONCLUSION: These data indicate that supposedly "benign" germline variants with little to no functional genic effect may, in aggregate, sculpt breast cancer subtypes and disease aggression through immunoediting. These data also indicate that immunoediting pressures differ during the course of a patient's disease, potentially informing the timing of therapeutic interventions. Exploiting germline-mediated immunoediting may inform the development of biomarkers that predict risk of invasive breast cancer recurrence and further refine risk stratification within invasive breast cancer subtypes. ∎
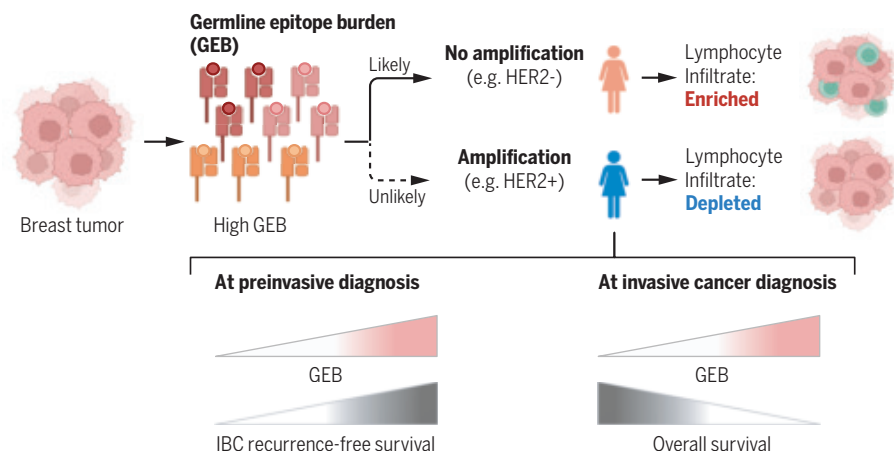
Germline-mediated immunoediting sculpts cancer subtypes and metastatic proclivity. During tumorigenesis, lesions with high GEB in cancer genes are less likely to acquire somatic amplification of that gene. In preinvasive breast tumors, high GEB is protective against invasive breast cancer (IBC) recurrence. However, established tumors that acquire somatic amplification are forced to develop an immune suppressive and evasive phenotype and are more aggressive [Figure created using Biorender.com].

READ THE FULL ARTICLE AT
https://doi.org/10.1126/science.adh8697
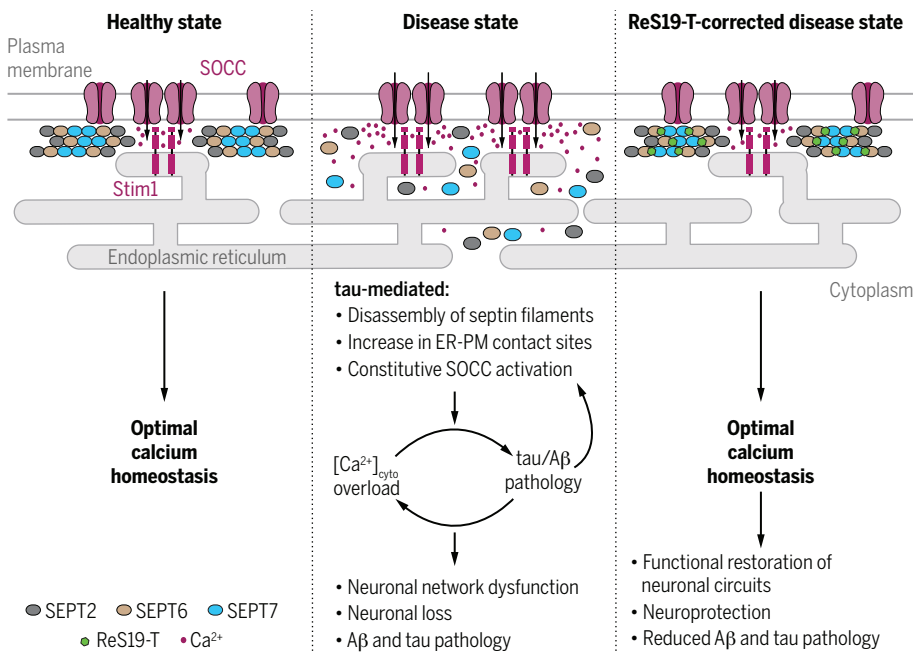
RESEARCH ARTICLE SUMMARY

NEURODEGENERATION

Pharmacological modulation of septins restores calcium homeostasis and is neuroprotective in models of Alzheimer's disease

Katrien Princen†, Tom Van Dooren†, Marit van Gorsel, Nikolaos Louros, Xiaojuan Yang, Michael Dumbacher, Ilse Bastiaens, Kristel Coupet, Shana Dupont, Eva Cuveliers, Annick Lauwers, Mohamed Laghmouchi, Thomas Vanwelden, Sofie Carmans, Nele Van Damme, Hein Duhamel, Seppe Vansteenkiste, Jovan Prerad, Karolien Pipeleers, Olivier Rodiers, Liese De Ridder, Sofie Claes, Yoni Busschots, Lentel Pringels, Vanessa Verhelst, Eveline Debroux, Marinka Brouwer, Sam Lievens, Jan Tavernier, Melissa Farinelli, Sandrine Hughes-Asceri, Marieke Voets, Joris Winderickx, Stefaan Wera, Joris de Wit, Joost Schymkowitz, Frederic Rousseau, Henrik Zetterberg, Jeffrey L. Cummings, Wim Annaert, Tom Cornelissen, Hans De Winter, Koen De Witte, Marc Fivaz*, Gerard Griffioen*

INTRODUCTION: Currently, 55 million individuals worldwide suffer from dementia, a figure anticipated to double every 20 years. Alzheimer's disease (AD) makes up 60 to 80% of all dementia cases and is one of the top 10 causes of death, with no effective prevention or treatment available. AD is a neurodegenerative disease, pathologically defined by the progressive buildup in the brain of two types of proteinaceous deposits, amyloid β (Aβ) and tau tangles. Aβ-targeting therapeutic strategies have for the most part dominated the AD drug development space and led to the recent US Food and Drug Administration approval of monoclonal antibodies that clear Aβ plaques and decelerate cognitive decline. However, the clinical benefits of these treatments remain modest, underscoring the need for new drug targets and therapeutic concepts other than Aβ-targeting therapies.

RATIONALE: Abnormal calcium signaling is a pivotal aspect of AD, being implicated in both neuronal network dysfunction and cell death, and is intricately connected to both Aβ and tau pathology. Therefore, targeting calcium dyshomeostasis in AD is a promising therapeutic strategy. However, given the central role of calcium ions in neuronal communication and cell physiology, nonselective manipulation of the calcium concentration inside (nerve) cells may cause serious adverse effects. To overcome this challenge, we set out to identify calcium influx pathways excessively activated in pathological conditions and developed a cell-based model of tau toxicity that strictly depends on calcium entry induced by diseased tau. Using this toxicity assay, we then screened a chemical library to identify small molecules that attenuate calcium influx without affecting calcium levels in a nonpathological context.

RESULTS: A promising "hit" from this screen was further optimized into a class of closely related molecules named ReS19-T. Target deconvolution studies revealed that ReS19-T compounds bind to septin isoforms, with the highest affinity for septin 6. Septins are cytoskeletal components that assemble into filaments at the cell cortex. We show that pathological tau destabilizes septin filaments, resulting in unrestrained activation of store-operated calcium channels (SOCCs) and calcium overload. By promoting septin polymerization, ReS19-T restores the integrity of septin filaments and prevents spurious activation of SOCCs in conditions of tau pathology. ReS19-T has no effect on physiological (store-operated) regulation of SOCCs in the nonpathological state. Administration of ReS19-T to tau- or Aβ-driven mouse models of neurodegeneration fully restored hippocampal long-term potentiation (a form of synaptic plasticity associated with the formation of new memories), rescued spatial memory deficits, and normalized brain oscillatory activity. Finally, ReS19-T mitigated the formation of Aβ plaques and hyperphosphorylated tau aggregates.

CONCLUSION: Our research sheds new light on the potential for targeting the septin cytoskeleton as a new and effective therapeutic strategy for AD. ReS19-T, which regulates SOCC activity in disease states, demonstrates promising neuroprotective effects, offering hope for transformative AD treatments. The clinical translatability of this therapeutic concept is currently being assessed in AD patients. ∎

Mechanism of action of ReS19-T. In the disease state, tau pathology disrupts septin filament assembly, causing aberrant (store-independent) activation of SOCCs and a prolonged rise in cytoplasmic calcium levels, setting off a series of self-amplifying pathophysiological events. ReS19-T binding to septins promotes filament assembly at the cell cortex, preventing spurious activation of SOCCs and thus restoring calcium homeostasis and neural circuit connectivity and preventing neuronal loss.

S READ THE FULL ARTICLE AT
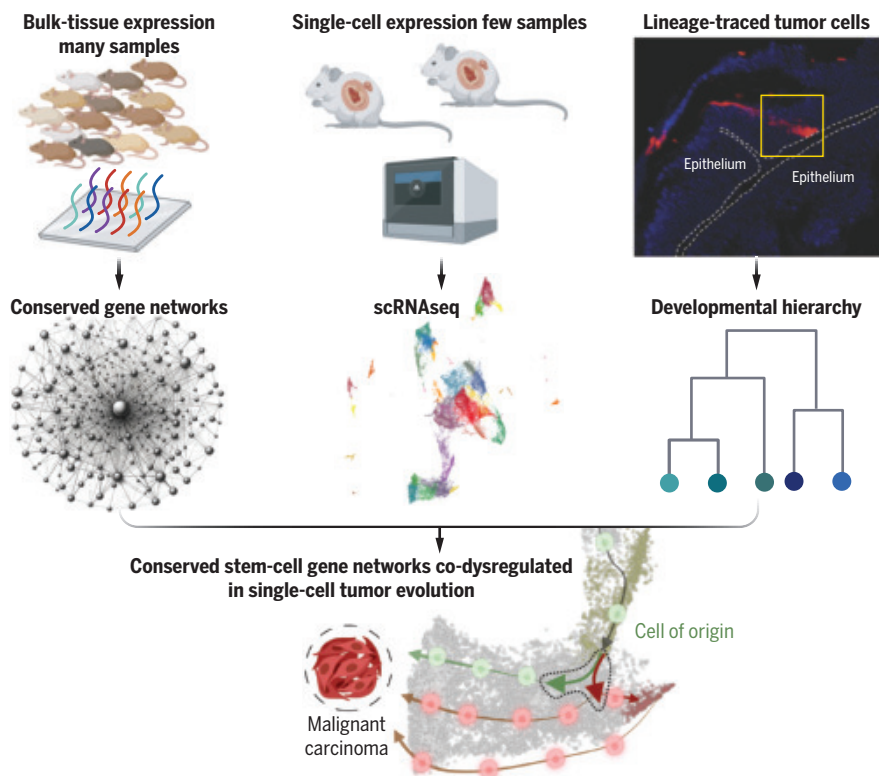https://doi.org/10.1126/science.add6260

CANCER

Stem-cell states converge in multistage cutaneous squamous cell carcinoma development

Mark A. Taylor†, Eve Kandyba†, Kyle Halliwill, Reyno Delrosario, Matvei Khoroshkin, Hani Goodarzi, David Quigley, Yun Rose Li, Di Wu, Saumya R. Bollam, Olga K. Mirzoeva, Rosemary J. Akhurst, Allan Balmain

INTRODUCTION: Human tumors arise as a consequence of exposure to environmental agents including mutagens and tumor-promoting chemicals, but cancer incidence is also heavily influenced by complex genetic and lifestyle factors. We replicated this complex etiology in mice by generating a genetically heterogeneous population from crosses between two diverse strains and exposing them to initiators and promoters of skin carcinogenesis. This controlled genetic complexity enabled us to create gene expression networks (metagenes) from hundreds of normal skin and tumor samples, enabling an analysis of how gene networks, rather than single genes, evolve during multistage carcinogenesis. We applied this approach to analysis of stem cells, which play an important role in normal tissue homeostasis but are also known to be highly expressed in cancer cells, where they contribute to the cancer hallmark lineage plasticity, drug resistance, and poor treatment outcomes.

RATIONALE: Tumor cell plasticity has been attributed to the existence of cancer stem cells (CSCs) but there is presently no consensus as to how CSCs relate to their normal tissue counterparts, to the cells of origin of tumors, or even whether they exist. Stem cells have been extensively studied in both bulk-tissue samples and at the single-cell level but hierarchical relationships between these cell populations in cancers have been difficult to identify. We reasoned that analysis of stem cell networks, rather than of single genes, may reveal such relationships. We generated gene networks for a wide range of stem cell markers from hundreds of samples taken from normal skin, benign tumors, and malignant tumors, and visualized expression of these network metagenes in single cells derived from multiple stages of carcinogenesis. By combining these modalities, we leveraged bulk-tissue sampling breadth and single-cell resolution to track multisample stem cell states as they evolved during the transition from normal skin to malignant carcinomas.

RESULTS: Individually, stem cell genes were sporadically expressed in single cells without clear patterns but analysis of their corresponding network metagenes revealed a convergence of stem cell states in early-stage tumors that was not seen in matched normal skins. *Lgr6+* stem cells from tumors generated progeny that expressed lineage plasticity markers *Sox2*, *Pitx1*, *Foxa1*, and *Cd44*, as well as genes associated with quiescence and tumor suppression. This cell state was strongly anticorrelated with an alternative state expressing markers of cell proliferation and DNA damage responses. Transitions between these states could be induced by treating carcinomas with cisplatin, which reduced proliferation and activated the cell plasticity state, or by inhibition of the master regulator of differentiation *Pp2a*, leading to suppression of the plasticity state and sensitization to drugs that kill dividing cells.

CONCLUSION: By tracing the expression of stem cell networks at the single-cell level during multistage carcinogenesis we identified cell populations expressing two alternate cell states with opposite phenotypes: One expressed a rapid cycling cancer hallmark while the other expressed the slow-cycling lineage plasticity cancer hallmark. We propose a simplified model of carcinogenesis that identifies convergent stem cell states at different stages of tumor progression. Manipulation of the gene networks underlying these cell states influenced the transition between them and may provide a rich source of potential targets for combinatorial cancer therapy. ∎

Stem cell states converge at early stages of carcinogenesis. Robust gene networks can be generated from many bulk-tissue samples. Since they derive from many samples, they are conserved across independent instances of a cancer. Single-cell expression tracks those networks in fewer samples but at single-cell resolution. Empiric lineage tracing unambiguously orders parent-progeny cells. By combining all three at multiple stages of cancer development, we traced how stem cell networks were convergently expressed in a small number of single-cell paths in benign tumors as they developed into florid malignancy. [Image created with BioRender.]

READ THE FULL ARTICLE AT
https://doi.org/10.1126/science.adi7453

MISINFORMATION

Quantifying the impact of misinformation and vaccine-skeptical content on Facebook

Jennifer Allen*, Duncan J. Watts, David G. Rand

INTRODUCTION: Researchers and public health officials have attributed much of the low uptake of the COVID-19 vaccine in the US to misinformation on social media. However, it is unclear whether misinformation had (i) the widespread exposure and (ii) the causal impact on vaccination intentions required to meaningfully alter the trajectory of US vaccination efforts. Moreover, content that raises questions about vaccines without containing outright falsehoods (which we term "vaccine-skeptical") might also play a role in driving vaccine refusal. In this work, we examine to what extent misinformation flagged by fact-checkers on Facebook (as well as content that was not flagged but is still vaccine-skeptical) contributed to US COVID-19 vaccine hesitancy.

RATIONALE: We posit that two conditions must be met for content to have widespread impact on people's behavior: People must see it, and, when seen, it must affect their behavior. That is, we define "impact" as the combination of exposure and persuasive influence.

We apply this framework to quantify the impact that (mis)information on Facebook had on COVID-19 vaccination intentions in the US by combining experimental estimates of persuasive effects with Facebook exposure data. To begin, we conducted two experiments (total $N = 18,725$) on the survey platform Lucid measuring the causal effect of 130 vaccine-related headlines on vaccination intentions. We then used Facebook's Social Science One dataset to measure exposure to all 13,206 vaccine-related URLs that were popular on Facebook during the first 3 months of the vaccine rollout (January to March 2021). Finally, we developed a pipeline that incorporates the wisdom of crowds and natural language processing (NLP) to predict the persuasive effect of each Facebook URL from our survey estimates.

RESULTS: Analyzing our survey experiments, we found that while exposure to fact-checked misinformation can cause vaccine hesitancy, the degree to which a story implies health risks from vaccines best predicts negative persuasive influence. Our first experiment showed that misinformation containing false claims about the COVID-19 vaccine reduced vaccination intentions by 1.5 percentage points ($P = 0.00004$). Our second experiment tested both true and false claims and found that content suggesting that the vaccine was harmful to health re-duced vaccination intentions, irrespective of any potential effect of the headline's veracity.

Examining exposure on Facebook, we found that flagged misinformation URLs received 8.7 million views during the first 3 months of 2021, accounting for only 0.3% of the 2.7 billion vaccine-related URL views during this time period. In contrast, stories that were not flagged by fact-checkers but that nonetheless implied that vaccines were harmful to health—many of which were from credible mainstream news outlets—were viewed hundreds of millions of times.

We then used our crowdsourcing and NLP procedure to extrapolate the treatment effects of the 130 items to the 13,206 vaccine-related Facebook URLs. The URLs flagged as misinformation by fact-checkers were, when viewed, more likely to reduce vaccine intentions (as predicted by our model) than unflagged URLs. However, after weighting each URL's persuasive effect by its number of views, the impact of unflagged vaccine-skeptical content dwarfed that of flagged misinformation. Subsetting to those URLs predicted to induce hesitancy, we estimated that unflagged vaccine-skeptical content lowered vaccination rates by −2.28 percentage points {confidence interval (CI): [−3.4, −0.99]} per US Facebook user, compared with −0.05 percentage points (CI: [−0.07, −0.05]) for flagged misinformation—a 46-fold difference. Even though flagged misinformation had more of an impact when viewed, the differences in exposure were so large that they almost entirely determined the ultimate impact. For example, a single vaccine-skeptical article published by the *Chicago Tribune* titled "A healthy doctor died two weeks after getting a COVID vaccine; CDC is investigating why" was seen by >50 million people on Facebook (>20% of Facebook's US user base) and received more than six times the number of views than all flagged misinformation combined.

CONCLUSION: We find that flagged misinformation does causally lower vaccination intentions, conditional on exposure. However, given the comparatively low rates of exposure, this content had much less of a role in driving overall vaccine hesitancy compared with vaccine-skeptical content, much of it from mainstream outlets, that was not flagged by fact-checkers. Our work suggests that while limiting the spread of misinformation has important public health benefits, it is also critically important to consider gray-area content that is factually accurate but nonetheless misleading. ■

Fact-check rating: ■ Flagged misinformation ■ Not flagged
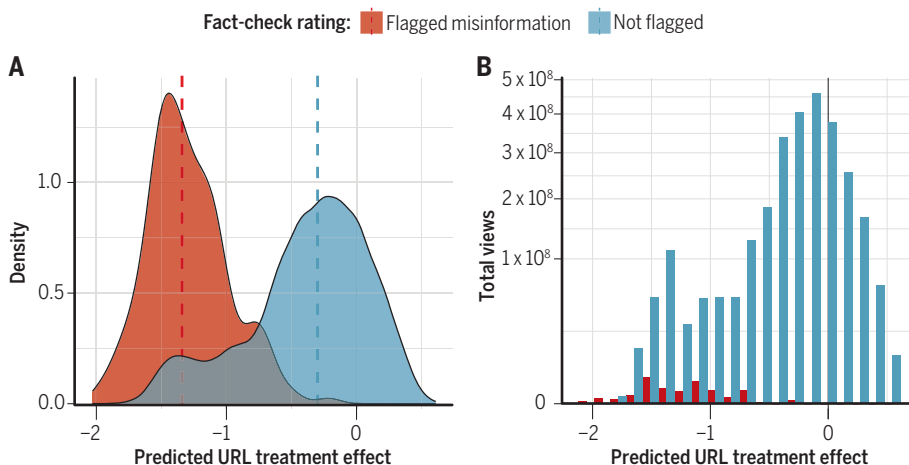
Impact of flagged misinformation versus unflagged content. (**A**) Distribution of 13,206 predicted URL treatment effects on vaccination intentions for flagged misinformation (red) versus unflagged content (blue). (**B**) The same histogram as in (A), weighted by the number of views each URL received on Facebook. Although misinformation has more negative persuasive effects, it is seen far less—and thus has a lesser impact—than unflagged content.

S READ THE FULL ARTICLE AT
https://doi.org/10.1126/science.adk3451

RESEARCH ARTICLES

MISINFORMATION

Supersharers of fake news on Twitter

Sahar Baribi-Bartov[1], Briony Swire-Thompson[2], Nir Grinberg[1]*

Governments may have the capacity to flood social media with fake news, but little is known about the use of flooding by ordinary voters. In this work, we identify 2107 registered US voters who account for 80% of the fake news shared on Twitter during the 2020 US presidential election by an entire panel of 664,391 voters. We found that supersharers were important members of the network, reaching a sizable 5.2% of registered voters on the platform. Supersharers had a significant overrepresentation of women, older adults, and registered Republicans. Supersharers' massive volume did not seem automated but was rather generated through manual and persistent retweeting. These findings highlight a vulnerability of social media for democracy, where a small group of people distort the political reality for many.

The pathways to news have substantially changed in the past two decades. The rise of social media as a vector for news created new challenges for democracies because large segments of society can be rapidly exposed to misinformation while others are unaware of this exposure taking place. Although prior work has examined the role of foreign influence campaigns and automated accounts (bots) in spreading misinformation on social media (1–3), relatively little work has focused on the role of ordinary citizens in propagating misinformation online. Recent work has consistently found that a small fraction of people—referred to as supersharers—account for the majority (80%) of fake news shared by registered voters on social media (4–6). Because of the rarity of supersharers, it is extremely difficult to study a meaningfully sized sample of supersharers using traditional research methods (e.g., surveys or experiments). Apart from supersharers' existence, we know little about the scale and scope of supersharers' influence online, the distinctive characteristics of supersharers, or the technical affordances that give rise to their online dominance.

Supersharers undermine a key pillar of deliberative democracy—equal representation of voices in a debate (7)—by flooding the digital sphere with their content. If trusted, their content may further the fragmentation of society into disjoint communities of belief. Arguably, the closest parallel to supersharing is the use of information flooding by authoritarian governments as a strategy to control and divert public opinion (8); yet, no prior work, to the best of our knowledge, has examined the

use of flooding by voters in a democracy. To fully understand misinformation today and devise effective mitigation strategies, research must expand beyond the incidental sharers of misinformation and examine people who distort political discussion by the sheer volume of their actions.

This study leverages a panel of 664,391 registered US voters on Twitter (now X) to identify and study 2107 supersharers. We first address fundamental questions about supersharers' importance: Are they effectively "shouting" into a void where no one is listening, or are they finding large audiences online? Are supersharers vocal actors with little influence over their networks, or are they prominent actors supplying a demand for political misinformation? If supersharers are embedded in real human social networks, as suggested by prior work (4), they are likely to have real-world relationships with some of their followers (9), which places the communication in a different context of social trust. People who follow supersharers are likely to be exposed to more misinformation and potentially repeated exposure, both of which are contributing factors to belief in false claims (10, 11). Over time, repeated exposure may have long-term implications, such as changing the norms of accepted behavior (12).

Another important piece of the puzzle is the sociodemographic characteristics of supersharers. Other than supersharers' existence, little is known about these individuals. One could predict that supersharing is conducted by young, male, and tech-savvy individuals who feel disenfranchised by mainstream society (13). Alternatively, supersharers may be an extension of the so-called average person, who is exposed to and shares misinformation—i.e., older, male, and right-leaning individuals (4–6). Mitigation strategies may differ depending on who the supersharers are. For example, to counter young, technologically sophisticated

individuals would require a more sophisticated approach.

Finally, it is unclear how supersharers technically share so much misinformation. Prior work has suggested that supersharers are cyborgs, using automation tools to auto-tweet on behalf of the user (4). Research has also identified automated accounts, known as social bots, as responsible for spreading disproportionate amounts of fake political content on social media (3). Extensive use of automation by supersharers may indicate that they are part of a larger influence campaign, much like Russia's foreign interference in the 2016 US presidential election (1, 14), China's domestic propaganda to divert public attention at critical times (15), and South Korea's campaign to support the incumbent president (16). Therefore, it is unclear to what extent automation explains the volume generated by supersharers.

This work addresses three research questions (RQs). RQ1: How important are supersharers on Twitter and in their networks? RQ2: Who are the supersharers? RQ3: What are the affordances of social media that enable supersharers to share a massive volume of fake news without facing moderation?

Method

To identify supersharers, we leveraged a large-scale panel of 664,391 registered US voters who were active on Twitter during the 2020 US presidential election (from August to November 2020). We identify supersharers ($N = 2107$) as the most prolific sharers of fake news that account for 80% of fake news content shared on the platform.

Similar to prior work (4, 6), we rely on a source-level definition of fake news as domains that portray as legitimate news outlets but do not have the "editorial norms and processes for ensuring the accuracy and credibility of information" (17). We rely on the manually labeled list of fake news sites by Grinberg et al. (4), updated using NewsGuard ratings, and demonstrate the robustness of the findings to different operationalizations (see supplementary materials, section S3). To focus on political news, we restrict the analysis to tweets with external links that were identified as political by a machine learning classifier that we trained and validated against human coders. See the materials and methods for more details and additional robustness checks. Throughout, we refer to the platform as Twitter (rather than X) because our data were collected in 2020.

We address our research questions by contrasting supersharers with two main reference groups: the heaviest sharers of nonfake political news (SS-NF, $N = 11,199$; defined as the set of panelists that account for 80% of nonfake political news) and a similarly sized ($N = 11,199$)

[1]Software and Information Systems Engineering, Ben-Gurion University, Be'er Sheva, Israel. [2]Network Science Institute, Department of Political Science, Department of Psychology, Northeastern University, Boston, MA, USA.
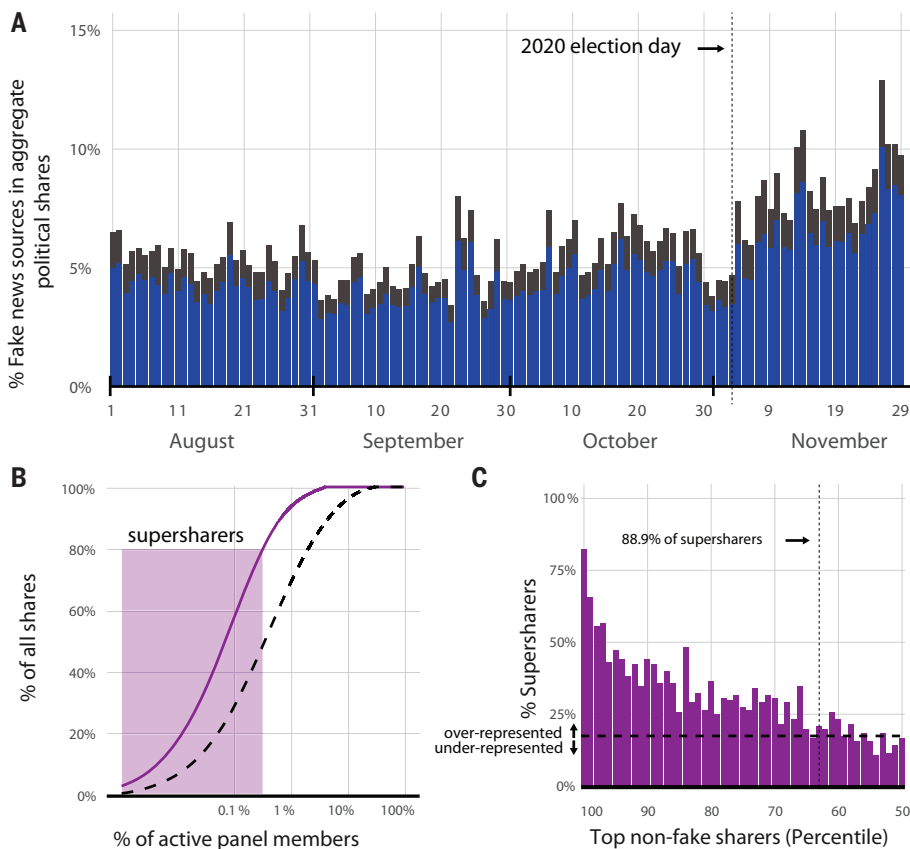*Corresponding author. Email: nirgrn@bgu.ac.il

Fig. 1. Prevalence over time and concentration of fake news sharing. (A) Percentage of fake news sources in aggregate political shares. Blue bars show the fraction of fake news shared strictly by supersharers, and black bars show the fraction shared by the rest of the panel. **(B)** Concentration of content from fake news sources shared by panel members. The purple-shaded area highlights the volume of fake news (80%) shared by the supersharers (0.3% of the population). **(C)** Percentage of supersharers in the top percentiles of nonfake political sharers, defined as panelists accounting for 80% of nonfake political content shared. A dashed horizontal line designates the average in this subpopulation.

random sample of panelists. Some of the analyses compare a third group aiming to capture average fake news sharers, defined as users who shared three or more tweets linking to fake news sources over the study period and who are not in the supersharers group (average fake news sharers, $N = 10,464$).

Results

We first sought to investigate how much fake news was shared throughout the 2020 election. On an average day, 7.0% [95% confidence interval (CI): 6.7%, 7.4%] of all political news shared by the panel of 664,391 individuals linked to fake news sources. However, an extremely small fraction of our sample (0.3%; only 2107 people) accounted for 80% of the tweets linking to fake news sources. We label these individuals supersharers. Figure 1B shows the cumulative distributions of fake and non-fake news sharing by the panel. It highlights that fake news sharing (solid purple line) is considerably more concentrated in the popu-

lation compared with nonfake political news sharing (dashed black line). An additional analysis showed that the level of concentration of fake news is not typical on Twitter (supplementary materials, section S8). The blue bars in Fig. 1A show that supersharers' dominance persisted throughout the election period. On a daily basis, the average supersharer posted considerably more links to political news (15.9 a day versus 5.0 for the SS-NF and 0.3 for the panel) and considerably more links to fake news sources (2.8 a day versus 0.1 for the SS-NF and 0.01 for the panel; see supplementary materials, section S1, for more details). In contrast to the 2016 election, content sharing rose after the election, mostly propelling allegations of election fraud (see supplementary materials, section S2, for more details). Figure 1C further shows that supersharers dominated nonfake political news sharing, as reflected in their overrepresentation in the top percentiles of nonfake political news sharing. These findings establish that supersharers were able to disse-

minate massive volumes of content on Twitter during the 2020 US presidential election.

To address our first research question regarding supersharers' importance (RQ1), we examined three measures of online influence. First, we examined the breadth of supersharers' reach among the 641,144 panelists for whom we have complete network information. We found that 5.2% of registered voters on Twitter directly follow a supersharer. To better understand supersharers' individual importance, we distinguish between network (topological) influence and engagement with their content. Pei *et al.* (*18*) showed that the sum of nearest neighbors' degrees is a reliable measure of network influence across different networks. Using this measure, we found that supersharers had significantly higher network influence than both the panel and the SS-NF groups ($P < 0.001$). The median supersharer ranked in the 86th percentile in the panel in terms of network influence and measured 29% higher than the median SS-NF (supplementary materials, section S11). Next, we measured engagement with supersharers' content as the fraction of panelists who replied, retweeted, or quoted supersharers' tweets relative to their number of followers in the panel. More supersharers had people engaging with their content compared with the panel ($P < 0.001$), and more panelists engaged with supersharers' content compared with all groups ($P < 0.001$; see supplementary materials, section S11, for details).

Supersharers' importance also stems from the people who follow them and the amounts of fake news that supersharers provide for them. Following the approach used in prior work (*2, 4, 19*), we examined the composition of content available to panelists from the accounts that they follow (see materials and methods for more details). Using this approach, we found that about a fifth of the heaviest consumers of fake news in the panel follow a supersharer. For example, 22.1% of panelists in the top decile of fake news consumption follow a supersharer (see supplementary materials, section S10, for additional thresholds). Moreover, the average follower of a supersharer was 2.5 times as likely to get political news linking to fake news sources from their network compared with the average panelist (absolute rates of 4.11% versus 1.66%). Supersharers accounted for nearly a quarter [24.4% (95% CI: 24.1%, 24.8%)] of the fake news available to their average follower and were the only source of fake news for 11.3% of their followers.

Next, we studied the distinctive sociodemographic characteristics of supersharers (RQ2). Based on logistic regression models distinguishing supersharers from each reference group separately, we found that supersharers have a significantly higher proportion of women, older adults, and Republican individuals compared with all reference populations ($P < 0.01$; full

model specifications are in the supplementary materials, section S4). The gender differences stem from overrepresentation of women among Republican supersharers but not Democrat supersharers (supplementary materials, section S12). Supersharers also had a significantly higher percentage of Caucasians compared with the panel and the SS-NF groups ($P < 0.001$) but no significant difference compared with the average fake news sharers. These differences are robust to different operationalizations of fake news (supplementary materials, section S3), thresholds for considering users as supersharers (supplementary materials, section S5), presence of outliers (supplementary materials, section S6), and matched-sample specifications (supplementary materials, section S12).

Figure 2 provides descriptive statistics for the key significant differences captured by the regression models. For example, it shows that supersharers had a significantly higher percentage of women (59%) compared with all reference groups (average fake news sharer, 49%; SS-NF, 52%; and panelists, 50%), and

the average supersharer is 58.2 years old, which is 5 years older than the average fake news sharer and 17 years older than the average panelist. It also shows that supersharers had the highest proportion of Republicans (64%), including the Republican-leaning group of average fake news sharers ($P < 0.001$).

Our analyses also identified significant geographic and socioeconomic differences. Supersharers were overrepresented in three US states: Florida, Arizona, and Texas ($P < 0.05$; additional contrasts are provided in the supplementary materials, section S13). The regression models distinguishing supersharers from the reference groups also identified significant differences in education attainment and annual income drawn from the US census ($P < 0.001$; supplementary materials, sections S1 and S4). Supersharers came from tracts of slightly lower educational attainment—an average of 0.3 fewer education years relative to the panel and SS-NF groups and a smaller difference relative to average fake news sharers. Relative to income expected based on education, supersharers' annual income was, on

average, $2500 US dollars (USD) higher than that of the SS-NF and average fake news sharers groups. Although these findings are robust across different model specifications, their small magnitude should be noted.

Finally, we investigated the affordances that supersharers use to produce a massive volume of content (RQ3). To thoroughly examine the potential use of automation, we used three separate approaches to identify automation and compare their results across groups. First, we used the bot detection tool Botometer (20) in conjunction with manual labeling to provide an upper bound for the amount of bots in our sample. We found that no more than 7.1% (95% CI: 2.0%, 12.2%) of supersharers can be considered as bots with no significant difference from the SS-NF group ($P = 0.35$), although the panel had a lower rate than both groups (1.2%; $P < 0.001$). Supplementary materials, section S6, further shows that the sociodemographic findings are robust to a small fraction of bots remaining in the sample.

Next, we examined posting times because irregular patterns can indicate the use of automation or app use (21). We found that supersharers are not significantly different from the reference groups in the time of day used for posting, the length or number of sessions per day, or the time between posts (see supplementary materials, section S6, for details). Moreover, we found no indication in tweets metadata that supersharers use apps that support automation more than other groups ($P = 0.75$).

The largest difference that we observed for supersharers relative to other groups is their rate of retweeting ($P < 0.001$). Three out of every four tweets (74.7%) posted by the average supersharer were retweets, which is considerably higher than the 59.9% rate found in the SS-NF group and the 32.7% rate in the panel. Our findings cannot rule out the use of more sophisticated forms of automation; however, they point to a more parsimonious explanation, where a large portion of supersharers' content is generated by manual and persistent retweeting.

Discussion

This study examined supersharers' importance, their distinctive sociodemographic characteristics, and the affordances that enabled supersharers to share massive volumes of fake news. Before this study, knowledge about supersharers (apart from their existence) was speculative.

Despite being only 0.3% of the population, supersharers reached 5.2% of registered voters in our sample and about a fifth of the heaviest consumers of fake news. To put this in perspective, it has been estimated that 3.4% of Americans on Twitter followed an account controlled by Russia's foreign influence campaign in 2016 (2). Another measure of scale
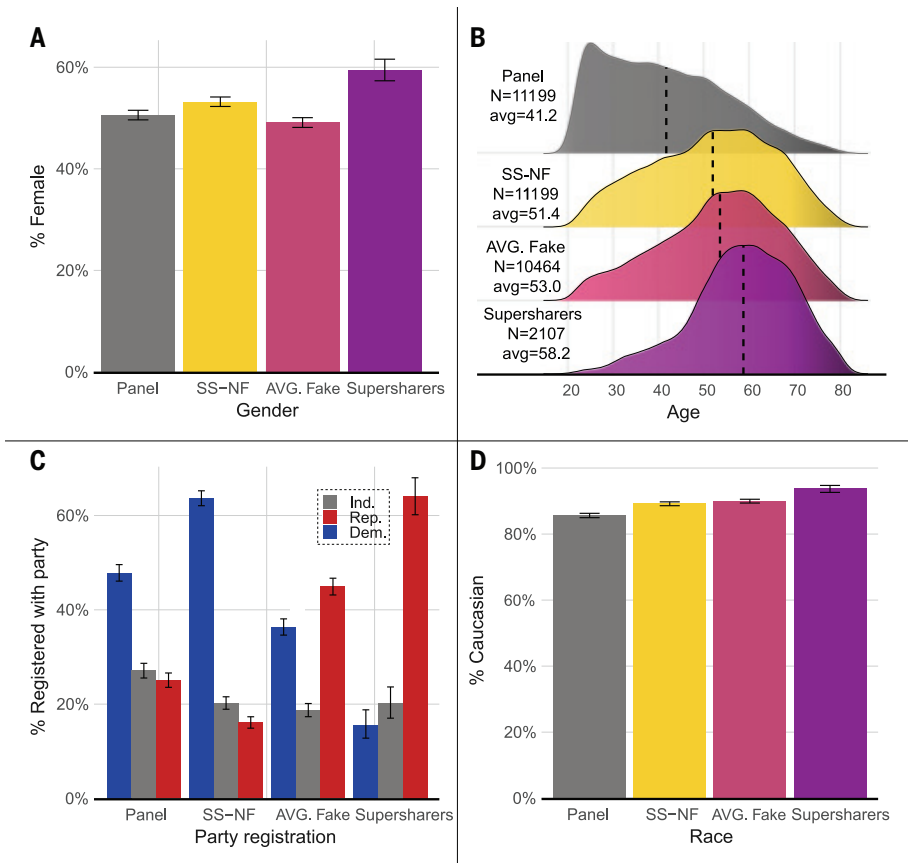

Fig. 2. Demographic differences between supersharers and three reference populations: SS-NF, average fake news sharers, and a random sample of the panel. (**A**) Gender. (**B**) Age distribution. (**C**) Party of registration. Ind, Independents; Rep, Republican; Dem, Democrat. (**D**) Race. (A), (C), and (D) show averages with 95% bootstrapped CIs. Supersharers have a significantly higher proportion of women, older adults, and Republican individuals compared with all reference populations ($P < 0.01$; full models are in supplementary materials, section S4).

can be based on the amount spent by the Biden and Trump campaigns on digital advertisements during the 2020 presidential election, which is estimated at $435 million USD (22). Roughly speaking, the candidates would have spent $20 million USD to get the same level of reach that supersharers have. Supersharers not only found a sizable audience online but were found to be influential members of their networks that provide approximately a quarter of the fake news to their followers. Across all our measures, supersharers received disproportionately more online attention.

As for sociodemographics, we found that supersharers were significantly more likely to be women, older adults, and right-leaning; were more likely to originate from Texas, Florida, and Arizona; and had small differences in education and relative income. Although some of these findings align with prior work regarding age and political leaning (4, 6), the association with gender and other geographical characteristics was not previously established, to the best of our knowledge. This image is certainly distinct from the stereotype of social media manipulators as young, alt-right, and male hackers (13). The reasons behind this demographic composition are unclear. One reason could be higher political participation by older adults and women (23, 24). Another reason may be that supersharing offers women an alternative form of activism, independent of the political establishment (25). Finally, it is possible that several individual differences may contribute to this behavior, such as perceived inequality (26), perceived threat to status (27), true and false news discernment ability (28, 29), or even differences in sharing motivations (30).

In terms of technical affordances, we did not find evidence of widespread use of automation by supersharers, as suggested by prior work (4). Our results point to a simpler explanation: Supersharers were highly active and persistent retweeters. It is possible that the absence of automation is why many supersharers evaded Twitter's attempts to purge inauthentic behavior. This highlights the vulnerability of social media platforms to so-called low-tech social manipulation.

Practical implications

Our research shows that platform interventions that target supersharers or impose retweet limits could be highly effective at reducing a large portion of exposure to fake news on social media. Interventions that target supersharers would only affect a tiny fraction of the population and would have large benefits because of supersharers' relative importance on Twitter (supplementary materials, section S9). It is an open question whether interventions can change the motivations behind supersharers' activity and whether these could affect supersharers' local communities.

Limitations and future directions

Several limitations should be noted. First, our sample may contain systematic differences from a fully representative sample. It is unclear whether people who could be matched from voter records differ from those who could not, in particular eligible but unregistered voters. Second, the capacity to share massive amounts of content exists on other social media platforms, but the extent to which this strategy is used outside of Twitter is unknown. Third, Twitter was an important platform in American politics in 2020, but large changes in its user base (31)—now users of X—may affect who is supersharing.

There are also several avenues for future work to extend this research. The causal mechanisms and motivations behind supersharers' activity are not yet clear. We do not know whether supersharers' actions are a form of political activism, unintentional, or an intentional attempt to misinform others. Addressing these questions is important for advancing our understanding of supersharers and for devising more appropriate interventions. Future research should investigate supersharing on other social platforms and measure the impacts of supersharers' activity on followers' political attitudes and behaviors.

Supersharers are an extremely interesting population that requires further examination given their disproportionate negative influence on our information ecosystem. Their reach suggests that they are not part of a small and isolated community, nor do supersharers seem to function as bridges to fake news for unwitting audiences. Instead, the results cast supersharers as influential members of local communities where misinformation is prevalent. As such, supersharers may provide a window into the social dynamics in parts of society where a shared political reality is eroding. Our work is a first step to understanding these individuals, but their behavior, their motivations, and the consequences of their actions warrant further research.

REFERENCES AND NOTES

1. C. A. Bail et al., Proc. Natl. Acad. Sci. U.S.A. 117, 243–250 (2020).
2. G. Eady et al., Nat. Commun. 14, 62 (2023).
3. C. Shao et al., Nat. Commun. 9, 4787 (2018).
4. N. Grinberg, K. Joseph, L. Friedland, B. Swire-Thompson, D. Lazer, Science 363, 374–378 (2019).
5. A. Guess, B. Nyhan, J. Reifler, "Selective Exposure to Misinformation: Evidence from the Consumption of Fake News during the 2016 U.S. Presidential Campaign" (European Research Council, Working Paper, 2018); https://about.fb.com/wp-content/uploads/2018/01/fake-news-2016.pdf.
6. A. Guess, J. Nagler, J. Tucker, Sci. Adv. 5, eaau4586 (2019).
7. J. Habermas, The Theory of Communicative Action, Volume 2: Lifeworld and System: A Critique of Functionalist Reason (Beacon Press, 1984).
8. M. E. Roberts, Censored: Distraction and Diversion Inside China's Great Firewall (Princeton Univ. Press, 2018).
9. C. Lampe, N. Ellison, C. Steinfield, in Proceedings of the 2006 20th Anniversary Conference on Computer Supported Cooperative Work (Association for Computing Machinery, 2006), pp. 167–170.
10. L. K. Fazio, D. G. Rand, G. Pennycook, Psychon. Bull. Rev. 26, 1705–1710 (2019).
11. R. Dahlke, J. Hancock, "The effect of online misinformation exposure on false election beliefs," OSF Preprints (2022); https://doi.org/10.31219/osf.io/325tn.
12. D. A. Effron, M. Raj, Psychol. Sci. 31, 75–87 (2020).
13. A. Marwick, R. Lewis, "Media Manipulation and Disinformation Online" (Data & Society Research Institute, 2017); https://datasociety.net/library/media-manipulation-and-disinfo-online/.
14. A. Badawy, A. Addawood, K. Lerman, E. Ferrara, Soc. Netw. Anal. Min. 9, 31 (2019).
15. G. King, J. Pan, M. E. Roberts, Am. Polit. Sci. Rev. 111, 484–501 (2017).
16. F. B. Keller, D. Schoch, S. Stier, J. Yang, Polit. Commun. 37, 256–280 (2020).
17. D. M. J. Lazer et al., Science 359, 1094–1096 (2018).
18. S. Pei, L. Muchnik, J. S. Andrade Jr., Z. Zheng, H. A. Makse, Sci. Rep. 4, 5547 (2014).
19. S. González-Bailón et al., Science 381, 392–398 (2023).
20. K.-C. Yang, O. Varol, P.-M. Hui, F. Menczer, in Proceedings of the AAAI Conference on Artificial Intelligence (AAAI Press, 2020), pp. 1096–1103.
21. C. M. Zhang, V. Paxson, in International Conference on Passive and Active Network Measurement, N. Spring, G. F. Riley, Eds. (Springer, 2011), pp. 102–111.
22. T. N. Ridout, E. F. Fowler, M. M. Franz, Forum 18, 465–492 (2021).
23. A. Goerres, Br. J. Polit. Int. Relat. 9, 90–121 (2007).
24. R. Igielnik, "Men and women in the U.S. continue to differ in voter turnout rate, party identification" (Pew Research Center, 2020); https://web.archive.org/web/20240408224740/https://www.pewresearch.org/short-reads/2020/08/18/men-and-women-in-the-u-s-continue-to-differ-in-voter-turnout-rate-party-identification/.
25. M. Deckman, in Tea Party Women: Mama Grizzlies, Grassroots Leaders, and the Changing Face of the American Right (New York Univ. Press, 2016), pp. 30–97.
26. B. G. S. Casara, C. Suitner, J. Jetten, J. Exp. Soc. Psychol. 98, 104245 (2022).
27. M. A. Craig, J. A. Richeson, Psychol. Sci. 25, 1189–1197 (2014).
28. M. Dobbs, J. DeGutis, J. Morales, K. Joseph, B. Swire-Thompson, Community Psychol. 1, 46 (2023).
29. R. K. Garrett, R. M. Bond, Sci. Adv. 7, eabf1234 (2021).
30. S. Y. Syn, S. Oh, J. Inf. Sci. 41, 553–569 (2015).
31. L. Cava, L. M. Aiello, A. Tagarelli, Sci. Rep. 13, 21626 (2023).
32. S. Baribi-Bartov, B. Swire-Thompson, N. Grinberg, Supersharers of Fake News on Twitter, dataset, Dryad (2024); https://doi.org/10.5061/dryad.44j0zpcmq.

SUPPLEMENTARY MATERIALS

science.org/doi/10.1126/science.adl4435
Materials and Methods
Supplementary Text
Figs. S1 to S5
Tables S1 to S15
References (33–44)
MDAR Reproducibility Checklist

OCEAN CIRCULATION

Heinrich event ice discharge and the fate of the Atlantic Meridional Overturning Circulation

Yuxin Zhou[1,2]*† and Jerry F. McManus[1,2]

During Heinrich events, great armadas of icebergs episodically flooded the North Atlantic Ocean and weakened overturning circulation. The ice discharges of these episodes constrain the sensitivity of overturning circulation to iceberg melting. We reconstructed these ice discharges to be as high as 0.13 sverdrup (Sv) (1 Sv = 1 million cubic meters per second) during Heinrich event 4 and to average 0.029 Sv over all episodes. The present-day Greenland Ice Sheet calving of icebergs is comparable to that of a mid-range Heinrich event. As the future Greenland Ice Sheet recedes from marine-terminating outlets, its iceberg calving likely will not persist long enough for icebergs alone to cause catastrophic disruption to the Atlantic overturning circulation, although the accelerating Greenland runoff and continued global warming remain threats to the circulation stability.

The large-scale ocean circulation pattern known as the Atlantic Meridional Overturning Circulation (AMOC) helps regulate a vast reservoir of heat and carbon and plays a key role in driving Earth's climate (1). During the last glacial period, when great armadas of icebergs flooded the North Atlantic (2), the AMOC underwent abrupt changes (3, 4) whose impact was felt both regionally and hemispherically (5). Termed Heinrich events (HEs) (6), the episodes—at least six of them during the last glacial period—saw some icebergs travel >3000 km from North America to Europe and deposit sediment (initially held within the ice) centimeters to decimeters in thickness over much of the subpolar North Atlantic, or even meters thick at some proximal locations (7).

The relationship between the AMOC changes and iceberg melting is complex. Because ice sheets are a source of fresh water, the release of the icebergs to the North Atlantic has been proposed as a mechanism capable of reducing the density of surface waters and thus disrupting the formation of North Atlantic Deep Water (NADW) by inhibiting open-ocean convection (8). However, it has been suggested that the HE-associated circulation slowdowns might be caused not by iceberg melting but by the internal variability of the AMOC (9–16), although most studies acknowledge the role of melting icebergs in contributing to and accelerating the observed disruptions of the AMOC (9–13, 16).

Given that the strength of the AMOC appears sensitive to changes in meltwater input, it is remarkable that existing estimates of the freshwater fluxes associated with HEs still differ over a range of two orders of magnitude (Fig. 1). This spread of uncertainty hinders our ability to constrain with confidence the amount of freshwater sufficient to lead to a widespread

disruption to the AMOC as seen during HEs (3, 4, 17). Although the modern AMOC may be in a different state than its glacial counterpart, such information may be relevant to understanding future climate change. For example, some studies show that the recent acceleration in the melting of the Greenland Ice Sheet (GrIS) is exceptional over at least the past 350 years (18) and may already be having an impact on the AMOC (19–21).

Freshwater flux can be calculated by (21):

$$FWF = R + D$$

where *FWF* is the freshwater flux, *R* is runoff, and *D* is ice discharge. Icebergs are more effective than runoff at transporting positive buoyancy (fresh water) to regions of deep-water formation in the North Atlantic (22, 23). Unlike runoff, icebergs, through latent heat exchange, additionally enhance sea-ice formation, which prevents the sea surface from losing heat to the atmosphere and thus further suppresses deep convection (24–27). Even though the share of ice discharge in the total GrIS mass loss is projected to decrease over time (1, 28, 29), given the association of icebergs with furthering AMOC slowdowns during HEs, their impact on future AMOC stability cannot be simply ignored. Therefore, a better understanding of the HE ice discharge may aid in predicting how the strength of the AMOC might respond to the present and future changes of the GrIS.

To quantify the HE ice discharges, we implemented an observation-based method using quantified sedimentary mass fluxes. Reconstructions of sedimentary mass flux based on the powerful geochemical tool of excess thorium-230 ($^{230}Th_{xs}$) normalization are widely available in the North Atlantic (30). We compiled new and published $^{230}Th_{xs}$-derived mass-flux data from the last glacial cycle in the North Atlantic. The total mass flux at any given location is influenced by many factors, including the deposition of ice-rafted debris (IRD), biogenic and hemipelagic sediment, eolian dust, and volcanic input, as well as bottom-current reworking.

During HEs, the influence of IRD flux dominates sediment deposition across the subpolar North Atlantic Ocean—HE mass flux is at least one order of magnitude higher than non-HE mass flux in the belt of IRD deposition (31, 32). The contrast indicates that the increase in IRD flux overwhelms other mass-flux components during these intervals, so that the increase in overall sediment flux is predominantly due to IRD deposition (31). By subtracting the glacial non-HE mass flux from the peak HE mass flux, we can thus estimate the additional increase in IRD flux associated with the peak flux [Fig. 2A; details provided in supplementary materials (SM), materials and methods].

The peak IRD flux can then be converted to peak ice discharge; this requires that we make reasonable and educated assumptions about the concentration and distribution of IRD in icebergs and the iceberg sizes (Fig. 2B). Based on iceberg observations from the Arctic and the Atlantic (SM, materials and methods), our idealized iceberg model assumes that the height of the icebergs is 260 m, the average height of the basal debris–rich zone is 2 m, and the average IRD concentration in the zone is 50% by weight. During HEs, IRD is likely distributed throughout the entire iceberg (33), equivalent to a 0.59% IRD concentration by weight relative to the iceberg in our model. Because the IRD content in any sediment core does not distinguish individual icebergs, the iceberg dimension and the distribution of the entrained IRD may vary without impacting our results as long as the population mean of IRD concentration stays the same. We ran a Monte Carlo simulation to quantify the uncertainty of our ice-discharge results, factoring in the uncertainties in the instrumental measurements, the thorium normalization parameters, the chronologies, and the relative proportion of IRD weight to iceberg weight. We also calculated the total volume of freshwater discharged during HEs with a slightly different methodology: Instead of calculating the surge peak mass flux, we integrated the mass flux in two-thousand-year (kyr) windows that capture each HE, and deducted the glacial non-HE mass flux, using the same informed assumptions about the relationship of debris and freshwater in melting icebergs.

Although our mass-flux dataset spans the past 140 kyr continuously (fig. S1), for the sake of focusing on the episodic ice discharge, in this study we describe the results for the Younger Dryas (YD), HE 1 (H1) to H6, and HQ, which is a HE recently observed in sediments between 65 and 70 thousand years ago (ka) (32) (Fig. 3). HQ was first predicted in an ice-sheet modeling study (12), and the "Q" stands for "question mark" because of the lack of physical evidence of its existence at the time. The magnitude of the ice discharge in the latitude band 20°N to 70°N is largest during H4, reaching 0.130 Sv, whereas the smallest ice discharge,

[1]Lamont-Doherty Earth Observatory of Columbia University, Palisades, NY 10964, USA. [2]Department of Earth and Environmental Sciences, Columbia University, New York, NY 10027, USA.
*Corresponding author. Email: yuxin_zhou@ucsb.edu
†Present address: Department of Earth Science, University of California, Santa Barbara, CA 93106, USA.
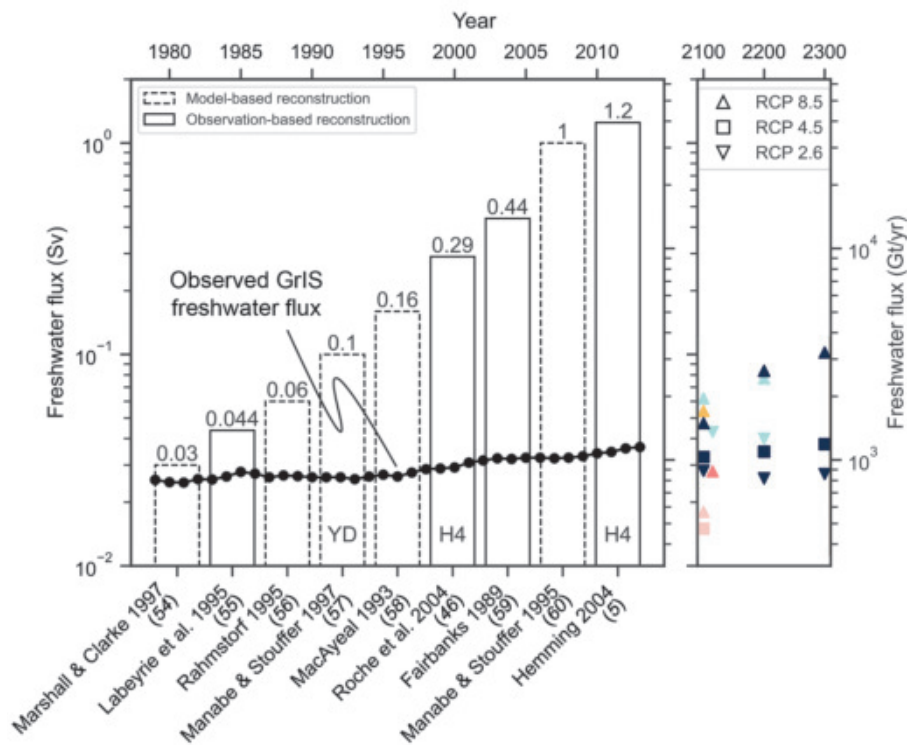
Fig. 1. Estimates of freshwater flux during HEs from the literature. Dashed-line bars are model-based fluxes. Solid-line bars are observation-based fluxes. The annotations at the bases of bars mark event-specific estimates. The absence of such annotation means that the estimate is for a generic freshwater-discharge event. The numbers above bars are the freshwater-flux values in Sv. Note the log scale of the y axis. Also shown are the historical GrIS freshwater flux (21) and the projected GrIS freshwater flux in 2100, 2200, and 2300. The markers with the same color come from the same study: dark blue, (50); light blue, (52); orange, (29); red, (53); and pink, (28). Studies on the HE freshwater flux are cited below the x axis (5, 46, 54–60). Triangles pointing up, squares, and triangles pointing down denote RCP 8.5, 4.5, and 2.6 projections, respectively. GrIS, Greenland Ice Sheet; H, Heinrich event; YD, Younger Dryas. 1 Sv = 10^6 m^3 s^{-1}.
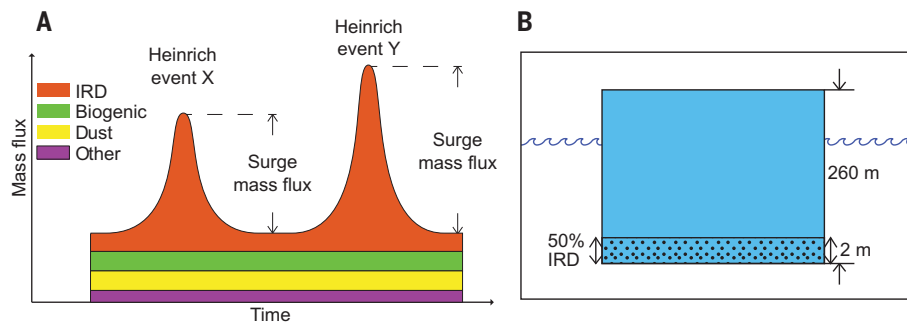
Fig. 2. Cartoons illustrating the simple model used in this study to calculate ice discharge. (**A**) An idealized mass-flux record to illustrate surge mass flux. The flux of IRD is isolated by taking the difference between HE and non-HE mass flux. We designate this difference the surge mass flux. This calculation assumes that the changes in the other sedimentary components are small compared with the changes in the IRD flux. (**B**) An idealized iceberg schematic. To calculate the ice discharge from surge mass flux, we assume that the average height of the icebergs is 260 m, the average height of the basal debris–rich zone is 2 m, and the average IRD concentration in the zone is 50% by weight (schematic dimension not to proportion). The resulting IRD concentration is 0.59% (relative to the entire iceberg). The horizontal dimension of the iceberg is irrelevant because we aim to estimate the ice discharge per area.

during H3, is two orders of magnitude smaller, at 0.003 Sv. The prominence of H4 ice discharge relative to other HEs was pointed out previously (5, 31). We note that YD is not typically considered an event of iceberg discharge, but we nevertheless include this event for completeness. Furthermore, H3, H6, and HQ are "atypical" HEs because of their relatively low IRD concentrations and different sedimentary compositions (6, 32). Our results show that the atypical HEs and the YD have the lowest ice discharges, which is consistent with prior research (31, 32, 34). The standard deviation of the ice-discharge reconstructions from the Monte Carlo simulation, relative to the mean, is the lowest in H2, followed by H1, H5, H4, H3, YD, H6, and HQ. The uncertainty does not seem to correlate with any single variable, instead likely reflecting the interplay between the instrumental uncertainty, which varies study by study, and the age uncertainty, which increases in older sediments.

Ice-discharge comparison

We next compared our HE ice-discharge results with various observational and theoretical methods in the literature. The spatial distribution of the HE ice discharges that we reconstructed broadly fits the pattern first identified in the reconstruction of detrital sand fluxes across the so-called IRD belt (35) and subsequently confirmed by compilations of IRD layer thickness (36, 37) and iceberg modeling (23, 38, 39). In terms of the magnitude of the ice discharge, our reconstructions also compare favorably with previous results (Fig. 4). A previous study estimated the ice discharge of H1 or H2 to be 0.016 Sv (40), which is lower than the average of the two events in our results (0.022 Sv) but within the same order of magnitude. Another study reconstructed the ice discharges of H1, H2, H4, and H5 to be 0.04 Sv on average, with an uncertainty envelope of 0.02 to 0.08 Sv (39). Our average for the same events is 0.05 Sv. Those two previous studies used vastly different methods than ours to arrive at their results; one based on estimates of an ice stream's discharge rate and the other based on a combination of an IRD-loaded iceberg drift model and the IRD-thickness data.

In addition to the peak flux of ice discharge, the total volume of the discharge is also important to consider. In a best-case scenario, the reconstruction of ice discharges during HEs should ideally yield the variation of the flux throughout the entire duration of HEs, but such highly resolved information is extremely difficult to obtain. In the absence of estimates of the flux variations over time, the total volume of discharge can be considered alongside the flux estimates for an additional perspective on our reconstructions. Using the 2-kyr HE durations as we defined in table S1 to calculate the total volumes of ice discharge, we compared our HE ice-discharge volume results with the published literature (fig. S2). Our volume estimate
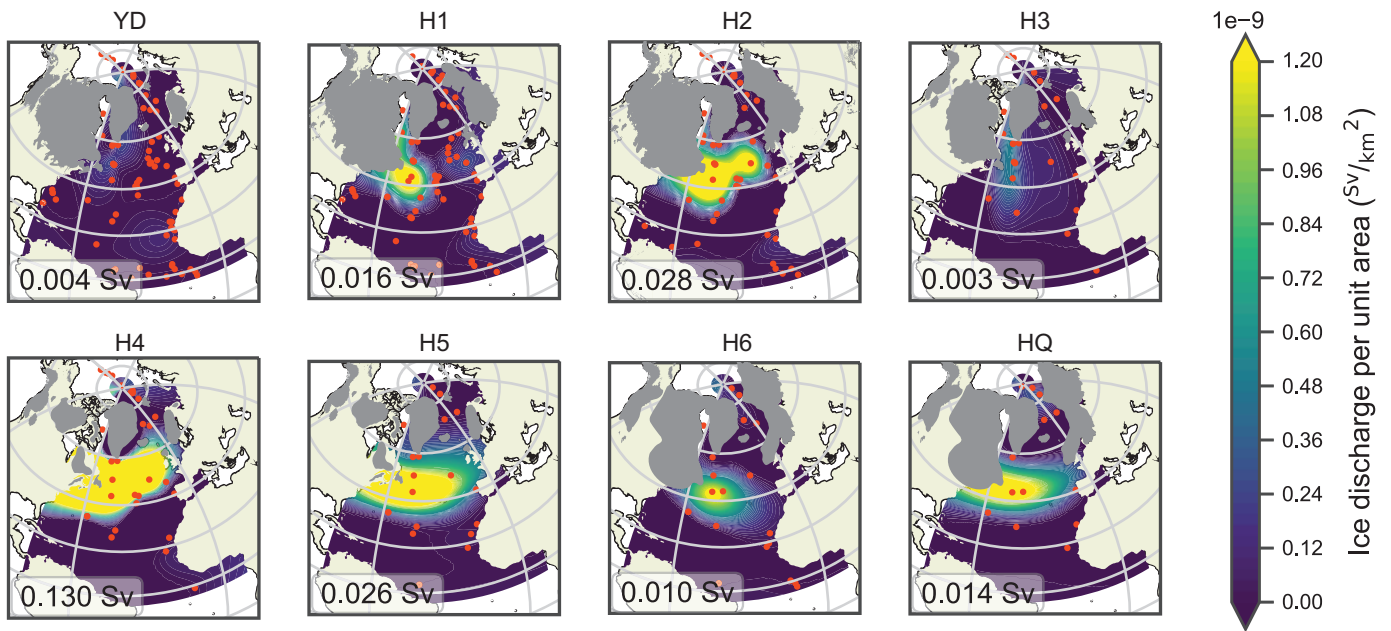
Fig. 3. The ice-discharge estimates from this study. The dots indicate core locations available during each period. The colored contour is the interpolation of the average ice discharge during each period. Gray areas indicate the ice-sheet extent during each period (*61–64*). The number in the lower-left corner is the peak ice discharge between 20°N to 70°N during each event.

for the average of H1 and H2 is 4.4×10^{14} m^3, compared with a previous estimate (*40*) of 3.8×10^{14} m^3. The average of H1, H2, H4, and H5 is 1.5×10^{15} m^3 according to our reconstruction, whereas in a previous study (*39*), the estimate for the same events is 6.4×10^{14} m^3. Using 1 kyr and 4 kyr as the HE durations does not meaningfully change our results (Extended Data Fig. 2). We point out that the volume and flux estimates are produced with slightly different methodologies, and our volume estimates are not simply the product of the flux estimates and length of time of HEs.

Discussion

As noted above, a much-desired goal of studying HE ice discharge rests on the potential to provide insights into the likely response of the AMOC to present and future GrIS melting. However, before we delve into the implications of our study for AMOC predictability, there are three issues worth consideration.

First, the variability of IRD concentration in icebergs during HEs may be large. Although we attempt to constrain the uncertainty of IRD concentration using the Monte Carlo simulation, our calculation is based on the observations of modern icebergs. It is an inherently difficult task to estimate the composition of extinct icebergs calved from an extinct ice sheet. We cannot rule out that the icebergs extant during HEs were dramatically cleaner or dirtier than they are today, although we are not aware of any evidence suggesting so. To provide an idea of the sensitivity of our results to the configuration of our idealized iceberg
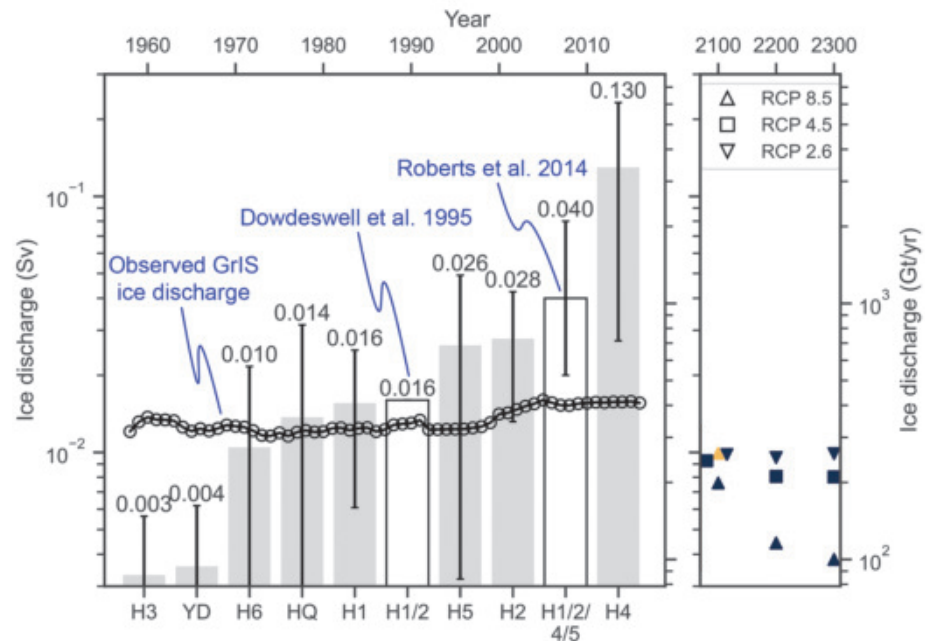
Fig. 4. Estimates of ice discharges in 20°N to 70°N during Younger Dryas and every HE of the last glacial period, ranked by the magnitudes. Error bars show the standard deviation of the Monte Carlo simulation. The numbers above bars are the ice-discharge values in Sv. Also shown are two previous HE ice-discharge reconstructions (*39, 40*), the historical GrIS ice discharge (*65*), and the projected GrIS ice discharge in 2100, 2200, and 2300. The dark blue markers are from (*50*), and the orange marker is from (*29*). Triangles pointing up, squares, and triangles pointing down denote RCP 8.5, 4.5, and 2.6 projections.

model, if the average icebergs were half or twice as thick, the ice-discharge results would be about half or twice the original values. If the average IRD concentration in the debris-rich layers was 25 or 100% by weight (100% is physically impossible because an ice matrix is needed to hold the IRDs in place), the ice-discharge results would be 250 or 23% of the original values.

Lastly, if half of the icebergs are sediment-free, the ice-discharge results would be twice the original values.

Second, our reconstructed HE iceberg discharges may not be useful for predicting how a stable AMOC regime would respond to perturbations. This is because the HE iceberg discharges seem only responsible for precipitating a moderately weakened AMOC to its eventual slowdown (9–13, 16). The forcing required to cause an initial perturbation to the AMOC is beyond the scope of this study.

Third, the sensitivity of the present-day AMOC to meltwater perturbations may be different from that of its glacial state when HEs occurred; i.e., past AMOC sensitivity may be of limited utility to predict the modern and future sensitivity if the AMOC is at a fundamentally different starting point. This is a current topic of debate, and there are some arguments for a higher AMOC sensitivity in its glacial state (41, 42) and others against (43, 44).

Implications

Our reconstructed HE ice discharges offer at least two potentially important insights into the AMOC sensitivity.

First, regarding the present and short-term future of the AMOC, the observed GrIS ice discharge is already comparable to a mid-range HE, not including the weakest (the YD and H3) and the strongest (H4) events. This point is concerning for the state of the AMOC because circulation was severely disrupted during mid-range HEs (3, 4). However, the modern AMOC has been relatively stable (45), a departure from the initial conditions when HE iceberg melting started (9–16). The AMOC may not have weakened enough for the GrIS ice discharge—even at a mid-range HE level—to have a substantial impact. Additionally, HEs are estimated to be about 250 years in duration (5, 6, 31, 46). The current level of GrIS ice discharge may simply not have continued long enough to cause dramatic circulation changes.

A second important insight from our study relates to the longer term, when the projected AMOC decline by 2100 will reach 24 to 39% depending on the Shared Socioeconomic Pathways (SSPs) (1, 47). The projected weakening of the AMOC by 2100 seems to set up an initial condition similar to those observed just before HEs, when iceberg discharges were underway. The current level of GrIS ice discharge, if allowed to go on for hundreds of years, could cause dramatic circulation slowdowns. However, the projected GrIS ice discharge by 2100 and beyond will slow down to be within the range of the weakest HE event (H3) and the YD. This is because GrIS is primarily a land-based ice sheet (48). The GrIS will likely see a decrease in ice discharge by the end of the century as it recedes from marine-terminating outlets (29). As a result, the current level of GrIS ice dis-charge likely will not go on for long enough for it alone to cause a mid-range, HE-level AMOC slowdown. By contrast, the ice sheet likely responsible for the majority of HE ice discharge, the Laurentide Ice Sheet (LIS), had wide ice streams grounded deep beneath sea level (12), similar to the modern West Antarctic Ice Sheet (WAIS) (49), enabling ice discharge to continue long enough to induce widespread circulation slowdowns. In the more drastic emission-reduction scenarios [representative concentration pathway (RCP) 2.6 and 4.5], GrIS ice discharge will persist at a relatively higher level than in the worst-case emission scenario (RCP 8.5) (50).

Although surface melting–induced runoff is less effective at disrupting the AMOC than ice discharge, it cannot be entirely ignored. Runoff is projected to increase and overtake ice discharge as the leading cause of GrIS mass loss by 2100 (1, 28, 29). Therefore, the future trajectory of the AMOC strength will likely be determined by a "tug of war" in influence between the decelerating but more effective ice discharge and the accelerating but less influential runoff. Compounded with continued warming and the resultant increase in surface water buoyancy (51, 52), the fate of the AMOC remains precariously unclear.

REFERENCES AND NOTES

1. B. Fox-Kemper, H. T. Hewitt, C. Xiao, "Ocean, Cryosphere and Sea Level Change" in *Climate Change 2021: The Physical Science Basis. Working Group I Contribution to the Sixth Assessment Report of the Intergovernmental Panel on Climate Change*, V. Masson-Delmotte *et al.*, Eds. (Cambridge Univ. Press, 2021), pp. 1211–1362.
2. H. Heinrich, *Quat. Res.* **29**, 142–152 (1988).
3. J. F. McManus, R. Francois, J. M. Gherardi, L. D. Keigwin, S. Brown-Leger, *Nature* **428**, 834–837 (2004).
4. J. Lynch-Stieglitz, *Annu. Rev. Mar. Sci.* **9**, 83–104 (2017).
5. S. R. Hemming, *Rev. Geophys.* **42**, RG1005 (2004).
6. W. Broecker, G. Bond, M. Klas, E. Clark, J. McManus, *Clim. Dyn.* **6**, 265–273 (1992).
7. R. Hesse, *Can. J. Earth Sci.* **53**, 71–100 (2016).
8. W. S. Broecker, *Nature* **372**, 421–424 (1994).
9. J. Álvarez-Solas, A. Robinson, M. Montoya, C. Ritz, *Proc. Natl. Acad. Sci. U.S.A.* **110**, 16350–16354 (2013).
10. J. Álvarez-Solas *et al.*, *Nat. Geosci.* **3**, 122–126 (2010).
11. S. Barker *et al.*, *Nature* **520**, 333–336 (2015).
12. J. N. Bassis, S. V. Petersen, L. Mac Cathles, *Nature* **542**, 332–334 (2017).
13. I. R. Hall *et al.*, *Geophys. Res. Lett.* **33**, L16616 (2006).
14. S. A. Marcott *et al.*, *Proc. Natl. Acad. Sci. U.S.A.* **108**, 13415–13419 (2011).
15. K. C. Martin *et al.*, *Nature* **617**, 100–104 (2023).
16. J. Álvarez-Solas *et al.*, *Clim. Past* **7**, 1297–1306 (2011).
17. S. Rahmstorf, *Nature* **419**, 207–214 (2002).
18. L. D. Trusel *et al.*, *Nature* **564**, 104–108 (2018).
19. C. W. Böning, E. Behrens, A. Biastoch, K. Getzlaff, J. L. Bamber, *Nat. Geosci.* **9**, 523–527 (2016).
20. L. Caesar, S. Rahmstorf, A. Robinson, G. Feulner, V. Saba, *Nature* **556**, 191–196 (2018).
21. Q. Yang *et al.*, *Nat. Commun.* **7**, 13545 (2016).
22. A. Condron, P. Winsor, *Geophys. Res. Lett.* **38**, L03705 (2011).
23. M. Fendrock, A. Condron, D. McGee, *Paleoceanogr. Paleoclimatol.* **37**, e2021PA004347 (2022).
24. J. I. Jongma, H. Renssen, D. M. Roche, *Clim. Dyn.* **40**, 1373–1385 (2013).
25. T. J. W. Wagner *et al.*, *Earth Planet. Sci. Lett.* **495**, 157–163 (2018).
26. M. Bügelmayer, D. M. Roche, H. Renssen, *Cryosphere* **9**, 821–835 (2015).
27. A. P. Wiersma, J. I. Jongma, *Clim. Dyn.* **35**, 535–549 (2010).
28. N. R. Golledge *et al.*, *Nature* **566**, 65–72 (2019).
29. L. Muntjewerf *et al.*, *Geophys. Res. Lett.* **47**, e2019GL086836 (2020).
30. K. M. Costa *et al.*, *Paleoceanogr. Paleoclimatol.* **35**, e2019PA003820 (2020).
31. J. F. McManus, R. F. Anderson, W. S. Broecker, M. Q. Fleisher, S. M. Higgins, *Earth Planet. Sci. Lett.* **155**, 29–43 (1998).
32. Y. Zhou *et al.*, *Earth Planet. Sci. Lett.* **564**, 116910 (2021).
33. M. Fendrock, A. Condron, D. McGee, *Paleoceanogr. Paleoclimatol.* **38**, e2022PA004583 (2023).
34. G. C. Bond, R. Lotti, *Science* **267**, 1005–1010 (1995).
35. W. F. Ruddiman, *Science* **196**, 1208–1211 (1977).
36. H. Rashid, R. Hesse, D. J. W. Piper, *Earth Planet. Sci. Lett.* **205**, 281–293 (2003).
37. F. E. Grousset *et al.*, *Paleoceanography* **8**, 175–192 (1993).
38. R. C. Levine, G. R. Bigg, *Paleoceanography* **23**, PA4213 (2008).
39. W. H. G. Roberts, P. J. Valdes, A. J. Payne, *Earth Planet. Sci. Lett.* **386**, 1–9 (2014).
40. J. A. Dowdeswell, M. A. Maslin, J. T. Andrews, I. N. McCave, *Geology* **23**, 301–304 (1995).
41. E. V. Galaasen *et al.*, *Science* **343**, 1129–1132 (2014).
42. J. Lynch-Stieglitz *et al.*, *Nat. Geosci.* **7**, 144–150 (2014).
43. Z. Mokeddem, J. F. McManus, D. W. Oppo, *Proc. Natl. Acad. Sci. U.S.A.* **111**, 11263–11268 (2014).
44. S. L. Weber, S. S. Drijfhout, *Geophys. Res. Lett.* **34**, L22706 (2007).
45. B. I. Moat *et al.*, *Ocean Sci.* **16**, 863–874 (2020).
46. D. Roche, D. Paillard, E. Cortijo, *Nature* **432**, 379–382 (2004).
47. W. Weijer, W. Cheng, O. A. Garuba, A. Hu, B. T. Nadiga, *Geophys. Res. Lett.* **47**, e2019GL086075 (2020).
48. M. Morlighem *et al.*, *Geophys. Res. Lett.* **44**, 11051–11061 (2017).
49. P. Fretwell *et al.*, *Cryosphere* **7**, 375–393 (2013).
50. M. Vizcaino *et al.*, *Geophys. Res. Lett.* **42**, 3927–3935 (2015).
51. P. Bakker *et al.*, *Geophys. Res. Lett.* **43**, 12252 (2016).
52. J. T. M. Lenaerts *et al.*, *Geophys. Res. Lett.* **42**, 6373–6381 (2015).
53. H. Goelzer *et al.*, *Cryosphere* **14**, 3071–3096 (2020).
54. S. J. Marshall, G. K. C. Clarke, *J. Geophys. Res.* **102** (B9), 20615–20615 (1997).
55. L. Labeyrie *et al.*, *Philos. Trans. R. Soc. Lond. B Biol. Sci.* **348**, 255–264 (1995).
56. S. Rahmstorf, *Nature* **378**, 145–149 (1995).
57. R. Manabe, R. J. Stouffer, *Paleoceanography* **12**, 321–336 (1997).
58. D. R. MacAyeal, *Paleoceanography* **8**, 775–784 (1993).
59. R. G. Fairbanks, *Nature* **342**, 637–642 (1989).
60. S. Manabe, R. Stouffer, *Nature* **378**, 165–167 (1995).
61. C. L. Batchelor *et al.*, *Nat. Commun.* **10**, 3713 (2019).
62. A. S. Dyke, A. Moore, L. Robertson, *Deglaciation of North America* (Geological Survey of Canada Ottawa, 2003).
63. J. Ehlers, P. L. Gibbard, P. D. Hughes, Eds. *Quaternary Glaciations - Extent and Chronology: A Closer Look* (Elsevier, 2011).
64. A. L. C. Hughes, R. Gyllencreutz, Ø. S. Lohne, J. Mangerud, J. I. Svendsen, *Boreas* **45**, 1–45 (2016).
65. J. L. Bamber *et al.*, *J. Geophys. Res. Oceans* **123**, 1827–1837 (2018).
66. Y. Zhou, J. F. McManus, Supplementary data for "Heinrich event ice discharge and the future fate of the Atlantic Meridional Overturning Circulation," Figshare (2024); https://doi.org/10.6084/m9.figshare.22223806.v3.
67. Y. Zhou, Supplementary data for "Heinrich event ice discharge and the future fate of the Atlantic Meridional Overturning Circulation," Figshare (2024); https://doi.org/10.6084/m9.figshare.25633881.v1.

BIOMATERIALS

A three-dimensionally architected electronic skin mimicking human mechanosensation

Zhi Liu[1,2]†, Xiaonan Hu[1,2]†, Renheng Bo[1,2]†, Youzhou Yang[1,2], Xu Cheng[1,2,3,4], Wenbo Pang[1,2], Qing Liu[1,2], Yuejiao Wang[1,2], Shuheng Wang[1,2], Shiwei Xu[1,2], Zhangming Shen[1,2], Yihui Zhang[1,2]*

Human skin sensing of mechanical stimuli originates from transduction of mechanoreceptors that converts external forces into electrical signals. Although imitating the spatial distribution of those mechanoreceptors can enable developments of electronic skins capable of decoupled sensing of normal/shear forces and strains, it remains elusive. We report a three-dimensionally (3D) architected electronic skin (denoted as 3DAE-Skin) with force and strain sensing components arranged in a 3D layout that mimics that of Merkel cells and Ruffini endings in human skin. This 3DAE-Skin shows excellent decoupled sensing performances of normal force, shear force, and strain and enables development of a tactile system for simultaneous modulus/curvature measurements of an object through touch. Demonstrations include rapid modulus measurements of fruits, bread, and cake with various shapes and degrees of freshness.

Humans can accomplish dexterous manipulation, environmental exploration, and perception of physical properties of touched objects, among other tactile tasks as a result of skin's decoupled sensing capabilities of multimodal mechanical stimuli and the brain's learning and processing capabilities of perceived signals. Biological studies showed that our skin's sense of mechanical stimuli originates from the transduction of mechanoreceptors in the skin (1–3), which converts the forces applied to the skin into electrical signals that propagate to the central nervous system (CNS) through the axons. Merkel cells and Ruffini endings are two types of slowly adapting mechanoreceptors, which reside at the bottom of the epidermis and within the dermis, respectively, with a densely distributed array in three-dimensional (3D) space (4–7). Because Merkel cells—supported by collagen fiber networks in the dermis—are very close to the skin surface, they are highly sensitive to the forces applied to the skin as the induced stress decays rapidly from the loading region (4, 5). In comparison to Merkel cells, Ruffini endings are distributed much farther from the skin surface and therefore are not as sensitive to external forces (e.g., pressure) even when the skin itself is stretched (6, 7). As a result of such 3D distribution of mechanoreceptors (Fig. 1A, left), Merkel cells and Ruffini endings can effectively perceive the external forces and the strain of the skin, respectively.

Imitating the above spatial distribution of mechanoreceptors in the skin can enable developments of artificial electronic skins capable of decoupled sensing of normal/shear forces and strains, but remains highly challenging, due to the difficulties in realizing a complexly architected 3D electronic device with well-controlled 3D distributions of sensing components. Although many inspiring and exciting developments of electronic skins have been reported, such as epidermal electronics (8, 9), neuromorphic skin electronic systems (10–13), skin-integrated electronic systems (14, 15), electronic skins with intrinsically stretchable electronic components (16–19), and electronic skins for multiparameter sensing (20–23) and haptic interfaces (24–27), none of them have imitated the 3D spatial distribution of mechanoreceptors. Additionally, decoupled measurements of normal force, shear force, and tensile strain, at a spatial resolution close to human skin, also remains elusive.

We report a bioinspired design of 3D architected electronic skin (denoted as 3DAE-Skin) adopting a skin-like multilayer construction, where force and strain sensing components are arranged in a 3D layout that mimics that of Merkel cells and Ruffini endings in the skin (Fig. 1A). Microfabrication techniques allow formation of a lithographically defined multilayered electronic device consisting of laminated force and strain sensing arrays, which was transformed into biomimetic 3D configuration through precisely controlled mechanical assembly (28–30). A heterogeneous encapsulation strategy of the 3D architected device ensures that the surrounding soft materials of force and strain sensing components have similar mechanical properties to those of Merkel cells and Ruffini endings in the skin. Experimental and theoretical studies of 3DAE-Skin show excellent decoupled sensing performances of normal force, shear force,

and strain. A tactile system based on the 3DAE-Skin, data acquisition circuits, and deep learning aided signal processing module is developed, which can simultaneously measure the elastic modulus and local principal curvature components of an object through a simple touch.

Bioinspired design and fabrication of the 3DAE-Skin

Figure 1A presents the bioinspired design concept of the 3DAE-Skin. Similar to the tri-layer construction of skin, the 3DAE-Skin consists of three layers: "epidermis," "dermis," and "hypodermis." The thickness and elastic modulus of those layers are close to those of the skin (table S1): ~145 µm and ~436 kPa (epidermis), ~600 µm and ~107 kPa (dermis), and ~4.5 mm and ~52 kPa (hypodermis). The sensing components and associated electrical circuits are embedded mainly in the dermis layer and the signals generated from sensing components are collected and processed through modules of data acquisition and deep learning aided signal processing, similar to the function of the CNS (fig. S1).

Figure 1, B and C, shows an expanded view of the geometric layout of the 3DAE-Skin and its representative functional unit. The 3DAE-Skin consists of three parts: functional, substrate, and encapsulation. The functional part encompasses an array (5 × 5) of 3D structured units, which are interconnected with the connection pad. Each of the 3D functional unit adopts a nine-layer construction (Fig. 1C and figs. S2 and S3), including two force sensing layers (5 nm Cr / 60 nm Au), two strain sensing layers (5 nm Cr / 60 nm Au), and five polyimide (PI) layers (1.2 µm for the top and bottom layers, and 0.8 µm for all the other layers) that encase each of the sensing layers. Microfabrication techniques (see Materials and Methods and figs. S4 and S5 for details) allow manufacturing of such multilayered electronic device in pre-defined planar layout. Transfer printing and mechanically guided assembly (figs. S6 and S7) enable transformation of the 2D electronic device into desired 3D configuration on top of the elastomeric substrate [a bilayer of Dragon Skin (10 Slow, Smooth-On, Easton, PA, US; mix ratio = 1:1; elastic modulus ~150 kPa; ~0.5 mm) and Eco-flex (00-20, Smooth-On, Easton, PA, US; mix ratio = 1:5; elastic modulus ~40 kPa; ~4 mm)]. In particular, a distributed 3D architecture is adopted to ensure different distances of force and strain sensing components (i.e., piezoresistive sensors) from the surface of 3DAE-Skin, where force sensing components are arranged on eight-armed cage mesostructures with a relatively large height (~600 µm) whereas strain sensing components are located on arch mesostructures with a smaller height (~250 µm). The eight-armed cage mesostructure

¹Applied Mechanics Laboratory, Department of Engineering Mechanics, Tsinghua University, Beijing 100084, P.R. China. ²Laboratory of Flexible Electronics Technology, Tsinghua University, Beijing 100084, P.R. China. ³Department of Materials Science and Engineering, National University of Singapore, Singapore 119276, Singapore. ⁴Institute for Health Innovation & Technology (iHealthtech), National University of Singapore, Singapore 119276, Singapore.
*Corresponding author. Email: yihuizhang@tsinghua.edu.cn
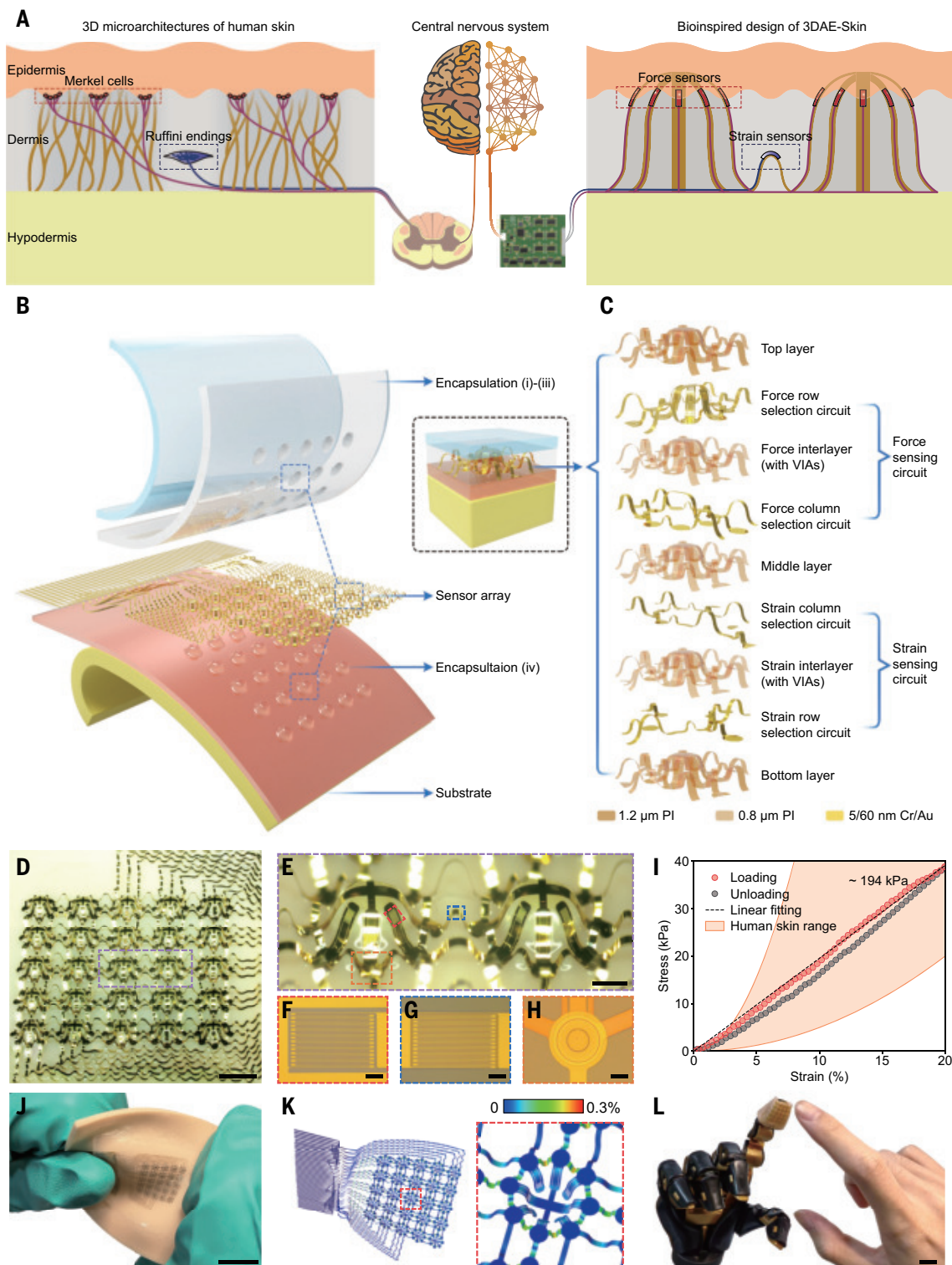†These authors contributed equally to this work.

Fig. 1. Bioinspired design and fabrication of the 3DAE-Skin. (**A**) Schematic illustration of the bioinspired design concept of the 3DAE-Skin, which involves a comparison between the architecture of the 3DAE-skin and its artificial tactile system, with that of the skin and tactile system of a human. (**B**) Expanded view of the multilayered construction of an entire 3DAE-Skin device that comprises a sensor array and multiple layers of encapsulation. (**C**) Expanded view of a representative functional unit in which four layers of gold circuits are sandwiched by five layers of PI to form force and strain sensors. (**D**) Image of the interconnected sensor array. Scale bar, 2 mm. (**E**) Enlarged view of the functional unit. Scale bar, 500 μm. (**F** to **H**) Enlarged view of the force sensor (F) and strain sensor (G), as well as bonding site with vertical interconnect access (H). Scale bars, 50 μm. (**I**) Mechanical responses of the 3DAE-Skin under tensile tests, in comparison to those of human skin marked by the orange region. (**J** and **K**) Optical image (J) and FEA results (K) on the deformed configuration of the device being twisted by ~60°, indicating an excellent deformability. The color in (K) represents the maximum principal strain in the gold circuit. (Inset) enlarged view of a functional unit. (**L**) Optical image of the 3DAE-Skin attached to the fingertip of a prosthetic model. Scale bar, 5 mm.

can facilitate the decoding of normal force and directional shear force, according to the outputs of piezoresistive sensors on the different arms. Although the resistive sensors employed in the current study have higher energy consumption and slower response time than piezoelectric or triboelectric sensors, they are better suited to mimic the slow adapting receptors in human skin, as they have the capability to produce continuous signals in response to sustained stimuli (*31*).

Encapsulation of the functional part with different layers and materials (Fig. 1B, i to iv) yields skin-like mechanical properties. In particular, a heterogeneous encapsulation strategy (Fig. 1B and figs. S8 and S9) leverages capillary forces to allow filling of inner regions of all cage mesostructures with polydimethylsiloxane (PDMS) [Sylgard 184, Dow Corning, Midland, MI, US; mix ratio = 1:15; elastic modulus ~1.5 MPa; encapsulation (iv)], and other regions of the dermis layer with relatively soft material [Ecoflex 00-20, mix ratio = 1:5; elastic modulus ~40 kPa; ~600 µm; encapsulation (iii)]. Introduction of two additional elastomer layers, i.e., Ecoflex 00-20 [mix ratio = 1:1; elastic modulus ~110 kPa; ~120 µm; encapsulation (ii)] and PDMS [Guinie Advanced Materials, Hangzhou, ZJ, China; Elastic modulus ~2 MPa; ~25 µm thick; encapsulation (i)], forms a surface protection (corresponding to the epidermis layer of the 3DAE-Skin) and completes the heterogeneous encapsulation.

Figure 1, D to H, provides optical images of a fabricated 3DAE-Skin and magnified views of the functional unit, force/strain sensors, and vertical interconnect access holes. The device was encapsulated only at the inner regions of cage mesostructures to render improved visual quality. Optical images of the fully encapsulated device (with a total thickness of ~5.25 mm) appear in fig. S10. The cage mesostructure has a lateral dimension of ~1.8 mm, with an arm width of ~250 µm. The encapsulated 3DAE-Skin is very soft, with an effective elastic modulus of ~194 kPa, according to the uniaxial tensile testing (Fig. 1I). The mechanical responses of indentation tests at two typical locations of the 3DAE-Skin appear in fig. S11, from which effective compressive moduli of ~225 kPa and ~119 kPa can be derived. Both the responses of the 3DAE-Skin under uniaxial tension and indentation fall in the typical ranges of human skin responses (Fig. 1I and fig. S11). Because the heterogeneous encapsulation strategy exploits very soft materials to encase the sensors and interconnects, the 3DAE-Skin is also very flexible and stretchable and can be compliantly integrated with the fingertip of a prosthetic hand (Fig. 1, J to L, and movie S1). Finite element analyses (FEA) (see supplementary text for details) can capture complex deformations of 3D mesostructures and strain distributions of metal-

lic layers during various loading conditions (Fig. 1K and fig. S12). According to tensile testing (fig. S13), the maximum uniaxial strain that the 3DAE-Skin can withstand before the failure of its electrical performance is ~45%, corresponding to an effective stress of ~84 kPa.

Decoupled sensing mechanisms and performances of the 3DAE-Skin

The 3DAE-Skin relies on 3D microarchitecture to convert the external normal/shear force into the strain changes of piezoresistive sensors on the eight-armed cage mesostructure, and then into resistance changes that can be recorded quantitatively. Consider a functional unit that undergoes the loading of a normal force (F_N) and a shear force (F_S with an angle of θ with respect to the x axis), as shown in Fig. 2A. Owing the geometric feature of cage mesostructure, the analysis of its static equilibrium (fig. S14) can link normal force (F_N) and shear force components (F_{Sx} and F_{Sy}) explicitly to the relative resistance changes of eight sensors as

$$F_N = \sum_{i=1}^{8} \left[S_{(i)} \frac{\Delta R_{(i)}}{\Delta R_{0(i)}} \right] \tag{1}$$

$$F_{Sx} = C \sum_{i=1}^{8} \left[S_{(i)} \frac{\Delta R_{(i)}}{R_{0(i)}} \cos \frac{(i-1)\pi}{4} \right] \text{ and}$$

$$F_{Sy} = C \sum_{i=1}^{8} \left[S_{(i)} \frac{\Delta R_{(i)}}{R_{0(i)}} \sin \frac{(i-1)\pi}{4} \right], \tag{2}$$

where $\Delta R_{(i)}/R_{0(i)}$ is the relative resistance change of the ith sensor (i = 1…8), $S_{(i)}$ is the sensitivity that can be calibrated using the experiment by only applying a normal force, and C is a dimensionless shape factor that measures the difference of induced strain at the sensors under loadings of only normal and shear forces. Then the total shear force and its loading angle can be given by

$$F_S = \sqrt{F_{Sx}^2 + F_{Sy}^2} \text{ and } \theta = \tan^{-1}(F_{Sy}/F_{Sx}). \tag{3}$$

Optimization of the sensor location in the arm, based on mechanics analyses and FEA enables both a relatively high sensitivity and a large linear range of the force sensing (supplementary text and figs. S15 to S18). Along the thickness direction (total thickness ~4.8 µm), placing the sensor layer at the quarter section point (i.e., 1.2 µm from the top surface) could ensure a reasonably high sensitivity (fig. S19), while avoiding possible failure during microfabrication. The effect of the elastic modulus of the encapsulant inside the cage mesostructure on the sensitivity and linear range is also investigated, showing that a rigid encapsulant can enlarge the linear range but decrease the

sensitivity in the meantime, due to the increased mechanical constraint (fig. S19). As such, a moderately rigid material (PDMS, mix ratio = 1:15; elastic modulus ~1.5 MPa) is exploited. The influences of elastic modulus and thickness of other encapsulation/substrate layers are also studied (fig. S20), where the elastic modulus of the encapsulation (iii) plays more evident roles than the other parameters.

Figure 2B shows the sensing performance of the 3DAE-Skin when the sensor array is compressed by a flat indenter, where the pressure denotes the normal reaction force divided by the loading area. The sensitivity to the pressure loading is around 5×10^{-5} kPa^{-1}, with a linear range of ~80 kPa. Although the encapsulated 3DAE-Skin is quite soft (tensile modulus ~194 kPa), the response is still fast, with a response time of ~0.25 s during a rapid removal of the pressure load (60 kPa). The pressure sensing is stable and reliable during ~3000 cycles of pressure (60 kPa) loading/unloading (Fig. 2C). The wrinkles formed on top of the encapsulated device [due to the introduction of a very thin protective layer (25 µm); see movie S1] have negligible influences on the sensing performance (fig. S21). Although the 3DAE-Skin can endure low-speed compression repeatedly, the reliability under sudden, harsh mechanical impacts could be a concern.

Figure 2, D and E, illustrates the sensing performance of the 3DAE-Skin under shear loadings (applied to a central unit) along different directions. Six different loading angles (θ = 0°, 45°, 112.5°, 180°, 225° and 292.5°) were considered in the experiment, and five shear force magnitudes were applied for each loading angle. The predictions of shear force and loading angle based on Eqs. (2) and (3) agree well with the prescribed values for all the different loading conditions. The sensitivity to the shear force is around 6×10^{-4} N^{-1}. In comparison to the four-armed mesostructure design (*32–34*), the eight-armed mesostructure design provides shear deformation information along more in-plane angles, and therefore offers more accurate predictions of shear force and loading angle (fig. S22). For example, the mean absolute errors (0.008 N and 1.5°) of shear force magnitude and angle of eight-armed device are smaller than those (0.030 N and 5.4°) of the four-armed one. A comparison to representative shear sensing devices reported previously (table S2) suggests that our 3DAE-Skin shows one of the minimum levels of mean relative errors.

The sensing of the tensile strain exploits a similar piezoresistive effect and the piezoresistive sensors are arranged on perpendicularly oriented arch mesostructures to sense the strain components along these directions. Figure 2F and fig. S23 suggest a reliable sensing performance during 10,000 cycles of uniaxial stretching (strain amplitude ~20%) applied to
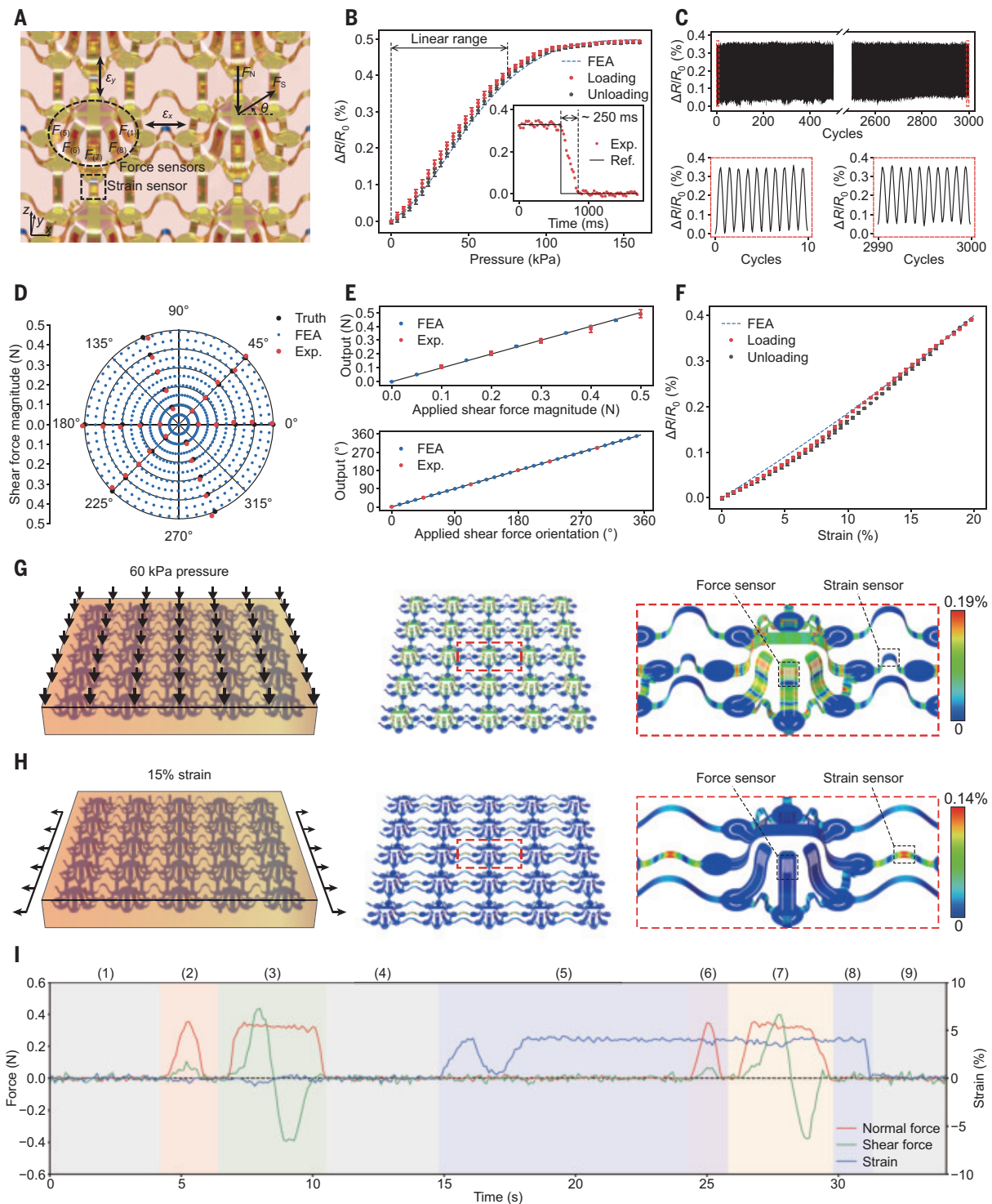
Fig. 2. Decoupled sensing mechanisms and performances of the 3DAE-Skin. (**A**) Schematic diagram of the functional unit under typical loadings of normal/shear forces and biaxial tension, where the force and strain sensors are marked. (**B** and **C**) Normal force sensing performance, including the quasistatic response (average relative resistance change of resistance of 8 force sensors) during a loading-unloading cycle (up to ~160 kPa, with a loading rate of 2 kPa/s) (B), the dynamic response under a fast unloading (B, inset), and the loop responses during 3000 cycles of loading and unloading (amplitude ~60 kPa, and frequency ~1 Hz) (C). (**D** and **E**) Shear force sensing performance, including the

representation of the force vector in the polar coordinate (D), the response of force magnitudes and orientations when shear forces with different levels and directions are applied, respectively (E). (**F**) Strain sensing performance during a loading-unloading cycle (up to ~20%, with a loading rate of 0.2%/s). (**G**) Distribution of the maximum principal strain in the metal layers of the 3DAE-Skin when the device is under a pressure of 60 kPa. (**H**) Similar results were achieved when the 3DAE-Skin is under a uniaxial stretch of 15%. (**I**) Decoupled responses of the 3DAE-Skin under different types of mechanical loadings. Error bars in (B) and (F) are SD values based on 5 individual measurements.

the 3DAE-Skin, with a sensitivity of ~0.02. All the piezoresistive sensors (240 in total) for force and strain sensing in the fabricated 3DAE-Skin work normally and show quite uniform sensitivity (figs. S24 and S25). Additionally, the temperature rise of these piezoresistive sensors in the 3DAE-Skin is typically very low (below 0.3 K) during operation (fig. S26), and therefore, the associated heating effect on the sensing performance is negligible.

The biomimetic 3D architecture allows decoupled sensing of normal/shear force and tensile strain. Under compressive loading, the maximum principal strain induced in the 3DAE-Skin shows a rapid decay from the loading point. Because the force sensing components are very close to the skin surface and the eight-armed cage mesostructures are much more rigid than the other regions, the maximum principal strains (~0.012%) induced in strain sensing components are much smaller than those (~0.17%) in force sensing components (Fig. 2G for 60 kPa pressure). In this case, the magnitude (~0.012%) of the maximum principal strain in strain sensing components is also much smaller than the value (~0.14%) in strain sensing components under 15% uniaxial stretching. A similar degree of strain difference can be observed under shear loading (fig. S27). Under uniaxial stretching, the maximum principal strains induced in force sensing components are much smaller than those in strain sensing components, owing to the strain isolation of relatively rigid cage mesostructures (Fig. 2H). For example, the peak strain magnitude of force sensing components is only around 0.009% under 15% uniaxial stretching, which is much smaller than the value (~0.17%) under 60 kPa pressure. This set of comparisons illustrates the underlying mechanism of the decoupled sensing capability. Figure 2I and movie S2 provide experimental results during a sequential process of pure pressure loading, coupled loading of pressure and shear force, pure uniaxial stretch, coupled loading of uniaxial stretch and pressure, and coupled loading of stretch, pressure, and shear force. The responses of normal/shear forces and strain quantitatively demonstrate the decoupled sensing capability of the 3DAE-Skin. Additionally, the characterization of strain and shear force sensing was performed under pressure values of 0, 20, and 40 kPa (fig. S27), where slight influences of applied pressure can be observed, providing further evidence of the decoupled sensing capability.

Spatiotemporal mapping of normal/shear forces and strain

The 3DAE-Skin is integrated with the data acquisition circuit and signal processing module to form a tactile system (Fig. 3A, figs. S28 to S30, and table S3). The data acquisition circuit allows individual addressing of each piezoresistive sensor in the array without crosstalk (Fig. 3B) (with ~50 kS/s sampling rate and 16-bit resolution). Based on the temporal relative resistance change of all 240 piezoresistive sensors in the 3DAE-Skin, the signal processing module allows visualization of the spatiotemporal distribution of normal/shear forces and strain according to Eqs. (1) to (3), and quantitative decoding of the tactile information (e.g., the location of the applied force, the elastic modulus, and local principal curvature components of an object) through a deep learning neural network (DNN) model. A spatiotemporal map (fig. S31) is introduced to visualize the distributions of sensed normal/shear forces and strain, in which 25 colored octagons are exploited to represent force responses, with the color (or size) of each octagon denoting the magnitude of normal force and the black arrow (or distortion of each octagon) denoting the magnitude and direction of shear force. The horizontal and vertical spacings between adjacent octagons represent the normal strain components along the two directions. The red-dotted octagon is the baseline in the force-free state and the strain magnitude is magnified by 10 times for a better visualization. Figure 3, C to G, and movie S3 provide experimental results of spatiotemporal variations in normal/shear forces and strain, when the 3DAE-Skin touches three 3D-printed relief structures (i.e., letters T, H and U) (0.5 mm in thickness and 8 mm in lateral dimension; 1.75 GPa; see fig. S32 for details). Figure 3D presents the time histories of pressure and shear force components at the 9 units in the central region, and strain responses at the adjacent 12 units. The responses of all force/strain units are provided in figs. S33 and S34, and the raw data of relative resistance change in the 10 piezoresistive sensors of a typical unit are in fig. S35. Figure 3, E to G, shows the spatiotemporal maps at three typical moments (t = 13.9 s, 25.9 s, and 34.4 s). When the 3DAE-Skin is pressed on the T-shaped relief structure through a non-uniform compression, the spatial distribution of the pressure is captured (Fig. 3E). When both normal and shear forces are applied during the interaction, tensile strains are induced at one side of the 3DAE-Skin (Fig. 3F), noting that the relief structure is much more rigid than the 3DAE-Skin. The last example in Fig. 3G corresponds to a complex loading condition in which a spatially non-uniform shearing coupled with pressing is applied. The spatially varying directions of the arrows serve as evidence that the coupled normal/shear forces could be well-measured in various units of the 3DAE-Skin. Additionally, the torque applied to the letter "U" is well correlated with spatially directed arrows of relevant units (Fig. 3G), indicating the potential of the 3DAE-Skin in torque sensing.

Super-resolution sensing (35, 36) of the 3DAE-Skin–based tactile system is made possible by incorporating a DNN model (see supplementary text for details) that establishes the implicit mapping between the location and magnitude of an applied normal force and relative resistance changes of 240 piezoresistive sensors in the 3DAE-Skin (Fig. 3, H to J, figs. S36-S38, and table S4). With aid of the DNN model, the prediction accuracy of loading position has been substantially improved, in comparison to the case of the linear interpolation (fig. S39). An evident reduction (from 1.086 mm to 0.117 mm) of the root-mean-square error can be observed. Such a resolution (0.117 mm) of the normal force sensing is very close to the resolution of force sensing by human hands (37–39). In the condition of combined normal and shear force loadings, the utility of DNN model can also enable a super-resolution sensing, as evidenced by the improved prediction accuracy of loading position (fig. S40 and table S5).

A comparison of the performance/capability (table S6) among state-of-art electronic skins and real human skin shows the advancement of the proposed 3DAE-Skin, especially in the decoupled perception of normal force, shear force and strain. Such fully decoupled mechanosensation is challenging to achieve, based on electronic skins with 2D structural layouts (fig. S41) or other designs reported previously (table S6).

Simultaneous quantitative measurements of elastic modulus and principal curvature components

Quantitative measurements of an object's elastic modulus and principal curvature components are pivotal for applications of prosthetic hands (31, 40, 41) as object shape is unknown in many practical situations. When touching an object, human fingertips usually rely on the sensed force distribution and its own skin deformation to infer the softness and local shape of the object. Similarly, the 3DAE-Skin–based tactile system can distinguish the softness of two objects through different levels of induced strains in the 3DAE-Skin and identify the local curvature through different normal/shear force distributions (e.g., Fig. 4A). Development of a DNN model (see supplementary text for details) that correlates the elastic modulus (E) and principal curvature components (κ_1 and κ_2) with relative resistance changes of 240 piezoresistive sensors allows prediction of the elastic modulus of an object without knowing its shape. The dataset was constructed based on a diversity of samples with 51 different surface shapes (ellipsoidal, spherical, cylindrical, and planar) and 15 different moduli (from 40 kPa to 3.9 MPa) (figs. S42 to S44 and tables S7 and S8). The data consisted of 30,600 samples that were split into datasets
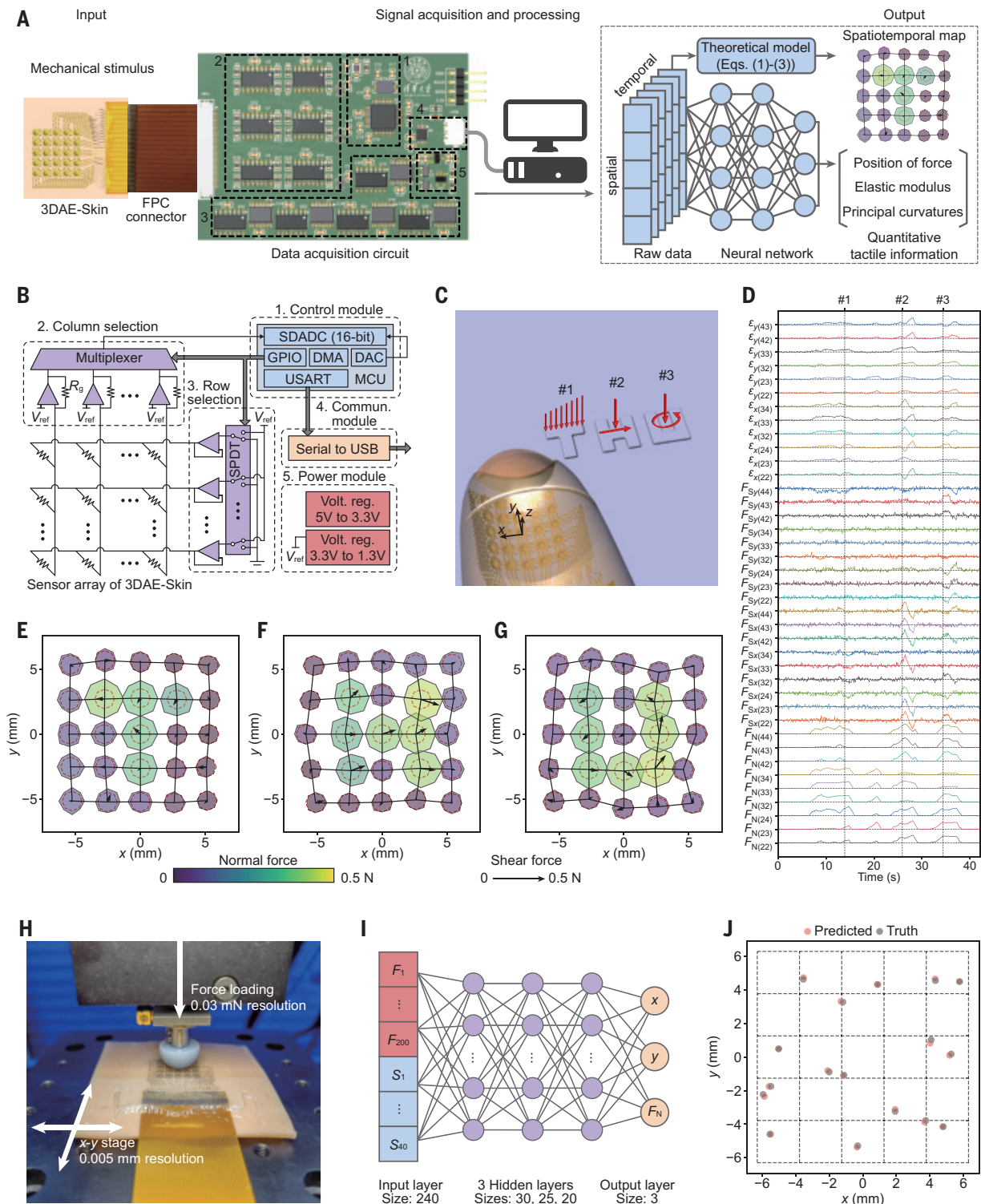
Fig. 3. Spatiotemporal mapping of forces and strain using the 3DAE-Skin–based tactile system. (**A**) Schematic illustration and working mechanism of the 3DAE-Skin–based haptic system. The black dashed boxes in the photo of the PCB indicate different components of the circuit: (1) control module; (2) column selection module; (3) row selection module; (4) communication module; (5) power module. A separate computer is utilized for DNN training and testing. (**B**) Block diagram of the data acquisition circuit in which the number of each module indicates the corresponding labeled component in (A). (**C**) Schematic illustration of the test of the spatiotemporal mapping in which artificial finger with integrated 3DAE-Skin touched the three letters of "THU" with different loading modes. (**D**) Temporal recordings of typical signals during the test in (C), including pressure and shear force (both x- and y-axis) signals from 9 selected units and strain signals from 12 selected units. (**E** to **G**) Visualization of the tactile sensation at three moments of the test shown in (C). (**H**) Optical image of the experimental setup used to collect data for realizing the spatial super-resolution of pressure sensing aided by deep learning. (**I**) Schematic diagram of the DNN model for the super-resolution sensing. F, force sensor; S, strain sensor. (**J**) Prediction results of loading positions by the trained DNN model on a part of the test set.
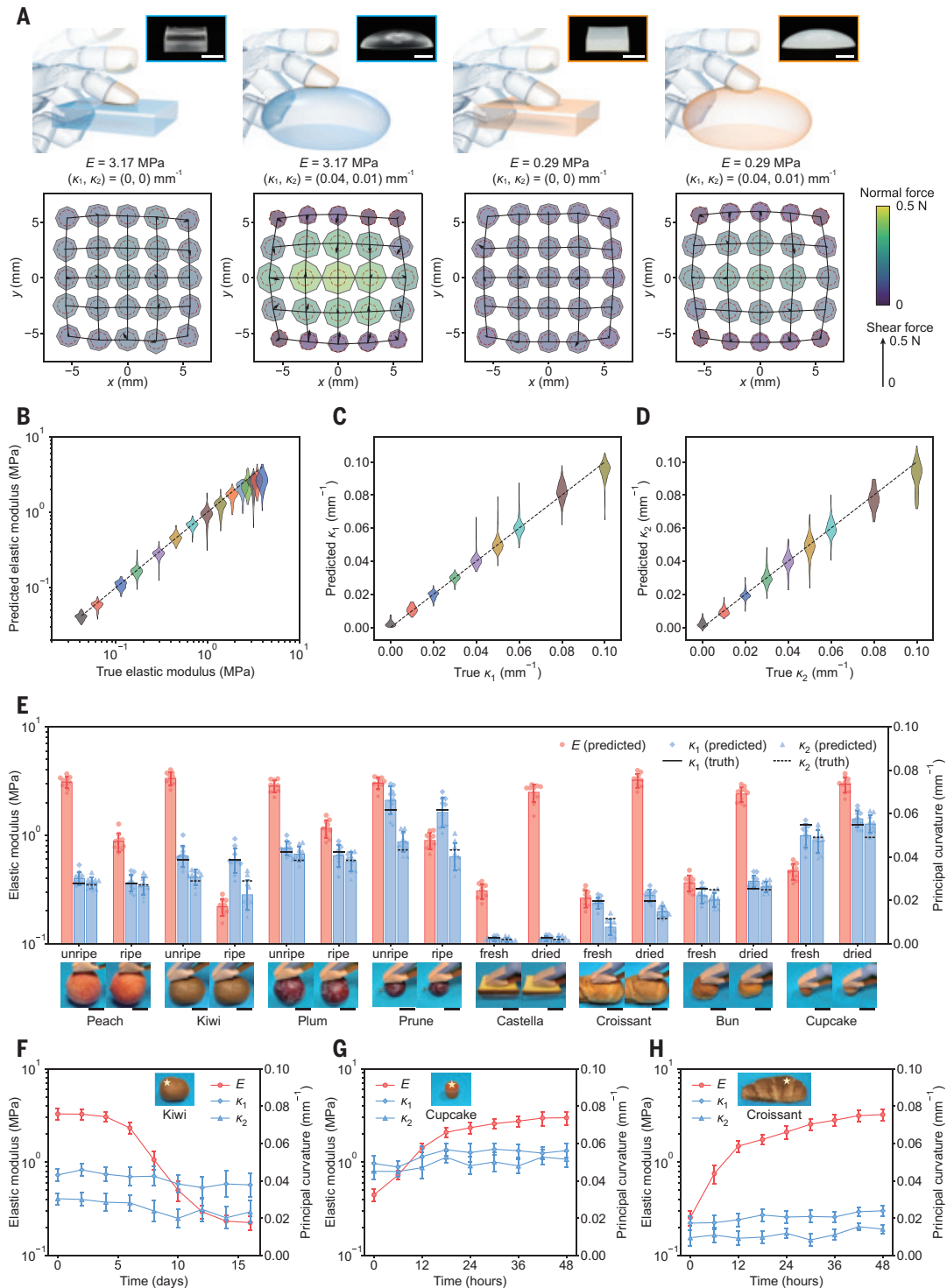
Fig. 4. Simultaneous quantitative measurements of elastic modulus and principal curvature components. (**A**) Visualized tactile information when the 3DAE-Skin contacts four standard samples with different combinations of elastic modulus (E) and surface shape characterized by the principal curvature components (κ_1 and κ_2). The first row shows the schematic illustrations with optical images of real samples as insets (scale bars, 2.5 cm). The second row shows the corresponding spatiotemporal maps. The normal resultant force is fixed at around 0.5 N during those tests. (**B** to **D**) Testing results of elastic modulus and principal curvature components based on the developed tactile system. A total of 765 samples with various elastic moduli and surface shapes were tested experimentally to construct the dataset.

(**E**) Simultaneous measurements of elastic modulus and principal curvature components of eight different foods, including four kinds of fruits (peach, kiwi, plum, and prune), each with distinct levels of ripeness, and four kinds of bread/cake (castella, croissant, bun, and cupcake) in both fresh and dried conditions. Scale bars, 4 cm. The ground truths of principal curvature components are denoted by solid black line (for κ_1) and black dash line (for κ_2), respectively. (**F** to **H**) Long-term monitoring of the elastic modulus and principal curvatures of (F) kiwi, (G) cupcake, and (H) croissant left in air for 16, 2, and 2 days, respectively. The stars denote the regions touched by the 3DAE-Skin. The average values of 5 independent predicted results are shown with SD values.

of training, validation, and testing with a ratio of around 8:1:1. The use of DNN model ensures more accurate predictions than other classical machine-learning models such as linear regression, KNN regression, and random forest regression models (fig. S45). Figure 4, B to D, shows testing results of 2700 samples from the testing set, where reasonably good predictions of the elastic modulus can be observed in the range of 40 kPa to 3.9 MPa, for a number of differently shaped objects. Similar to human skin, the 3DAE-Skin–based tactile system can measure the modulus values that are comparable to its own effective tensile modulus (~194 kPa). When the elastic modulus (e.g., > 1 MPa) of the target object is much higher than the 3DAE-Skin modulus, the target object barely deforms during the interaction, leading to a reduction of the prediction accuracy as compared with the cases when E is close to 194 kPa. Owing to the relatively small spacing (2.5 mm) of the force sensing units, the 3DAE-Skin–based tactile system can provide reasonably good predictions of local curvature components when they are up to around 0.1 mm^{-1}. Videos showing simultaneous modulus and curvature measurements of eight selected samples are presented in movie S4. Reducing the number of operational sensors in the 3DAE-Skin leads to an increase of the mean relative error of modulus prediction (fig. S46).

The ripeness or freshness of some food (e.g., kiwi, peach, cake, and bread) is challenging to distinguish using image recognition or other computer vision methods (42–44). The 3DAE-Skin–based tactile system presented could provide a possible rapid solution through touch. We measured the elastic moduli of four fruits (kiwi, peach, plum, and prune, with the principal curvature components ranging from ~0.02 to ~0.07 mm^{-1}) in both unripe and ripe states (Fig. 4E and movies S5 and S6). Fruit shape changes very slightly during ripening, but it gradually becomes softer during this process. For example, the modulus of the kiwi decreases slightly in the first 6 days and then rapidly until the kiwi is overripe at day 14 (Fig. 4F). The modulus (~0.2 MPa) of the ripe kiwi (day 14) is an order of magnitude lower than that (~3.2 MPa) of the unripe kiwi (day 0). Similarly, the modulus (~0.9 MPa) of the ripe peach (day 14) is also much smaller than that (~3.1 MPa) of the unripe peach (day 0). By contrast, fermented bread or cake tends to become more rigid during long-term air exposure, as a result of drying-induced hardening. Figure 4G shows that the modulus of the cupcake increases rapidly (from ~0.45 MPa to ~2.3 MPa) during the first day and relatively slowly (to ~3.0 MPa) during the following day, because the dehydration is mostly complete in the first 24 hours. The croissant shows more significant hardening (from ~0.3 MPa to ~3.3 MPa).

Conclusions

The bioinspired 3D architected designs, heterogeneous encapsulation strategies, and microfabrication technologies allow for the development of 3DAE-Skin that mimics the spatial arrangement of Merkel cells and Ruffini endings in human skin, as well as the skin's multilayer geometrical/mechanical characteristics. Such bioinspired designs leverage the 3D distribution of force and strain sensing components and the engineered stiffness variations in E-Skin to achieve decoupled sensing of normal/shear forces and tensile strains. Integration of the 3DAE-Skin with data acquisition/processing modules aided by deep learning algorithms allows development of a tactile system capable of normal/shear force sensing with spatial resolution comparable to human skin, as well as simultaneous modulus and curvature measurements through a simple touch of an object. Demonstrations on the modulus measurement of fruits, bread, and cake with diverse shapes suggest applications in the assessment of the food whose rigidity changes with time. The capabilities to quantitatively assess the contact state and the object information in real time also have important implications for human-machine interactions, humanoid robots, smart prostheses, and auto inspection instruments. For example, by measuring friction coefficients between the device and different target objects, the 3DAE-Skin system can potentially distinguish a rough surface from a smooth one (fig. S47). Although the presented 3DAE-Skin is developed to imitate the perception of fingertip, the design and fabrication methods are scalable and can be extended for uses in other types of prosthetic/robotic systems. Further improvements in the cell density of 3DAE-Skin can be achieved by reducing the structural dimensions of the 2D precursor design and increasing the magnitude of biaxial prestrain used in the 3D assembly (fig. S48), noting that there should be a limit considering the resolution of photolithography.

REFERENCES AND NOTES

1. A. Zimmerman, L. Bai, D. D. Ginty, *Science* **346**, 950–954 (2014).
2. A. Handler, D. D. Ginty, *Nat. Rev. Neurosci.* **22**, 521–537 (2021).
3. R. S. Johansson, J. R. Flanagan, *Nat. Rev. Neurosci.* **10**, 345–359 (2009).
4. A. Iggo, A. R. Muir, *J. Physiol.* **200**, 763–796 (1969).
5. S. M. Maricich et al., *Science* **324**, 1580–1582 (2009).
6. M. R. Miller, H. J. Ralston 3rd, M. Kasahara, *Am. J. Anat.* **102**, 183–217 (1958).
7. M. R. Chambers, K. H. Andres, M. von Duering, A. Iggo, *Q. J. Exp. Physiol. Cogn. Med. Sci.* **57**, 417–445 (1972).
8. D. H. Kim et al., *Science* **333**, 838–843 (2011).
9. S. Lee et al., *Science* **370**, 966–970 (2020).
10. B. C. K. Tee et al., *Science* **350**, 313–316 (2015).
11. Y. Kim et al., *Science* **360**, 998–1003 (2018).
12. W. W. Lee et al., *Sci. Robot.* **4**, eaax2198 (2019).
13. W. Wang et al., *Science* **380**, 735–742 (2023).
14. S. Xu et al., *Science* **344**, 70–74 (2014).
15. H. U. Chung et al., *Science* **363**, eaau0780 (2019).
16. D. Jung et al., *Science* **373**, 1022–1026 (2021).
17. S. Wang et al., *Nature* **555**, 83–88 (2018).
18. T. Sekitani et al., *Science* **326**, 1516–1519 (2009).
19. Z. F. Liu et al., *Science* **349**, 400–404 (2015).
20. C. M. Boutry et al., *Nat. Electron.* **1**, 314–321 (2018).
21. C. M. Boutry et al., *Sci. Robot.* **3**, eaau6914 (2018).
22. G. Li, S. Liu, L. Wang, R. Zhu, *Sci. Robot.* **5**, eabc8134 (2020).
23. I. You et al., *Science* **370**, 961–965 (2020).
24. Y. Yu et al., *Sci. Robot.* **5**, eaaz7946 (2020).
25. K. Yao et al., *Nat. Mach. Intell.* **4**, 893–903 (2022).
26. Y. Yu et al., *Sci. Robot.* **7**, eabn0495 (2022).
27. J. Kim et al., *Nat. Commun.* **5**, 5747 (2014).
28. S. Xu et al., *Science* **347**, 154–159 (2015).
29. Y. Zhang et al., *Nat. Rev. Mater.* **2**, 17019 (2017).
30. X. Cheng et al., *Science* **379**, 1225–1232 (2023).
31. A. Chortos, J. Liu, Z. Bao, *Nat. Mater.* **15**, 937–950 (2016).
32. S. M. Won et al., *ACS Nano* **13**, 10972–10979 (2019).
33. M. Han et al., *Nat. Biomed. Eng.* **4**, 997–1009 (2020).
34. J. W. Kwak et al., *Sci. Transl. Med.* **12**, eabc4327 (2020).
35. Y. Yan et al., *Sci. Robot.* **6**, eabc8801 (2021).
36. H. Sun, G. Martius, *Sci. Robot.* **7**, eabm0608 (2022).
37. K. O. Johnson, J. R. Phillips, *J. Neurophysiol.* **46**, 1177–1192 (1981).
38. H. E. Wheat, A. W. Goodwin, A. S. Browning, *J. Neurosci.* **15**, 5582–5595 (1995).
39. M. Hollins, S. R. Risner, *Percept. Psychophys.* **62**, 695–705 (2000).
40. E. D'Anna et al., *Sci. Robot.* **4**, eaau8892 (2019).
41. S. Raspopovic, G. Valle, F. M. Petrini, *Nat. Mater.* **20**, 925–939 (2021).
42. D. Barik, M. Mondal, in *2010 2nd International conference on education technology and computer* (IEEE, 2010), vol. 2, pp. V2-170–V172.
43. H. Guan, J. Zhang, in *2016 IEEE International conference on robotics and biomimetics (robio)* (IEEE, 2016), pp. 1685–1690.
44. G. Tatiya, J. Sinapov, in *2019 International conference on robotics and automation (ICRA)* (IEEE, 2019), pp. 7872–7878.

SUPPLEMENTARY MATERIALS

science.org/doi/10.1126/science.adk5556
Materials and Methods
Supplementary Text
Figs. S1 to S48
Tables S1 to S8
References (45–60)
Movies S1 to S6

QUANTUM MATERIALS

Solid-state continuous time crystal in a polariton condensate with a built-in mechanical clock

I. Carraro-Haddad[1,2]†, D. L. Chafatinos[1,2]†, A. S. Kuznetsov[3], I. A. Papuccio-Fernández[1,2], A. A. Reynoso[1,2], A. Bruchhausen[1,2], K. Biermann[3], P. V. Santos[3]*, G. Usaj[1,2,4,5]*, A. Fainstein[1,2]*

Time crystals (TCs) are many-body systems that display spontaneous breaking of time translation symmetry. We demonstrate a TC by using driven-dissipative condensates of microcavity exciton-polaritons, spontaneously formed from an incoherent particle bath. The TC phases are controlled by the power of a continuous-wave nonresonant optical drive exciting the condensate and the interaction with cavity phonons. Those phases are, for increasing power, Larmor-like precession of the condensate pseudo-spins—a signature of continuous TC; locking of the frequency of precession to self-sustained coherent phonons—stabilized TC; and doubling of TC's period by phonons—a discrete TC with continuous excitation. These results establish microcavity polaritons as a platform for the investigation of time-broken symmetry in nonhermitian systems.

Symmetries govern the behavior of physical systems. However, ordinary material crystals constitute a well-known example in which a quantum many-body system spontaneously breaks space translation symmetry. Similarly, time crystals have been proposed as quantum systems exhibiting spontaneous breaking of the time translation symmetry (TTS) (*1*). It was soon realized, however, that time-independent Hamiltonians necessarily lead to stationary ground states (*2*). Far from closing the subject, this conclusion stimulated the search for conditions under which time crystals could still emerge. One direction explores periodically driven many-body Hamiltonians (*3*, *4*), leading to stable states with periods distinct from the drive, often identified by period doubling (PD). These "discrete time crystals" (DTCs) have been observed in diverse physical systems, including cold atoms (*5*), magnons in superfluid ^{3}He (*6*, *7*), nuclear spins (*8*), photonic devices (*9*), and quantum computer qubits (*10*). However, the search for a time crystal closer to the original idea of a time-dependent ground state of a many-body quantum system in the absence of an external time-dependent driving has not waned.

It has been theoretically argued that TTS can naturally break in an open quantum system in which dissipation stabilizes time-crystal dynamics compensating for losses through continuous pumping (*5*, *6*, *11–16*). These systems are termed "continuous time crystals" (CTCs) because their Hamiltonians are time-independent. Probably the closest experimental implementation of such a CTC is the recent report of an open atom-cavity system that oscillates between two checkerboard density patterns when destabilized by an additional quasi-resonant continuous laser drive (*17*, *18*). We report here a CTC implemented in a driven-dissipative exciton-polariton system (*19*). Contrary to previous proposals, our solid-state many-body quantum time crystal spontaneously forms from an incoherent particle bath that is loaded with a continuous nonresonant optical drive. We demonstrate PD concerning an internal mechanical clock in this CTC state.

A polaromechanical CTC loaded from an incoherent reservoir

Our solid-state CTC system is based on polaritons, quasiparticles that result from the strong coupling between quantum-well (QW) excitons and photons in a gallium arsenide (GaAs)–based semiconductor intracavity trap. These are bosonic excitations that show many notable phenomena that derive from their mutual Coulomb interactions and dissipative nature (because of the excitonic and photonic component, respectively) (*20–22*). Being composite bosons, they transition to a nonequilibrium Bose-Einstein condensate (*23*). Our traps also confine ~20-GHz mechanical vibrations that very efficiently couple to polaritons through deformation potential interaction (*24*, *25*). QWs are positioned to enhance simultaneously the coupling of excitons to both phonons and photons. We previously showed that two polariton traps with energy levels detuned at the phonon energy led to self-oscillation of a coherent mechanical wave (phonon lasing) (*26*, *27*). In this work, we reveal that the polariton ground state in a single trap can develop

nonlinear self-sustained dynamics, intimately affected by mechanics in ways that expose characteristics of both continuous and discrete time crystals.

As depicted in Fig. 1A, a semiconductor solid-state device designed to trap polaritons is subject to nonresonant continuous-wave (cw) optical excitation, with a spot of diameter between 3 and 10 μm placed on top of the trap. Electron-hole particles are optically injected at low temperatures (5 K) and high energies and left to relax and find their stationary dynamics. Energy loss occurs through emission of phonons, erasing the phase information set by the drive until a relaxation bottleneck leads to exciton reservoir build-up (depicted at the top of traps in Fig. 1A). This reservoir is, a priori, unpolarized by construction because it is generated by the non-resonant linearly polarized laser. This reservoir acts as the bath feeding the polariton ground state (GS) of a nominally square 3- by 3-μm trap fabricated by laterally micropatterning the spacer region of an otherwise planar microcavity (*28*, *29*). For the experiments reported here, the photon-to-exciton energy detuning in the planar regions of the wafer ranges from ~–12 to –9 meV (polariton modes have a larger photonic character). The lateral patterning leads to traps with a barrier height of ~10 meV, and depending on the trap lateral size, the cavity confinement can blue-shift the modes up to ~5 meV, increasing their exciton character (supplementary materials, materials and methods) (*30*).

At low excitation power (P_{cw}), we observed a single confined level of the trap (Fig. 1, A and B, i). At these powers, the spin-up and spin-down populations of the reservoir are perfectly balanced. On increasing P_{cw}, a condensation occurs at a threshold P_{th} signaled by a strong nonlinear increase in the level occupation, accompanied by a narrowing of the line down to a fraction of a gigahertz (coherence times of a few nanoseconds) as well as by an energy blue-shift determined by polariton-polariton and polariton-reservoir interactions. Upon further increasing P_{cw}, a series of qualitative changes occur (Fig. 1, A and B). First, there is a spontaneous splitting of the lines representing a two-level system (Fig. 1, A and B, ii) attributed to the $\sigma = \pm$ polarization degree of freedom of the condensate, which is linked to the spin of the excitons and the polarization of the cavity photons through angular momentum selection rules (*31–34*). A spontaneous symmetry breaking has occurred, which is accompanied by a self-induced imbalance of the spin population in the reservoir. It follows (Fig. 1, A and B, iii) the locking of the splitting to the frequency of the acoustic phonon confined in the same trap, v_m~20 GHz, where v_m is the phonon frequency. Last, (Fig. 1, A and B, iv) sidebands emerge separated by $v_m/2$ ~ 10 GHz GHz,
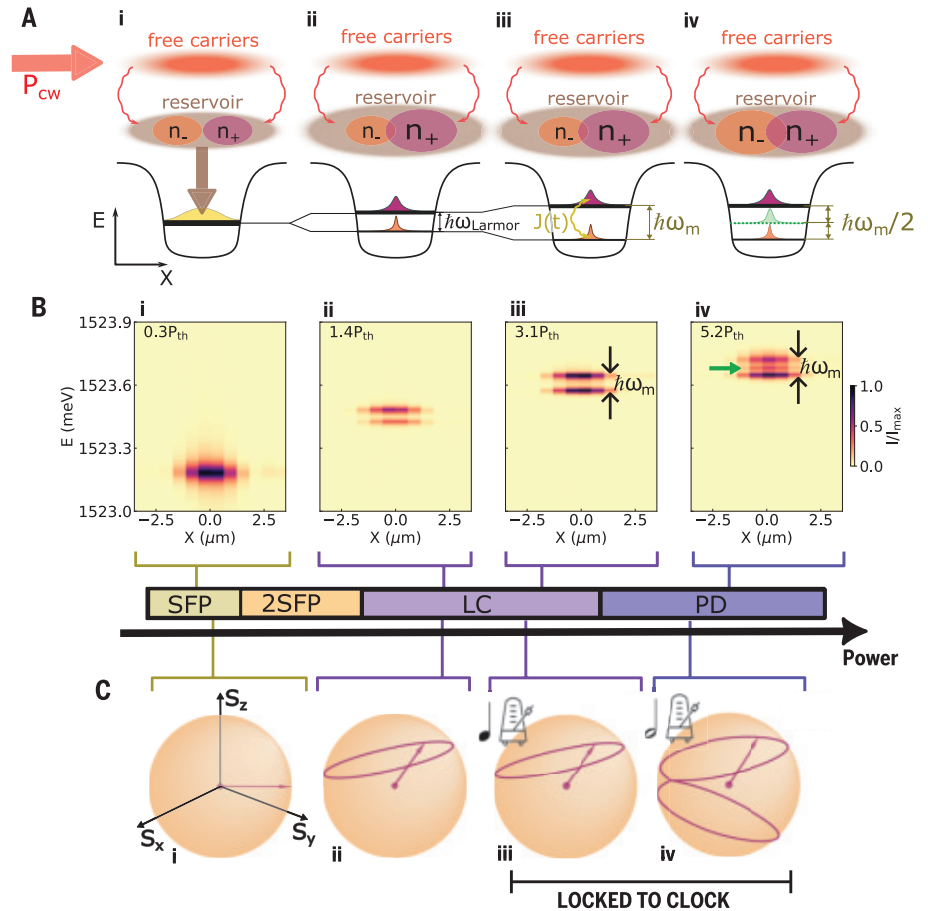
[1]Centro Atómico Bariloche and Instituto Balseiro, Comisión Nacional de Energía Atómica (CNEA)–Universidad Nacional de Cuyo (UNCUYO), Bariloche 8400, Argentina. [2]Instituto de Nanociencia y Nanotecnología (INN-Bariloche), Consejo Nacional de Investigaciones Científicas y Técnicas (CONICET), Bariloche 8400, Argentina. [3]Paul-Drude-Institut für Festkörperelektronik, Leibniz-Institut im Forschungsverbund 10117 Berlin e.V., 10117 Berlin, Germany. [4]Theorie van Kwantumsystemen en Complexe Systemen (TQC), Universiteit Antwerpen, B-2610 Antwerpen, Belgium. [5]CENOLI, Université Libre de Bruxelles–CP 231, B-1050 Brussels, Belgium.
*Corresponding author. Email: santos@pdi-berlin.de (P.V.S.); usaj@cab.cnea.gov.ar (G.U.); afains@cab.cnea.gov.ar (A.F.)
†These authors contributed equally to this work.

Fig. 1. Polariton spinor time crystal with internal clock. (**A**) Experimental implementation and dynamics with increasing nonresonant cw laser power P_{cw}. (**B**) Spectrally resolved photoluminescence images of a 3- by 3-μm square trap for the four powers in (A). A cw linearly polarized pump laser nonresonantly injects free carriers with P_{cw}. These relax, forming an incoherent exciton reservoir feeding a polariton trap. Because of linear-polarized pumping and carrier relaxation, at low powers exciton spin-up and spin-down populations in the reservoir are balanced, leading to a degenerate polariton ground state [(A) and (B), i]. Increasing P_{cw} breaks TTS, initiating spontaneous Larmor-like precession (continuous time crystal), indicated by pseudospin state splitting [(A) and (B), ii]. The spontaneous symmetry breaking has led to a spin unbalance in the reservoir. Polariton dynamics induces coherent mechanical oscillation, back-acting to lock Larmor precession to confined phonon frequency $\omega_m/2\pi \sim 20$ GHz [(A) and (B), iii]. Further power increase results in self-induced mechanical oscillation leading to PD (sidebands split by $\hbar\omega_m/2$) [(A) and (B), iv]. (**C**) Spinor representation for states evolving from single or double stable fixed points [(i), SFP and 2SFPs, respectively], to a LC corresponding to Larmor-like precession with either a (ii) self-determined or (iii) locked frequency, and last (iv) to PD locked to the mechanical clock.

Experimental evidence of spontaneous breaking of TTS

The sequence of spectra leading to the spatial images in Fig. 1B are shown in Fig. 2A for increasing cw excitation power $P_{cw} > P_{th}$ (Fig. 2A, bottom to top). Another example, obtained for a 2- by 2-μm square trap, is shown in Fig. 2B. These spectra represent the component of the emission, linearly polarized along one of the axes of the square traps. The polariton ground state of the smaller trap is blue-shifted by ~2.5 meV with respect to the larger one owing to confinement, so that its character is more excitonic. Both structures display a slightly different behavior, but the phenomenology is broadly the same. Above threshold, we observed the mode to split into two, with the splitting increasing with power. When $P_{cw} \sim 2P_{th}$, the mode separation locks to the phonon frequency (Fig. 2A) or to half of it (Fig. 2B), and after this

signaling a PD with respect to v_m. This two-level system can be interpreted in terms of the dynamics of a spinor in the presence of synthetic fields (Fig. 1C). The orbits, which reflect self-induced time crystalline oscillations of the condensate polarization, will be explained with the theory in this work.

locking, the sidebands emerge separated by $v_m/2$. These sidebands, reflecting PD, are indicated with up arrows in the figures [additional experimental examples of CTC behavior can be found in (30)].

The observed sidebands are definitive "smoking-gun" evidence for the emergence of a coherent time dynamics involving and modulating the exciton-polaritons (34)—that is, of a time crystal. Additionally, we obtained direct information of the time dependence by measuring the time-resolved spatial first-order coherence function $g^{(1)}(r, \tau)$, as schematized in Fig. 2C (30). $g^{(1)}(r, \tau)$, for a situation as in Fig. 1B, iv, is presented in Fig. 2D. It displays clear temporal oscillations with a period that exactly matches the inverse of $1/v_m \sim 50$ ps, provides evidence of PD, and is consistent with the spectral line-splitting as simultaneously obtained and presented in Fig. 2E.

Theoretical model of a polariton condensate coupled to a dynamical reservoir and a mechanical clock

The results shown in Figs. 1 and 2 emerge from the intricate interplay of nonresonant driving, coupling to excitons in a dynamic reservoir, cavity dissipation, interactions in a many-body

quantum system, and the tailored coupling and feedback with confined phonons. In the condensate regime, the occupation is large, and number fluctuations can be neglected in a first approximation. This leads to a semiclassical description in terms of a coherent state, which is coupled to a mean-field bath. To describe this system, we used the generalized Gross-Pitaevskii equations (gGPEs) for the condensate field $\tilde{\psi}_\sigma$ and reservoir population $\tilde{n}_\sigma$ (22, 32–36), coupled to a mechanical oscillator of displacement x (27)

$$i\hbar\frac{d\tilde{\psi}_\sigma}{dt}\left(\varepsilon_\sigma + U_0|\tilde{\psi}_\sigma|^2 + U_0^R\tilde{n}_\sigma\right)$$
$$-\left(J + i\hbar\gamma_d\right)\tilde{\psi}_{\bar\sigma} + \frac{i\hbar\gamma}{2}\left(\tilde{n}_\sigma - 1\right)\tilde{\psi}_\sigma \quad (1)$$

$$\frac{d\tilde{n}_\sigma}{dt} = \gamma_R\left[p_\sigma - \left(1 + |\tilde{\psi}_\sigma|^2\right)\tilde{n}_\sigma\right] \quad (2)$$

$$\ddot{x} = -\Gamma\dot{x} - \omega_m^2 x$$
$$+ 4\omega_m\delta g_0\rho_0 \text{Re}\left(\tilde{\psi}_+^*\tilde{\psi}_-\right) \quad (3)$$

A model similar to Eqs. 1 and 2 has been used to explain the rupture of spatial translation symmetry (spatial PD) in a polariton condensate (37).

In these equations, $\tilde{\psi}_\sigma$ and $\tilde{n}_\sigma$ have been scaled with the corresponding polariton and
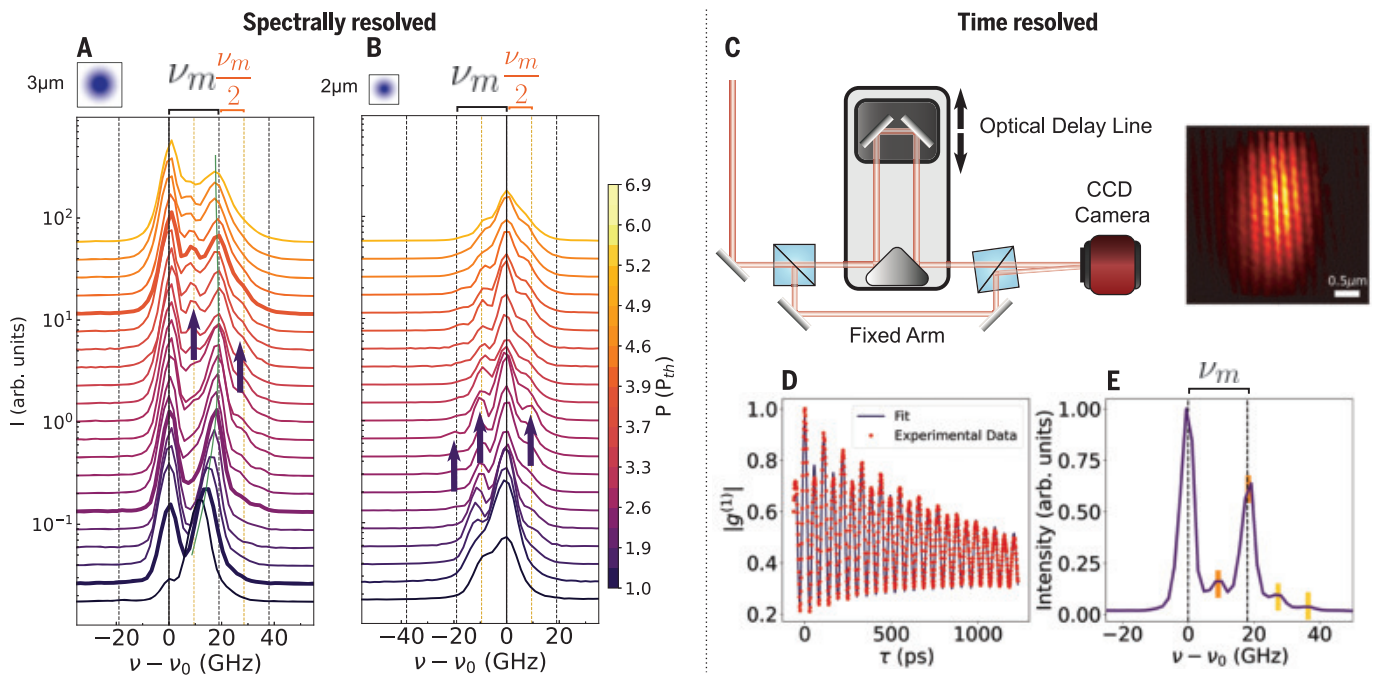
Fig. 2. Spectra and time-resolved coherence function. (**A** and **B**) Photoluminescence spectra examples collected for vertical polarization (along one axis of the square traps), for increasing cw excitation power (bottom to top) in individual 3- by 3-μm and 2- by 2-μm square traps, respectively. The curves are lines connecting points, each peak defined by 4 or 5 points. Thicker lines in (A) indicate spectra corresponding to spatial images in Fig. 1B. Frequencies are referenced to the most intense peak v_0, subtracting the interaction-induced blue-shift. Vertical dashed lines indicate multiples of the phonon frequency $v_m \sim 20$ GHz and its half ($v_m/2$). Up arrows indicate peaks related to PD. (**C**) Experimental set-up scheme for off-axis digital holography and image obtained for a given delay τ defined by the delay line position. Light collected from the polariton condensate ground state is divided by a nonpolarizing beamsplitter (BS), with 50% directed to a fixed arm and the other 50% directed to a delay line. The two beams impinge with an angle, creating an interference pattern on a charge-coupled device. (**D**) Example of time-dependent $g^{(1)}(r, \tau)$ for a 2- by 2-μm square trap taken at $P = 4.5P_{th}$, with Larmor-like precession and period-doubling locked to the phonon frequency $v_m \sim 20$ GHz, along with corresponding simultaneously measured spectra in (**E**). The continuous line in (D) is a fit, leading to the frequencies indicated with short vertical thick lines in (E). The decay time derived from the fit is τ ~ 1 ns, which coincides with the measured coherence time of the condensate.

reservoir average populations $\sqrt{\rho_0}$ and n_0, respectively. ε_σ is the polariton bare energy, and U_0 and U_0^R account for the same-spin Coulomb interaction between polaritons and with excitons in the reservoir, respectively (30). The complex coupling $-(J + i\hbar\gamma_d)$ contains two contributions: (i) a Josephson-like coupling $(-J)$, which arises from the energy splitting of the X and Y linearly polarized states, and (ii) a dissipative coupling $(-i\hbar\gamma_d)$ originated on the difference between the effective decay rates of the $X - Y$ linearly polarized modes [experimental proof of different linewidths of the spinor modes is included in (30)] (38). Here, $\psi_X = (\tilde{\psi}_+ + \tilde{\psi}_-)/\sqrt{2}$ and $\psi_Y = (\tilde{\psi}_+ - \tilde{\psi}_-)/\sqrt{2}$ represent the linearly polarized base, natural because of the symmetry of the trap. The last term in Eq. 1 represents the stimulated gain from the exciton's reservoir (proportional to $\tilde{n}_\sigma$) and the bare polariton decay rate (γ). Equation 2 describes the dynamics of the reservoir, which is controlled by the pump power. Here, $p_\sigma = P_\sigma/P_{th}$, where P_σ is the external cw driving of the σ reservoir, and $P_{th} = \gamma\gamma_R/R$ is the condensation threshold power

defined by the exciton's decay rate (γ_R) and the stimulated decay to the condensate R (spin-flip between the reservoirs is not included). The condensate field and the reservoir are identified by their pseudospin or spin σ because these are the proper variables owing to the optical selection rule by which photons of circular polarization couple only to excitons of a given spin. However, the complex coupling $-(J + i\hbar\gamma_d)$ will lead to solutions for the condensates in a trap that do not have a purely circular pseudospin character. Moreover, experiments and theory do not assume any optically induced polarization. If any polarization appears, it reflects a spontaneous breaking of symmetry.

Equation 3 describes the confined phonon mode of frequency $\omega_m/2\pi \sim 20$ GHz and corresponds to a damped harmonic oscillator with damping Γ and a driving force provided by the polariton modes (27). δg_0 here is related to the optomechanical coupling factor (deformation potential interaction) by which the phonon strain modulates the exciton energy (39). The coupling of the polaritons to the phonons is introduced by assuming that J depends on the vibrational

coordinate $x(t)$, $J = J_0 + \hbar\delta g_0 x$, thus providing the bridge with the physics of cavity optomechanics (40). A finite coherent mechanical oscillation is not assumed as preexistent. All three of Eqs. 1 to 3 need to be solved self consistently. The external drive being continuous, any time dependence on the macroscopic variables $\tilde{\psi}_\sigma, \tilde{n}_\sigma$, and x will reflect a spontaneous breaking of TTS.

A clear physical picture of the resulting dynamics can be grasped by changing to a spinor description in the Poincaré sphere (41) through a pseudospin transformation $S_j = \tilde{\Psi}^\dagger \sigma_j \tilde{\Psi}$, where σ_j are the different Pauli matrices. Each component of the pseudospin takes the form $S_x = 2\text{Re}(\tilde{\psi}_+ \tilde{\psi}_-^*) = 2\cos(\theta)\sqrt{N_+ N_-}$, $S_y = 2\text{Im}(\tilde{\psi}_+ \tilde{\psi}_-^*) = 2\sin(\theta)\sqrt{N_+ N_-}$, and $S_z = |\tilde{\psi}_+|^2 - |\tilde{\psi}_-|^2 = N_+ - N_-$. Here, N_σ and $\theta = \theta_+ - \theta_-$ are defined by the Madelung transformation $\tilde{\psi}_\sigma = \sqrt{N_\sigma}e^{i\theta_\sigma}$. The polarization of the photon component of the polaritons maps directly onto their pseudospin, with the magnitude and sign of S_x, S_y, and S_z being positive for the horizontal, diagonal, or circular right polarization of the emitted light (vertical, anti-diagonal, or circularly left, if the components

are negative). Using this notation, we obtained the following set of equations (*41*)

$$\frac{d\boldsymbol{S}}{dt} = \frac{1}{\hbar}\boldsymbol{B} \times \boldsymbol{S} + \boldsymbol{SE} + \Gamma\boldsymbol{S} \qquad (4)$$

where

$$\boldsymbol{B} = 2J\hat{\boldsymbol{x}} - (U_0 S_z + 2U_0^{\mathrm{R}} m)\hat{\boldsymbol{z}},$$
$$\boldsymbol{E} = -2\gamma_d\hat{\boldsymbol{x}} + \gamma m\hat{\boldsymbol{z}}, \Gamma = \gamma(n-1) \qquad (5)$$

with $n = (\tilde{n}_+ + \tilde{n}_-)/2$ and $m = (\tilde{n}_+ - \tilde{n}_-)/2$, and where we assumed $\varepsilon_+ = \varepsilon_-$.

Equation 4 shows that the condensate spinor follows dynamical equations that resemble those in magnetic resonance (MR) phenomena, albeit with some important differences. The first term with the vector product leads to Larmor precession (*42*). The second term can be associated with a synthetic crystal-field $\boldsymbol{E}$ favoring specific spinor orientations. The last term mimics the phenomenological way in which spin decay is usually introduced, where Γ describes the net gain of the system. Equation 5 shows that $\boldsymbol{B}$ has two components, one in the x direction, originated in the Josephson coupling J (in the energy splitting of the X-Y modes), and another along z, which is nonlinear and changes with the population imbalance of the $(+, -)$ modes (S_z) and that of the reservoirs (m). This latter term implies that in general, a Larmor precession can lead to a time dependence of $\boldsymbol{B}$. This feedback is critical first to induce a spontaneous polarization of the condensate and then for establishing self-sustained dynamics (limit cycle). The second line in Eq. 5 shows that the field $\boldsymbol{E}$ has an x component that reflects the coupling introduced by the difference of dissipation between the X and Y modes and a z component that derives from the difference in gain between the $(+, -)$ modes caused by the reservoir imbalance m. It involves again a nonlinearity and thus can be time dependent if a self-sustained dynamics sets in. A coupling between the dynamics of the reservoir bath and that of the polaritons in the traps is critical for observing the time crystal behavior in our system (*30*).

A time dependence of $\boldsymbol{B}$ can also arise from the mechanical field $x(t)$. In our case, $x(t)$ is self-consistently determined by solving for the mechanical dynamics coupled to the polariton equations Eqs. 1 and 2 (*26*, *27*). If a threshold situation occurs in which self-induced coherent mechanics set in, this leads to an oscillating $\boldsymbol{B}(t)$ field, with an x component that approximately will follow $B_x(t) = 2J_0 + 2J_{\mathrm{m}}\cos(\omega_{\mathrm{m}}t)$, where $J_{\mathrm{m}} = \hbar\delta g_0\sqrt{n_p}$ and n_p is the number of phonons (*30*). Because the synthetic field associated with J in Eq. 5 is aligned along $\hat{x}$, an externally induced mechanical modulation $J(t)$ could allow for coherent control strategies such as those in MR based on in-plane pulsed radiofrequency

resonant fields [a possible polaromechanical implementation of such coherent control is presented in (*30*)].

Continuous time crystalline phases tuned by the excitation power

In Fig. 3, A and B, we compare the calculated dynamics without the phonons ($\delta g_0 = 0$) and with them ($\delta g_0 \neq 0$), respectively. These calculations were obtained for a time-independent drive with $p_+ = p_- = p$—that is, without any induced polarization of the reservoir. The shown colormaps display the energy spectrum as a function of normalized laser power p. The power spectrum of the phonon displacement $[\,|x(\omega)|^2\,]$ is shown in Fig. 3B, left, for the spectral region around the confined phonon frequency, whereas Fig. 3B, right, maps the power spectrum corresponding to the polariton modes around the bare frequency ω_0. Frequencies are scaled to the confined phonon frequency $\omega_{\mathrm{m}}/2\pi \sim 20$ GHz. The phonon spectral map displays a single line at ω_{m}, with an intensity that directly reflects the emergence of a self-induced coherent mechanical oscillation (observed mainly around $2.4 \lesssim p \lesssim 3.7$). For the polariton spectra, besides a blue-shift of the spectra, mainly determined by the reservoir average population (n) through U_0^{R}, a rich scenario develops with increasing external pumping.

Focusing first on Fig. 3B and the corresponding Poincare spheres in Figs. 3C, the sequence proceeds as (i) the formation of synchronized condensates at low pumping [one stable fixed point (SFP)] (*36*) then (ii) a symmetry-breaking pitchfork bifurcation (*43*) to two SFPs of the same frequency [also identified as a spin-bifurcation point in (*32*, *44*)], with unequal occupation of the two pseudospins σ (emergence of a synthetic magnetic field). The corresponding attractors, selectively accessed depending on the initial conditions, are identified by red and blue colors. (iii) Loss of the stability of the SFPs in the system results in two possible limit cycle dynamics [self-induced persistent Larmor-like precession (*45*)] that lock to the phonon frequency ω_{m}, the point at which the Larmor-like precession drives the mechanics (self-induced coherent mechanical oscillations were realized with cw pumping only, and the different phases were tuned only through the excitation power) (*26*, *27*). (iv) A transition to PD dynamics locked at half the phonon frequency, $\omega_m/2$. The latter arises, as evidenced in Fig. 3C, from the merging of the two possible orbits in (iii). Additional information about the spinor orbits can be obtained from polarization-resolved spectra and through on-purpose generation of an imbalance of the reservoir by means of optical spin orientation (*30*).

On further increasing the excitation power, the system may unlock its Larmor frequency from the mechanical "clock" (illustrated above $p \sim 3.7$ in Fig. 3B), and even at higher powers it

can eventually attain again a synchronized state (SFP) through a Hopf bifurcation from the limit cycle with polarization orthogonal to that observed at low powers (*30*). Depending on the chosen parameters, before (iii) the system may go first through a chaotic region (*46*). Indications of this can be observed in Fig. 3, A and B, between $p \sim 1.7$ and $p \sim 2.4$. Comparing Fig. 3, A and B, the presence of the phonons does not change the orbits and different regimes qualitatively; the most notable effect is the more robust presence of the limit cycle (LC) and PD regimes (in Fig. 3, A and B, the more extended region where PD is observed when the mechanics is present). From an experimental point of view, when locked the frequency of the LCs and the PD orbits are set by the phonon frequency. By contrast, when the coupled mechanics is not present the Larmor-like precession frequency depends on the polariton population (Fig. 3A) and thus is subject to intensity noise because the latter is directly affected by interactions with the reservoir. It is our experimental observation that sidebands are very rarely observed when the spinor modes are unlocked. By contrast, both LC and PD sidebands always emerge when the split levels lock to the phonon frequency [examples of this effect are presented in (*30*)]. The phonon "clock," which has a coherence time three to four orders of magnitude longer than that of the condensate (*47*), stabilizes the dynamics by making the frequencies constant and independent of p, thus facilitating the observation of the whole phenomenon.

Discussion and outlook

It follows from our systematic investigation of the model represented by Eqs. 1 to 3 that the dynamics of the reservoir, and specifically of the population imbalance m, is crucial for the observation of the discussed complex dynamics. We found that only when the reservoir population is left to respond in time to that of the trapped-polariton dynamics, for parameter values that are physically reasonable, the LCs and PD emerge (*30*). Also, the reservoirs' polarization m is only different from zero if there is a spontaneous symmetry breaking of the condensate polarization leading to $S_z \neq 0 (m \simeq -S_z)$. It is this spontaneous symmetry breaking that leads to the pitchfork bifurcation shown in Fig. 3C and subsequently to the instability of the two SFP, leading to the self-induced LC Larmor-like precession. Because of this spontaneous character, the phase of the LC and PD orbits described above is fully arbitrary. This is a major requirement for time crystalline behavior, naturally satisfied in our system, which is only driven nonresonantly, with a cw optical linearly polarized excitation and with reservoir excitons losing any phase memory from the laser excitation conditions through relaxation. The second strong requirement for a time crystal is the robustness against large variations of the
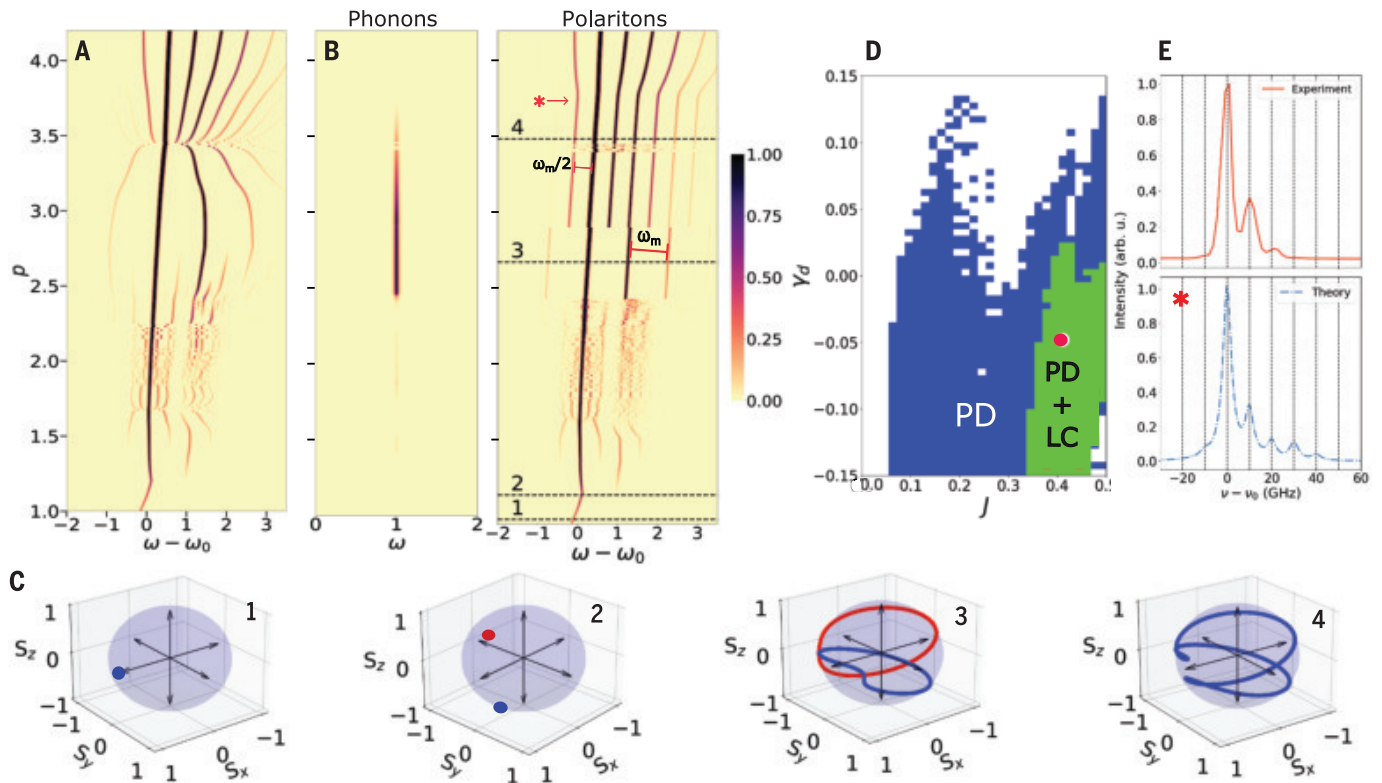
Fig. 3. Theory of continuous polaromechanical time crystal. (A and **B)** Calculated power spectrum color maps from Eqs. 1 to 3 as a function of $p = P_{cw}/P_{th}$ without and with applied mechanics, respectively (P_{th} is the condensation threshold power). Simulation parameters are $2J = 0.45$, $\Delta\varepsilon = 0$, $\hbar\delta g_0 = 0.85$, $2\hbar\gamma_d = -0.05$, $U_0 = 0.25$, $U_0^R = 3.6$, $\hbar\gamma_R = 0.4$, and of $\hbar\delta g_0$ (scales in terms $\hbar\omega_m$ GHz). (B) (Left) Phonon spectra $[|x(\omega)|^2]$. (Right) polariton spectra around $\hbar\omega_0 \left[|\psi_+(\omega)|^2 + |\psi_-(\omega)|^2\right]$. Horizontal dashed white lines in (B) indicate powers corresponding to orbits on normalized Poincare spheres in (**C**). Red and blue indicate distinct initial conditions, highlighting dynamical attractors. (**D**) Dynamical phase diagram as a function of real (J) and imaginary (γ_d) polariton coupling components. Green or blue indicates regions where, as a function of p, limit cycles locked at $\omega_m/2\pi = 20$ GHz (LC) and PD or only PD are observed. Red dot indicates parameters used in (B). (**E**) Example of (bottom) calculated and (top) experimental spectra, the former for the power indicated with an asterisk in (B).

relevant physical parameters. That this is the case is shown in Fig. 3D, where a phase diagram for the stability of the LC+PD dynamics is shown in green and that of only PD is shown in blue, as a function of the complex coupling $J + i\hbar\gamma_d$. There are large parameter regions where stable self-induced dynamical behavior exists, demonstrating the robustness of the limit cycles against perturbations, thus bringing further support for the emergence of a time crystal. The quite universal observation of similar dynamics in traps of different size and exciton-photon detuning further supports this conclusion. The qualitative agreement between the theoretical power dependencies in Fig. 3B and the experimental ones in Fig. 2, A and B, is also quantitative, as illustrated by characteristic spectra in Fig. 3E and other examples presented in (*30*), further bringing strength to the proposed model. Last, the model is also predictive in the sense that, as follows from Fig. 3, forced mechanical driving (instead of the self-induced one described so far) should also lead to PD behavior. This was experimentally tested by using coherent me-

chanical phonons externally generated with pulsed lasers (*48*) and is presented in (*30*).

We have measured the dynamics of a driven-dissipative, nonlinear cavity polariton system coupled to confined vibrations. Fed by a fully incoherent exciton bath, this system exhibits continuous time crystalline behavior involving the spinor of the trapped condensate's ground state and its coupling to a dynamic exciton reservoir and to confined phonons of the resonator. We observed PD without any external time-dependent harmonic driving, referenced to the mechanical coherent vibrations that are self induced by the polariton fluid. These self-induced mechanics stabilize and lock the frequency of the time crystal, acting as an internal clock. Our findings pave the way for exploring time crystals in open many-body quantum systems. We believe that the combination of nonlinear photonic arrays with self-induced oscillations as demonstrated in this work could serve as a test bed for dynamical gauge theories, with applications that include quantum simulators for quantum electrodynamics and quantum chromodynamics models (*49*). In ad-

dition, the demonstrated time modulation $J(t)$ induced by a mechanical driving could be used to control quantum gates based on polariton fluids, as has been proposed for classical and quantum computing (*30, 50, 51*).

REFERENCES AND NOTES
1. F. Wilczek, *Phys. Rev. Lett.* **109**, 160401 (2012).
2. P. Bruno, *Phys. Rev. Lett.* **111**, 070402 (2013).
3. K. Sacha, J. Zakrzewski, *Rep. Prog. Phys.* **81**, 016401 (2018).
4. D. V. Else, C. Monroe, C. Nayak, N. Y. Yao, *Annu. Rev. Condens. Matter Phys.* **11**, 467–499 (2020).
5. H. Keßler *et al.*, *Phys. Rev. Lett.* **127**, 043602 (2021).
6. S. Autti, V. B. Eltsov, G. E. Volovik, *Phys. Rev. Lett.* **120**, 215301 (2018).
7. S. Autti *et al.*, *Nat. Mater.* **20**, 171–174 (2021).
8. J. Zhang *et al.*, *Nature* **543**, 217–220 (2017).
9. H. Taheri, A. B. Matsko, L. Maleki, K. Sacha, *Nat. Commun.* **13**, 848 (2022).
10. P. Frey, S. Rachel, *Sci. Adv.* **8**, eabm7652 (2022).
11. Z. Gong, R. Hamazaki, M. Ueda, *Phys. Rev. Lett.* **120**, 040404 (2018).
12. F. Iemini *et al.*, *Phys. Rev. Lett.* **121**, 035301 (2018).
13. K. Tucker *et al.*, *New J. Phys.* **20**, 123003 (2018).
14. B. Zhu, J. Marino, N. Y. Yao, M. D. Lukin, E. A. Demler, *New J. Phys.* **21**, 073028 (2019).
15. B. Buča, J. Tindall, D. Jaksch, *Nat. Commun.* **10**, 1730 (2019).
16. A. Lazarides, S. Roy, F. Piazza, R. Moessner, *Phys. Rev. Res.* **2**, 022002 (2020).

17. H. Keßler, J. G. Cosme, M. Hemmerling, L. Mathey, A. Hemmerich, *Phys. Rev. A* **99**, 053605 (2019).
18. P. Kongkhambut *et al.*, *Science* **377**, 670–673 (2022).
19. A. V. Nalitov *et al.*, *Phys. Rev. A* **99**, 033830 (2019).
20. M. J. Hartmann, F. G. Brandao, M. B. Plenio, *Nat. Phys.* **2**, 849–855 (2006).
21. A. Amo *et al.*, *Nature* **457**, 291–295 (2009).
22. I. Carusotto, C. Ciuti, *Rev. Mod. Phys.* **85**, 299–366 (2013).
23. J. Kasprzak *et al.*, *Nature* **443**, 409–414 (2006).
24. A. Fainstein, N. D. Lanzillotti-Kimura, B. Jusserand, B. Perrin, *Phys. Rev. Lett.* **110**, 037403 (2013).
25. P. V. Santos, A. Fainstein, *Opt. Mater. Express* **13**, 1974 (2023).
26. D. L. Chafatinos *et al.*, *Nat. Commun.* **11**, 4552 (2020).
27. A. A. Reynoso *et al.*, *Phys. Rev. B* **105**, 195310 (2022).
28. K. Winkler *et al.*, *New J. Phys.* **17**, 023001 (2015).
29. A. S. Kuznetsov, P. L. J. Helgers, K. Biermann, P. V. Santos, *Phys. Rev. B* **97**, 195309 (2018).
30. Materials and methods, a detailed description of the theoretical model and simulations, some additional experiments showing continuous time crystalline behavior, experimental evidence of the presence of dissipative coupling, and the demonstration of discrete time crystalline behavior with pulsed laser excitation are available as supplementary materials.
31. I. A. Shelykh, A. V. Kavokin, G. Malpuech, *Phys. Status Solidi, B Basic Res.* **242**, 2271–2289 (2005).
32. H. Ohadi *et al.*, *Phys. Rev. X* **5**, 031002 (2015).
33. I. Gnusov *et al.*, *Phys. Rev. B* **102**, 125419 (2020).
34. H. Sigurdsson, *Phys. Rev. Res.* **2**, 023323 (2020).
35. K. Rayanov, B. L. Altshuler, Y. G. Rubo, S. Flach, *Phys. Rev. Lett.* **114**, 193901 (2015).
36. M. Wouters, *Phys. Rev. B Condens. Matter Mater. Phys.* **77**, 121302 (2008).
37. L. Zhang *et al.*, *Proc. Natl. Acad. Sci. U.S.A.* **112**, E1516–E1519 (2015).
38. I. L. Aleiner, B. L. Altshuler, Y. G. Rubo, *Phys. Rev. B Condens. Matter Mater. Phys.* **85**, 121301 (2012).
39. P. Sesin *et al.*, *Phys. Rev. Res.* **5**, L042035 (2023).
40. M. Aspelmeyer, T. J. Kippenberg, F. Marquardt, *Rev. Mod. Phys.* **86**, 1391–1452 (2014).
41. I. Chestnov, Y. G. Rubo, A. Nalitov, A. Kavokin, *Phys. Rev. Res.* **3**, 033187 (2021).
42. D. Read, T. C. H. Liew, Y. G. Rubo, A. V. Kavokin, *Phys. Rev. B Condens. Matter Mater. Phys.* **80**, 195309 (2009).
43. P. Hamel *et al.*, *Nat. Photonics* **4**, 311–315 (2015).
44. H. Sigurdsson *et al.*, *Phys. Rev. B* **96**, 155403 (2017).
45. H. Sigurdsson *et al.*, *Phys. Rev. Lett.* **129**, 155301 (2022).
46. R. Ruiz-Sánchez, R. Rechtman, Y. G. Rubo, *Phys. Rev. B* **101**, 155305 (2020).
47. A. S. Kuznetsov, D. H. O. Machado, K. Biermann, P. V. Santos, *Phys. Rev. X* **11**, 021020 (2021).
48. N. D. Lanzillotti-Kimura *et al.*, *Phys. Rev. Lett.* **99**, 217405 (2007).
49. S. Walter, F. Marquardt, *New J. Phys.* **18**, 113029 (2016).
50. Y. Xue *et al.*, *Phys. Rev. Res.* **3**, 013099 (2021).
51. J. Barrat *et al.*, Qubit analog with polariton superfluid in an annular trap. arXiv:2308.05555 [cond-mat.quant-gas] (2023).

NANOMATERIALS

Molecular templating of layered halide perovskite nanowires

Wenhao Shao[1]†, Jeong Hui Kim[1]†, Jeffrey Simon[2], Zhichen Nian[1], Sung-Doo Baek[1], Yuan Lu[3], Colton B. Fruhling[2], Hanjun Yang[1,4], Kang Wang[1,5], Jee Yung Park[1], Libai Huang[4], Yi Yu[3], Alexandra Boltasseva[2,6], Brett M. Savoie[1], Vladimir M. Shalaev[2,6], Letian Dou[1,4,6]*

Layered metal-halide perovskites, or two-dimensional perovskites, can be synthesized in solution, and their optical and electronic properties can be tuned by changing their composition. We report a molecular templating method that restricted crystal growth along all crystallographic directions except for [110] and promoted one-dimensional growth. Our approach is widely applicable to synthesize a range of high-quality layered perovskite nanowires with large aspect ratios and tunable organic-inorganic chemical compositions. These nanowires form exceptionally well-defined and flexible cavities that exhibited a wide range of unusual optical properties beyond those of conventional perovskite nanowires. We observed anisotropic emission polarization, low-loss waveguiding (below 3 decibels per millimeter), and efficient low-threshold light amplification (below 20 microjoules per square centimeter).

L ayered metal-halide perovskites, or two-dimensional (2D) perovskites, can be synthesized in solution, and their optical and electronic properties can be tuned by changing their composition (*1*). Growth of 1D forms of these materials has been limited to vapor-phase growth (*2, 3*) of $(BA)_2PbI_4$, where BA is butylammonium, or to lithographically templated solution-phase growth of $(BA)_2(MA)_{n-1}Pb_nI_{3n+1}$, where MA is methylammonium and the layer number n is 2 to 5 (*4, 5*). These methods have high processing complexity and cost as well as limited scalability and design flexibility. Notably, the structure of layered perovskites has inspired the use of bulky organic spacers with engineered bandgaps (*6, 7*) and intermolecular π interactions (*8*). We have found organic templating molecules that can break the in-plane symmetry of layered perovskites and

[1]Davidson School of Chemical Engineering, Purdue University, West Lafayette, IN 47907, USA. [2]Elmore Family School of Electrical and Computer Engineering, Purdue University, West Lafayette, IN 47907, USA. [3]School of Physical Science and Technology and Shanghai Key Laboratory of High-resolution Electron Microscopy, ShanghaiTech University, Shanghai 201210, China. [4]Department of Chemistry, Purdue University, West Lafayette, IN 47907, USA. [5]Key Laboratory of Photochemistry, Institute of Chemistry, Chinese Academy of Sciences, Beijing 100190, China. [6]Birck Nanotechnology Center, Purdue University, West Lafayette, IN 47907, USA.
*Corresponding author. Email: dou10@purdue.edu
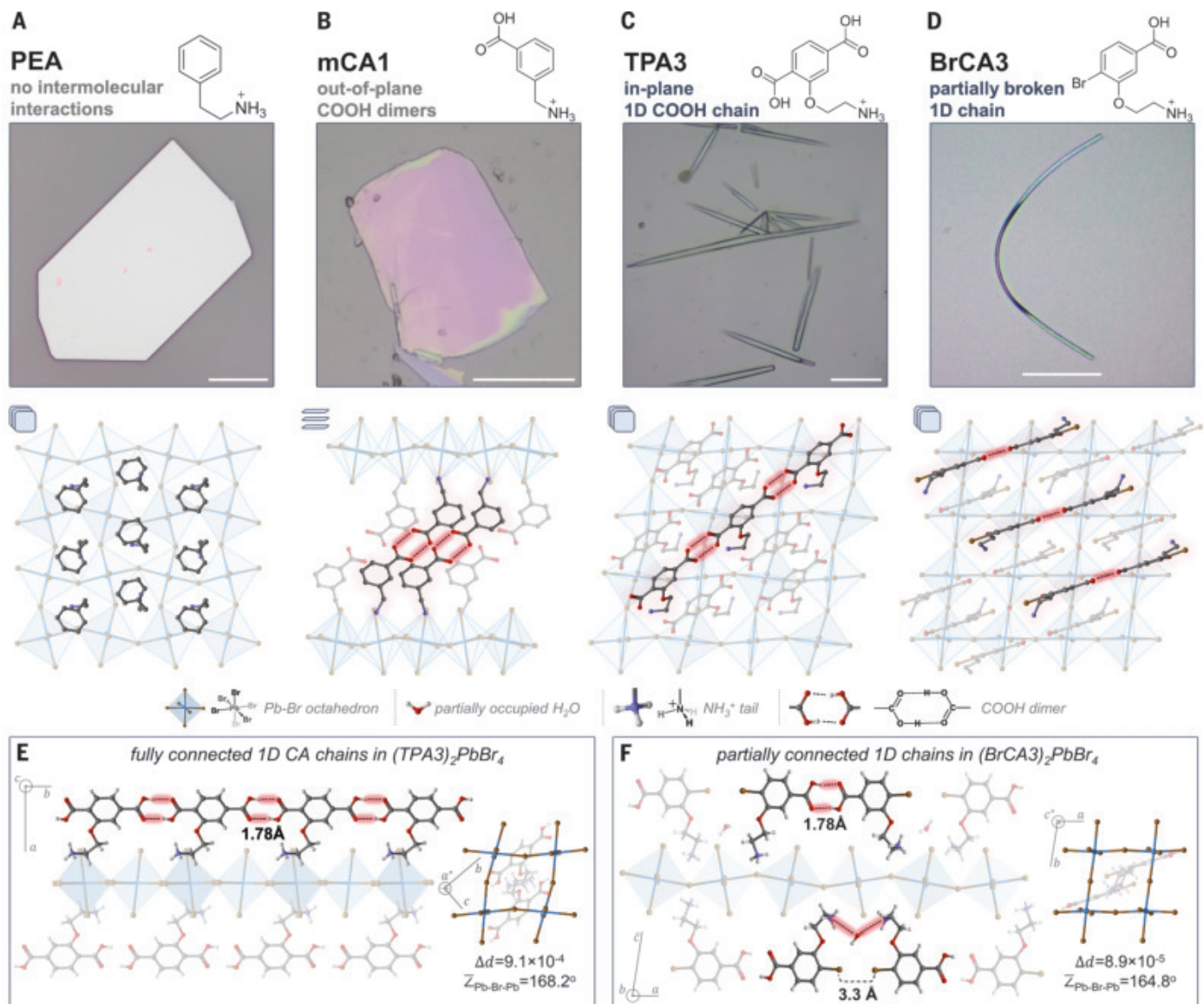†These contributed equally to this work.

induce 1D growth through secondary bonding interactions. Specifically, these molecules introduce in-plane hydrogen bonding that is compatible with both the ionic nature and octahedron spacing of halide perovskites. Nanowires of layered perovskites can be readily assembled in solution facilitated by the formation of a 1D H-bonded organic network. These nanowires with tailorable lengths and high-quality cavities provide an ideal platform to study anisotropic excitonic behaviors, light propagation, and lasing in layered perovskites. Our approach highlights the structural tunability of organic-inorganic hybrid semiconductors, which also brings unprecedented morphological control to layered materials.

In-plane unidirectional H bonding

Organic spacers for layered perovskites typically impose weak long-range order. For example, an out-of-plane view along the stacking direction of $(PEA)_2PbBr_4$, where PEA is phenyl-ethylammonium, shows weak intermolecular interactions in the organic layer (Fig. 1A). To align the cations, carboxylic acid (COOH) was chosen to dimerize through multiple H bonds, which have strong directionality and are widely used to drive the self-assembly and alignment of organic building blocks (*9*). Derivatizing PEA with COOH to the 3-position of the phenyl ring resulted in the out-of-plane formation of classic COOH dimers across the van der Waals gap

Fig. 1. A comparison among the morphology and crystal structures of layered [PbBr₄]²⁻ perovskites based on various organic cations. (A) PEA, phenylethylammonium. (B) mCA1, (3-carboxyphenyl)methanaminium. (C) TPA3, 2-(2,5-dicarboxyphenoxy)ethan-1-aminium. (D) BrCA3, 2-(2-bromo-5-carboxyphenoxy)ethan-1-aminium. The middle panels show the morphology of each crystal obtained with the floating growth method under a bright-field optical microscope (scale bars, 20 μm). Bottom panels highlight the alignment of cations viewed along stacking directions, except in $(mCA1)_2PbBr_4$, which was viewed perpendicular to the stacking direction because of the out-of-plane COOH dimers. H atoms are omitted for clarity. (E and F) Examinations of the 1D H-bonding chains in $(TPA3)_2PbBr_4$ (E) and $(BrCA3)_2PbBr_4$ (F) along with illustrations of octahedral distortion and lattice tilting, characterized by Pb-Br bond distance variation (Δd) and average Pb-Br-Pb angle ($\overline{\angle}_{Pb-Br-Pb}$), respectively. Despite similar $\overline{\angle}_{Pb-Br-Pb}$, Δd was reduced by an order of magnitude in $(BrCA3)_2PbBr_4$. Room-temperature crystal structures were used throughout this article, and all illustrations are based on actual crystal structures.

(Fig. 1B), as previously observed in 2D perovskites (*10*). However, this out-of-plane directionality did not alter the in-plane growth of layered perovskite crystals, and only 2D nanostructures were obtained.

To direct 1D growth, we first attempted to align the H bonds parallel to inorganic slabs. An additional COOH unit was introduced in the para position of the existing moiety to form a backbone resembling terephthalic acid (TPA), that we named TPA3 [2-(2,5-dicarboxyphenoxy)ethan-1-aminium; Fig. 1C]. The crystal structure of $(TPA3)_2PbBr_4$ revealed well-aligned, parallel 1D chains of TPA3 on top of 2D inorganic slabs driven by unidirectional intermolecular interactions (Fig. 1, C and E). Adjacent TPA moieties were connected along the [010] crystallographic direction with a spacing of 9.54 Å characterized by the aromatic centroid distance. Each 1D chain consisted of periodic COOH dimers with an average H-bonding distance of 1.78 Å.

This unidirectional in-plane connectivity in the organic layer led to the solution-phase self-assembly of layered perovskites exclusively into needles and wires (Fig. 1C and fig. S1). These 1D crystals had a mean aspect ratio as large as 28.9 (fig. S2). However, the TPA3-based structures exhibited several unsatisfactory morphological and optical properties. Growing high-quality crystals (fig. S3, A and B) required a very slow self-assembly process because fast growth usually led to poorly defined end facets (Fig. 1C and fig. S3, D to H) or even hyperbranched crystals, as observed in the case of $(TPA3)_2PbI_4$ (fig. S4, A and B, and movie S1). Negligible excitonic features were observed even from photoluminescence (PL) of
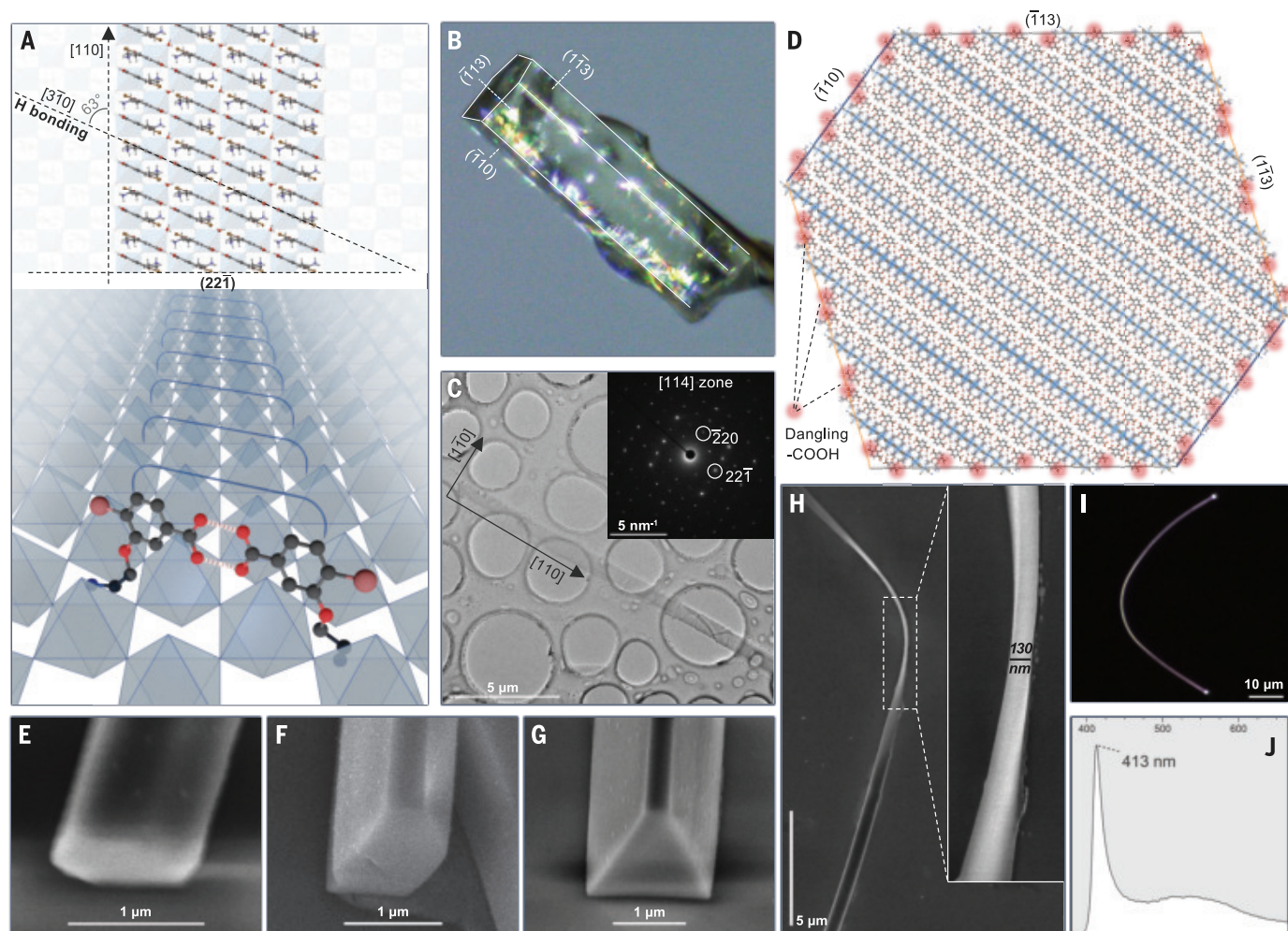
Fig. 2. Growth mechanism of 2D perovskite nanowires illustrated with (BrCA3)$_2$PbBr$_4$ and morphological and optical properties. (**A**) Stacking plane cross-sectional view. The 3D model (below) intuitively illustrates the molecular templating effect, involving pairs of BrCA3 dimers sitting on an inorganic slab. (**B**) A hexagonal cylindrical bulk crystal with side facets indexed as ($\bar{1}$10), ($\bar{1}$13), and (1$\bar{1}$3) by SC-XRD and their Friedel pairs. More examples are shown in fig. S8. (**C**) TEM images of a nanowire and its SAED pattern (inset) viewed along zone axis [114] showing the growth along [110]. (**D**) Cross-sectional view of the (22$\bar{1}$) end facet along [110]. The three pairs of facets indexed in (B) are marked. Red clouds represent the surface dangling COOH. All six facets exhibit pronounced coverage and protection by COOH. (**E** to **G**) Nanowire end facet morphology under scanning electron microscopy (SEM). (**H**) A 180°-twisted nanoribbon under SEM. (**I** and **J**) PL image (I) and spectrum (J) of the twisted nanowire presented in Fig. 1D, showing white emission.

slow-assembled (TPA3)$_2$PbBr$_4$ single crystals. The emission was dominated by a broad band that we attributed to self-trapped excitons or in-gap defect states (fig. S3, B and C) (*11*). The iodide counterpart instead presented broad excitonic emission (fig. S4, C to E). We hypothesized that strong H bonds disrupted the assembly of ionic species and led to extensive defect formation during crystal growth that drove hyperbranching. Considerable octahedral distortion was observed in (TPA3)$_2$PbBr$_4$ (characterized by the Pb-Br bond distance variation, $\Delta d = 9.1 \times 10^{-4}$; Fig. 1E) that was associated with quenched excitonic feature and broadband emission (*12*).

Partially broken 1D chains

To balance secondary bonding with ionic assembly, we partially disrupted the 1D H-bonding network by substituting one COOH unit in the TPA backbone with bromine, which prevented COOH dimers from twisting back to form out-of-plane H bonds. This candidate, BrCA3 [2-(2-bromo-5-carboxyphenoxy)ethan-1-aminium] maintained a similar in-plane connectivity but formed parallelly aligned "partially broken" 1D chains above inorganic slabs (Fig. 1D), which were parallel to the [3$\bar{1}$0] direction but deviated from the stacking directions of the octahedrons. Octahedral distortions were reduced by an order of magnitude ($\Delta d = 8.9 \times 10^{-5}$), presumably from the relief of stress in the H-bonded network. Each chain was constructed by pairs of BrCA3 through COOH dimerization with the same spacing and H-bonding distance as those in the TPA3 counterpart. Adjacent molecules were well separated at the

bromine terminal, with an intermolecular Br-Br spacing of 3.30 Å (Fig. 1F), and allowed the occupation of water molecules stabilized through H bonding with ammonium tails. Given the hygroscopic nature of halide perovskites, this partial occupancy of water is rather unusual.

The partially broken 1D connectivity introduced by BrCA3 promoted balanced and rapid 1D self-assembly of layered perovskites. Crystal growth was further accelerated at the droplet-air interface to produce high-quality nanowires. This floating growth method was originally developed (*13*) for capturing thin 2D sheets of layered perovskites and subsequent transfer preserving pristine morphology (materials and methods). The nucleation and 1D growth of (BrCA3)$_2$PbBr$_4$ were studied with in situ microscopy (movie S2) revealing a growth rate
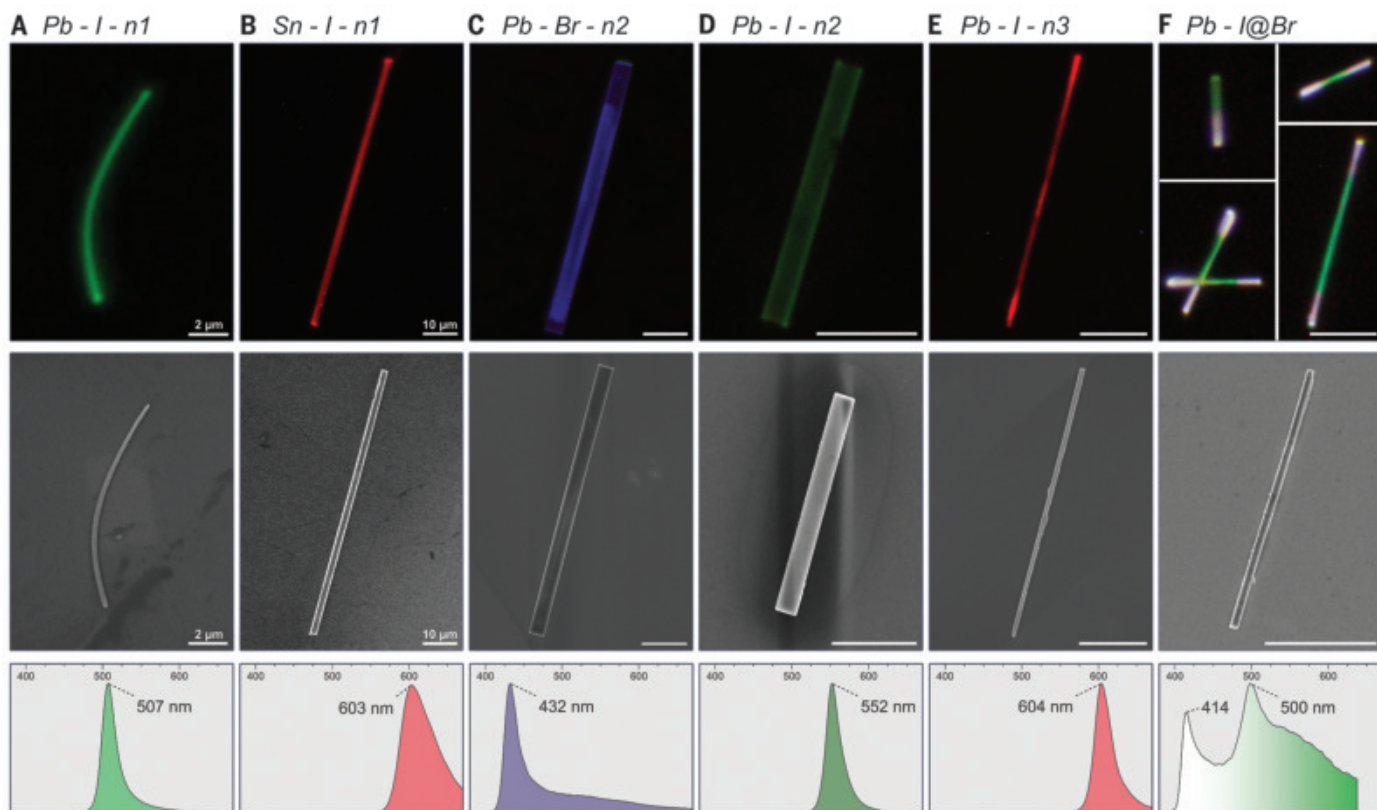
Fig. 3. The expanded library of layered 2D and quasi-2D perovskite nanowires. (**A**) (BrCA3)$_2$PbI$_4$. (**B**) (BrCA3)$_2$SnI$_4$. (**C**) (BrCA3)$_2$MAPb$_2$Br$_7$ (n = 2). (**D**) (BrCA3)$_2$MAPb$_2$I$_7$ (n = 2). (**E**) (BrCA3)$_2$MA$_2$Pb$_3$I$_{10}$ (n = 3). PL images (top), SEM images (middle), and PL spectra (bottom) of each candidate are included. (**F**) Longitudinal epitaxial heterostructures grown with the (BrCA3)$_2$PbI$_4$ core and bromide shell. The SEM image (middle) shows negligible trace of core-shell interfaces, in contrast to the easily distinguishable Br-I interface from the PL images above. Scale bars, 2 μm in (A) and 10 μm in (B) to (F).

that was ~40 times as fast along the long axis compared with the short (fig. S5). Nanowires of (BrCA3)$_2$PbBr$_4$ exhibited a mean length, width, and height of 8.45 μm, 409 nm, and 361 nm, respectively, and maintained a mean aspect ratio of 22.0 (fig. S6). A characteristic nanowire shown in Fig. 1D had an exceptional aspect ratio of >100 (~80 μm long and ~0.7 μm wide), well-defined end facets, and a twisted morphology. The solution-phase synthesis additionally allowed easy scaling-up, cleaning, and surface coating of nanowires with dense and uniform coverage (materials and methods and fig. S7).

Growth mechanism studies

Although the formation of 2D perovskite nanowires appeared to depend on the inherent 1D connectivity within the organic layer, additional studies were needed to determine whether their growth direction followed the H-bond direction of COOH dimers. We used single-crystal x-ray diffraction (SC-XRD) and selected-area electron diffraction (SAED) to face-index bulk crystals and nanowires of (BrCA3)$_2$PbBr$_4$, respectively (Fig. 2, A to C, and fig. S8). The long axis of each crystal was aligned with its [110] crystallographic direction and the short axis with [1$\bar{1}$0], both matching the octahedron stacking

direction. However, the COOH dimers (along [3$\bar{1}$0]) were at an angle of 63° relative to the [110] long axis, and the dimer orientation in the TPA3 counterpart was perpendicular to its long axis (fig. S9). These findings contradicted our initial intuitive hypothesis that nanowires would grow along the directional H bonds.

Instead, the COOH dimers hindered rather than facilitated the growth of layered perovskites. Alignment of cations correlated with the distinct exposure of COOH moieties at the side versus the end facets (here, side facets refer to all of the facets parallel to the long axis), as shown in Fig. 2D for the (22$\bar{1}$) end facet when viewed along the [110] growth direction. Six side facets were subsequently indexed as (1$\bar{1}$0), (1$\bar{1}$3), (1$\bar{1}$3), and their Friedel pairs according to the hexagonal cylindrical crystal previously investigated with SC-XRD (Fig. 2B and fig. S8A). Dangling COOH moieties were abundant on all six side facets (Fig. 2D) because of the near-perpendicular H-bond alignment with the long axis, [110]. Notably absent was the (001) facet parallel to the [PbBr$_4$]$^{2-}$ slabs, which was typically observed in conventional 2D perovskites but instead subdivided into (1$\bar{1}$3) and (1$\bar{1}$3), which further enhanced the surface exposure of COOH.

These findings suggested that surface dangling carboxylic acids would slow down crystal growth and lead to the preferred exposure of COOH-abundant surfaces. In previously reported polymer-assisted synthesis of oxide perovskite Pb(Zr/Ti)O$_3$ nanowires (*14*), the polymer was hypothesized to reduce the surface tension of certain crystallographic planes. Nanowire growth was thus driven by the coverage of high-energy exposed surfaces and left them as end facets. In our system, surface dangling carboxylic acids protected nanowire side facets by forming robust H bonds with water, and incoming cations must break the existing solvent shield. In fact, water was an essential solvent for 1D growth: Crystals randomly nucleated and clustered in nonaqueous media even within protic alcohols (fig. S10). Water passivation lowered the surface energy of COOH-abundant facets, but such an effect became particularly weak at the (22$\bar{1}$) end. As illustrated in fig. S11, the (1$\bar{1}$0) side facets were uniformly covered with dangling COOH moieties, whereas the density was nearly halved at (22$\bar{1}$), which was insufficient to protect it from incoming cations. Surface energies of notable facets calculated with density functional theory (DFT) revealed considerable

anisotropy after addressing the effects from water passivation, leading to higher surface energy at the $(22\bar{1})$ facet (fig. S11, F and G).

Thus, the molecular templating effect of in-plane COOH dimers aligned organic cations and drove the anisotropic surface termination of dangling COOH moieties that protected these surfaces through robust H bonding with aqueous solvent molecules. The discussions spanning crystal nucleation, molecular and unit cell level, nanowire morphology, and bulk crystals were integrated in fig. S12 and supplementary text 1. In particular, this mechanism points to the crucial alignment of H bonds with the growth direction (90° in TPA3 and 63° in BrCA3-templated counterparts), which affected the relative abundance of dangling COOH on side versus end facets and therefore the effect of 1D growth. A perfect perpendicular alignment in $(TPA3)_2PbBr_4$ led to rapid 1D growth but poor cavities in nanocrystals, whereas the seemingly imperfect

H-bond alignment in $(BrCA3)_2PbBr_4$ presented a well-balanced crystal growth and nanowires with excellent cavities.

Nanowires of $(BrCA3)_2PbBr_4$ displayed diverse morphologies that were commonly observed with hexagonal or acute trapezoidal end facets (Fig. 2, E to G). The interplay among side facets could lead to distinct termination morphology even within a single nanowire (fig. S13A). These intricate morphological features likely stem from the surface modification with dangling COOH, so a range of low-energy facets were exposed. Notably, narrow and thin crystals (~30 nm) also exhibited smooth terminations (fig. S13B). They easily bend or twist; Fig. 2G shows 180° twisting of a nanoribbon. High-resolution transmission electron microscopy (TEM) provided additional structural characterizations despite the high sensitivity of 2D perovskite nanowires to electron beam damage (fig. S14). Optically, $(BrCA3)_2PbBr_4$ exhibited white PL at room temperature with a sharp ex-

citonic peak at 413 nm and lower-energy broad emission band (Fig. 2, I and J). The PL characteristics were unaffected by bending or twisting.

An expanded library of layered perovskite nanowires

We used the BrCA3 spacer to synthesize a wide range of layered perovskites. For example, BrCA3-based nanowires with $[PbI_4]^{2-}$ and $[SnI_4]^{2-}$ matrices were readily obtained (Fig. 3, A and B). These candidates exhibited better stability against ambience, heat, and light compared with PEA-based structures (figs. S15 to S17). High aspect ratios were generally achievable in quasi-2D perovskites, such as $n = 2$ $(BrCA3)_2MAPb_2Br_7$ (Fig. 3C) and $n = 2$ and $n = 3$ in lead-iodide counterparts (Fig. 3, D and E). Epitaxial growth of these nanowires originated from their end facets. Representative diblock or triblock longitudinal heterostructures obtained with deliberate fast nucleation of $(BrCA3)_2PbBr_4$ on the as-grown iodide cores (materials and methods) had interfaces between the core and shell that were morphologically indiscernible (Fig. 3F), but the longitudinal extension of bromide segments could be distinguished by its distinctive white PL. Coaxial growth around the side facets of iodide cores remained negligible because dangling COOH groups on each side facet shielded as-grown crystals against the coaxial nucleation of additional layers. Enhanced core and shell resolution was further achieved through selectively exciting bromide or iodide sections (fig. S18, A to E). In contrast to those synthesized with 3D halide perovskites with a gradient ion distribution (15), nanowire heterostructures based on layered perovskites had enhanced stability against halide migration that preserved Br-I interface contrast (fig. S18F).

The use of partially broken 1D H-bonded chain was expanded by substituting bromide groups in BrCA3 with fluoride or methyl groups. These derivatives also enabled 1D growth of layered perovskite nanowires (fig. S19). Optically, compared with $(BrCA3)_2PbBr_4$, the emission was yellowish green for the methyl analog but bluish white for the fluoride analog. Although broadband emission reduced the color purity, it also facilitated color tunability in layered perovskite nanowires with subtle variation of organic spacers.

Unusual optical properties

Morphologically restricting the growth of layered perovskites into 1D nanowires led to distinctive optical properties along, perpendicular, or both to the stacking direction of these layered structures. Emission typically displayed weak linear polarization [degree of polarization (DOP) < 3%] with propagation direction approximately along their long axes (fig. S20), which we attributed to the anisotropic confinement of electric field within high–aspect
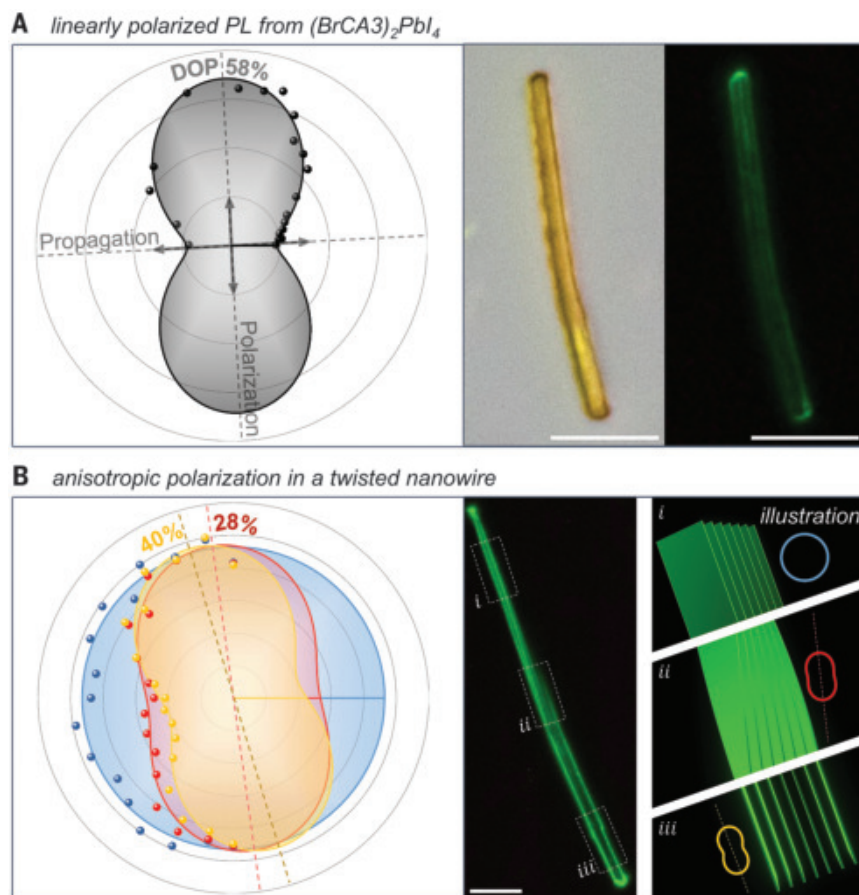
Fig. 4. Anisotropic emission polarization. (A) Linearly polarized PL detected from a nanowire of $(BrCA3)_2PbI_4$ with a high DOP of 58% and PL propagated almost perpendicular to the long axis. **(B)** The mechanism was revealed from a twisted nanowire showing strong emission polarization only when viewed perpendicular to its stacking direction (bottom). This twisted crystal is modeled on the right, where the blue circle and the red and yellow peanut shapes are exact extracts from the polar graph (left), showing the varying polarization profile along the twisting action with a DOP of 28% (red, section ii) and 40% (yellow, section iii). Scale bars, 10 μm.
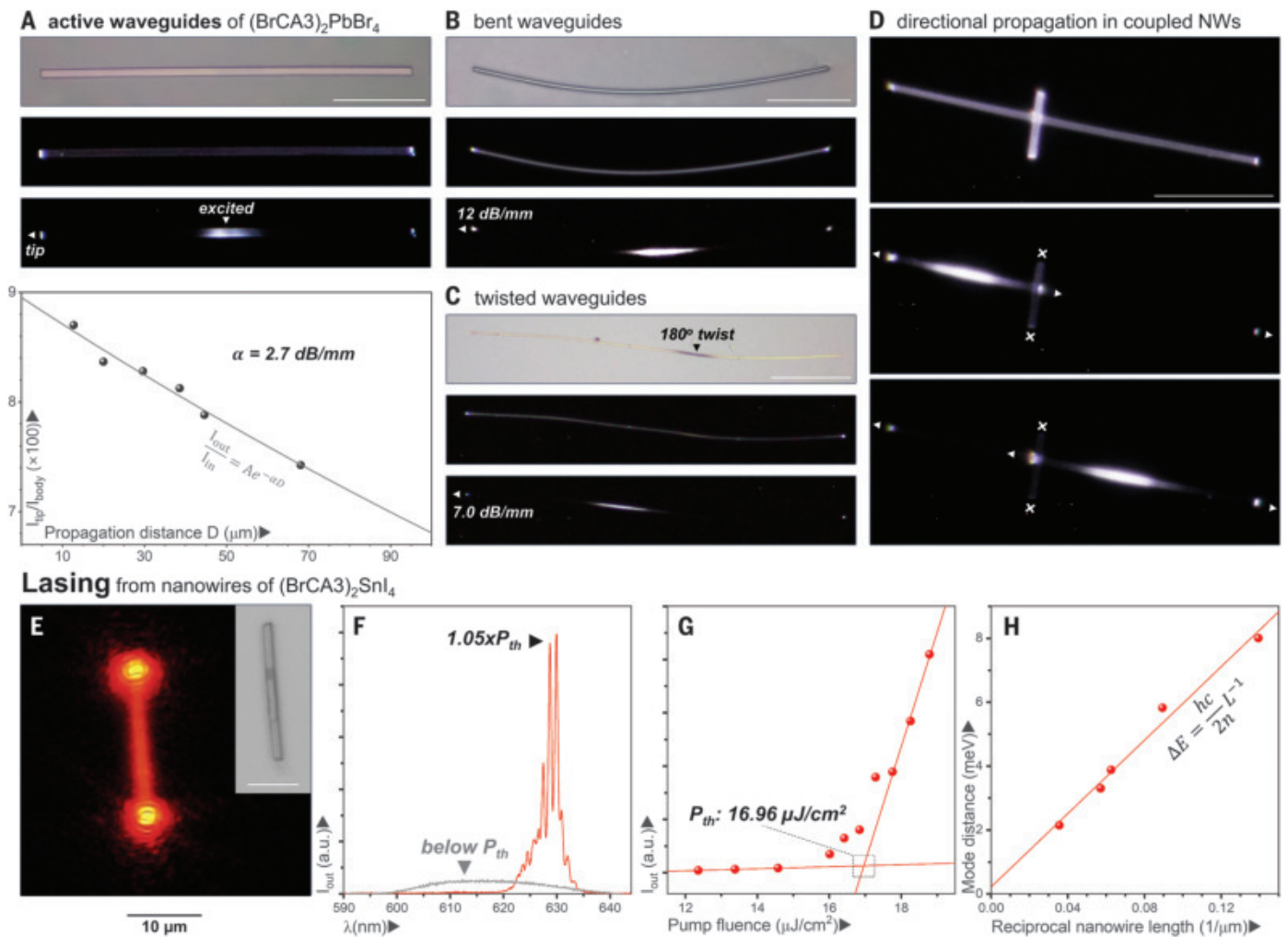
Fig. 5. Waveguiding and lasing. (**A**) Intrinsic loss coefficients measured from a straight nanowire of $(BrCA3)_2PbBr_4$ and extracted from the plot (bottom) of propagation distance–dependent relative tip emission intensity. (**B** and **C**) Bent (B) and twisted (C) nanowires were examined, showing low loss coefficients as well. (**D**) A pair of cross-coupled nanowires (NWs) excited at the horizontal waveguide from left or right of the intersection. (**E**) A representative nanowire of $(BrCA3)_2SnI_4$ pumped above the threshold at 88 K, showing majority emission from the two end facets with coherent interference patterns. (Inset) Grayscale brightfield image. (**F**) Emission spectra of the stimulated lasing (red) versus the spontaneous emission (gray). a.u., arbitrary units. (**G**) Threshold response examined from integrated outcoupled emission plotted against the pump fluence. (**H**) Mode distance against the reciprocal nanowire length examined from a series of lasing nanowires, which was fitted according to Fabry-Perot modes. Scale bars, 20 μm.

ratio nanostructures (*16*). However, a 58% DOP was observed from a representative candidate of $(BrCA3)_2PbI_4$ (Fig. 4A), where the emission propagated almost perpendicular to its long axis, in contradiction with our previous observations.

Layered perovskites exhibited intrinsic emission polarization caused by the in-plane confinement of excitons (*17*). Such a phenomenon is challenging to observe in 2D plates when viewed along the stacking direction in a typical epidetection setup, whereas nanowires offer accessibility to their side facets. Therefore, when viewing perpendicular to the stacking direction, strong linearly polarized PL was revealed that propagated perpendicular to the long axes, which could explain the observation in Fig. 4A.

We examined a piece of twisted $(BrCA3)_2PbI_4$ nanowire to resolve the origin of its polariza-

tion dependence (Fig. 4B). Twisting allowed the observation of both in-plane and out-of-plane optical properties within a single nanowire. As illustrated subsequently, inorganic slabs were originally stacked parallel to the substrate on the top of the image, and then crystal gradually twisted to allow the view perpendicular to its stacking direction. The twisting action allowed the observation of diverse polarization profile within the same crystal, which was further quantified and spatially resolved. Emission polarization was negligible at the top, but the crystal gradually exhibited linearly polarized emission with slowly rotated polarization direction along the twisting action, resulting in a DOP of 40% at the bottom. This demonstration of twist-dependent tunable emission polarization from a single

semiconductor nanowire arose from the combination of layered crystal structure, 1D growth kinetics, and the twisted morphology.

Nanowires of layered perovskites are candidates for active waveguides given their tailorable length, emission tunability, and flexibility. Waveguide losses were assessed from several ~100-μm-long wires of $(BrCA3)_2PbBr_4$ according to their propagation distance–dependent relative tip emission intensity collected and analyzed with far-field PL images (materials and methods). Nanowires of $(BrCA3)_2PbBr_4$ exhibited intrinsic loss coefficients as low as 2.7 dB/mm, as observed in straight samples (Fig. 5A). Best-performing contemporary inorganic (*18*, *19*) and organic (*20*) semiconductor waveguides typically exhibit losses within 10 dB/mm. Narrow and bent nanowires (Fig. 5B),

or even strongly twisted ones (Fig. 5C), had similar losses to those of wide and straight waveguides as they remained crystalline after bending or twisting.

Waveguides could be coupled to transport light to adjacent crystals and create a complex optical network (*18*). A few coupled nanowires were examined through tip-tip interactions or cross-intersections (Fig. 5D and fig. S21), demonstrating proof-of-concept potentials to construct more-complex optical networks. Directional propagation of light within 1D nanowires was necessary to ensure efficient coupling of waveguides. Figure 5D shows a perpendicular pair of cross-coupled waveguides that formed multiple scattering sites. Because of the 1D propagation of light, only the right end of the intersection could be illuminated when excitation light was injected from the left side of the intersection, and vice versa. Minimal outcoupled light was detected from the vertical nanowire when the horizontal crystal was excited.

Building on previous studies of semiconductor nanowire lasers (*21*) and lasing in 3D halide perovskites (*22, 23*), we investigated the light amplification behavior of BrCA3-based nanowires. In lead-based layered perovskites, the lasing threshold is often constrained by the strong exciton-phonon interaction or Auger recombination (*7*). Enhanced lasing performances have been pursued in quasi-2D systems (*24, 25*). Tin-based 2D perovskites may exhibit lasing performances surpassing those of their lead counterparts, as has been shown in recent studies (*26*). However, their lasing thresholds are still in the ~100-μJ/cm^2 regime with substantial sample-to-sample variation; both limitations arise from the lack of a well-established cavity. Temperature-dependent and time-resolved PL studies comparing $(BrCA3)_2SnI_4$ and $(BrCA3)_2PbI_4$ revealed higher exciton-phonon coupling and contribution from self-trapped excitons or defect states in the lead counterpart (figs. S22 and S23), both of which are not conducive to efficient lasing.

Emission from the two end facets in nanowires of $(BrCA3)_2SnI_4$ gradually became dominant with increasing pump fluence (fig. S24) and was accompanied by the appearance of spatial interference patterns (Fig. 5E) and multimode lasing at the lower-energy side of the spontaneous emission band (Fig. 5F). We monitored the integrated emission intensity across the threshold to determine a lasing threshold of 17 μJ/cm^2 (Fig. 5G) versus that of ~100 μJ/cm^2 observed in contemporary tin-based layered perovskites. The bright localized emission from the tips and multimode lasing from this ~16.0-μm-long nanowire were both consistent from the strong waveguiding behavior under Fabry-Perot modes. Mode spacing (ΔE) from a series of nanowires with varying lengths (L) decreased with L and followed a linear trend

with the reciprocal nanowire length ($1/L$), confirming the Fabry-Perot cavity characteristics (Fig. 5H and fig. S25).

Discussion

The method to manipulate the morphology of layered perovskites by introducing robust intermolecular interactions between organic spacers is distinctive to the special crystal structures of organic-inorganic hybrid materials and requires more comprehensive investigations. In our implementation, the COOH dimer was originally exploited to enforce 1D connectivity within the organic layer. Unexpectedly, this directionality was transferred to the assembled system. Through a thorough examination, the molecular templating effect was elucidated as aligning spacers using in-plane directional H bonds, which further drove the anisotropic surface termination of dangling COOH that protected these facets through robust H bonds with aqueous solvent molecules. Subsequently, balanced growth conditions and high-quality nanowires were achieved through subtle yet crucial manipulation over the alignment of H bonds with respect to growth direction. 2D perovskite nanowires based on BrCA3 incited a range of unusual optical properties. The intrinsic excitonic nature of layered halide perovskites enabled facile observation and control of polarized emission. These nanowires also revealed exceptional cavity qualities, which could be used as active waveguides with low propagation loss coefficients and to facilitate light amplification with low thresholds compared with other systems.

Morphological control with directional supramolecular synthons proves to be a generally applicable strategy for various layered perovskite structures and diverse organic spacers. However, its merit extends to a broad range of organic-inorganic hybrid materials. Particularly, the selection of functional groups and intermolecular interactions to be incorporated within the organic layer transcends far beyond COOH dimers and the H-bonding network. For example, π interactions (π-π, π-p, or σ-π), electrostatic forces, and even chirality could also be readily implemented (*8*). Further explorations in this regard will introduce enhanced versatility in these hybrid layered materials as the next-generation semiconductors, where the collective benefits of conventional organic and inorganic counterparts readily converge.

REFERENCES AND NOTES

1. B. Saparov, D. B. Mitzi, *Chem. Rev.* **116**, 4558–4596 (2016).
2. D. Ghoshal et al., *Adv. Opt. Mater.* **7**, 1900039 (2019).
3. P. Yadav et al., *Chem. Mater.* **35**, 3300–3306 (2023).
4. Y. Zhao et al., *J. Am. Chem. Soc.* **143**, 8437–8445 (2021).
5. J. Feng et al., *Nat. Electron.* **1**, 404–410 (2018).
6. Y. Gao et al., *Nat. Chem.* **11**, 1151–1157 (2019).
7. W. Shao, S. Yang, K. Wang, L. Dou, *J. Phys. Chem. Lett.* **14**, 2034–2046 (2023).
8. L. Yan, C. J. Gloor, A. M. Moran, W. You, *Appl. Phys. Lett.* **122**, 240501 (2023).
9. G. R. Desiraju, *Angew. Chem. Int. Ed.* **34**, 2311–2327 (1995).
10. M. B. AlShammari et al., *Chem. Phys. Lett.* **702**, 8–15 (2018).
11. S. Kahmann, E. K. Tekelenburg, H. Duim, M. E. Kamminga, M. A. Loi, *Nat. Commun.* **11**, 2344 (2020).
12. L. Mao, Y. Wu, C. C. Stoumpos, M. R. Wasielewski, M. G. Kanatzidis, *J. Am. Chem. Soc.* **139**, 5210–5215 (2017).
13. D. Pan et al., *Nat. Nanotechnol.* **16**, 159–165 (2021).
14. G. Xu et al., *Adv. Mater.* **17**, 907–910 (2005).
15. Y. Wang et al., *ACS Nano* **11**, 3355–3364 (2017).
16. J. Wang, M. S. Gudiksen, X. Duan, Y. Cui, C. M. Lieber, *Science* **293**, 1455–1457 (2001).
17. M. Wang, Z. Yang, C. Zhang, *Adv. Opt. Mater.* **9**, 2002236 (2021).
18. M. Law et al., *Science* **305**, 1269–1273 (2004).
19. X. Wang et al., *Science* **381**, 784–790 (2023).
20. Y. Li et al., *ACS Appl. Mater. Interfaces* **9**, 8910–8918 (2017).
21. M. H. Huang et al., *Science* **292**, 1897–1899 (2001).
22. G. Xing et al., *Nat. Mater.* **13**, 476–480 (2014).
23. H. Zhu et al., *Nat. Mater.* **14**, 636–642 (2015).
24. H. Zhang et al., *Angew. Chem. Int. Ed.* **57**, 7748–7752 (2018).
25. J. Y. Park et al., *Nat. Chem.* **15**, 1745–1753 (2023).
26. Y. Li et al., *Sci. Adv.* **9**, eadh0517 (2023).

EVOLUTION

Imbalanced speciation pulses sustain the radiation of mammals

Ignacio Quintero[1]*, Nicolas Lartillot[2], Hélène Morlon[1]

The evolutionary histories of major clades, including mammals, often comprise changes in their diversification dynamics, but how these changes occur remains debated. We combined comprehensive phylogenetic and fossil information in a new "birth-death diffusion" model that provides a detailed characterization of variation in diversification rates in mammals. We found an early rising and sustained diversification scenario, wherein speciation rates increased before and during the Cretaceous-Paleogene (K-Pg) boundary. The K-Pg mass extinction event filtered out more slowly speciating lineages and was followed by a subsequent slowing in speciation rates rather than rebounds. These dynamics arose from an imbalanced speciation process, with separate lineages giving rise to many, less speciation-prone descendants. Diversity seems to have been brought about by these isolated, fast-speciating lineages, rather than by a few punctuated innovations.

Understanding the tempo and mode by which lineages diversify is fundamental to explaining the variation of biodiversity across space, time, and taxa (1). The notable diversity present across the tree of life generally results from episodes of fast lineage diversification that underlie successful evolutionary radiations (2). Special attention has been given to understanding the timing of such pulses with respect to major abiotic events and the mode in which these pulses occur in some lineages and not in others, with no general consensus. Throughout the more than 200 million year (Myr) evolutionary history of mammals, for instance, environmental factors such as the radiation of flowering plants (i.e., the Cretaceous Terrestrial Revolution), the Cretaceous-Paleogene (K-Pg) extinction event, the Paleocene-Eocene Thermal Maximum (PETM), and other major environmental events likely spurred distribution shifts and extinctions, together with new ecological opportunities, generating widespread diversification pulses (3–6). Most often discussed is the role of the K-Pg event, with hypotheses that posit that fast diversification occurred either before, at, or after the event, dubbed as an "early," "explosive," or "delayed" rise of extant mammals, respectively (3–5, 7–11).

A long-standing paradigm holds that such shifts in the speed of diversification occur discretely and sporadically, driven by changes in the environment or the acquisition of adaptive evolutionary novelties, that is, "key innovations" (Fig. 1A) (12–16). Here, fast diversification is clade-wide, linked to the rapid filling of a niche space that has been freed from other occupants (e.g., due to environmentally driven

mass extinctions) or opened by a major evolutionary innovation. Since early observations that richness is highly unevenly distributed across the tree of life (17), much effort has been devoted to identifying the clade-wide increases in diversification rates that supposedly occurred at the origin of the most diverse spe-

cies groups (13, 18–20). However, evidence of substantial intraclade heterogeneity in diversification rates, beyond that expected from large clade-level dynamics, challenges this paradigm (21–27). An alternative view considers changes in diversification rates to be less predictable and more dynamic, giving prominence to the role of contingency in driving evolutionary outcomes (Fig. 1B) (28, 29). Here, the interplay between species' evolving ecologies and their particular spatial and environmental contexts could occasionally lead to short periods of fast diversification in specific lineages.

A fine-grained consideration of diversification

In this work, we developed the "birth-death diffusion" model (Fig. 1B) (30), which was designed to provide a flexible framework that simultaneously enables the reconstruction of overarching diversification dynamics and of fine-grained stochasticity of speciation and extinction rates. The process starts with a lineage with speciation rate λ_0 and extinction rate μ_0. Lineage-specific speciation $\lambda_l(t)$ and extinction $\mu_l(t)$ rates then evolve in time following a geometric Brownian motion (Fig. 1B).
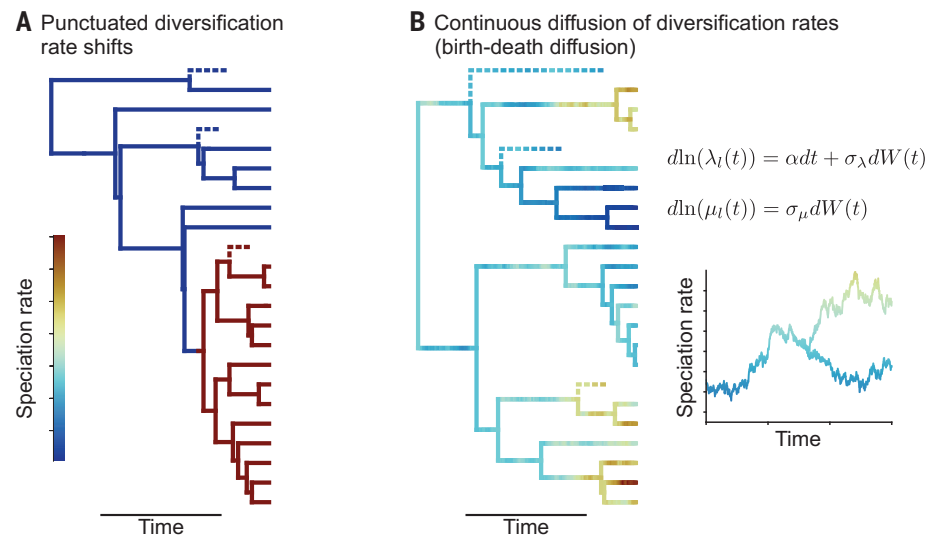

$$dln(\lambda_l(t)) = \alpha dt + \sigma_\lambda dW(t)$$

$$dln(\mu_l(t)) = \sigma_\mu dW(t)$$

Fig. 1. Punctuated versus diffused changes in diversification. (**A** and **B**) Hypothetical evolutionary history of a clade under two contrasting views of diversification, highlighted by differences in how speciation rates vary: (A) punctuated shifts in speciation, here shown as a clade-wide discrete increase (red) from the background rate (blue) as predicted by, for example, the sudden appearance of adaptive innovations; and (B) diffusion of speciation rates, assumed under our birth-death diffusion model, as predicted by a temporally dynamic interplay between species traits and their environment. In the birth-death diffusion model, for lineage *l* at time *t*, the changes in speciation $\lambda_l(t)$ and extinction $\mu_l(t)$ rates during a small time *dt* are given by the geometric Brownian process, the equations for which are shown in the figure. Here, α represents a drift term, σ_λ and σ_μ the diffusion rates, and $W(t)$ the Wiener process (i.e., standard Brownian motion). Lineages that are not observed in the phylogenetic tree of present-day species because they went extinct are represented with dashes. Our data augmentation framework takes a tree of present-day species as input and outputs posterior samples of complete trees, including both observed and unobserved lineages, with associated rate estimates.

[1]Institut de Biologie de l'ENS (IBENS), Département de Biologie, École Normale Supérieure, CNRS, INSERM, Université PSL, 75005 Paris, France. [2]Université Claude Bernard Lyon 1, CNRS, VetAgroSup, LBBE, UMR 5558, F-69100 Villeurbanne, France.
*Corresponding author. Email: ignacioquinterom@gmail.com

Rates are inherited at speciation; this hypothesis of inheritance is implicit (and in fact stronger) in all phylogenetic and paleontological diversification models that assume rate homogeneity within specific time bins or subclades and is justified by the inheritance of traits that may modulate diversification rates. A drift term α reflects temporal trends in speciation and avoids the "runaway species selection" that the birth-death diffusion model and others with inherited speciation rates sometimes produce (14, 26, 31). Two diffusion terms, σ_λ and σ_μ, reflect variability in speciation and extinction rates, respectively. The model can be simplified by imposing constraints. For example, we can assume no extinction, constant extinction rate, or constant turnover (ratio of extinction to speciation rate). Finally, we can constrain the extinction rate to follow a specific trajectory, such as a curve (or subclade-specific curves) separately estimated from the fossil record.

Given a phylogeny of present-day species, we developed an approach to obtain "complete" trees under the birth-death diffusion model, that is, trees with all of the extinct and unsampled lineages, together with instantaneous lineage-specific diversification rate estimates (fig. S1) (30). Our approach relies on Bayesian data augmentation techniques, which provide a probabilistic model-based imputation. Contrary to other imputation methods, the augmented data that arise from this procedure do not influence the posterior parameters of the model given the observed data (32). This allows us to estimate paleodiversity curves, that is, variations in species richness through time, as well as speciation rates averaged over both lineages that are observed in the empirical tree and lineages that are not. We accounted for potential missing species in the extant phylogeny using clade-specific sampling probabilities. We validated the approach using simulations (figs. S2 to S9) (30). Importantly, whereas the Brownian diffusion assumption may lead to smoothing of the reconstructed diversification trajectories, simulations under scenarios of cross-species variation in speciation rates along time or punctuated diversification rate shifts in specific lineages along the tree (i.e., the scenario depicted in Fig. 1A) show that the birth-death diffusion model is able to recover sudden variations (figs. S8 and S9).

When constraining extinction rates to follow estimates from the fossil record, the birth-death diffusion model exploits the advantages of the complementary sources of evolutionary information provided by neontological and paleontological data. Time-calibrated phylogenetic trees built from genetic data contain topological information under a branching process, providing information on ancestral-descendant relationships across thousands of lineages, whereas fossil information provides direct evidence of past extinction dynamics, including mass extinction events (33–35).
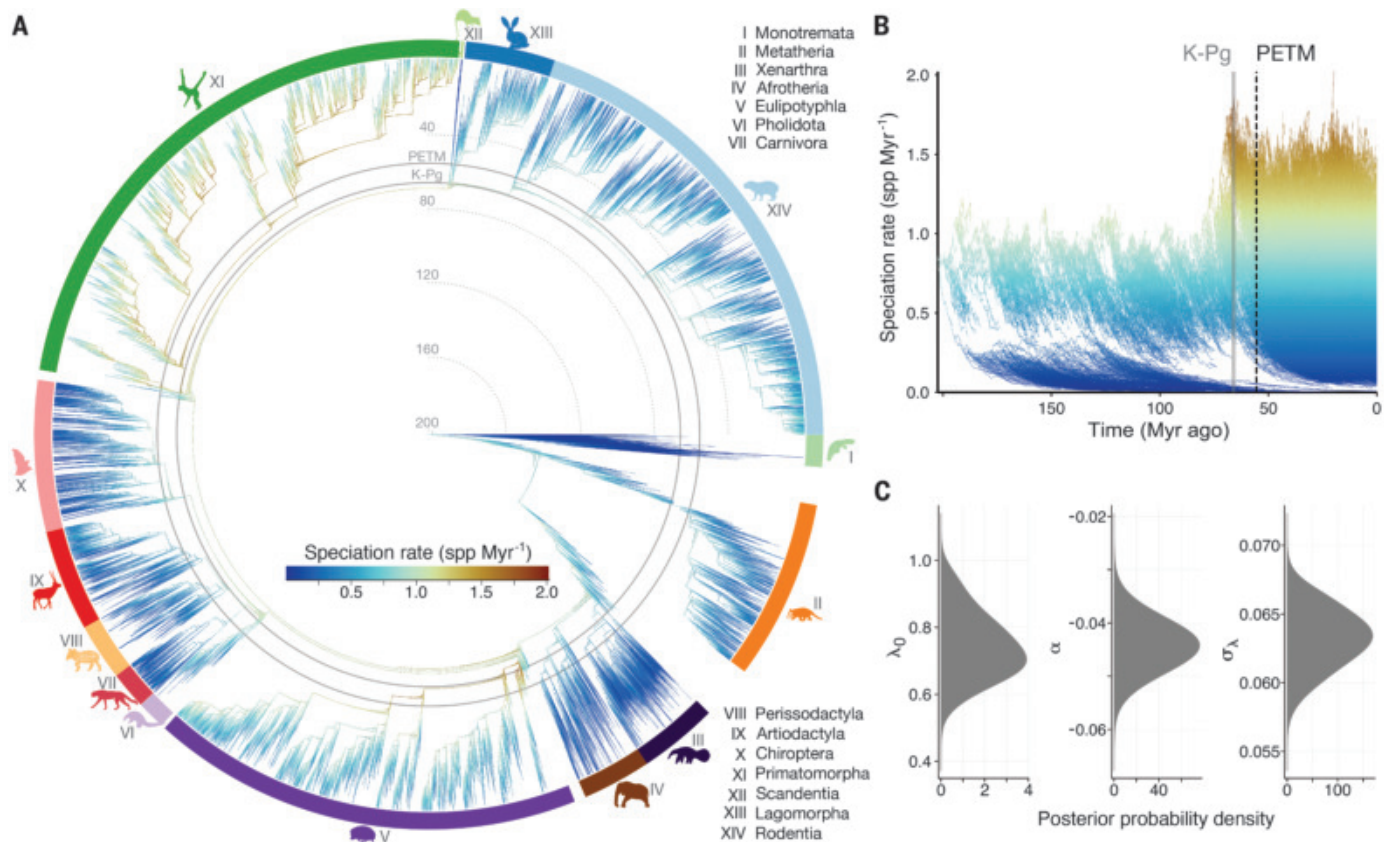
Fig. 2. Mammal diversification dynamics informed by their phylogeny and fossils under the birth-death diffusion model, with extinction rates estimated from the fossil record. (**A**) Complete radiation of mammals, incorporating the tree of extant species and lineages that went extinct or were not sampled at present (one representative complete tree sample from the birth-death diffusion posterior); warmer colors represent higher speciation rates. The surrounding colored radian arcs identify the crown-plus-stem diversity of the 14 mammal clades with embedded species silhouettes from PhyloPic (phylopic.org) and roman numerals for identification. Lineages without any surrounding color correspond to those that are not part of the stem diversity of any of these clades (e.g., stem therians and eutherians). Dashed gray lines specify the timescale every 40 Myr into the past, and solid gray lines specify, in order, the K-Pg mass extinction event and PETM. (**B**) Lineage speciation rates through time plotted for the same complete tree sample as in (A). The gray solid line demarcates the K-Pg boundary and the black dashed line the PETM. (**C**) Posterior distributions for the three parameters of the birth-death diffusion model (with extinction estimated from the fossil record): speciation rate at the root λ_0, drift α, and diffusion in speciation rates σ_λ.

Heterogeneity of diversification rates in mammals

We applied the birth-death diffusion model to the evolutionary history of mammals, combining the latest time-calibrated species-level tree for the group (36) with their paleontological record. The dating of this tree is consistent with a more recent one with increased whole-genome sampling (10) and supports a "long fuse" model of mammalian diversification with interordinal divergences occurring mostly before, and intraordinal divergences after, the K-Pg boundary, particularly after the PETM (37). Applying the birth-death diffusion model to the species-level tree allows us to interpret node ages and branching patterns in terms of diversification dynamics.

We first estimated temporal variation of extinction rates from 84,576 fossil occurrences using PyRate, a model that detects the number, magnitude, and temporal placement of rate changes while controlling for sampling and preservation biases within a Bayesian framework (30, 35). We estimated such extinction curves independently for 14 major mammal clades, as well as for Theria (placentals, marsupials, and their extinct relatives) and Eutheria (placentals and their extinct relatives) used to constrain extinction rates for stem taxa (fig. S10). These curves recover a peak in extinction rates at the K-Pg event (around 66 Myr ago) and PETM (around 55.5 Myr ago; fig. S10). The K-Pg event caused high extinction of metatherians (marsupials and their extinct relatives) and stem eutherians; at the PETM, extinction targeted mostly stem eutherian lineages again, in concordance with previous evidence (5), and, to a lesser degree, Eulipotyphla. The completeness of the fossil record is very uneven across clades. More generally, the fossil record is subject to various sources of temporal, spatial, and taxonomic preservation biases (30), which is reflected in different degrees of uncertainty around our extinction-curve estimates (fig. S10). Although these inherent biases affect any inference of deep-time dynamics, our measure of uncertainty around the extinction curves allows us to test the robustness of ours. In addition, to obtain per-species extinction-rate estimates, we used clade-specific species-by-genus estimates, which are sensitive to present taxonomic knowledge. Different species-by-genus estimates would change the magnitude of the extinction curves but not their dynamics.

We applied our data augmentation inference of the birth-death diffusion model to the mammal phylogenetic tree, with extinction constrained by the fossil estimates, which provided us with a posterior sample of complete mammal trees (Fig. 2A). Congruent with previous empirical assessments of diversification heterogeneity in mammals (25) and other groups (23, 26, 38), we found substantial variation across lineages in speciation rates (Fig. 2, A and B), with a median posterior diffusion coefficient for speciation rates of σ_λ = 0.063, interpreted as an expected change of about 6.3% per Myr (Fig. 2C). Estimated lineage-specific speciation rates range from close to 0.005 events per lineage per Myr in some monotremes, up to more than 1.5 species per Myr (spp. Myr^{-1}) in Primatomorpha (Fig. 2A and fig. S11), with an average of about 0.7 spp. Myr^{-1}. Primates experienced fast species turnover, characterized by both high speciation and extinction rates (figs. S11 and S12). In comparison, the species-rich rodents and bats have lower speciation rates but were also less affected by extinction, resulting in a faster accumulation of species than primates (Fig. 2A and figs. S11 and S12). These results confirm the role played by differences in both speciation and extinction rates in explaining among-clade differences in present-day species richness (33). Over the full history of mammals, we estimate a posterior average of about 145,000 extinct species (around 96% of species extinct). These estimates of past diversification and diversity are comparable to paleontological estimates (33).

At the scale of all mammals, we recovered a clear mass extinction event at the K-Pg boundary (Fig. 3A). At the PETM, we found an almost imperceptible slowdown in species accumulation: The diversity loss experienced by mostly stem eutherians (fig. S10) is almost fully balanced by the radiation of crown placental lineages. We also applied the birth-death diffusion model using other extinction assumptions (no extinction, constant extinction, constant turnover, and extinction diffusion; figs. S14 to S17). Irrespective of the assumption on extinction, we consistently found an overall expectation for lineages to decrease their speciation rates by about 4% per Myr (posterior median for drift α = −0.044; Fig. 2C). Analyses with extinction diffusion recover similar estimates of the diffusion coefficient for speciation rates to
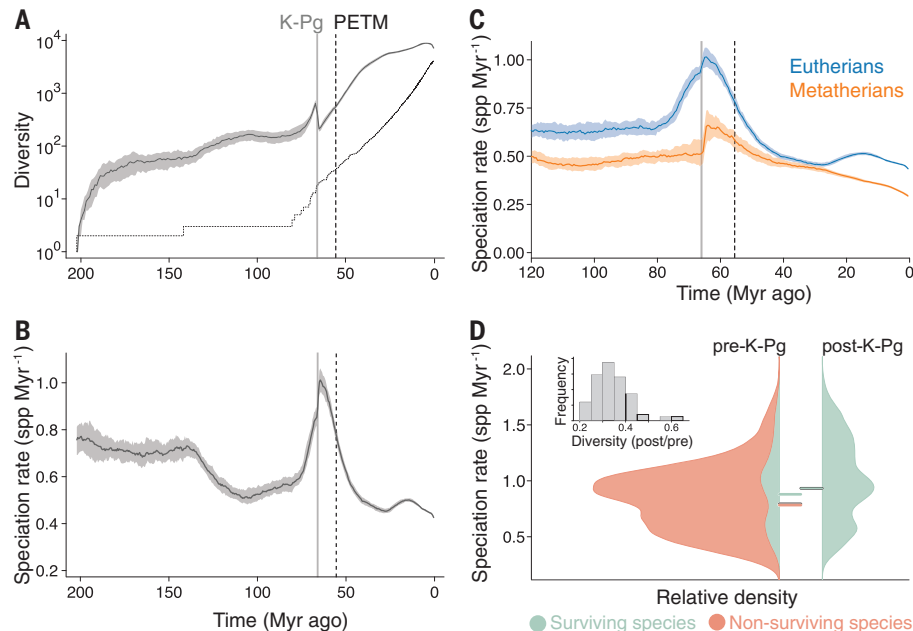

Fig. 3. Wiping out of slowly speciating lineages during the K-Pg mass extinction event.
(**A**) Distribution through time of the estimated number of therian mammal lineages (placentals, marsupials, and their extinct relatives). The solid line shows the median, the shaded region indicates the 50% credible interval (CI), and the dotted line shows the lineage-through-time plot obtained from the tree of present-day mammals. (**B**) Average speciation rates across all therian mammals, which displays an increase before the K-Pg event followed by a sharp increase at the K-Pg boundary, with a slowdown in the aftermath. The solid line shows the median, and the shaded region indicates the 50% CI, across all data-augmented trees. (**C**) Average speciation rates (median and 50% CI across all data-augmented trees) for eutherians (placentals and their extinct relatives in blue) and metatherians (marsupials and their extinct relatives in orange). Speciation rates increased before the K-Pg boundary in eutherians but not metatherians and then increased abruptly at the K-Pg boundary in metatherians and, to a lesser extent, in eutherians. (**D**) Density distributions of speciation rates before the onset (67 Myr ago) and end (65 Myr ago) of the K-Pg boundary across all data-augmented trees, colored by lineages that survived (light green) or went extinct (light red). Horizontal bars show the average speciation rates for each of these groups separately, colored respectively, and combined (black; note that the colored bars overlap the black bars). The inset shows the posterior frequency distribution of the proportion of therian mammal diversity that survived the K-Pg extinction event, across all data-augmented trees.

analyses with homogeneous extinction (figs. S14 to S17), suggesting that the variability of speciation rates is not inflated when assuming homogeneous extinction. The analyses that did not use the fossil record to constrain extinction rates yielded lower diversity estimates, regardless of their respective extinction assumption (figs. S14 to S17), and did not detect mass extinction events. This corroborates the importance of integrating fossil-based extinction rate estimates in recovering deep-time diversity dynamics (*33, 39*).

Extinction of slowly speciating lineages at the K-Pg boundary

The average speciation rate across all therian mammals was relatively high and stable throughout the Jurassic, mirroring early crown mammal radiations (*4*) (Fig. 3B). This period was followed by a decrease at the onset of the Cretaceous and an increase during the late Cretaceous that led to the diversification of most extant placental orders (*10, 36*) (Fig. 3, B and C). Coinciding with the K-Pg extinction event, average speciation rates increased abruptly (Fig. 3, B and C). These temporal trends are robust to uncertainty around the phylogenetic tree and the extinction curves (fig. S13).

The abrupt increase of speciation rates at the K-Pg extinction event was driven by the extinction of slowly speciating lineages rather than a collective increase in speciation rates across lineages (Fig. 3D). Our results show that, on average, about 34% of therian diversity survived the K-Pg boundary (comparison at 67 and 65 Myr ago), with an average pre–K-Pg boundary speciation rate of about 0.78 spp. Myr^{-1} for extinct lineages (predominantly stem metatherians and eutherians) and of about 0.88 spp. Myr^{-1} for those that survived (Fig. 3D; mean difference of 0.096 spp. Myr^{-1}, Welch's t test, $p < 10^{-99}$). This is driven mostly by the fact that metatherians, which had slower speciation rates, experienced more extinctions than eutherians (average speciation rates at the outset of the K-Pg extinction event of 0.52 and 0.88 spp. Myr^{-1}, with surviving percentages of 3.5 and 43%, respectively); indeed, only very few metatherians survived the K-Pg extinction event (posterior average of 4.25 lineages). The preferential extinction of slowly speciating lineages also occurred both within metatherians and eutherians: It was particularly strong within metatherians (mean difference of 0.09 spp. Myr^{-1}, Welch's t test, $p < 10^{-18}$) and marginally significant in eutherians (mean difference of 0.009 spp. Myr^{-1}, Welch's t test, $p = 0.055$). This sorting process is expected under a model of "speciational evolution" (i.e., speciation-driven phenotypic change), where clades undergoing frequent speciation have an evolutionary advantage (*40, 41*). At mass extinction events in particular, higher diversity and variability among
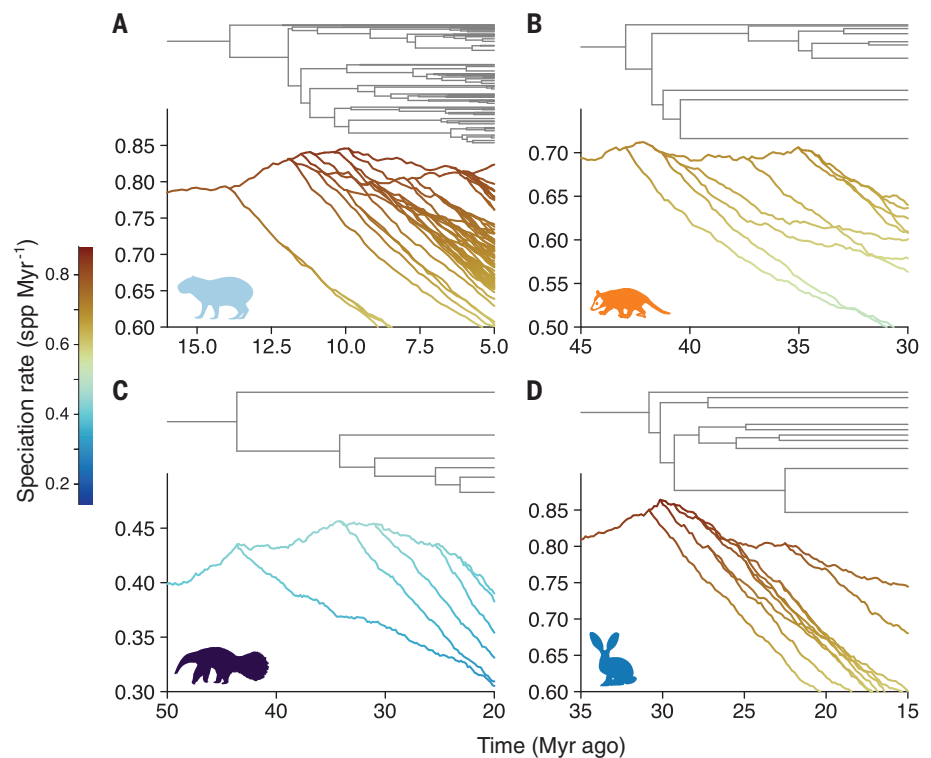
Fig. 4. Imbalanced speciation in mammals. (A to **D)** Four illustrative examples of how speciation rates vary in the mammal tree, obtained by zooming into parts of the tree of (A) Rodentia, (B) Marsupialia, (C) Xenarthra, and (D) Lagomorpha. Shown at the top of each panel, in gray, is the section of the tree, and shown at the bottom is the evolution of speciation rates along the respective branches, represented both by color and the position on the *y* axis. For clarity, the posterior median lineage-specific speciation rates in the tree of present-day mammals is shown, rather than complete trees with extinct lineages.

descendant species increases the chances that at least one of them survives. These results differ from those expected under an explosive-rise scenario of ecological release after mass extinctions and are not a necessary outcome of our model assumptions (fig. S18).

Of particular interest is whether mass extinctions primarily affected lineages with high background extinction rates. Although our (necessary) assumption of homogeneous extinction rates within each of the 16 clades precluded us from precisely evaluating this question at the species level, the fact that the K-Pg mass extinction event wiped out more metatherians, with lower background extinction rates (about 0.49 spp. Myr^{-1} at the onset of the K-Pg boundary), than eutherians (0.61 spp. Myr^{-1}) suggests that this need not be the case (fig. S10). These results support a decoupling between background and mass extinctions (*42*). Regardless of the effect of background extinction rates, the disappearance of more-slowly speciating lineages at the K-Pg mass extinction event, rather than a collective increase of speciation rates across surviving lineages, resulted in an increase in average speciation rates (Fig. 3). After the K-Pg mass extinction event, speciation slowed down (Fig. 3B). We found a

decreasing trend across most of the Cenozoic, mirroring trends in rates of morphological evolution (*6*), until around the early Miocene, when a surge in speciation rates is seen [Fig. 3, B and C; this pattern was also robust to phylogenetic uncertainty (fig. S13)], mostly driven by the renewed diversification of primates, artiodactyls, lagomorphs, and, more recently, rodents (fig. S12).

Our results refute the explosive- and delayed-rise hypotheses wherein mammals were suppressed in their ecomorphological and taxonomic diversity during the Cretaceous and experienced a release at or after the K-Pg extinction event that spurred their diversification (*37*). Indeed, inference under simulations characterizing ecological release scenarios after (or not) mass extinction events does not conform to the empirical pattern observed across mammals (fig. S18). Instead, our results suggest an early rise scenario, wherein rates of speciation increased before the K-Pg boundary, leading to the appearance of several major extant mammal orders (*3, 10*). Average speciation rates increased again at the K-Pg boundary, but this was because more-slowly speciating lineages were filtered out rather than because an ecological release spurred diversification. This

is concordant with recent phylogenetic and paleontological evidence that suggests that a major ecomorphological and taxonomic diversification of mammals occurred before the K-Pg boundary that coincided with the rise of angiosperms (*4, 6, 43, 44*) and increased continental fragmentation (*10*). Underlying these overarching temporal patterns, however, we did not find a correlated burst of diversification across all mammals during the Late Cretaceous. Rather, early eutherian lineages alone drove this period of fast diversification (Fig. 3C). Presumably, this foregoing rise in diversification rates conferred higher probabilities to be represented by daughter lineages after the K-Pg boundary on several eutherian lineages than, for instance, on their metatherian counterparts. These temporal trends were obtained by averaging over all lineages (observed and unobserved) in the complete trees as a result of our data augmentation approach and would not have been properly characterized by only averaging over lineages that survived to the present and were sampled (figs. S11 and S12).

Imbalanced speciation pulses

Under speciation dynamics driven by cross-lineage abiotic effects and infrequent evolutionary novelties (*12–16, 45*), we would expect a few scattered speciation rate shifts along the tree with subsequent homogeneous rates. Instead, we found substantial among-lineage heterogeneity, confirming recent results in birds (*26, 27*).

Bursts of speciation vary substantially in magnitude and seem to occur repeatedly, asynchronously, and ephemerally. Indeed, dissecting among increases in speciation rates along the branches of the tree (or "pulses"), we uncovered a recurrent pattern of imbalanced, or asymmetrical, speciation rates, wherein, along consecutive nodes, only one of the daughter species sustains high speciation rate levels (Fig. 4). We characterized this imbalance for the largest pulses across mammals by quantifying the distribution of subsequent speciation rates (*30*). We found that the frequency of lineages with subsequent speciation rates that remain higher than the prepulse speciation rate is usually around 50% and never larger than 75% (fig. S19). This pattern holds across all our model assumptions on extinction (fig. S20 to S23). In comparison, the same analyses performed on simulations with clade-level speciation shifts (*18, 20, 46*) resulted in >95% of the speciation rates remaining higher than the prepulse level for the duration of the pulse (fig. S9). Such patterns of imbalanced speciation could arise from founder speciation events, frequently observed in speciation studies, in which small populations become isolated from the main population by chance events (*14, 47, 48*). Here, the initial low abun-

dance of peripheral isolates limits their potential to generate new species, whereas the diversification potential of the main population remains largely unaffected (*14, 49*). This provides an interpretation for the observed tendency for speciation rates to decline through time (as evidenced by the negative estimate for α; Figs. 2C and 4) due to imbalanced speciation rather than diversity dependence (*50, 51*). This interpretation is further supported by the lack of evidence for speciation bursts at the aftermath of the K-Pg mass extinction, which would be expected if diversification was controlled by intra- or interclade diversity-dependent processes (fig. S18).

Conclusions

G. G. Simpson considered adaptive radiations, which are characterized by clade-wide shifts in speciation and diversity-dependent dynamics, to be the main source of life's extraordinary diversity (*13*). Our results support a more nuanced, dynamic, and less predictable diversification process, wherein the complex interplay of species traits and the specific environment they experience periodically propitiates suitable conditions for separate speciation pulses. These ephemeral pulses reveal an imbalanced nature, in which a faster-speciating lineage gives rise to multiple slowly speciating ones. These species, in turn, become increasingly vulnerable to extinction, which is often precipitated en masse during major environmental changes. Although our findings underscore the role of contingency in diversification, general deterministic effects, including particular combinations of body size (*52*) and dispersal propensity with certain landscape configurations (*10, 53, 54*), should increase the probability of occurrence and persistence of fast-speciating lineages. Diversity seems to depend on such lineages rather than on clade-wide adaptive radiations.

REFERENCES AND NOTES

1. G. G. Simpson, *Tempo and Mode in Evolution*, Columbia Biological Series, No. 15 (Columbia Univ. Press, 1944).
2. D. Schluter, *The Ecology of Adaptive Radiation* (Oxford Univ. Press, 2000).
3. R. W. Meredith *et al.*, *Science* **334**, 521–524 (2011).
4. D. M. Grossnickle, S. M. Smith, G. P. Wilson, *Trends Ecol. Evol.* **34**, 936–949 (2019).
5. N. S. Upham, J. A. Esselstyn, W. Jetz, *Curr. Biol.* **31**, 4195–4206.e3 (2021).
6. A. Goswami *et al.*, *Science* **378**, 377–383 (2022).
7. O. R. Bininda-Emonds *et al.*, *Nature* **446**, 507–512 (2007).
8. T. Stadler, *Proc. Natl. Acad. Sci. U.S.A.* **108**, 6187–6192 (2011).
9. M. S. Springer, N. M. Foley, P. L. Brady, J. Gatesy, W. J. Murphy, *Front. Genet.* **10**, 1241 (2019).
10. N. M. Foley *et al.*, *Science* **380**, eabl8189 (2023).
11. E. Carlisle, C. M. Janis, D. Pisani, P. C. J. Donoghue, D. Silvestro, *Curr. Biol.* **33**, 3073–3082.e3 (2023).
12. A. H. Miller, in *Ornithologie als Biologische Wissenschaft*, E. Mayr, E. Schuz, Eds. (Carl Winter, 1949), pp. 84–88.
13. G. G. Simpson, *The Major Features of Evolution* (Columbia Univ. Press, 1953).
14. E. Mayr, *Animal Species and Evolution* (Harvard Univ. Press, 1963).
15. L. Van Valen, *Evolution* **25**, 420–428 (1971).
16. J. P. Hunter, *Trends Ecol. Evol.* **13**, 31–36 (1998).
17. J. C. Willis, *Age and Area: A Study in Geographical Distribution and Origin of Species* (Cambridge Univ. Press, 1922).
18. M. E. Alfaro *et al.*, *Proc. Natl. Acad. Sci. U.S.A.* **106**, 13410–13414 (2009).
19. R. S. Etienne, B. Haegeman, *Am. Nat.* **180**, E75–E89 (2012).
20. D. L. Rabosky, *PLOS ONE* **9**, e89543 (2014).
21. S. B. Heard, D. L. Hauser, *Hist. Biol.* **10**, 151–173 (1995).
22. A. de Queiroz, *Syst. Biol.* **51**, 917–929 (2002).
23. T. J. Davies *et al.*, *Proc. Natl. Acad. Sci. U.S.A.* **101**, 1904–1909 (2004).
24. M. J. Donoghue, *Paleobiology* **31**, 77–93 (2005).
25. T. J. Davies *et al.*, *Proc. Natl. Acad. Sci. U.S.A.* **105**, 11556–11563 (2008).
26. O. Maliet, F. Hartig, H. Morlon, *Nat. Ecol. Evol.* **3**, 1086–1092 (2019).
27. F. Ronquist *et al.*, *Commun. Biol.* **4**, 244 (2021).
28. S. J. Gould, in *Self-organizing Systems: The Emergence of Order*, Life Series Monographs, F. E. Yates, A. Garfinkel, D. O. Walter, G. B. Yates, Eds. (Springer, 1987), pp. 113–130.
29. M. J. Benton, B. C. Emerson, *Palaeontology* **50**, 23–40 (2007).
30. Materials and methods are available as supplementary materials.
31. J. M. Beaulieu, B. C. O'Meara, *Evolution* **69**, 1036–1043 (2015).
32. M. A. Tanner, W. H. Wong, *J. Am. Stat. Assoc.* **82**, 528–540 (1987).
33. C. R. Marshall, *Nat. Ecol. Evol.* **1**, 0165 (2017).
34. D. Silvestro, R. C. M. Warnock, A. Gavryushkina, T. Stadler, *Nat. Commun.* **9**, 5237 (2018).
35. D. Silvestro, N. Salamin, A. Antonelli, X. Meyer, *Paleobiology* **45**, 546–570 (2019).
36. S. Álvarez-Carretero *et al.*, *Nature* **602**, 263–267 (2022).
37. J. D. Archibald, D. H. Deutschman, *J. Mamm. Evol.* **8**, 107–124 (2001).
38. S. B. Heard, *Evolution* **50**, 2141–2148 (1996).
39. T. B. Quental, C. R. Marshall, *Trends Ecol. Evol.* **25**, 434–441 (2010).
40. E. A. Lloyd, S. J. Gould, *Proc. Natl. Acad. Sci. U.S.A.* **90**, 595–599 (1993).
41. O. Sanisidro, M. C. Mihlbachler, J. L. Cantalapiedra, *Science* **380**, 616–618 (2023).
42. D. Jablonski, *Science* **231**, 129–133 (1986).
43. G. P. Wilson, W. A. Clemens, J. R. Horner, J. H. Hartman, Eds., *Through the End of the Cretaceous in the Type Locality of the Hell Creek Formation in Montana and Adjacent Areas* (Geological Society of America, 2014).
44. T. J. D. Halliday, A. Goswami, *Biol. J. Linn. Soc. London* **118**, 152–168 (2016).
45. M. J. Benton, *Science* **323**, 728–732 (2009).
46. S. Höhna *et al.*, bioRxiv 555805 [Preprint] (2019); https://doi.org/10.1101/555805.
47. P. J. Wagner, D. H. Erwin, "Phylogenetic patterns as tests of speciation models" in *New Approaches to Studying Speciation in the Fossil Record*, D. Erwin, R. Anstey, Eds. (Columbia Univ. Press, 1995), pp. 87–122.
48. B. T. Smith *et al.*, *Nature* **515**, 406–409 (2014).
49. A. R. Templeton, *Genetics* **94**, 1011–1038 (1980).
50. D. Moen, H. Morlon, *Trends Ecol. Evol.* **29**, 190–197 (2014).
51. O. Hagen, K. Hartmann, M. Steel, T. Stadler, *Syst. Biol.* **64**, 432–440 (2015).
52. M. Cardillo *et al.*, *Science* **309**, 1239–1241 (2005).
53. R. G. Moyle, C. E. Filardi, C. E. Smith, J. Diamond, *Proc. Natl. Acad. Sci. U.S.A.* **106**, 1863–1868 (2009).
54. I. Quintero, M. J. Landis, W. Jetz, H. Morlon, *Proc. Natl. Acad. Sci. U.S.A.* **120**, e2220672120 (2023).
55. I. Quintero, Supplementary dataset for "Imbalanced speciation pulses sustain the radiation of mammals" [Dataset]. Zenodo (2024); https://doi.org/10.5281/zenodo.11084498.

NANOPARTICLES

Spontaneous weathering of natural minerals in charged water microdroplets forms nanomaterials

B. K. Spoorthi[1], Koyendrila Debnath[2], Pallab Basuri[1], Ankit Nagar[1], Umesh V. Waghmare[2], Thalappil Pradeep[1,3]*

In this work, we show that particles of common minerals break down spontaneously to form nanoparticles in charged water microdroplets within milliseconds. We transformed micron-sized natural minerals like quartz and ruby into 5- to 10-nanometer particles when integrated into aqueous microdroplets generated via electrospray. We deposited the droplets on a substrate, which allowed nanoparticle characterization. We determined through simulations that quartz undergoes proton-induced slip, especially when reduced in size and exposed to an electric field. This leads to particle scission and the formation of silicate fragments, which we confirmed with mass spectrometry. This rapid weathering process may be important for soil formation, given the prevalence of charged aerosols in the atmosphere.

Nanoparticles of minerals exist naturally in soil, and some of them are essential for life (1). Microdroplets have been a topic of interest over the past decade, and the confined environment within them is known to cause chemical synthesis at an accelerated rate, as well as other processes such as the formation of nanoparticles (2). We decided to explore whether natural minerals could disintegrate in microdroplets, through a process opposite to chemical synthesis.

For our experiments, we prepared micron-scale particles of natural quartz (SiO_2) and ruby (Cr-substituted Al_2O_3) for use in an electrospray setup (Fig. 1, A and B). We ground commercial millimeter-sized quartz particles well using a mortar and pestle and used centrifugation to separate the differently sized particles that formed. We carefully excluded all the particles smaller than 1 µm in size and used particles of 5 to 10 µm that were suspended in water for the experiment (Fig. 1C). Even after ultrasonication to detach any adhered particles, we found some smaller particles attached to a few larger ones (Fig. 1C). These adhering particles had dimensions greater than 100 nm (fig. S1). We took an optical image of the ground quartz powder and an optical microscopic image of the separated particles that we used for electrospray (fig. S2). We electrosprayed a suspension of about 0.1 mg/ml of the separated quartz particles through a capillary tube that had an inner diameter of 50 µm at a

[1]Department of Chemistry, Indian Institute of Technology Madras, Chennai 600036, India. [2]Theoretical Sciences Unit, Jawaharlal Nehru Centre for Advanced Scientific Research, Bangalore 560064, India. [3]International Centre for Clean Water, IIT Madras Research Park, Chennai 600113, India.
*Corresponding author. Email: pradeep@iitm.ac.in
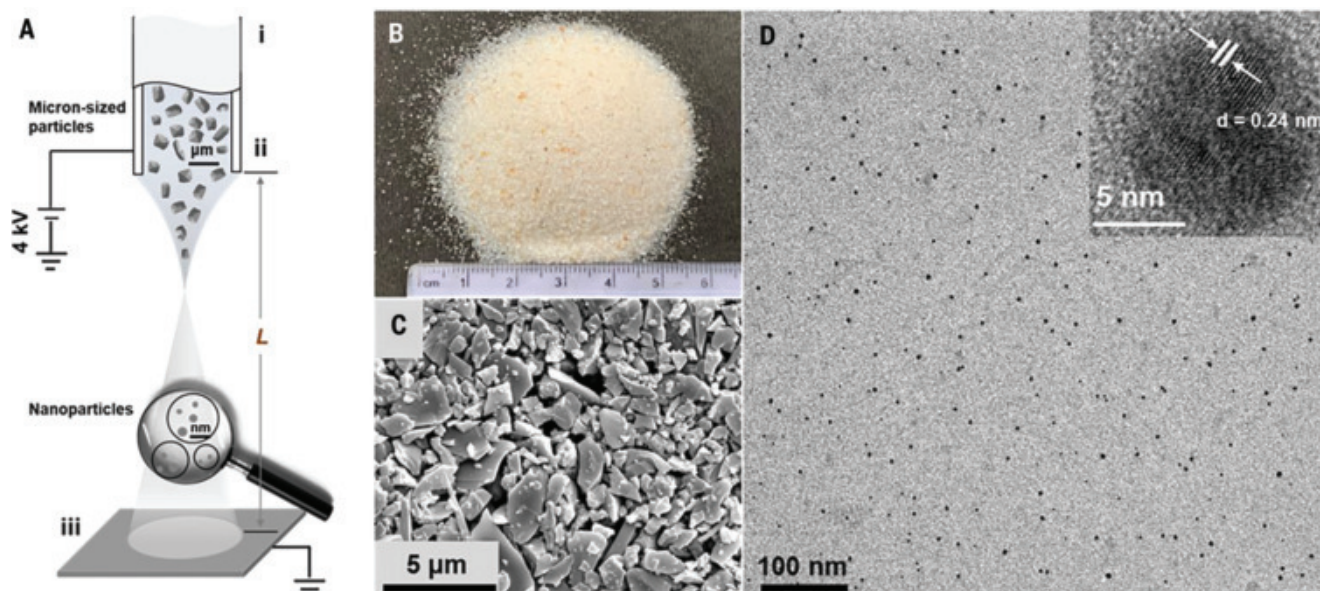
Fig. 1. Process of disintegration of natural quartz in microdroplets.
(**A**) Schematic representation of the disintegration of mineral particles in microdroplets. Setup components include (i) the electrospray emitter, (ii) a spray capillary with a 50-µm inner diameter, and (iii) the conducting substrate at a distance of L = 1.5 cm from the tip of the emitter. (**B**) A photograph of the natural quartz. (**C**) Field-emission scanning electron microscopy (FESEM) image of ground and separated natural quartz used for electrospray, showing that the size range of particles is between 1 and 5 µm. A few smaller particles that are naturally adhered to the micron-sized particles remain attached even after ultrasonication. (**D**) TEM image of natural quartz after electrospray with a high-resolution image of a particle shown in the inset. The plane shown is (110), where d is lattice spacing.

flow rate of 0.5 ml/hour and observed the resulting plume (Fig. 1A). We collected the product of electrospray 1.5 cm away from the spray tip, which resulted in a flight time on the order of 10 ms, consistent with similar experiments (3, 4). The product that was deposited on a transmission electron microscopy (TEM) grid had only 5- to 10-nm-diameter particles (Fig. 1D) throughout the grid. Under higher magnification, particles of different morphologies were observed. The particles showed the (110) plane of quartz (inset of Fig. 1D). Sonication had no effect on the breaking of silica particles. Experimental methods are presented in the supplementary materials, including a video of the electrospray process (movie S1).

To ensure that our initial observations were truly representative of the process, we performed measurements on larger quantities of samples. We built a multinozzle electrospray unit composed of six nozzles. We electrosprayed 1 liter of the suspension that contained 100 mg of the crushed micron-sized particles discontinuously over a month at the optimized conditions (spray voltage and distance) and a 3 ml/hour flow rate, and a deposit was collected on an aluminum sheet. The electrospray-deposited particles were strongly adherent to the substrate. We scraped about 60 mg of the powder off the substrate for bulk analysis. This left about 20 mg on the substrate, which we determined gravimetrically. We avoided hard scratching to remove the remaining product on the substrate. This gave us a collection efficiency of ~80% for our electrospray setup. We made x-ray diffraction measurements of the scraped-off powder using Cu Kα radiation to confirm that it was made of quartz (fig. S3) in the form of nanoparticles of ~16-nm average diameter. We calculated the particle size using the Scherrer formula. Independent analysis, the details of which are presented in the supplementary materials, showed the collection yield of electrospray deposition to be 81%.

We obtained similar experimental results with ruby (Fig. 2, A to C) and fused alumina (Fig. 2, D to F). These experiments show that both natural minerals and their synthetic analogs can be fragmented in charged microdroplets. The synthesis of materials using electrospray requires optimized conditions (5). For our single-spray experiments, the electrospray voltage was 4.0 kV, the tip-to-collector distance was 1.5 cm, and particle loading was 0.1 mg/ml.

Optimized experimental parameters

In the case of silica, below a spray voltage of 2.5 kV, the spray did not occur. From 3.0 kV onward, the spray was uniform. This potential was the threshold at which the electric field breaks the limit of surface tension and forms a plume containing charged microdroplets from the tip of the emitter. The required potential for this varies for different solutions and suspensions. In our experiments, the threshold potential for a stable spray was higher than usual, mainly because we electrosprayed a fine suspension of quartz. Below 2.5 kV, only micron-sized particles were seen in the outcome. We observed maximum fragmentation at the optimized conditions. Particles fragmented well at 4.5 kV. At 5.5 kV, we even observed finer nanostructures (fig. S4). We characterized the samples before and after electrospray by Raman spectroscopy (fig. S5) and energy dispersive spectroscopy. We observed fragmentation only with positive applied potential.
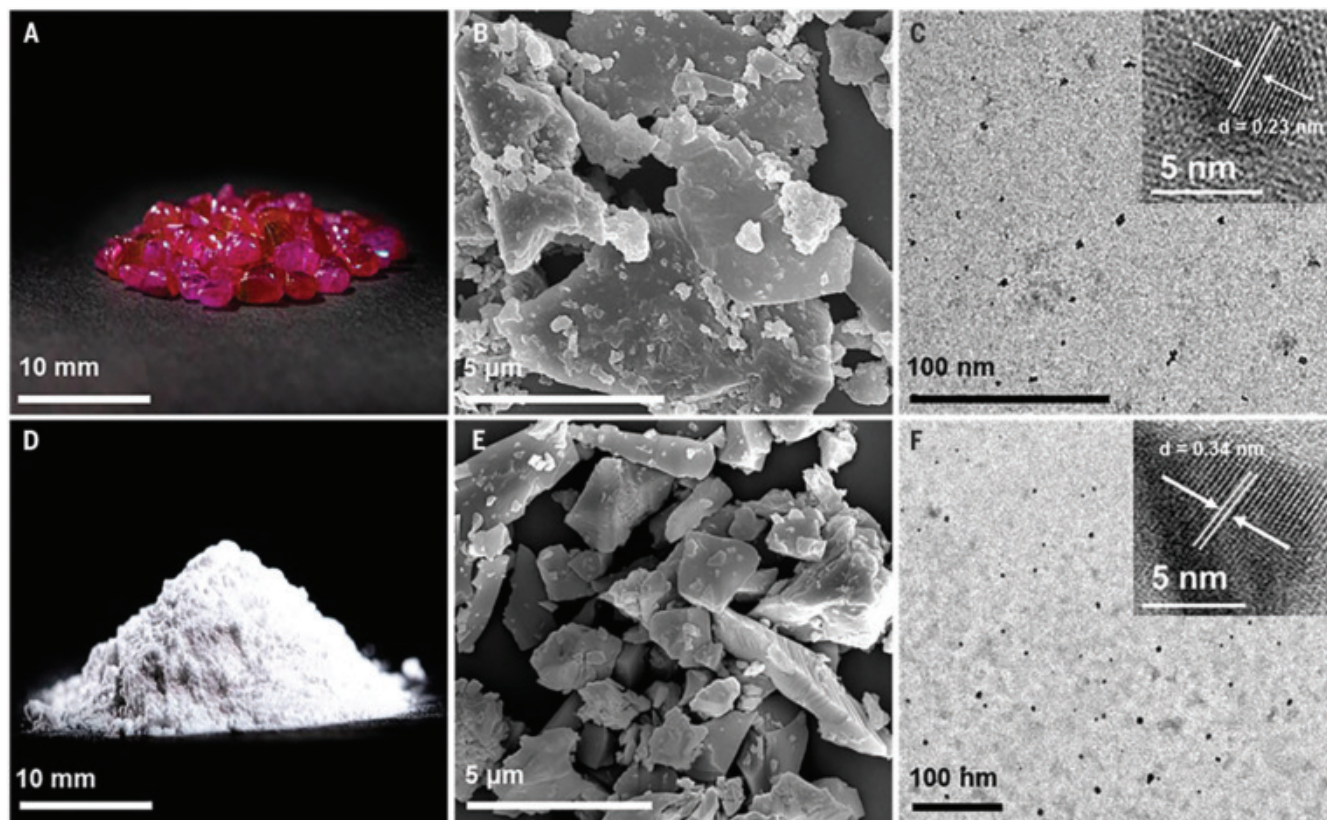

Fig. 2. Process of disintegration of natural and synthetic alumina in microdroplets. (**A**) Photograph of natural ruby. (**B**) FESEM image of ground and separated natural ruby before electrospray. (**C**) TEM image of natural ruby after electrospray at optimized conditions. The inset shows a high-resolution image of a particle. The plane marked is (110). (**D**) Photograph of fused alumina powder. (**E**) FESEM image of ground and separated fused alumina before electrospray. (**F**) TEM image of fused alumina after electrospray at optimized conditions. The inset shows a high-resolution image of a particle. The plane marked is (012) of α-alumina. In (B) and (E), some smaller particles are observed to be attached to the micron-scale particles naturally.

Understanding the phenomenon

To understand the mechanism of formation of quartz nanoparticles starting from larger particles, we used first-principles density functional theory calculations to determine the effects of reduced size, electric field, and pH on the processes of cleavage and slip in bulk and a (110) terminated slab of SiO$_2$. The α-SiO$_2$ structure of quartz belonging to the $P3_221$ (trigonal) space group was used. We chose the (110) plane because it was the one we observed with TEM. Cleavage and slip are two competing processes by which particles can break apart. We define bulk as meaning that the crystal has periodicity along all three directions. We define slab as the breaking of periodicity along the c axis, exposing the (110) surface. Cleavage across the (010) plane was introduced by subjecting the crystal to uniaxial tensile strain localized at a single (010) plane (by increasing the separation along the b direction) to create two separate constituents (Fig. 3A). We estimated the cleavage energy (two times the surface energy) as the difference between the total energy (E_{tot}) of a crystal cleaved along a specific plane and the total energy of the uncleaved relaxed crystal, which is the energy scale relevant to brittle fracture. During the cleavage of bulk and slab SiO$_2$, the energy of cleavage saturates as the separation between surfaces of cleaved parts (Fig. 3B) grows beyond 6 Å. The cleavage energies of the slab are notably lower than that of the bulk, which indicates increased ease in brittle cleavage with reduction in dimension. Consequently, nanocrystals of SiO$_2$ are more susceptible to fracture than its bulk form. Cleavage of a slab results in the formation of edges in addition to surfaces, and we note surface and edge reconstruction with concave-convex shapes in cleaved slab with lattice constant $b = 10$ Å, where cleavage energy saturates, in contrast to its absence in the cleaved surface of bulk (Fig. 3, C and D).

We examined the competing deformation instability of bulk and slab SiO$_2$. This instability leads to the formation of a stacking fault on the (010) plane, which is achieved with slip localized at a single (010) plane. To accomplish this, we transformed the unit cell vector $\vec{b}$ to yield the generalized stacking fault vector, $\vec{b} \rightarrow \vec{b}_0 + (x, 0, z)$, where $\vec{b}$ is the periodic cell vector and $x, z \in [0, 1]$ are the fractional coordinates (see Fig. 4A). For better understanding, the formation of slip is illustrated
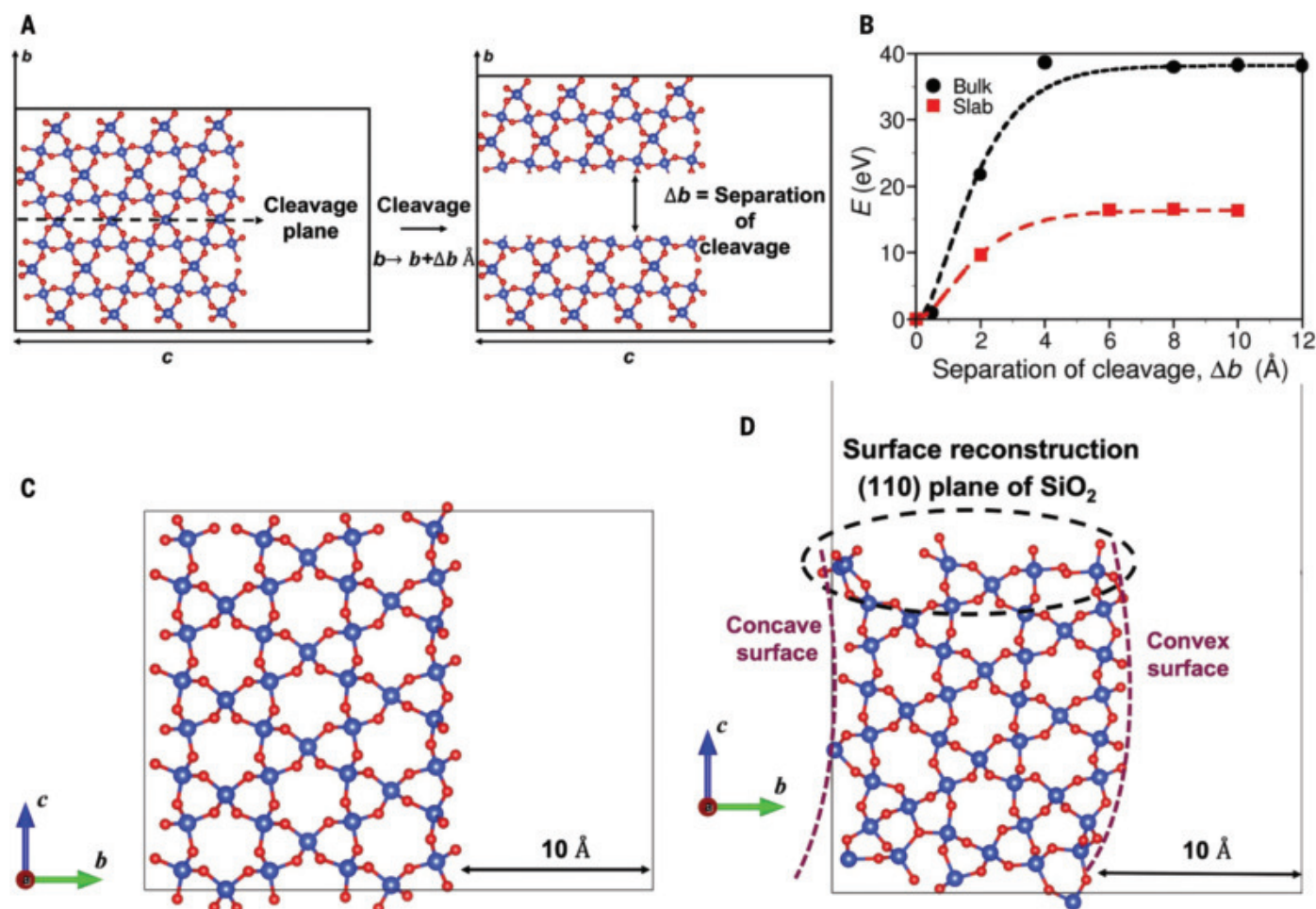
Fig. 3. The process of cleavage and surface reconstruction visualized with first-principles simulations. (**A**) Schematic of the (110) terminated slab of SiO$_2$ (left) acted on by uniaxial tensile strain (along the b axis), resulting in two cleaved surfaces (right). The distance, Δb is a measure of separation of the cleaved surfaces, which is composed of vacuum. (**B**) The relaxed energies of bulk and slab of SiO$_2$ as a function of separation. The energy surface is constructed using the energy functional form, $E_\infty - E_\infty(1 + x)e^{-x}$, where E_∞ is the energy of the system in which the cleaved crystals are separated by infinite distance and $x = \Delta b/l$ (where l is the length scale in this system) for the relaxed structures as a function of separation. The cleavage energies of slab are lower than that of bulk, indicating that nanoscale crystals of SiO$_2$ are much easier to break than the bulk. (**C** and **D**) Optimized structures of the (110) surface of (C) bulk [black data in (B)] and (D) slab SiO$_2$ [red data in (B)] with a cleavage thickness of 10 Å. We observed concave and convex deformations in the slab. However, no such deformation was seen in the bulk structure. In addition, surface and edge reconstructions were also observed in slab-SiO$_2$ upon cleavage. Silicon atoms are shown in blue, and oxygen atoms are in red.

in fig. S6. Stacking faults are locally stable at (x, z) = (0, 0.5), (0.5, 0), and (0.5, 0.5) slip configurations, and their energies relative to the reference structure (x, z) = (0, 0) are used to estimate stacking fault energies (SFEs):

$$\frac{E_{\mathrm{slip}}(x, z) - E_{\mathrm{slip}}(0, 0)}{A}$$

In this equation, $A = ad$, where a is the cell vector and d is the thickness of the slab. Negative SFEs of the (0, 0.5) and (0.5, 0.5) slips in the slab of SiO_2 mean spontaneous formation of extended stacking faults (table S1). This contrasts with the stacking faults in bulk SiO_2, which have positive energies as expected, implying formation of finite-sized stacking faulted regions bordered by partial dislocations (table S1). Thus, both the processes (cleavage and stacking fault formation) are energetically more favorable in the slab than in the bulk. The stability (negative SFE) of the stacking fault in the slab is linked with the creation of a step (relaxed structures reveal shear deformations or steps along the b direction) (Fig. 4, B and C) and associated reconstruction blunting the fault edges at the surface. Our results show that slip is the primary mechanism that drives the possible formation of nanoparticles in SiO_2.

Our first-principles analysis of the processes of cleavage and slip in bulk and (001) terminated slab (an alternative plane) of SiO_2 revealed that the mechanisms of nanocrystal formation in SiO_2 are not very sensitive to the specific choice of surface (tables S2 and S3). To understand the process of the disintegration of alumina, we simulated the cleavage and slip of a (001) terminated slab of α-Al_2O_3, which has the corundum structure ($R\bar{3}c$ space group) as in silica. The results presented in tables S4 and S5 suggest that its fragmentation to form nanocrystals is indeed driven by the mechanism of slip, similar to silica.

We next investigated the effects of hydrogen (H) atoms on the structure and energies of stacking faults in the (0, 0.5) and (0.5, 0.5) slip configurations. We used H atoms to model protons, which are known to be present in microdroplets, because simulations of a charged system within periodic boundary conditions need to be compensated with opposite charge. Upon addition of a H atom to the structure with slip vector (x, z) = (0.5, 0.5), the SFE remained negative. In addition, an H atom is found to destabilize the (0, 0.5) slip system (table S6). Compared with the (0, 0.5) stacking fault structure without an H atom (fig. S7A), substantial local structural distortions arise with H at the sites near the interacting H atom (fig. S7B). Further, interaction with two H atoms results in the formation of silicate fragments or the chipping away of silicate, suggesting that the H atom facilitates fragmentation of a natural

mineral such as quartz in microdroplets (fig. S7C). Application of an electric field, as is typical in electrospray experiments ($E = 10^8$ V/m along the c axis in Fig. 4) improves the stability of (0, 0.5) and (0.5, 0) stacking faults in SiO_2 (table S6).

Our theoretical analysis of mechanical instabilities in bulk and a nanoslab of SiO_2 (cleavage and slip in response to localized uniaxial and shear strains, respectively) suggests that the stacking faults and resulting steps at the surface of SiO_2 may occur in the initial stage of fragmentation into nanoparticles, and the interactions with H atoms and electric field enhance this process, leading to the formation of silicate fragments. Because the cleavage energies decrease substantially with a reduction in dimension, namely, from bulk to slab, we expected fragmentation to follow readily, with possible nucleation at the steps, or the sites of chemical interaction with protons. In addition to the stacking faults and resulting steps, several aspects of the microdroplet environment can drive the fragmenta-

tion process. Chemical reaction rate constants can be increased by a factor of more than 10^6 in such confinement (2). Several factors such as pH (6), reactive species such as radicals (7), their surface segregation, strong electric field at the interface (8), and others are likely to contribute additionally to these effects, and some of these may accelerate the process.

Formation of silicates in microdroplets

To test the hypothesis of formation of silicates by microdroplet-induced fragmentation, we electrosprayed 5 mg of silica in 50 ml of water at the optimized conditions on an aluminum substrate. The product was collected, redispersed in water, and centrifuged at 10,000 rpm to remove any larger particles. The upper layer was used for mass spectrometric measurements. In the negative ion mass spectrum of the deposited silica (Fig. 5A), the peaks appeared at mass/charge ratios (m/z) 60.9, 76.9, 94.9, 154.9, and 172.9. This spectrum was compared with that of 200 µM standard sodium silicate solution at pH 8.5 (Fig. 5B).
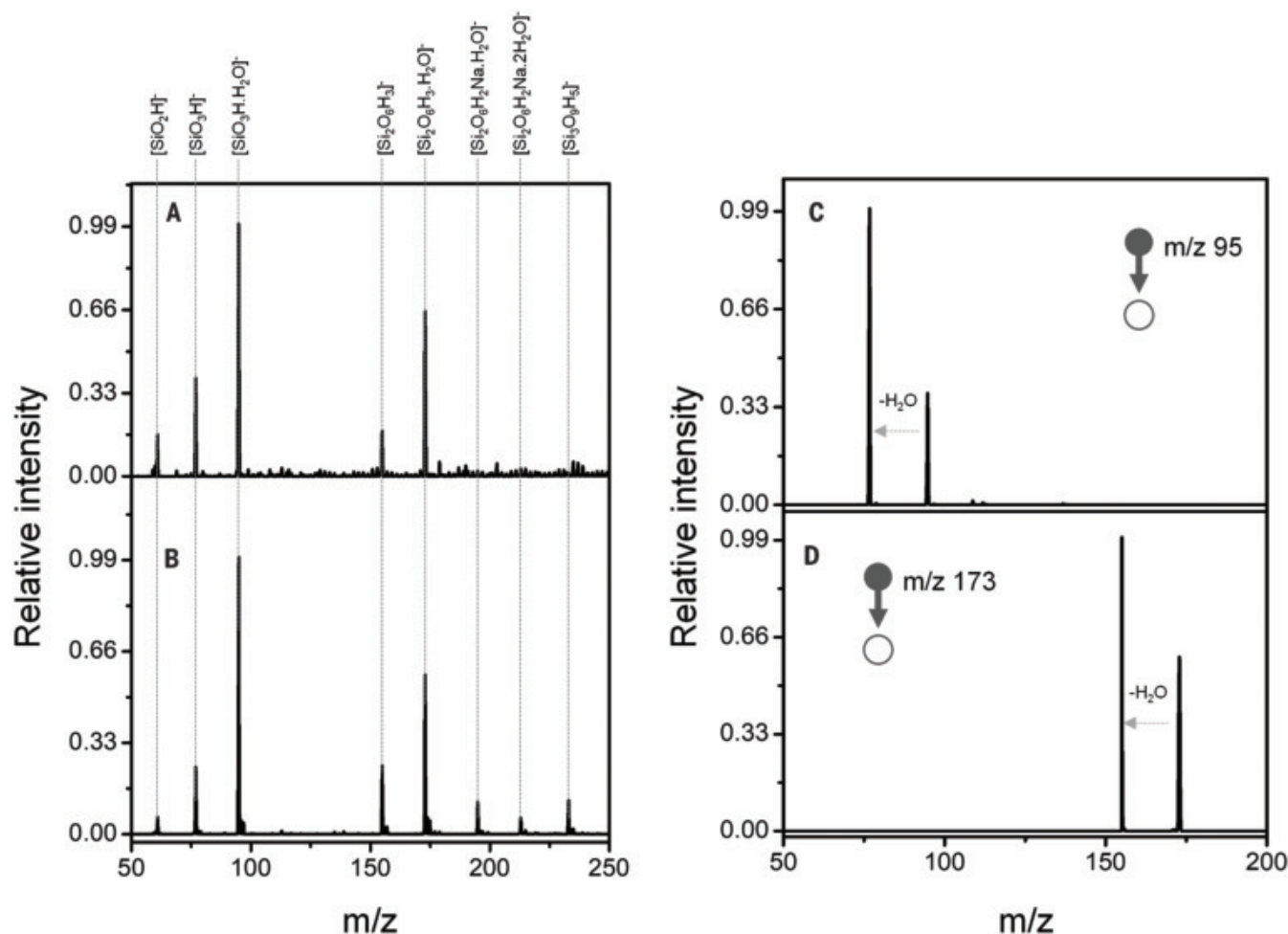

Fig. 4. Stacking fault or slip localized at a (010) plane. (**A**) Schematic of the (110) terminated slab of SiO_2 acted on by localized shear strain (slip) on (010) plane introduced through a generalized stacking fault vector $\vec{f} = x\vec{a} + z\vec{c}$, where $\vec{a}$ and $\vec{c}$ are periodic cell vectors and ($x, z \in [0, 1]$) are the fractional coordinates. (**B** and **C**) Relaxed stacking fault structures with (B) (x, z) = (0.5, 0.5) and (C) (x, z) = (0, 0.5). The stacking fault or slip on the (010) plane is introduced by tilting $\vec{b}$ (dashed boxes). Two-unit cells along the b direction are shown for clearer visualization. Silicon atoms are shown in blue, and oxygen atoms are in red.

Fig. 5. Mass spectra of silica samples. (**A** and **B**) Full-range negative ion mass spectrum of (A) the deposited silica showing the peaks due to silicates compared with that of (B) standard sodium silicate. (**C** and **D**) Tandem mass spectra of (C) [SiO₃H.H₂O]⁻ and (D) [Si₂O₆H₃. H₂O]⁻, showing water loss during fragmentation.

We observed peaks at m/z 60.9, 76.9, 94.9, 154.9, and 172.9 due to [SiO₂H]⁻, [SiO₃H]⁻, [SiO₃H.H₂O]⁻, [Si₂O₆H₃]⁻, and [Si₂O₆H₃. H₂O]⁻, respectively. In addition, we observed peaks at higher masses at m/z 194.9 [Si₂O₆H₂Na. H₂O]⁻, m/z 212.9 [Si₂O₆H₂Na. 2H₂O]⁻, and m/z 232.9 [Si₃O₉H₅]⁻. We did not observe sodium adduct peaks of the standard sodium silicate in the spectrum of deposited silica. Tandem mass spectrometric analysis for sodium silicate (fig. S8) and deposited silica (Fig. 5, C and D) showed the expected features. Two peaks at m/z 94.9 and 172.9 showed the loss of water, confirming the formation of [SiO₃H.H₂O]⁻ and [Si₂O₆H₃. H₂O]⁻ complexes.

Plausible mechanisms

With respect to the energy needed for such processes, our calculations suggest that physical effects in microdroplets are particularly important. Microdroplet convection and shock waves that produce pressures in the megabar range (9) are likely in droplets, which could trigger such effects. We suggest that the observed phenomenon is critically influenced by

the following factors: (i) Droplet fission occurs due to Coulomb repulsion. We know from the literature that the droplets produced at low flow rates (typically ~5 μl/min) have a narrow distribution of sizes, with the most abundant radius in the range of 1.5 μm. Such an electrospray droplet was shown to have an electric charge of ~10⁻¹⁴ C, which corresponds to ~60,000 singly charged ions (10). In our case, the droplet sizes are larger, in the range of approximately tens of micrometers (11); produced at a flow rate of 0.5 ml/hour, that is, 8.3 μl/min; and large enough to accommodate the parent particles. The droplet size reduces along the flight path, which results in the explosion of the droplets. This explosion produces smaller droplets that experience larger stresses (9), leading to the breakage of particles. (ii) Erosion of the quartz particles in the charged droplets and solubility of quartz in water (6 parts per million at 25°C) together bring SiO₂ species into the solution. We tested the possible effect of enhanced acidity in microdroplets on the mineral particles in a separate experiment by electrospraying pure water on the parent mine-

rals for 4 hours (fig. S9). We saw surface roughening in this experiment, although the changes are much less pronounced than those shown in Fig. 1. The reactive species at the droplet-air interface may play an important role in these events. (iii) The dissolution and reprecipitation of silica particles may occur in microdroplets. The solubility of quartz in water is influenced by factors such as electrostatic forces, hydration-induced ionization, pH, and Laplace pressure. The interaction between charged silica particles and water droplets is substantial, resulting in the formation of reactive species. We observed the formation of silicate ions during the process (Fig. 5). These ions may reprecipitate under specific conditions. Charged microdroplets can modify surface chemistry, promoting dissolution that leads to nano-sized silica particles. However, these chemical events may occur slowly and therefore may not fully explain the phenomenon of formation of crystalline nanoparticles. (iv) The H₂O radical cation present in the microdroplets (7) can also contribute to the observed phenomenon. To probe this possibility, we analyzed the formation

of nanoparticles from silica by simulating it as a charged system. The H_2O radical cation present in the microdroplets may pull out electrons from silica, and we have simulated the process by removing an electron from the system and adding a compensating jellium background to remove electrostatic divergence of the charged periodic system. Our results confirm that the generalized SFE of slip along the (010) plane is negative [see (0.5, 0.5) slip configuration of the SiO_2 slab in table S7]. (v) The nanoparticles that form may catalyze the fission of microdroplets. This assumption is supported by a study in which it was shown theoretically that nanoparticles actively fragment droplets (12). Accelerated droplet fission further accelerates the particle disintegration. We present a schematic of the fragmentation process in fig. S10.

Atmospheric water droplets, such as clouds and fog, can acquire charges not only because of the ionic species present inside them but also because of contact electrification (13). These charges on naturally occurring droplets cannot be ignored. As we have demonstrated, under the right conditions, electrosprayed microdroplets can break hard particles, including complex minerals, and the potential of naturally occurring atmospheric droplets to do the same needs to be explored. If this process does happen, it would be important for weathering and the production of natural nanoparticles (1). Soil forms through rock weathering, a process that involves multiple factors, and it takes 200 to 400 years to yield 1 cm of it, composed of varied particle sizes. Our study highlights the role of charged microdroplets of water in unprecedented weathering, which, to our knowledge, had not yet been explored. Disintegration of minerals makes nascent surfaces, which may participate in catalysis that leads to new chemical transformations in droplets in the presence of reactive species. "Microdroplet showers" composed of nanoparticles and molecules falling on Earth may be of importance to the chemical and biological evolution of the planet.

REFERENCES AND NOTES

1. M. F. Hochella Jr. *et al.*, *Science* **363**, eaau8299 (2019).
2. Z. Wei, Y. Li, R. G. Cooks, X. Yan, *Annu. Rev. Phys. Chem.* **71**, 31–51 (2020).
3. J. K. Lee, S. Kim, H. G. Nam, R. N. Zare, *Proc. Natl. Acad. Sci. U.S.A.* **112**, 3898–3903 (2015).
4. A. Wortmann *et al.*, *J. Am. Soc. Mass Spectrom.* **18**, 385–393 (2007).
5. D. Sarkar *et al.*, *Adv. Mater. Interfaces* **5**, 1800667 (2018).
6. H. Wei *et al.*, *Proc. Natl. Acad. Sci. U.S.A.* **115**, 7272–7277 (2018).
7. L. Qiu, N. M. Morato, K.-H. Huang, R. G. Cooks, *Front Chem.* **10**, 903774 (2022).
8. D. Zhang, X. Yuan, C. Gong, X. Zhang, *J. Am. Chem. Soc.* **144**, 16184–16190 (2022).
9. M. S. Krivokorytov *et al.*, *Phys. Rev. E* **95**, 031101 (2017).
10. S. Banerjee, S. Mazumdar, *Int. J. Anal. Chem.* **2012**, 282574 (2012).
11. P. Basuri *et al.*, *Chem. Sci.* **13**, 13321–13329 (2022).
12. F. Sicard, J. Toro-Mendoza, A. Striolo, *ACS Nano* **13**, 9498–9503 (2019).
13. Z. Tang, S. Lin, Z. L. Wang, *Adv. Mater.* **33**, e2102886 (2021).

METALLURGY

Shearing brittle intermetallics enhances cryogenic strength and ductility of steels

Feng Wang[1]†, Miao Song[1]†, Mohamed N. Elkot[2,3], Ning Yao[4], Binhan Sun[4], Min Song[1]*, Zhangwei Wang[1]*, Dierk Raabe[2]*

Precipitates are crucial for crafting mechanically strong metallic materials. In this work, we report the dislocation cutting of B2 (ordered body-centered cubic) nanoprecipitates, typically considered nonshearable intermetallics, in a lightweight compositionally complex steel during cryogenic tensile loading. Shearing is enabled by the high strength level for dislocation glide within the austenitic matrix, attributed to the substantial strengthening from subnanoscale local chemical ordering zones and the pronounced solid solution strengthening from the multiprincipal elements in the matrix. This mechanism not only harnesses the intense strengthening and strain hardening provided by otherwise impenetrable brittle nanoprecipitates but also introduces ductility through their sequential shearing with ongoing deformation. Our steel thus showcases ultrahigh cryogenic tensile strength up to 2 gigapascal at a remarkable tensile elongation of 34%. This study reveals a new strategy for designing high-performance structural materials.

The mechanical strength of alloys can be substantially enhanced by the presence of a secondary phase. To achieve a high dispersion of the second phase, quenching and aging of metastable solid solutions at moderate homologous temperature is a standard approach. This process, known as precipitation hardening, has been the basis of strengthening in metallic materials (1) since its introduction in Al alloys more than a century ago (2). The strengthening effect originates from the resistance to dislocation motion, the linear plasticity-carrying lattice defects in metallic materials. This process can proceed either by dispersing coherent particles through which dislocations must pass under higher stress or by forcing dislocations to bypass impenetrable precipitates through Orowan looping, a mechanism in which dislocations wrap around the precipitates, also requiring a stress increment (3). Capillary-driven particle coarsening, a process that occurs during aging, typically shifts the mechanism from the former to the latter, i.e., from dislocation cutting to bowing and looping, whereas the reverse transition typically remains elusive in precipitation-hardened alloy systems (4, 5).

However, the Orowan looping mechanism, although offering substantial strengthening (6), is associated with dislocation pileups around impenetrable particles, which increases the likelihood of material decohesion owing to stress concentrations (7). This phenomenon often renders the interfaces between the matrix and hard particles susceptible to crack nucleation, leading to a substantial reduction in the alloy's ductile compliance and damage-tolerant load-bearing capacity, as quantified through its ductility in uniaxial tensile testing (8, 9). Such a fundamental trade-off problem has triggered efforts to bring coherent nanoprecipitates into alloys that facilitate a

¹State Key Laboratory of Powder Metallurgy, Central South University, Changsha, China. ²Max Planck Institute for Sustainable Materials, Düsseldorf, Germany. ³Department of Metallurgical and Materials Engineering, Suez University, Suez, Egypt. ⁴Key Laboratory of Pressure Systems and Safety, Ministry of Education, East China University of Science and Technology, Shanghai, China.
*Corresponding author. Email: msong@csu.edu.cn (M.S.); z.wang@csu.edu.cn (Z.W.); d.raabe@mpie.de (D.R.)
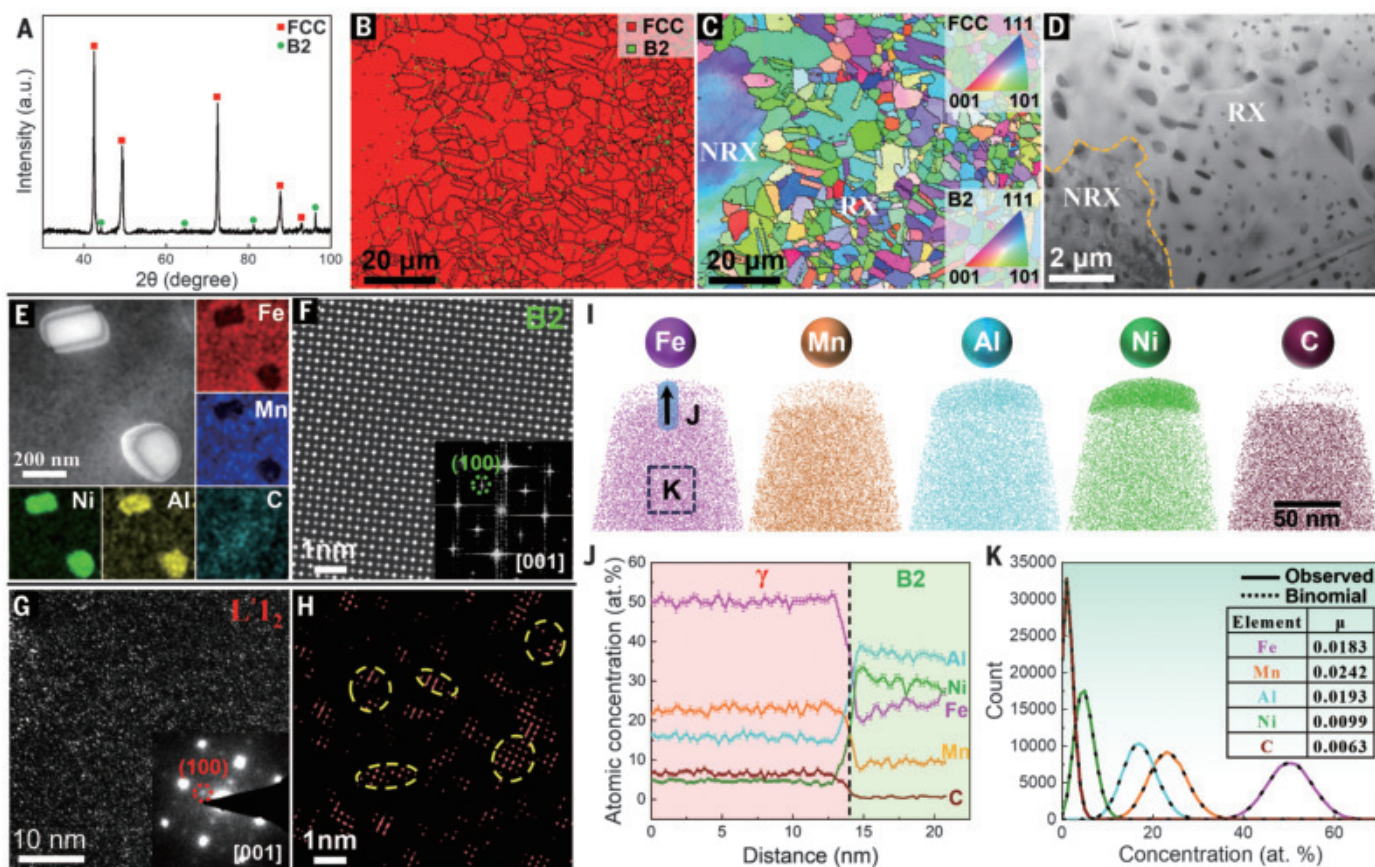†These authors contributed equally to this work.

Fig. 1. Microstructures of the hierarchical CCS. (**A**) X-ray diffraction pattern indicating the peaks of FCC matrix and B2 phase. A.u., arbitrary units; θ, diffraction angle. (**B**) EBSD phase map showing the distributions of FCC and B2 phase. (**C**) EBSD inverse pole figure map revealing the grain sizes in recrystallized (RX) and nonrecrystallized (NRX) regions. (**D**) LAADF-STEM image demonstrating the homogeneous distribution of B2 particles. (**E**) HAADF-STEM image and EDS maps of B2 phases. (**F**) High-resolution HAADF-STEM image and associated FFT pattern (inset) under $[001]_{B2}$ zone axis depicting the ordered atomic structure of the B2 phase. (**G**) TEM dark-field image of L'1₂-type LCO taken by (100) superlattice diffraction in the inserted SAED pattern under the $[001]_\gamma$ zone axis. (**H**) Inverse FFT image, obtained from the extra reflections, revealing the LCO regions (several of which are circled). (**I**) Three-dimensional (3D) reconstructed atomic maps of Fe, Mn, Al, Ni, and C elements. (**J**) 1D compositional profiles across the interface between the matrix and the B2 phase. (**K**) Frequency distribution analysis of atoms within the austenite matrix compared with the ideal binomial random distribution. The μ value characterizes the extent of elemental distribution randomness; 0 signifies complete random distribution, whereas 1 indicates elemental association. At. %, atomic %.

beneficial strength-ductility reconciliation, a strategy exemplified by maraging (*10*) and lightweight steels (*11*), high-strength Al alloys (*12, 13*), and certain medium- or high-entropy alloys (M/HEAs) (*14, 15*).

Challenging this conventional wisdom, we introduce a paradigm shift from Orowan looping to dislocation cutting in a material strengthened by a B2 (ordered body-centered cubic, BCC) intermetallic compound that serves as the precipitate. The B2 phase is historically deemed as nonshearable in face-centered cubic (FCC) alloys during tensile deformation (*6*). This advancement allows us to harness the full potential of the strengthening and strain hardening effects associated with dislocation bowing while also exploiting the ductility benefits through eventual stress relaxation by means of dislocation shearing of these precipitates. We demonstrate this breakthrough in a lightweight compositionally complex steel (CCS) tailored for cryogenic applications, responding to the surging demand for affordable materials that can serve in the transportation sector and for storage of liquid gas energy carrier molecules, the emerging basis of the global energy supply.

Specifically, we have realized the unexpected cut-through of B2 intermetallic compounds during cryogenic deformation of a hierarchically structured CCS. The nanostructure hierarchy encompasses B2 intermetallic nanoprecipitates (~195-nm size) and subnanoscale (~5-Å size) local chemical ordering (LCO) zones. The ordering strengthening, provided by a high number density of LCO zones (3.6×10^{17} m^{-2}), in concert with the solid solution strengthening of the austenite matrix with multiple principal elements, creates a friction stress >1 GPa (*16*). Such a high matrix stress level required for dislocation glide enables the cut-through of the strong yet usually brittle B2 phase by dislocation slip during tensile deformation at near–liquid nitrogen temperature. The reason is that the dislocation flow stress of the matrix has become so high, which allows it to overcome the stress barrier necessary for shearing the B2 particles. This general approach demonstrates that by accomplishing sufficiently high matrix stress levels, the otherwise damage-prone Orowan looping effect can be bolstered into a compliant particle-shearing mechanism without creating damage nucleation at the heterointerfaces. This transition promotes a ductile, rather than a brittle, response of the entire material while also lending the CCS considerable strengthening effect, with ultimate tensile strength up to 2 GPa. Consequently, our study reveals a new path toward the development of strong and ductile metallic materials.
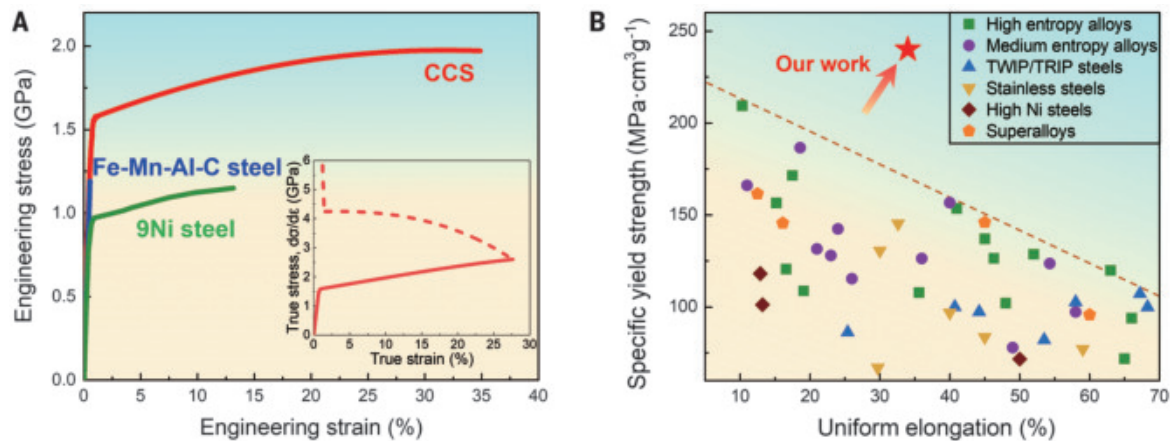
Fig. 2. Cryogenic mechanical properties of the CCS. (**A**) Uniaxial tensile engineering stress-strain curves of the CCS compared with those of age-hardening Fe-Mn-Al-C lightweight steel and 9Ni steel (*24*). (Inset) True stress (solid line) and strain hardening rate (dashed line) curves as a function of true strain of our CCS. σ, true stress; ε, true strain; dσ/dε, strain hardening rate.

(**B**) Comparison of specific yield strength versus uniform elongation of studied CCS with those of reported M/HEAs (*26–47*), TWIP or TRIP steels (*48–51*), stainless steels (*52–56*), high Ni steels (*24, 53*), and superalloys (*57–60*) at the near–liquid nitrogen temperature. The relevant detailed data are listed in table S1.

Results and discussion

We conceived the CCS with a chemical composition of Fe-26Mn-16Al-5Ni-5C (at. %) through a chemically and structurally reengineered Fe-Mn-Al-C lightweight steel based on the concept of HEAs (*17*). Leveraging the multiprincipal element approach from HEAs, we facilitated the formation of subnanoscale LCO, a precursor state of the spinodal decomposition observed earlier in lightweight steels (*18*, *19*), and the formation of B2 nanoprecipitates induced by high Al (16 at. %) and Ni (5 at. %) content (*17*). We produced the CCS by induction melting, followed by cold rolling and annealing at 1000°C for 15 min (*16*). These processing steps sculpted a desirable hierarchical microstructure characterized by finely interspersed LCO and B2 phases across various length scales.

The x-ray diffraction pattern (Fig. 1A) and electron backscatter diffraction (EBSD) phase map (Fig. 1B) reveal a duplex phase structure consisting of the B2 precipitate and the FCC austenite matrix. The EBSD inverse pole figure map (Fig. 1C) shows that the recrystallized region constitutes 77% of the area with an average grain size of 5.5 μm, whereas the remaining 23% is nonrecrystallized with a grain size of 26 μm. The low-angle annular dark-field (LAADF) scanning transmission electron microscopy (STEM) image (Fig. 1D) reveals a uniform distribution of the precipitates in both recrystallized and nonrecrystallized regions with an average size of ~195 nm (fig. S1). The energy-dispersive x-ray spectroscopy (EDS) analysis, based on the high-angle annular dark-field (HAADF) STEM observation (Fig. 1E), demonstrates that the precipitates are enriched in Ni and Al but depleted in Fe, Mn, and C. The periodicity in atomic intensity observed in the high-resolution HAADF-STEM image and extra reflections in fast Fourier transform (FFT) pattern along the [001] zone axis indicate an ordered BCC structure (Fig. 1F). According to these characterizations, the nanoprecipitates in the CCS are identified as NiAl-type B2 intermetallic compounds (*20*).

Subsequently, we examined the subnanoscale LCO within the austenite matrix. The {001} superlattice spots are distinctly visible in the selected-area electron diffraction (SAED) pattern (inset, Fig. 1G) along the [001] zone axis, indicating the formation of L'1$_2$-type (ordered FCC) LCO in the CCS. Using the superlattice reflections, the dark-field TEM image (Fig. 1G) was taken to light up LCO regions, which have an average size of ~5 Å and a number density of 3.6×10^{17} m^{-2} (fig. S1). We further present the inverse FFT image based on HAADF-STEM observations to illustrate the LCO configuration at atomic resolution, as highlighted by the yellow circles in Fig. 1H. The nearly zero lattice misfit (~0.01%) between the LCO regions and the matrix (fig. S2) exhibits superior coherency compared with the typical coherent κ-carbide nanoprecipitates in lightweight steels, which have a lattice misfit of ~2.0% (*21*, *22*). In addition, we performed atom probe tomography to analyze compositional fluctuation across different length scales. Atomic maps (Fig. 1I) show the element partitioning between the B2 nanoprecipitate and its surrounding austenite matrix, consistent with the STEM-EDS results (Fig. 1E). We provide the quantitative analysis of the chemical composition of each phase in Fig. 1J. We conducted a frequency distribution analysis of atoms (Fig. 1K), which revealed a homogeneous distribution of all elements between austenite and LCO. This observation

contrasts markedly with the κ-carbide nanoprecipitates, which exhibit strong partitioning of C (*23*), despite both κ-carbide and LCO having L'1$_2$ structure.

The CCS we examined has an ultrahigh yield strength of 1586 MPa and an ultimate tensile strength of 1976 MPa with a surprisingly high elongation of 34% at near–liquid nitrogen temperature (Fig. 2A). The high yield strength primarily arises from a sharp increase in the solid solution–related friction stress (up to 1 GPa), with precipitation strengthening also making a considerable contribution of 371 MPa (*16*). The pronounced strain hardening capability (inset, Fig. 2A) results in a substantial increase in strength (~390 MPa) during plastic deformation of the CCS, despite its already high yield strength. Such remarkable mechanical performance surpasses that of a 9Ni steel, a well-established steel used for cryogenic applications (*24*), serving in this work as a reference alloy. This achievement underscores that our hierarchical CCS, composed of B2 particles and LCO across varying length scales, resolves the challenges posed by traditional L'1$_2$ κ-carbide coherent precipitation hardening approaches in austenitic Fe-Mn-Al-C lightweight steels, which induced severe embrittlement owing to the stress concentration arising from coherency strains under cryogenic conditions (*25*) (Fig. 2A and fig. S3). Moreover, the combination of specific yield strength (~240 MPa·cm^3·g^{-1}) and uniform elongation (34%) of the CCS causes it to outperform M/HEAs (*26–47*), which are particularly renowned for excellent cryogenic mechanical properties, as well as representative steels for cryogenic applications, such as twinning-induced plasticity (TWIP) or transformation-induced plasticity (TRIP) steels (*48–51*), stainless

Fig. 3. The shear of LCO and B2 particle by dislocation slip.
(**A**) HAADF-STEM image showing the planar slip dislocations and sheared B2 particle at 3% strain. (**B** and **C**) Atomic structure evolution outside (B) and inside (C) the planar slip dislocation channels marked in (A). (i) High-resolution TEM images along the $[001]_\gamma$ zone axes (dislocations highlighted by yellow symbols). (ii) Corresponding FFT patterns and (iii) inverse FFT images obtained from the extra reflections showing the existence of L'1_2-type LCO (several of which are circled). (iv) Atomic elastic strain (ε_{xy}) distribution maps based on high-resolution TEM images. The horizontal (*x*) and vertical (*y*) directions correspond to the g vectors of the pink and green circles in FFT patterns. (**D**) EDS maps of the sheared B2 particle.
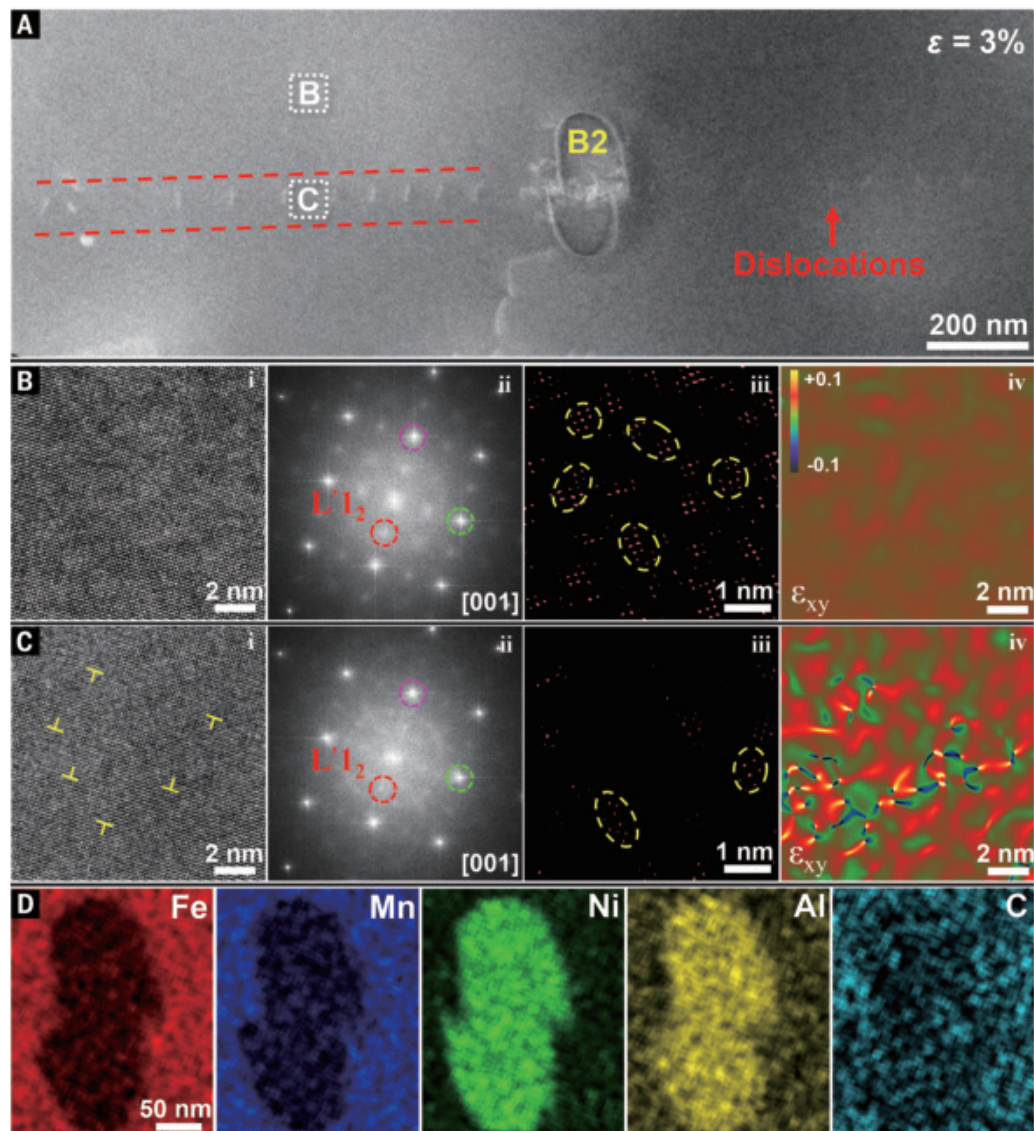
steels (*52–56*), high-Ni steels (*24, 53*), and superalloys (*57–60*) (Fig. 2B). Further considering the cost-effective composition (fig. S4), our CCS emerges as a promising alternative for structural materials in cryogenic environments.

To elucidate the underlying mechanisms responsible for the cryogenic mechanical properties, we investigated the deformation substructures of the CCS under low (~3%), medium (~10%), and high (~34%) engineering strains. We observed the interactions between dislocation slip and the LCO and B2 nanoprecipitates after initial plastic yielding (Fig. 3A). At a low strain of 3%, we detected the typical planar slip of dislocations commonly found in previously studied austenitic lightweight steels (*18*). The impact of the LCO on dislocation activities was revealed through high-resolution TEM observations [Fig. 3, B (i) and C (i)]. Comparatively, the (100) superlattice spot intensity is weaker inside the planar slip region than in

the area outside the dislocation-sheared region [Fig. 3, B (ii) and C (ii), and fig. S5]. Correspondingly, the inverse FFT images show that LCO zones occupy fewer areas after dislocation slip [Fig. 3, B (iii) and C (iii)]. These observations collectively suggest a gradual shear-enhanced dissolution of LCO induced by dislocation slip. We further conducted a geometrical phase analysis to detect the atomic strain fluctuations related to the interactions between dislocations and LCO. We observed a larger atomic strain field [Fig. 3, B (iv) and C (iv)] after planar dislocation slip, as the dislocations interacting with LCO created a higher level of lattice distortion compared with that of regions outside the slip region. The breaking of LCO produces extra resistance to dislocation motion, enhancing the strain hardening effect (*61*).

Contrary to the traditionally expected Orowan looping, we detected the cut-through of a B2

particle by planar slip of dislocations (Fig. 3A), further corroborated by its shape misalignment visible in the EDS maps (Fig. 3D), although dislocation bowing predominates at the onset of plastic deformation (fig. S6). To date, Orowan looping has been regarded as strengthening mechanism for hard impenetrable precipitates in a relatively soft FCC matrix (*18, 62*), which was also evidenced by pileups of high numbers of dislocations at the austenite-B2 interfaces in our CCS exposed to room temperature loading (fig. S7). Dislocation penetration and shearing of ultrastrong intermetallic compounds, previously considered nonshearable, through slip of dislocations in a high-strength FCC matrix hardened by LCO during tensile deformation, are indeed notable observations.

We uncovered the underlying shearing mechanism within the B2 particle through dislocation slip at a medium tensile strain of 10% (Fig. 4, A to E). As shown in the SAED pattern

Fig. 4. Microstructure evolution of the CCS during cryogenic tensile deformation. (**A**) LAADF-STEM image showing the cut-through of the B2 particle by dislocation slip at 10% strain. (**B**) Superimposed SAED pattern of the B2 and austenitic matrix along the $[10\bar{1}]_\gamma$ zone axis. (**C**) High-resolution HADDF-STEM image of the interface between austenitic matrix and B2 particle [marked region in (A)]. (**D**) The atomic image showing the decomposition of an $a/2\langle 011\rangle$ full dislocation into a 30° Shockley partial and a 90° Shockley partial in the austenitic matrix. b, Burgers vector. (**E**) The atomic image revealing an $a/2\langle 111\rangle$ full dislocation in the B2 particle. S and F indicate the starting and ending points of a Burgers circuit, respectively. Green arrows near S and F reveal the Burgers vector direction. (**F**) LAADF-STEM image of stacking fault nanobundles. The inserted high-resolution HADDF-STEM image shows faulted atomic planes (marked by the red line). (**G**) TEM dark-field image of parallel mechanical nanotwins at 34% strain, with an inset showing corresponding SAED pattern along the $[01\bar{1}]_\gamma$ zone axis. (**H**) High-resolution HADDF-STEM image of nanotwins along the $[01\bar{1}]_\gamma$ zone axis. TB, twin boundary. (**I**) LAADF-STEM image of a sheared B2 particle.
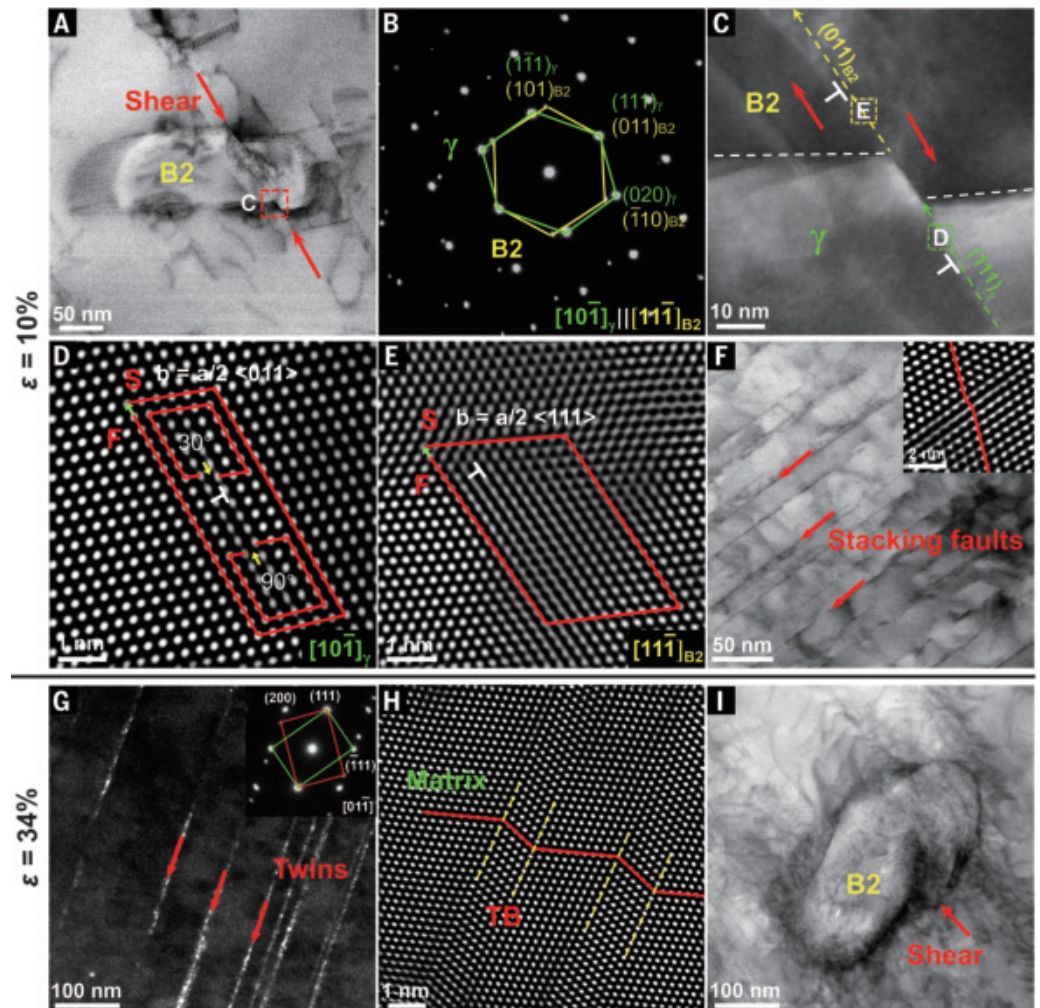
(Fig. 4B), the B2 particle traversed by dislocations (Fig. 4A) displays the Kurdjumov-Sachs (K-S) orientation relationship with the surrounding austenite matrix (Fig. 4B). A similar orientation relationship has been widely observed in various HEAs (*63, 64*). The zoomed-in HAADF-STEM image (Fig. 4C) shows the formation of a step with dozens of atomic-layers thickness (~11 nm) at the austenite-B2 interface. The high-resolution atomic configuration (Fig. 4D) revealed the existence of an $a/2\langle 011\rangle$ full dislocation (a, lattice constant) on the (111) slip plane within the matrix. Upon closer examination, the full dislocation has dissociated into two partial dislocations enclosing a short stacking fault (~5 nm). In addition, the dislocation slip plane (111) is aligned with the shearing plane within the B2 phase [(011)$_{B2}$] (Fig. 4C). Then, as we illustrate in Fig. 4E, an $a/2\langle 111\rangle$ dislocation slips in parallel with the (011)$_{B2}$ plane in the sheared B2 region. The shearing process involves full dislocations within the matrix that slip toward the austenite-B2 interphase, thereby initiating the nucleation and slipping of full dislocations within the B2 phase, parallel to the initial slipping plane in

the matrix. This continuous nucleation and slipping of full dislocations culminate in the formation of steps at the austenite-B2 interphase, the size of which is determined by the Burgers vector and the number of dislocations. Notably, under severe plastic deformation, various slipping systems within the matrix can be triggered. Nevertheless, the ease with which B2 particles can be sheared is closely related to the Schmid (orientation) factors of their slip systems and the external load. Using the Schmid factors for the various slip systems [see (*16*) on the shearing of B2 particles] and comparing them with our experimental results (Fig. 4, A to E) shows that the shearing path of the B2 particle preferentially propagates toward slip systems with the largest Schmid factors (0.487) (Fig. 4A). This observation is also corroborated by other sheared B2 phases (fig. S8), wherein the mismatch steps are negligible (≤4 nm) when the slip plane of the precipitate does not align well with the surrounding matrix, i.e., when the Schmid factor is small (≤0.396).

We also detected numerous stacking faults, as we confirmed by the high-resolution HAADF-

STEM image at the deformation stage of ~10% strain, that are arranged parallel to one another along the (111) slip plane (Fig. 4F). As deformation progresses toward the fracture strain (~34%), except for stacking faults, plenty of mechanical nanotwins appear in the austenite matrix (Fig. 4G). The high-resolution HAADF-STEM image captures the twinning of atomic planes under a common crystallographic $[01\bar{1}]_\gamma$ axis (Fig. 4H). The formation of abundant stacking faults and nanotwins, typically seen in materials with low stacking-fault energy (*65*), is a critical finding in this CCS under cryogenic load, as deformation at room temperature is entirely governed by dislocation slip owing to the alloy's very high stacking-fault energy (fig. S7).

We attribute the emergence of stacking faults and nanotwins in our CCS to a decreased stacking-fault energy at a lower temperature coupled with the enhanced flow stress encountered during cryogenic deformation. The stacking-fault energy decreased to 36 mJ/m^2 at near–liquid nitrogen temperature (*16*), similar to previous observations in M/HEAs (*66*) and austenitic steels (*65*). This

effect enables the activation of stacking faults and mechanical twinning. Furthermore, a high stress level, reaching a true stress of 1973 MPa at 10% strain (Fig. 2), promotes the formation of stacking faults and mechanical twinning (67). These planar defects introduce a high density of additional interfaces, impeding dislocation motion by reducing their mean free path, an effect that leverages substantial strengthening and strain-hardening effects (65, 68). The enhanced flow stress thus augments the shearing capability of dislocations. As a result, the majority of the B2 particles (85.7%) were found to have been undergoing shearing at high strains close to fracture (Fig. 4I and fig. S9).

At near–liquid nitrogen temperatures, the cut-through of B2 intermetallic particles by dislocations within the FCC austenite matrix in the CCS (Figs. 3 and 4) defies traditional wisdom, as dislocation bowing for hard intermetallic is the dominant observation across various FCC alloys—e.g., steels (18), Al alloys (69), Ni alloys (70), and M/HEAs (71)—whereas dislocation shearing prevails for coherent precipitation-hardened alloy systems (3). This distinct feature arises from an extremely high friction stress, >1 GPa at near-cryogenic temperatures (16), caused by the LCO zones and the high solid solution friction stress, which both enhance the resistance to dislocation glide in the austenitic matrix. Thus, with the addition of the pileup stresses from the planar slip of dislocations at 3% strain, the resolved shear stress acting on the B2-phase slip systems with the highest Schmid factor surpassed the critical value required for the shearing of B2 particles (16). The fraction of sheared B2 particles rose rapidly from between ~5.6 and 7.1% to 85.7% as the strain increased from 3 to 34% (16) as the flow stress increased greatly owing to the additional strain hardening provided by stacking faults and twinning. The sequential cut-through of B2 particles effectively mitigates the stress concentration at the heterointerfaces between austenite and B2 particles, which further inhibits the potential nucleation of cracks. Such resilience to damage, which is less observed in conventional metallic materials reinforced by hard intermetallic compounds, together with the activation of multiple strain hardening mechanisms within the austenite matrix, leads to unparalleled strength and ductility of the material at near–liquid nitrogen temperature.

Conclusions

Precipitation hardening by the use of a finely dispersed second phase in metallic alloys is a fundamental principle in the design of structural materials. We report a paradigm shift in this principle, revealing that brittle, incoherent, and nonshearable B2 intermetallics can be made ductile through strengthening the adjacent austenite matrix through LCO and massive solid-solution strengthening. This paradigm is realized by changing the deformation mechanism around the B2 particles from Orowan looping and dislocation pileup to particle shearing. With this approach, we add a newly described deformation mechanism to the field, which opens up opportunities of applying intermetallic phases as ductile strengthening features in ultrahigh strength and yet ductile metallic alloys to be unleashed.

REFERENCES AND NOTES

1. T. H. Courtney, *Mechanical Behavior of Materials* (Waveland Press, 2005).
2. A. Wilm, *Metallurgie* **8**, 223 (1911).
3. A. J. Ardell, *Metall. Trans., A, Phys. Metall. Mater. Sci.* **16**, 2131–2165 (1985).
4. Z. L. Guo, W. Sha, *Mater. Trans.* **43**, 1273–1282 (2002).
5. T. Gladman, *Mater. Sci. Technol.* **15**, 30–36 (1999).
6. S. H. Kim, H. Kim, N. J. Kim, *Nature* **518**, 77–79 (2015).
7. Z. P. Xiong, I. Timokhina, E. Pereloma, *Prog. Mater. Sci.* **118**, 100764 (2021).
8. M. F. Ashby, *Philos. Mag.* **14**, 1157–1178 (1966).
9. E. Nembach, *Particle strengthening of metals and alloys* (Wiley Interscience, 1997).
10. S. Jiang et al., *Nature* **544**, 460–464 (2017).
11. G. Frommeyer, U. Brüx, *Steel Res. Int.* **77**, 627–633 (2006).
12. W. Sun et al., *Science* **363**, 972–975 (2019).
13. H. Xue et al., *Nat. Mater.* **22**, 434–441 (2023).
14. T. Yang et al., *Science* **362**, 933–937 (2018).
15. Y. Yang et al., *Nature* **595**, 245–249 (2021).
16. Materials and methods are available as supplementary materials.
17. Z. Wang et al., *Sci. Adv.* **6**, eaba9543 (2020).
18. S. P. Chen, R. Rana, A. Haldar, R. K. Ray, *Prog. Mater. Sci.* **89**, 345–391 (2017).
19. C. Y. Chao, L. K. Hwang, T. F. Liu, *Scr. Metall. Mater.* **29**, 647–650 (1993).
20. R. D. Noebe, R. R. Bowman, M. V. Nathal, *Int. Mater. Rev.* **38**, 193–232 (1993).
21. W. W. Song, W. Zhang, J. von Appen, R. Dronskowski, W. Bleck, *Steel Res. Int.* **86**, 1161–1169 (2015).
22. W. K. Choo, J. H. Kim, J. C. Yoon, *Acta Mater.* **45**, 4877–4885 (1997).
23. M. J. Yao et al., *Acta Mater.* **106**, 229–238 (2016).
24. J. R. Strife, D. E. Passoja, *Metall. Trans., A, Phys. Metall. Mater. Sci.* **11**, 1341–1350 (1980).
25. M. N. Elkot, B. H. Sun, X. Y. Zhou, D. Ponge, D. Raabe, *Acta Mater.* **241**, 118392 (2022).
26. S. J. Sun et al., *Mater. Sci. Eng. A* **740-741**, 336–341 (2019).
27. B. Gludovatz et al., *Science* **345**, 1153–1158 (2014).
28. Q. Ding et al., *Nature* **574**, 223–227 (2019).
29. Y. H. Jo et al., *Nat. Commun.* **8**, 15719 (2017).
30. Y. Tong et al., *Acta Mater.* **165**, 228–240 (2019).
31. D. Y. Li et al., *Acta Mater.* **123**, 285–294 (2017).
32. T. Yang et al., *Scr. Mater.* **164**, 30–35 (2019).
33. S. B. Wang et al., *Acta Mater.* **201**, 517–527 (2020).
34. X. C. Wen et al., *Scr. Mater.* **231**, 115434 (2023).
35. T. Bhattacharjee et al., *Mater. Chem. Phys.* **210**, 207–212 (2018).
36. K. Tang et al., *Mater. Sci. Eng. A* **808**, 140927 (2021).
37. Q. Pan et al., *Science* **382**, 185–190 (2023).
38. Z. F. He et al., *Mater. Sci. Eng. A* **759**, 437–447 (2019).
39. N. Yao et al., *Acta Mater.* **236**, 118142 (2022).
40. D. D. Zhang, J. Y. Zhang, J. Kuang, G. Liu, J. Sun, *Acta Mater.* **220**, 117288 (2021).
41. D. D. Zhang, J. Y. Zhang, J. Kuang, G. Liu, J. Sun, *Acta Mater.* **233**, 117981 (2022).
42. D. C. Yang, Y. H. Jo, Y. Ikeda, F. Körmann, S. S. Sohn, *J. Mater. Sci. Technol.* **90**, 159–167 (2021).
43. Z. Jiang et al., *J. Mater. Sci. Technol.* **100**, 20–26 (2022).
44. H. Kwon et al., *Scr. Mater.* **204**, 114157 (2021).
45. J. Moon et al., *Scr. Mater.* **186**, 24–28 (2020).
46. K. Górecki, P. Bała, W. Bednarczyk, J. Kawałko, *Mater. Sci. Eng. A* **745**, 346–352 (2019).
47. J. Lee, J. W. Bae, P. Asghari Rad, H. S. Kim, *Scr. Mater.* **211**, 114511 (2022).
48. L. Tang et al., *Acta Mater.* **200**, 943–958 (2020).
49. S. S. Sohn et al., *Acta Mater.* **100**, 39–52 (2015).
50. C. S. Li, K. Li, J. B. Dong, J. K. Wang, Z. B. Shao, *Mater. Sci. Eng. A* **809**, 140998 (2021).
51. Q. Luo et al., *Mater. Sci. Eng. A* **753**, 91–98 (2019).
52. C. S. Zheng, W. W. Yu, *Mater. Sci. Eng. A* **710**, 359–365 (2018).
53. W. S. Park, M. S. Chun, M. S. Han, M. H. Kim, J. M. Lee, *Mater. Sci. Eng. A* **528**, 5790–5803 (2011).
54. X. R. Li et al., *J. Mater. Res. Technol.* **22**, 3375–3386 (2023).
55. N. Koga, T. Nameki, O. Umezawa, V. Tschan, K. P. Weiss, *Mater. Sci. Eng. A* **801**, 140442 (2021).
56. S. S. Wu et al., *Cryogenics (Guildf.)* **121**, 103388 (2022).
57. D. Wang et al., *Intermetallics* **155**, 107836 (2023).
58. Y. Wang, J. S. He, P. P. Hu, C. B. Xiao, X. T. Wang, *Mater. Des.* **236**, 112450 (2023).
59. Y. Q. Wang et al., *Mater. Charact.* **206**, 113422 (2023).
60. Y. Ono et al., *Mater. Trans.* **45**, 342–345 (2004).
61. X. Chen et al., *Nature* **592**, 712–716 (2021).
62. N. Ali et al., *Mater. Today Commun.* **33**, 104686 (2022).
63. R. Feng et al., *Nat. Commun.* **12**, 3588 (2021).
64. S. Dasari et al., *Acta Mater.* **202**, 448–462 (2021).
65. B. C. De Cooman, Y. Estrin, S. K. Kim, *Acta Mater.* **142**, 283–362 (2018).
66. W. D. Li et al., *Prog. Mater. Sci.* **118**, 100777 (2021).
67. Z. Wang et al., *Nat. Commun.* **13**, 3598 (2022).
68. Q. Pan et al., *Science* **374**, 984–989 (2021).
69. R. N. Lumley, *Fundamentals of Aluminium Metallurgy: Production, Processing and Applications* (Woodhead Publishing, 2011).
70. G. Gudivada, A. K. Pandey, *J. Alloys Compd.* **963**, 171128 (2023) Review.
71. L. Liu et al., *Adv. Sci. (Weinh.)* **8**, e2100870 (2021).

BIOMATERIALS

Active biointegrated living electronics for managing inflammation

Jiuyun Shi[1]†, Saehyun Kim[1]†, Pengju Li[2], Fuying Dong[3], Chuanwang Yang[4], Bryan Nam[5], Chi Han[3], Ethan Eig[1], Lewis L. Shi[6,7], Simiao Niu[3]*, Jiping Yue[1]*, Bozhi Tian[1,4,8]*

Seamless interfaces between electronic devices and biological tissues stand to revolutionize disease diagnosis and treatment. However, biological and biomechanical disparities between synthetic materials and living tissues present challenges at bioelectrical signal transduction interfaces. We introduce the active biointegrated living electronics (ABLE) platform, encompassing capabilities across the biogenic, biomechanical, and bioelectrical properties simultaneously. The living biointerface, comprising a bioelectronics layout and a *Staphylococcus epidermidis*–laden hydrogel composite, enables multimodal signal transduction at the microbial-mammalian nexus. The extracellular components of the living hydrogels, prepared through thermal release of naturally occurring amylose polymer chains, are viscoelastic, capable of sustaining the bacteria with high viability. Through electrophysiological recordings and wireless probing of skin electrical impedance, body temperature, and humidity, ABLE monitors microbial-driven intervention in psoriasis.

iomaterials that synergistically incorporate biomechanical (*1–3*), biogenic (*4–6*), and bioelectrical (*7–9*) properties offer the potential to establish lifelike, seamless, and multifaceted biointerfaces with tissues. Bioelectronics, in particular, have become indispensable for capturing physiological signals (*10–13*), monitoring inflammation as a diagnostic tool (*14, 15*), and executing biological modulation for targeted treatments (*16, 17*). However, the primary challenge with traditional bioelectronics is their integration with biological tissues, which arises from disparities in mechanical, chemical, and biological attributes (Fig. 1, A and B) (*18, 19*). The mechanical discrepancies in bioelectronics can lead to interfacial discontinuities, compromising signal fidelity (*20, 21*). Although hydrogels act as an intermediary layer to bridge the mechanical gap between electronics and biological systems, they may fall short in providing the necessary cellular functions for tissue modulation (Fig. 1C) (*22, 23*). Consequently, contemporary bioelectronics, when used to monitor inflammatory conditions, lack the biogenic capacity for concurrent immunoregulation (*14*). This limitation restricts the versatility of bioelectronics in addressing the complexi-

ties of various diseases. To expand the role of bioelectronics in tissue restoration and monitoring, there is a pressing need to design interface with enhanced bioactivity. Inherent biological systems such as bacteria and mammalian cells naturally exhibit cellular signal generation and transmission, which may be leveraged for inflammation management (*24*). However, the integration of these living entities into bioelectronics remains a challenge, mainly due to the absence of precise control mechanisms and a thorough understanding of the dynamics between foreign cells and host diseases.

We introduce the active biointegrated living electronics (ABLE) platform (Fig. 1, D and E). The ABLE platform comprises a living hydrogel at the tissue-electronics interface to impart essential biogenic properties for skin immunoregulation. The skin commensal bacterium *Staphylococcus epidermidis* from human skin flora was chosen as the living component in biointerfaces, which provides bioelectronics with capabilities to regulate inflammation and promote skin regeneration. The ABLE platform multifunctionality arises from synergistic interaction between the biogenic, biomechanical, and bioelectrical realms (Fig. 1B). Biogenic polymers enhance bacterial viability (Fig. 1B, item 1), and the bacteria themselves modulate the skin's immune environment (Fig. 1B, item 2). The bioelectronics within the system facilitate electrical sensing (e-sensing) to gather information from the skin (Fig. 1B, item 3) and utilize electrical stimulation (e-stimulation) to manage the biosafety of bacteria (Fig. 1B, item 4), addressing long-standing biohazard concerns of handling synthetic living materials with opportunistic pathogens (*25, 26*). The living hydrogel plays multiple roles: Its encapsulation fosters prolonged bacterial storage and viability (Fig. 1B, item 5), and its viscoelastic properties ensure stable skin interaction (Fig. 1B, item 6),

aid in information collection from the skin (Fig. 1B, item 7), and assist in biohazard management (Fig. 1B, item 8). Lastly, the hydrogel's skin-adhesion property facilitates long-term data acquisition (Fig. 1B, item 9).

Design and evaluation of the biogenic matrix in ABLE

We chose a hydrogel composite as the primary matrix for the living ABLE biointerface owing to its biomechanical and structural resemblance to biological tissues (*19*). We incorporated *S. epidermidis* as the living component, because this species is part of the human skin flora and can modulate biological activity in skin cells (*27*). To ensure the functionality of the living biointerface, the hydrogel matrix must support bacterial viability, with bioelectrical and biomechanical capabilities for interfacing with electronics and biological tissue.

In designing a hydrogel matrix conducive to the long-term viability of *S. epidermidis* (Fig. 1B, item 1), we drew inspiration from natural biofilms that promote bacterial survival and community regulation (*28*). To emulate the major biofilm components of proteinaceous matrix and exopolysaccharides, we created a biocompatible hydrogel matrix using a dual network of protein and polysaccharide polymers (Fig. 2A). We selected gelatin as the main protein matrix given its natural origin and superior hydrogel-forming properties (*29*). Compared with synthetic hydrogels such as polyacrylamide, gelatin exhibited superior biocompatibility with the bacteria, while also providing a natural environment for bacterial colony growth (fig. S1). To identify the polysaccharide component, we screened a library of materials including various biogenic and synthetic polymers. Tapioca starch best supported *S. epidermidis* viability and was selected as the polysaccharide (Fig. 2, B and C; table S1; and fig. S2). We further applied a gelatinization and retrogradation process through a heating-cooling cycle. This process diminished the crystallinity of the starch, altering the granular morphology and diffusing out the granule-enclosed amylose (Fig. 2D and fig. S3). The hydrated starch with exposed amylose content formed a biocompatible network with which bacteria interact (Fig. 2, C and E, and fig. S4). Gelatinization of starch prolongs bacterial viability inside hydrogel matrix (Fig. 2F). Altogether, we crafted a protein-polysaccharide hydrogel for bacterial encapsulation and immobilization (Fig. 2E and figs. S5 and S6), which promoted prolonged bacterial viability of at least 4 days (Fig. 2F). Additionally, the freeze-dried living hydrogel can be preserved for 30 days at −80°C. Owing to the hydrogel's ability to support bacterial growth, any loss of bacterial viability during storage can be recovered beyond its initial level by allowing the rehydrated hydrogel to sit at room temperature overnight. This feature, along with the

¹Department of Chemistry, University of Chicago, Chicago, IL 60637, USA. ²Pritzker School of Molecular Engineering, University of Chicago, Chicago, IL 60637, USA. ³Department of Biomedical Engineering, Rutgers University, Piscataway, NJ 08854, USA. ⁴The James Franck Institute, University of Chicago, Chicago, IL 60637, USA. ⁵Department of Biomedical Engineering, Columbia University, New York, NY 10027, USA. ⁶Pritzker School of Medicine, University of Chicago, Chicago, IL 60637, USA. ⁷Molecular Oncology Laboratory, Department of Orthopaedic Surgery and Rehabilitation Medicine, The University of Chicago Medical Center, Chicago, IL 60637, USA. ⁸The Institute for Biophysical Dynamics, University of Chicago, Chicago, IL 60637, USA.
*Corresponding author. Email: btian@uchicago.edu (B.T.); jipingyue@uchicago.edu (J.Y.); simiao.niu@rutgers.edu (S.N.)
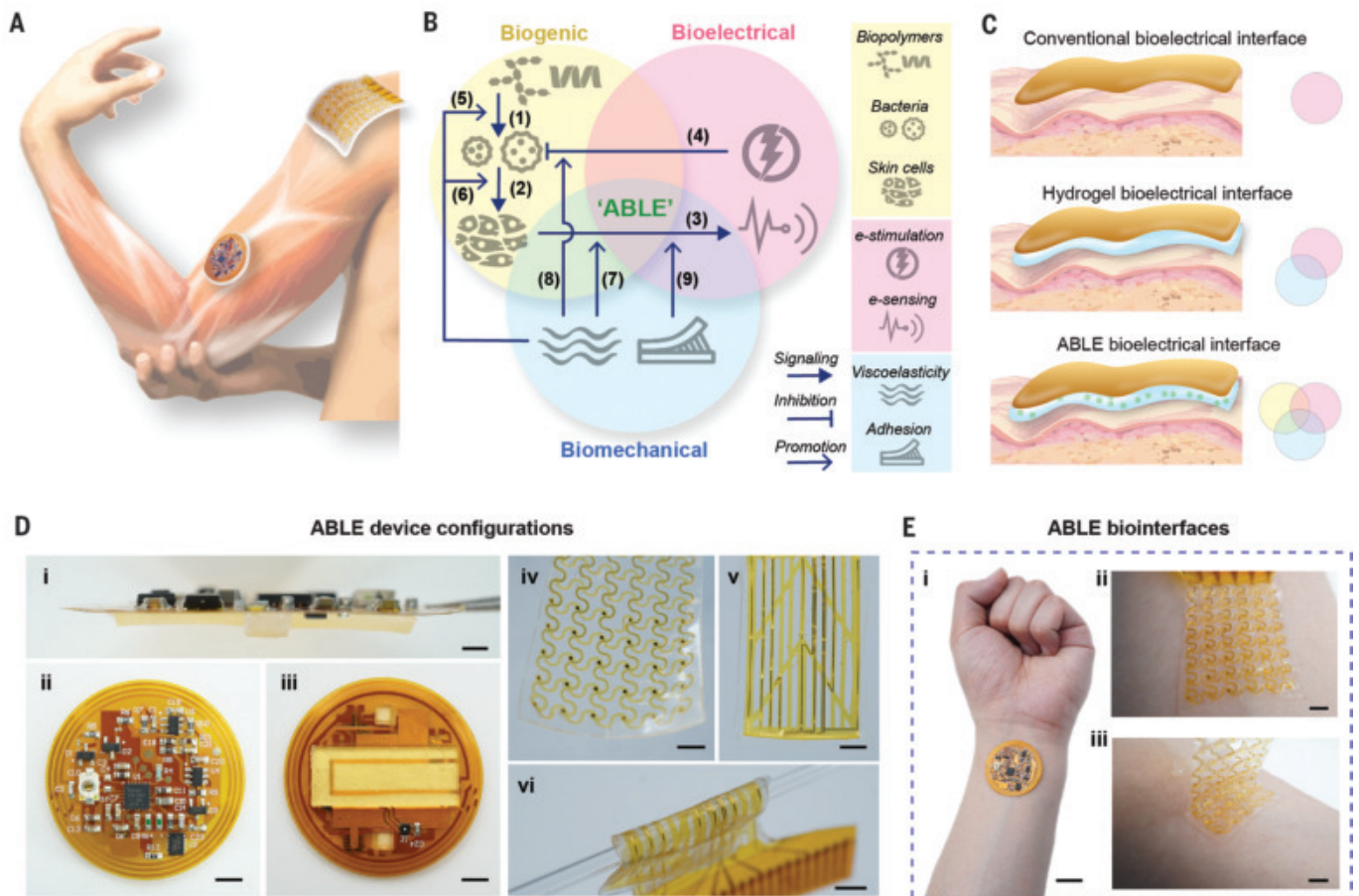†These authors contributed equally to this work.

Fig. 1. Living bioelectronics device with bioactive interface enables wireless skin disease diagnosis and therapy. (**A**) Schematic illustrates that living bioelectronics enable information collection, disease diagnosis, and therapy delivery. (**B**) The interplay across the three key dimensions through bioelectronics, hydrogel, and bacteria is crucial for biointegrated living electronics functionality. (1) Biopolymer enhances bacterial viability. (2) Bacteria modulate the skin immune environment. (3) Bioelectronics collects information from skin through electrical sensing (e-sensing). (4) Bioelectronics manages the biosafety of bacteria through electrical stimulation (e-stimulation). (5) Hydrogel encapsulation promotes long-term storage and viability of bacteria. (6) Viscoelasticity of the living hydrogel ensures a stable interaction with skin tissue. (7) Viscoelasticity of the hydrogel facilitates information collection from skin. (8) Biomechanical properties of the hydrogel assist biohazard management. (9) Skin-adhesion property of the hydrogel improves long-term information collection. (**C**) Compared to conventional bioelectronics interfaces, ABLE combines functionalities across the bioelectrical, biomechanical, and biogenic domains. (**D**) Photographs display the various ABLE device configurations. Scale bars: (i) 2 mm; (ii), (iii) 4 mm; (iv), (v), (vi) 3 mm. (**E**) Photographs show the ABLE bioelectrical interfaces. Scale bars: (i) 15 mm; (ii) 3 mm; (iii) 5 mm.

stability of electronic devices, indicates potential for industrialization and distribution (Fig. 1B, item 5, and Fig. 2G and fig. S7).

The living hydrogels display favorable bioelectrical and biomechanical characteristics, facilitating integration of bioelectronic devices with biological tissues (Fig. 1B, items 7 and 9). We observed the low impedance of the living hydrogels, <500 Ω at physiologically relevant frequencies of 10^2 to 10^5 Hz, using electrochemical impedance spectroscopy (EIS) (fig. S8). The living hydrogels have a high water content (>75%), possess tissue-compliant ultra-softness (shear modulus of 4 kPa), and remain stable across environmental variations (figs. S9 to S11). Further, the gelatinization process increases polymer chain mobility and enhances molecular interactions between the starch and gelatin polymers, as indicated by Fourier transform infrared analysis, which showed a shift of spectral features in the amide I region from 1600 to 1700 cm^{-1} (fig. S12). Intermolecular interactions enable more energy dissipation during mechanical deformation and thereby endow the living hydrogel with tissue-like viscoelasticity. The strain- and frequency-dependent modulus, fast stress relaxation, and mechanical hysteresis further confirmed the viscoelasticity (fig. S9). Such tissue-mimicking biomechanical properties promote a conformal biointerface with tissues, for seamless integration of bioelectronics (fig. S13). The biomechanical properties of the hydrogel are also adjustable for various tissue applications (fig. S14). The mechanical and electrochemical properties of the hydrogels are stable over a long period of time for electrophysiological recording (fig. S15). Furthermore, the abundance of hydroxyl groups in the starch polymer endows the living hydrogel with adhesive properties, enhancing the stability of the bioelectronic devices on the tissue (fig. S16).

We constructed a 15-channel mesh electronics array from bipolar input for surface electromyography (sEMG) intensity mapping (Fig. 2H and figs. S17 to S19). The living hydrogel was integrated with the multichannel array through spin-coating gel-casting techniques (fig. S20). We interfaced the electrophysiology-based ABLE device with the skin on a rat's leg and recorded the EMG signals evoked by sciatic nerve stimulation (fig. S21). The ABLE device formed conformal and adhesive interfaces with the skin on the rat leg and recorded the EMG
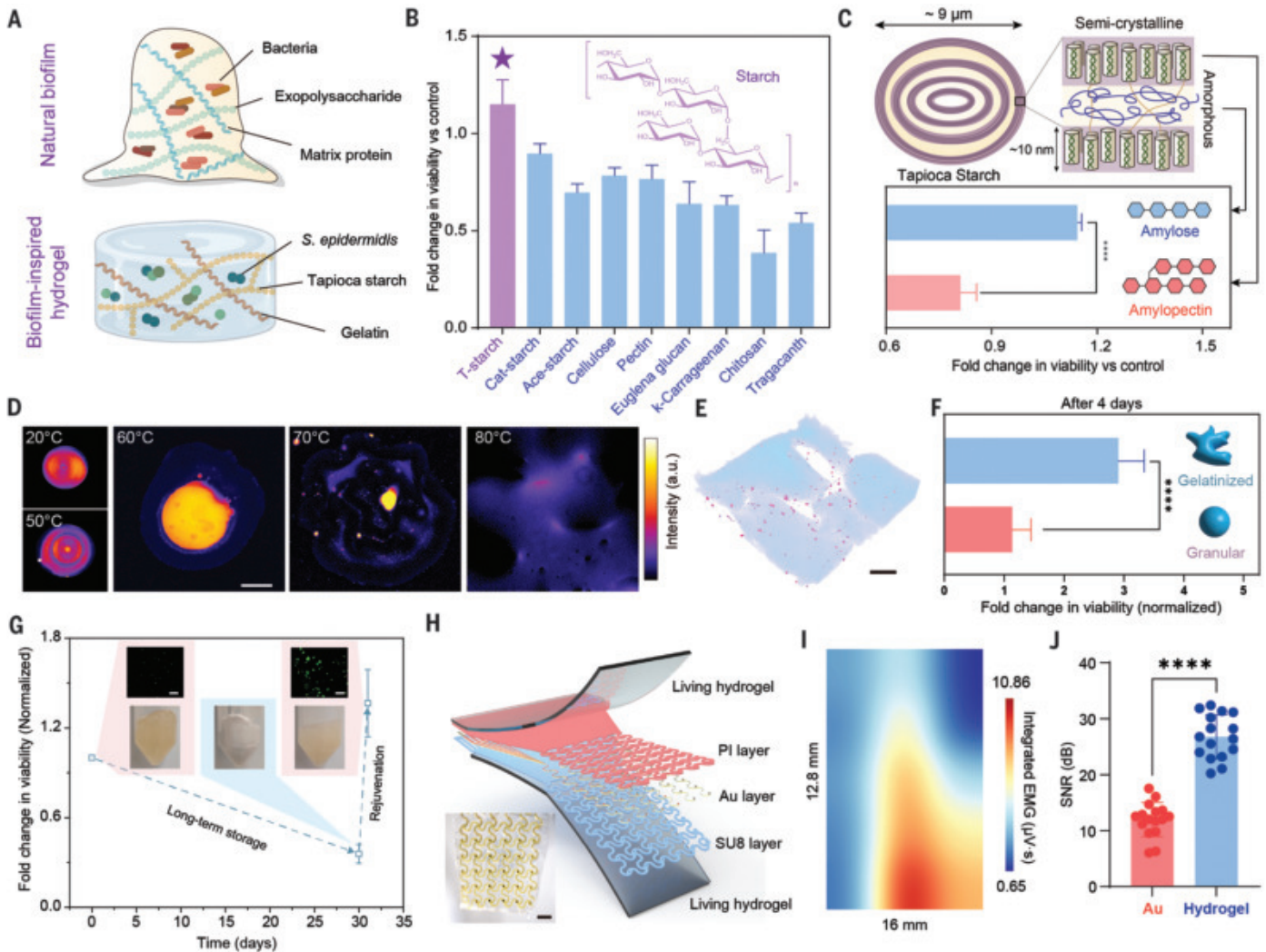
Fig. 2. Rational design of living biointerface for bioelectronics with biogenic, biomechanical, and bioelectrical functionality. (**A**) Mimicking the natural composition of biofilm, gelatin and starch are used as the protein and polysaccharide polymer in constructing the double network hydrogel, i.e., the living biointerface. (**B**) Tapioca starch best sustains bacteria viability among various polysaccharides. $n = 5$ independent experiments. (**C**) During gelatinization, amylose leaks from the amorphous lamella inside the starch granules and enhances bacteria viability. $n = 5$ independent experiments. (**D**) Fluorescent images indicate the structural transformation of starch granules after thermal treatment at different temperatures. Scale bar, 10 μm. (**E**) Confocal microscope imaging shows the distribution of *S. epidermidis* inside the living hydrogel matrix. Bacteria are stained with FM1-43 (red) and starch is stained with 8-amino-1,3,6-pyrenetrisulfonic acid (blue). Scale bar, 15 μm. (**F**) Gelatinization of starch promotes bacteria viability in the living hydrogel matrix for at least 4 days. $n = 5$ independent experiments. (**G**) Bacteria can be stored within the hydrogel matrix over a long-term period and rejuvenated with an overnight culture. Scale bar, 20 μm. $n = 5$ independent experiments. (**H**) Schematic diagram and photograph show the structural configuration of the living hydrogel hybrid mesh electronics device for sEMG recording. Scale bar, 3 mm. (**I**) Spatial intensity map reveals the sEMG activity across the 15 electrical channels at the rat leg. Size of region: 16 mm (horizontal) by 12.8 mm (vertical). (**J**) Comparison of SNR in gold bioelectronics biointerface versus living hydrogel coating indicated that living hydrogel-coated bioelectronics facilitate electrophysiological recording. $n = 15$ independent channels. P values are determined by paired t test, two tailed. All data are presented as mean values ± SD.

signals with an average signal-to-noise ratio (SNR) of 26.76 dB (figs. S20 and S21). Furthermore, given the stable and conformal biointerface, the ABLE device resolved a high sEMG spatial intensity map over an area of 16 mm by 12.8 mm (Fig. 2I). By contrast, a gold biointerface (electronics without living hydrogel) recorded EMG signals with an SNR of 12.00 dB, indicating that the conformal nature of the ABLE facilitates electrophysiological signal transmission (Fig. 2J). Moreover, the living biointerfaces are less invasive and reduce movement artifacts when compared to conventional bioelectronic scaffolds (figs. S22 and S23). The living biointerface also promoted the long-term stability of the bioelectronics in EMG signal recording over a 4-hour duration without significant SNR loss (fig. S24).

Skin disease monitoring and therapy with ABLE

We applied the ABLE devices to a psoriasis mouse model (Fig. 3A). Psoriasis is a chronic inflammatory disease that affects ~125 million people worldwide, with no complete cure (*30*). Current treatment options often involve small-molecule drugs with potential systemic side effects. We conducted a series of preclinical evaluations using ABLE in the imiquimod (IMQ)–induced psoriasis model (*31*). This model is widely used in in vivo research because of its clinical and histological similarities to human psoriasis, including characteristic symptoms such as desquamation, thickening of the epithelial
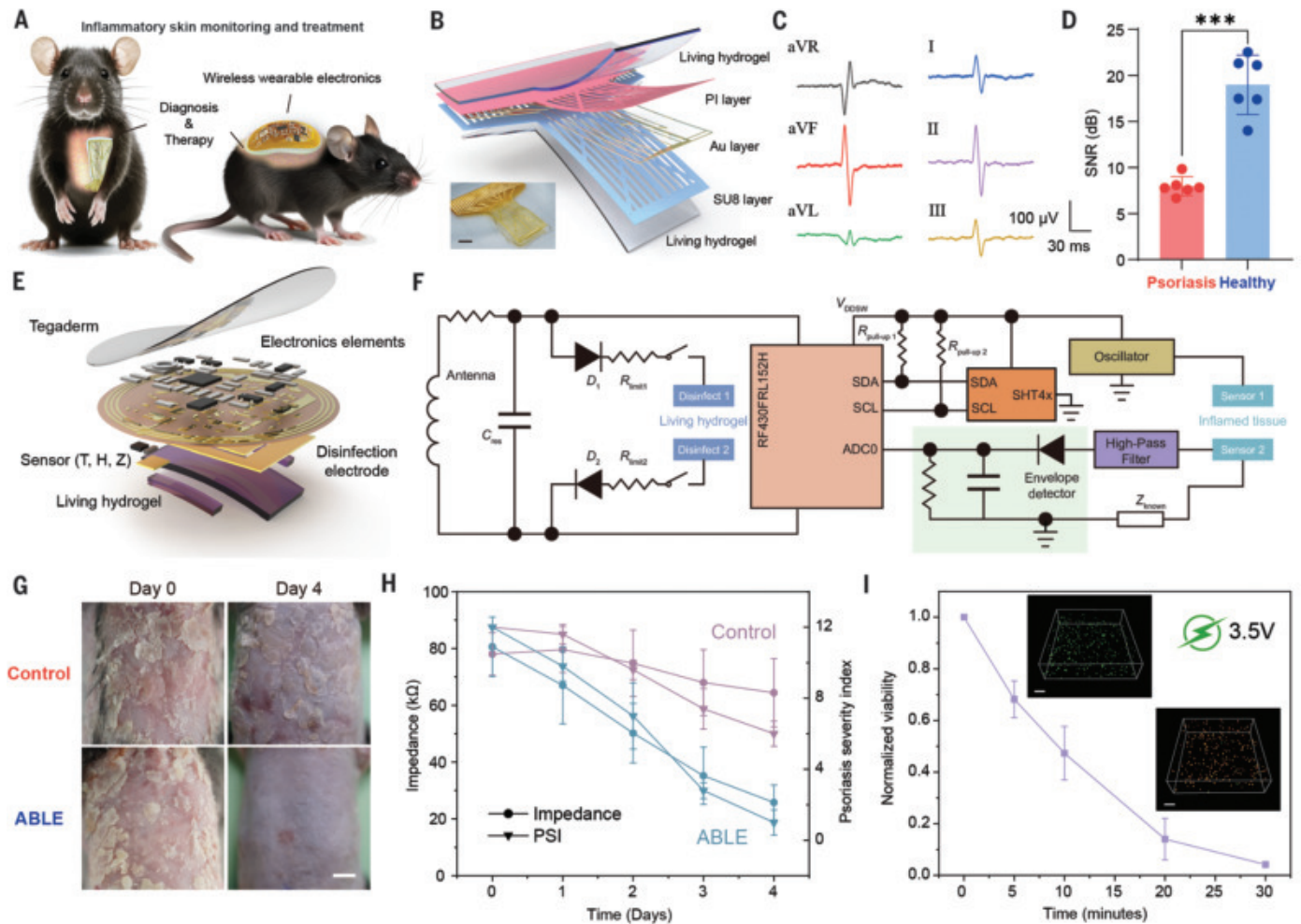
Fig. 3. ABLE enables electrophysiological signal recording, diagnosis of psoriasis, and treatment of psoriasis. (**A**) Schematic showing ABLE functionality in diagnosis and treatment of psoriasis. (**B**) Schematic diagram and photograph show the structural configuration of the living hydrogel hybrid mesh electronics device for sECG recording. Scale bar, 5 mm. (**C**) Representative six-lead electrocardiogram signals reveal heart rhythm in I, II, III, aVL, aVR, and aVF leads. (**D**) Living bioelectronics device reports lower SNR in ECG recording in psoriasiform skin compared to controls. $n = 6$ independent channels. (**E**) Schematic diagram shows the structural configuration of FPCB-based ABLE. (**F**) Circuit diagram of wireless bioelectronics for skin monitoring and living hydrogel modulation. (**G**) Representative photographs at day 0 and day 4 showing that ABLE treats psoriasis. Psoriasiform features including erythema, induration, and desquamation, are all substantially diminished. Scale bar, 5 mm. (**H**) Impedance of psoriasis skin lesions, as measured using ABLE, indicates recovery progress. Results align with the psoriasis severity index (PSI). $n = 5$ independent animals. (**I**) Disinfection electrodes on ABLE disinfect the living hydrogel through 3.5-V direct voltage within 30 min. Insets show confocal images of living hydrogel before (upper) and after (lower) disinfection. Bacteria were stained with Baclight Live/Dead kit containing SYTO9/PI. Scale bar, 20 μm. $n = 5$ independent experiments. Control: mice with imiquimod (IMQ)–induced psoriasis, no treatment. ABLE: mice with IMQ-induced psoriasis, treated with active biointegrated living electronics. P values are determined by paired t test, two tailed. All data are presented as mean values ± SD.

structure, skin inflammation, and dysregulated host skin microbiota (*32*).

We fabricated a mesh electronics device with a spin-coated living interface for six-lead surface electrocardiogram (sECG) recording (Fig. 1B, item 3; Fig. 3B; and fig. S19). Upon attachment to the chest area of healthy mice, the ABLE stably recorded the six-lead ECG (I, II, III, aVL, aVR, and aVF) with an average SNR of 18.97 dB (Fig. 3C). By contrast, the ABLE recorded a significantly lower SNR of 7.96 dB in mice with psoriasis symptoms (Fig. 3D), mainly attributed to the thickening of the psoriasiform skin. Hence, alterations in recorded electrophysiological signals offer qualitative in-

formation in the detection of skin diseases. When the ABLE device was applied to psoriatic skin for 4 days, we found that the SNR of recorded ECG was largely enhanced (day 0 versus day 4 recording) (fig. S25). This improvement suggests that the living components within the ABLE system play an important role in mitigating the symptoms of psoriasis in mouse skin. These results demonstrate how the ABLE system may be used to record electrophysiological signals while concurrently providing biogenic cues through living components to regulate inflammatory skin diseases (fig. S26).

To investigate the potential of ABLE in real-time monitoring and therapy and active circuit

control, we created a battery-free, wireless flexible printed circuit board (FPCB). The FPCB-based ABLE can achieve comprehensive interplay between the three components (i.e., hydrogel, bacteria, electronics) (Fig. 1B, item 3, and Fig. 3E). It is capable of (i) wireless energy harvesting and data transfer; (ii) real-time disease progress monitoring through skin impedance, humidity, and temperature sensing; and (iii) on-demand bacterial disinfection (Fig. 3F). The FPCB is highly flexible and functions effectively as it bends to conform to the skin tissue. It integrates a near-field communication (NFC) transponder (RF430FRL152H) for radio-frequency (RF) energy harvesting and wireless

data transfer according to the International Organization for Standardization (ISO) 15693 protocol (fig. S27). For comprehensive monitoring of inflammatory skin conditions, the FPCB incorporates an impedance sensor circuit along with a commercialized temperature and humidity digital sensor (SHT4x) (figs. S28 and S29). The SHT4x sensor was chosen here because of its noise robustness, measurement repeatability, and low-power consumption (3.3 μW) due to its digital nature. The SHT4x sensor was connected to the NFC transponder through the I2C protocol (Fig. 3F). The acquired sensing data can be wirelessly transferred and remotely analyzed to monitor disease recovery progress and provide information for bacterial modulation (33). Although application of living hydrogel in bioelectronics interfaces improved bioactivity for disease management, it presents practical challenges (25). One major concern is that the S. epidermidis can proliferate and colonize on skin, leading to infections and the development of virulence factors (34). Further, households are not equipped with proper biohazard containers to safely discard bacteria-laden materials. Thus, our FPCB included two modulation electrodes with triggers for delivering electrical current in terminal disinfection (Fig. 1B, items 4 and 8). To maximize disinfection efficiency, we added a thin Au film to the back of the FPCB, which promotes reactive oxygen species generation in the hydrogels-electronics interface (fig. S30). Using bioelectronics for disinfection management, we can apply opportunistic pathogens (e.g., commensal bacteria) to the skin and minimize their potential long-term influences on skin health (figs. S31 to S33). Notably, ABLE is a general platform accommodating various bacterial species by providing both a supporting matrix and disinfection approaches (fig. S34). In preclinical assessments, open-field movement tests confirmed that the lightweight and wireless ABLE does not hinder mouse mobility (fig. S35). Furthermore, we validated the functionality of sensors during movement or under different skin physiologies, confirming sensor reliability for research and data collection (fig. S29 and S36).

Incorporating the FPCB circuit in the ABLE design, we can integrate disease monitoring with drug-free skin cellular modulation for disease treatment (Fig. 3G). The constant decrease in impedance recorded by ABLE during the recovery process aligns well with the psoriasis severity index (PSI) of the mice skin over 4 days (Fig. 3H). Characteristic clinical symptoms of psoriasiform skin, including erythema, induration, and desquamation, were all largely reduced after ABLE treatment, indicating how living biointerfaces can modulate the local immune system. Humidity and temperature recordings over 4 days of treatment also provide essential information on the changing skin environments (fig. S37). Moreover, upon treatment completion, two disinfection electrodes positioned in the ABLE deliver direct current to the living hydrogel interface for 30 min of disinfection (Fig. 3I and figs. S38 and S39). This process effectively disinfects the bacteria present within the living interface, as supported by the confocal microscope imaging (Fig. 3I). This feature substantially reduces the biohazard risk associated with the living hydrogel. Compared with conventional psoriasis therapeutics, such as methotrexate (MTX), the combined use of ABLE and MTX exhibited substantially enhanced efficacy (figs. S40 and S41).

Mechanistic investigations of ABLE-based therapy

We studied how ABLE modulates the cellular environment in inflammatory skin conditions through biogenic cues (Fig. 1B, items 2 and 6). Although the role of S. epidermidis in mediating skin homeostasis is widely known (27, 35), there is minimal literature on its therapeutic effects in psoriasis, let alone translation to clinic. Our findings revealed a reduction in spleen weight on day 4, indicating that ABLE can modulate the whole-body immune system (fig. S42). The therapeutic effect also extends beyond the directly treated area to the adjacent psoriatic skin tissues (fig. S43). Hematoxylin and eosin (H&E) staining showed significant reduction of epidermal thickening (hyperplasia), parakeratosis and cutaneous inflammation in skin lesions following ABLE treatment (Fig. 4A, fig. S44, and table S2). The hydrogel matrix alone in combination with the bioelectronics device (i.e., vehicle without bacterial component) showed limited therapeutic effect on psoriasis (fig. S45). Immunohistochemistry analysis (IHC) of cytokeratin 14 and F4/80 demonstrated a notable decrease in macrophages activities after ABLE treatment (Fig. 4B). IHC of CD4 and CD8 indicated a significant reduction in the number of T helper cells and T cytotoxic cells (figs. S46 and S47). Flow cytometry analysis of immune cell populations in psoriatic skin tissues further confirmed the reduction in percentage of CD4-positive T cells after ABLE treatment (fig. S48). Additionally, immunostaining with Ki-67 indicated a reduction in epidermal proliferation (fig. S49). CD31 immunofluorescence and IHC staining both revealed fewer dilated blood vessels in ABLE-treated samples after 4 days compared to controls (mice with IMQ-induced psoriasis, no treatment) (Fig. 4C and fig. S50). Cytokine profiling analysis showed reduced levels of inflammatory cytokines, with notable reductions in interleukin-17 (IL-17), interferon-γ (IFN-γ), tumor necrosis factor–α (TNF-α), and IL-1, which play a crucial role in promoting recruitment of inflammatory cells to psoriatic plaque lesions, regulating keratinocyte proliferation, and disease development (Fig. 4D and figs. S51 and S52). These findings collectively highlight the potential of living bioelectronics in modulating the inflammatory microenvironment and key aspects of psoriasis pathogenesis, including immune dysregulation, cellular proliferation, neovascularization, and cytokine-mediated inflammation.

To gain further insight into ABLE modulation of skin microbiota, we conducted 16S ribosomal RNA gene sequencing analysis of the treated skin samples. Linear discriminant analysis effect size (LEfSe) results indicated that ABLE effectively modulated the skin microbiota, inducing a transition from a psoriatic state to a healthier state (Fig. 4E). A principal coordinates analysis plot of beta diversity showed that skin microbiota profiles in ABLE-treated mice were distinct from those in the control group but quite close to those in healthy mice (fig. S53). At the species level, we observed a low abundance of S. epidermidis on the skin (Fig. 4F), indicating low S. epidermidis–related safety concern under the bioelectronics control. Furthermore, the abundance of S. aureus, a species known to be associated with psoriasis progression (36), was also significantly reduced (Fig. 4F). We noticed that the abundance of other skin microbes, such as Rhodococcus erythropolis and Delftia acidovorans, was also modulated by ABLE (fig. S54). These findings require further systematic investigation given the limited studies in past literature. Altogether, changes in bacterial abundance can probably be attributed to the mutual interactions between different bacterial species and S. epidermidis (37). Further investigation by reverse transcription–quantitative polymerase chain reaction (RT-qPCR) also revealed that the skin microbes are unlikely to enter and colonize the ABLE devices (fig. S55).

We sought to investigate the molecular mechanisms underlying ABLE-based regulation of the immune system and skin microbiota. Previous research has reported the inverse relationship between S. epidermidis and S. aureus, wherein S. epidermidis activates the host innate and adaptive immune system against S. aureus by the toll-like receptor 2 (TLR2) on dendritic cells (27). This knowledge prompted us to explore the therapeutic effect of ABLE in the TLR2-knockout (KO) mouse strain B6.129-Tlr2[tm1Kir]/J. We found that ABLE treatment in TLR2-KO mice did not result in the same therapeutic effects observed for wild-type mice (fig. S56), as determined by PSI and H&E analysis (fig. S57). Additionally, CD4 and CD8 IHC analysis showed the continued accumulation of T helper cells and T cytotoxic cells in the skin lesion (fig. S58). These results suggest that the efficacy of living bioelectronics in treating psoriasis may be mediated through the functionality of the TLR2 in immune cells. The therapeutic efficacy of ABLE remains unaffected in other TLR-deficient models, such as
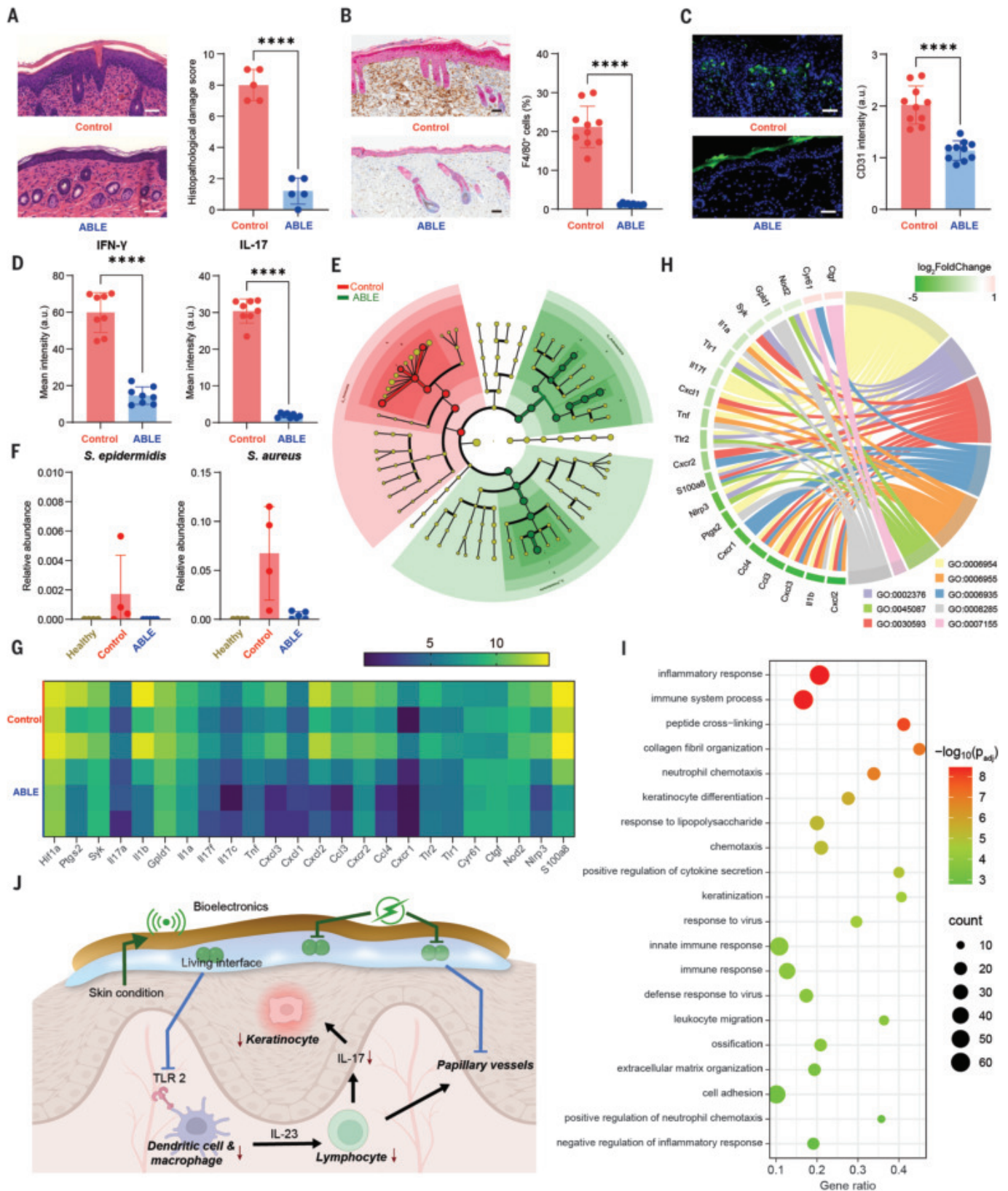
Fig. 4. ABLE for studying living biointerface-tissue interaction in disease treatment. (**A**) Representative images of H&E staining show substantially reduced pathological damage in psoriatic skin lesions of ABLE-treated mice.

Scale bar, 50 μm. Histological score analysis shows a lower level of histological inflammation and tissue damage. n = 5 independent animals. (**B**) Representative dual-immunohistochemical images of cytokeratin 14 and F4/80 staining indicate

significantly decreased percentages of dendritic cells and macrophages in psoriatic skin lesions of ABLE-treated mice. Scale bar, 50 μm. $n = 10$ independent samples. (**C**) Representative immunofluorescent images of CD31 staining indicate significantly decreased blood vessel formation in skin lesions of ABLE-treated mice. False positive signals in the ABLE image are due to unspecified staining in the stratum corneum. Scale bar, 50 μm. $n = 10$ independent samples. (**D**) Cytokine analysis of the skin lesion indicates significant down regulation of IFN-γ and IL-17, which play an important role in inflammatory cell recruitment and regulate keratinocyte hyperplasia. $n = 8$ independent samples. (**E**) LEfSe taxa analysis indicates altered bacterial diversity following ABLE treatment. (**F**) *S. epidermidis* is barely detected on skin during ABLE treatment. Relative abundance of

S. aureus is reduced after ABLE treatment. $n \geq 3$ independent animals. (**G**) Heatmap shows expression profile of psoriasis-related genes. (**H**) Gene ontology (GO) chord plot shows that several important psoriasis-related genes are categorized into different clusters. (**I**) GO enrichment analysis of significantly differentially expressed genes shows that ABLE regulates biological processes related to immune response and keratinocytes. (**J**) Proposed mechanism for ABLE regulation of the inflammatory skin environment and therapeutic effect in IMQ-induced psoriasis. Control: mice with IMQ-induced psoriasis, no treatment. ABLE: mice with IMQ-induced psoriasis, treated with ABLE. P values are determined by t test, two tailed. All data are presented as mean values ± SD.

TLR4-KO mouse strain B6(Cg)-Tlr4$^{tm1.2Karp}$/J (figs. S59 and S60). Furthermore, we investigated the contribution of TLR2 ligands produced by *S. epidermidis* to the anti-psoriasis effect of ABLE system. In vitro cellular cytokine analysis indicates that lipoteichoic acid (LTA) derived from *S. epidermidis* can down-regulate the expression of psoriasis-related cytokines and chemokines in plasmacytoid dendritic cells and epidermal cells (figs. S61 and S62). Additionally, histology and immunohistological analysis of immune cells in the in vivo study revealed that LTA regulates the skin immune environment (figs. S63 to S66). These pieces of evidence suggest that LTA might act as one of the TLR2 ligands mediating ABLE's immunoregulation function. However, it is important to note that LTA is not the only TLR2 ligand derived from *S. epidermidis*, nor is it solely responsible for the therapeutic efficacy (fig. S67). Various ligands or components from *S. epidermidis* may collectively contribute to the therapeutic effect on psoriasis.

Bulk RNA sequencing was conducted after 4 days of ABLE treatment. When comparing control group with ABLE group, we identified 1100 significantly altered genes, of which 695 were down-regulated (fig. S68). ABLE exerted substantial regulatory effects on genes associated with psoriasis progression and pathogenesis (Fig. 4G and fig. S68), including genes pertinent to the innate immune response (e.g., *Tlr2, Syk, Nod2*), infiltration by adaptive lymphocytes (e.g., *Syk, Nlrp3*), psoriatic epidermal hyperplasia (e.g., *Epgn, Hbegf, JunB, Gpld1*), skin inflammation (e.g., *Ccl3, Cxcl2, S100a8*), and angiogenesis (e.g., *Hif1a, Ptgs1*). Most of these psoriasis-related genes could be categorized into different gene ontology groups associated with immune and inflammatory processes (Fig. 4H). Furthermore, a top 30 enriched gene ontology analysis of all significantly differentially expressed genes revealed enrichments in processes related to keratinization, keratinocyte differentiation, immune system functions, and inflammatory responses (Fig. 4I). Treatment with vehicle alone (ABLE without *S. epidermidis*) resulted in a substantially smaller number of significantly modified genes (figs. S69 and S70). Both gene expression and gene ontology analysis indicated that

vehicle treatment lacked the involvement of genes related to inflammation and immune response. This observation underscores the pivotal role of the living components in the ABLE system in managing skin inflammation and facilitating therapeutic intervention through bioelectronics interfaces.

Collectively, we found that ABLE substantially modulates the inflammatory environment in psoriasis (Fig. 4J). First, ABLE mitigates the expression of the *Tlr2* gene, along with other genes pivotal to initiation of the innate immune response (e.g., *Syk, Nod2*). The importance of TLR2 in the therapeutic effect of ABLE in IMQ-induced psoriasis was manifested across our transcriptome-level analysis and in TLR2-KO mice experiments. This result strongly suggests that ABLE inhibits activation of dendritic cells and macrophages through biological signals. Second, ABLE treatment substantially mitigates infiltration of adaptive lymphocytes to skin lesions, as indicated by histology and flow cytometry analysis and reduced expression levels of genes associated with lymphocyte infiltration (e.g., *Syk, Nlrp3*). Third, both mRNA and protein levels of key cytokines, including IL-17, TNF-α, and IL-1, were markedly diminished following ABLE treatment. Finally, genes associated with psoriatic epidermal hyperplasia (e.g., *Epgn, Hbegf, JunB, Gpld1*) and papillary vessel dilation and angiogenesis (e.g., *Hif1a, Ptgs1*) exhibited down-regulation following ABLE treatment. These findings are in harmony with the therapeutic effects observed at the histological tissue level. In summary, ABLE treatment demonstrates potent therapeutic effects on IMQ-induced murine psoriasis by impeding the activation of initiating dendritic cells and subsequently curbing the inflammatory phases intrinsic to psoriatic pathogenesis.

Conclusions and outlook

We validated the efficacy of an integrated living biointerface-bioelectronics device, in the context of biomedical applications. Using the IMQ-induced psoriasis model, we demonstrate the potential for clinical adaptation of living bioelectronics devices that promote therapeutic effects through a living interface. The nexus between living materials and electrical systems presents new opportunities to explore the

interplay between biological and nonbiological systems. Although Helminthic therapy offers apparent benefits in some autoimmune diseases, the lack of exhaustive studies has led to constraints. The advent of living bioelectronics paves the way for controlled studies into the dynamics between potentially deleterious organisms and human tissues.

REFERENCES AND NOTES

1. Y. Jiang *et al.*, *Science* **375**, 1411–1417 (2022).
2. A. J. Boys *et al.*, *Adv. Mater.* **35**, 2207847 (2023).
3. H. Hu *et al.*, *Nature* **613**, 667–675 (2023).
4. X. Liu, M. E. Inda, Y. Lai, T. K. Lu, X. Zhao, *Adv. Mater.* **34**, e2201326 (2022).
5. M. E. Inda-Webb *et al.*, *Nature* **620**, 386–392 (2023).
6. X. Jiang *et al.*, *Adv. Mater.* **34**, e2201411 (2022).
7. K. B. Ramadi *et al.*, *Sci. Robot.* **8**, eade9676 (2023).
8. K. Nan *et al.*, *Nat. Rev. Mater.* **7**, 908–925 (2022).
9. J. L. Terrell *et al.*, *Nat. Nanotechnol.* **16**, 688–697 (2021).
10. M. Wang *et al.*, *Nat. Biomed. Eng.* **6**, 1225–1235 (2022).
11. W. Cheng *et al.*, *Nat. Mater.* **22**, 1352–1360 (2023).
12. Y. Jiang *et al.*, *Nature* **614**, 456–462 (2023).
13. Y.-S. Guan *et al.*, *Nat. Electron.* **5**, 881–892 (2022).
14. E. Song *et al.*, *Nat. Biomed. Eng.* **5**, 759–771 (2021).
15. Y. Gao *et al.*, *Sci. Adv.* **7**, eabg9614 (2021).
16. W. Ouyang *et al.*, *Nat. Biomed. Eng.* **7**, 1252–1269 (2023).
17. J. Park *et al.*, *Nat. Nanotechnol.* **15**, 690–697 (2020).
18. C. Wang *et al.*, *Science* **377**, 517–523 (2022).
19. T. Zhou *et al.*, *Nat. Mater.* **22**, 895–902 (2023).
20. Q. Yang *et al.*, *Nat. Mater.* **20**, 1559–1570 (2021).
21. J. Deng *et al.*, *Nat. Mater.* **20**, 229–236 (2021).
22. A. E. Rochford *et al.*, *Sci. Adv.* **9**, eadd8162 (2023).
23. C. Lim *et al.*, *Sci. Adv.* **7**, eadd8162 (2021).
24. M. Karin, H. Clevers, *Nature* **529**, 307–315 (2016).
25. T. C. Tang *et al.*, *Nat. Rev. Mater.* **6**, 332–350 (2021).
26. A. Rodrigo-Navarro, S. Sankaran, M. J. Dalby, A. del Campo, M. Salmeron-Sanchez, *Nat. Rev. Mater.* **6**, 1175–1190 (2021).
27. M. M. Severn, A. R. Horswill, *Nat. Rev. Microbiol.* **21**, 97–111 (2023).
28. K. Sauer *et al.*, *Nat. Rev. Microbiol.* **20**, 608–620 (2022).
29. M. Baumgartner *et al.*, *Nat. Mater.* **19**, 1102–1109 (2020).
30. J. E. Greb *et al.*, *Nat. Rev. Dis. Primers* **2**, 16082 (2016).
31. H. Liang *et al.*, *Sci. Adv.* **6**, eabb5274 (2020).
32. E. Bracho-Sanchez *et al.*, *Nat. Biomed. Eng.* **7**, 1156–1169 (2023).
33. Y. Jiang *et al.*, *Nat. Biotechnol.* **41**, 652–662 (2023).
34. M. Otto, *Nat. Rev. Microbiol.* **7**, 555–567 (2009).
35. J. L. Linehan *et al.*, *Cell* **172**, 784–796.e18 (2018).
36. H. Terui *et al.*, *Sci. Immunol.* **7**, eabm9811 (2022).
37. A. L. Byrd, Y. Belkaid, J. A. Segre, *Nat. Rev. Microbiol.* **16**, 143–155 (2018).

EVOLUTION

Coevolution with hosts underpins speciation in brood-parasitic cuckoos

N. E. Langmore[1]*, A. Grealy[1,2], H.-J. Noh[1], I. Medina[3], A. Skeels[1], J. Grant[1], K. D. Murray[1], R. M. Kilner[4], C. E. Holleley[2]

Coevolution between interacting species is thought to increase biodiversity, but evidence linking microevolutionary processes to macroevolutionary patterns is scarce. We leveraged two decades of behavioral research coupled with historical DNA analysis to reveal that coevolution with hosts underpins speciation in brood-parasitic bronze-cuckoos. At a macroevolutionary scale, we show that highly virulent brood-parasitic taxa have higher speciation rates and are more likely to speciate in sympatry than less-virulent and nonparasitic relatives. We reveal the microevolutionary process underlying speciation: Hosts reject cuckoo nestlings, which selects for mimetic cuckoo nestling morphology. Where cuckoos exploit multiple hosts, selection for mimicry drives genetic and phenotypic divergence corresponding to host preference, even in sympatry. Our work elucidates perhaps the most common, but poorly characterized, evolutionary process driving biological diversification.

M ost species are involved in coevolutionary interactions (1), in which closely interacting species impose selection pressures on one another that result in reciprocal evolutionary change. Coevolution can accelerate divergence, particularly in the face of gene flow, and is believed to be such an important mechanism of diversification that it is likely to explain why there are millions, rather than thousands, of distinctly specialized species (2). However, despite numerous calls for research, the paucity of evidence linking macroevolutionary patterns to microevolutionary processes driving speciation remains an outstanding empirical gap in our understanding of coevolutionary diversification (3–6).

A particularly tractable system for investigating coevolutionary diversification is the brood-parasitic reproductive strategy used by cuckoos that lay their eggs in the nests of other bird species and thereafter abandon their

young to the care of the host (7). Cuckoos vary in the costs they impose on hosts: In some species, cuckoo chicks evict the host young from the nest (evicting cuckoos), whereas in others, cuckoo chicks are reared alongside the host young (nonevicting cuckoos). This dichotomy in virulence predicts the intensity of selection for host defenses; hosts exploited by chick-killing parasites generally evolve defenses based on recognition and rejection of brood parasite young, whereas those exploited by more benign brood parasites evolve life-history strategies that tolerate the costs of parasitism (8, 9). Parasitism that results in the death of host young typically leads to a coevolutionary arms race; parasitism selects for host defenses, such as rejection of cuckoo young, which in turn select for counteradaptations in cuckoos, such as mimicry of host young, that deceive the host into accepting the parasite young (8, 9) (Fig. 1A).

When a brood parasite species exploits multiple different hosts, selection for mimicry of the eggs or nestlings of several different host species may drive genetic diversification of the parasite into distinct host-specific lineages, each of which mimics the eggs or nestlings of their respective host (10) (Fig. 1B). However,

the likelihood that such divergence ultimately results in the generation of new species depends on how mimetic traits are inherited, which differs between cuckoos that mimic host eggs and those that mimic host nestlings (7). Successful egg mimicry is achieved through maternal inheritance of egg color in cuckoos (10, 11); a female exploits the host that reared her and lays the same egg type as her mother, and the trait is obviously not expressed in sons. By contrast, mimetic traits at the nestling stage cannot be sex linked, as both male and female nestlings must be mimetic to survive. Instead, mimicked nestling traits, such as down feather color and distribution (12), skin and flange color (12, 13), and call structure (14), are complex traits (15) that are likely to be inherited from both parents (7, 16, 17). Therefore, when a cuckoo species is under divergent selection to mimic the nestlings of several different host species, we would predict assortative mating between males and females that specialize on the same host to reinforce local adaptation within host-specific lineages selected by host defenses. This could generate new, host-specific species (Fig. 1B) (7). Moreover, such host-shifts by parasites are predicted to lead to a greater tendency for parasites to speciate in sympatry than nonparasitic organisms, although this is not an inevitable outcome (18).

Macroevolutionary evidence that coevolution underpins speciation

Focusing on the subfamily Cuculinae, we began by exploring whether rates of speciation are greater in highly virulent, evicting cuckoos than in nonevicting and nonparasitic cuckoos. We used recently developed methods to quantify speciation rates (cladogenetic diversification rate shift model, ClaDS) (19) as well as other tree-based statistics that offer tip-rate estimates (20). Our results show that parasitic species that are highly virulent tend to have higher speciation rates on average when compared with species that are parasitic but nonevicting and when compared with nonparasitic species (Fig. 2, A and B, and fig. S1A). This is consistent with previous research, which shows that the most virulent cuckoo species have

[1]Research School of Biology, Australian National University, Canberra, Australia. [2]Australian National Wildlife Collection, National Research Collections Australia, CSIRO, Canberra, Australia. [3]School of Biosciences, The University of Melbourne, Melbourne, Australia. [4]Department of Zoology, University of Cambridge, Cambridge, UK.
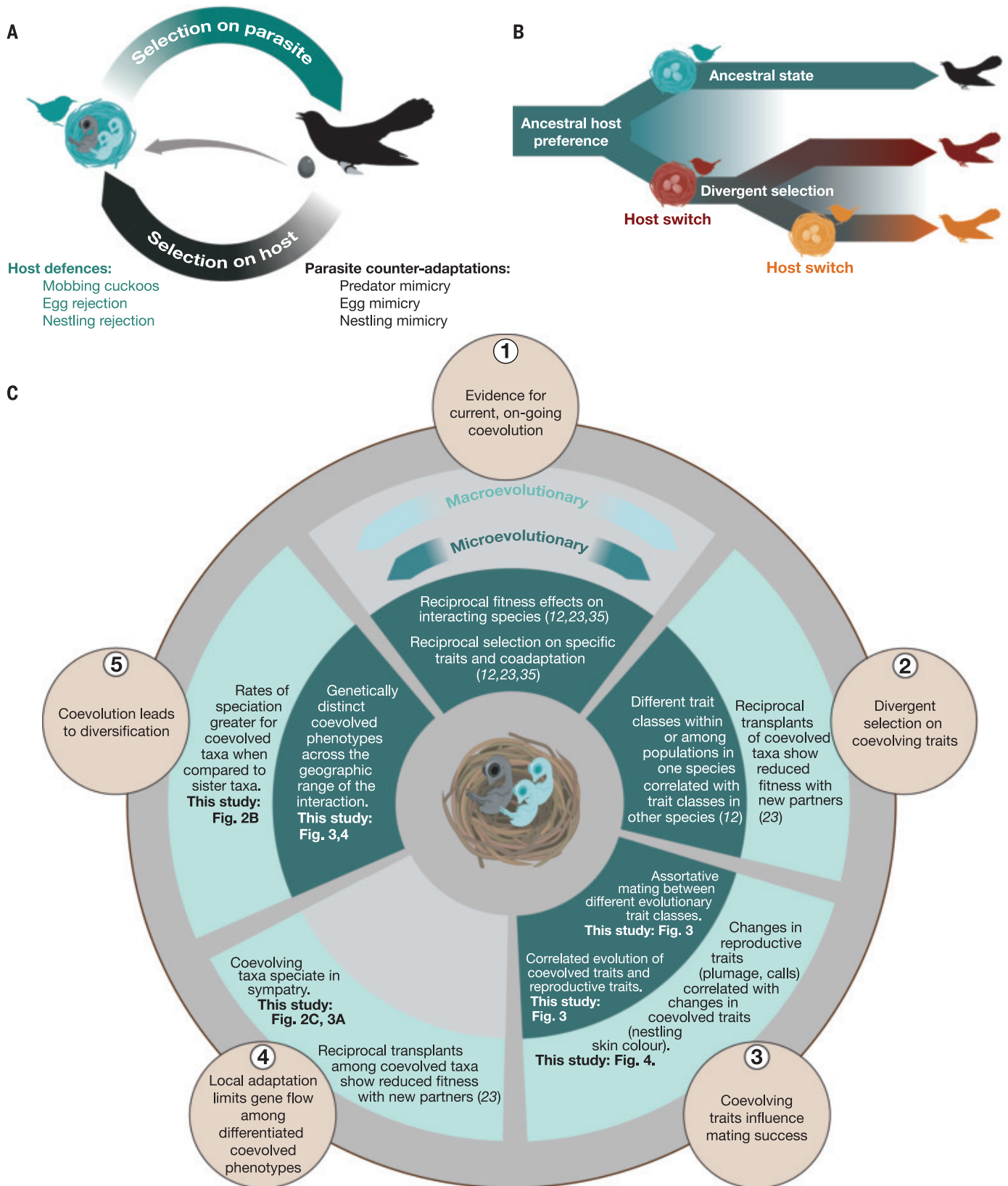*Corresponding author. Email: naomi.langmore@anu.edu.au

Fig. 1. Processes of coevolutionary diversification in cuckoo-host interactions and evidence from *Chalcites* cuckoos. (**A**) Coevolutionary arms races comprising defenses in hosts (*23, 59, 60*) and counteradaptations in brood parasites (*12, 59, 61*) are proposed to drive (**B**) coevolutionary diversification in brood parasites. (**C**) Evidence of coevolutionary diversification at microevolutionary and macroevolutionary scales [adapted from (*4*)] and the supporting evidence from current work on *Chalcites* spp.
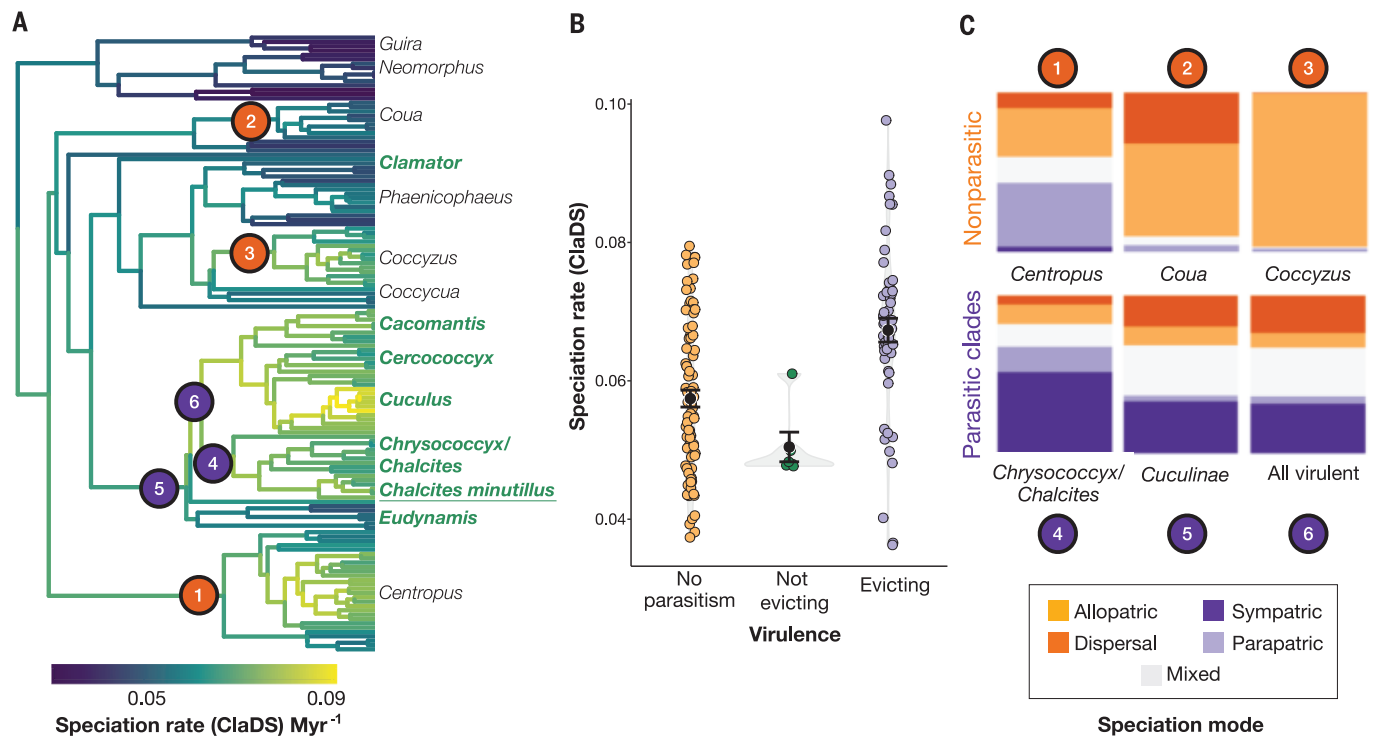
Fig. 2. Macroevolutionary patterns of speciation rates and mode in the Cuculidae. (**A**) Rates of speciation obtained from tip-rate analysis in ClaDS when using the MCC tree (19), with parasitic genera shown in bold. Parasitic species tend to show higher rates. Numbers on nodes represent clades used for speciation mode analyses in (C). The phylogeny presented is the maximum clade credibility tree (MCC) from 10,000 phylogenies downloaded from birdtree.org (62). (**B**) Comparison of speciation rates for different categories of parasitic lifestyle using the MCC tree. (**C**) Posterior probability of five different models of speciation from approximate Bayesian computation–based inference and linear discriminant analysis. Monophyletic clades used for analyses are indicated with a number in the phylogenetic tree (A).

more recognized subspecies (21), and with a simulation model showing that in sympatric host races, host race fidelity should increase over time and gene flow between host races should cease (22). We note, however, that given that there is a single origin of high virulence in cuckoos, there is no statistical power to test explicitly whether a parasitic lifestyle is responsible for the increased rates we report.

Further, if coevolutionary interactions between highly virulent cuckoos and hosts promote sympatric speciation of cuckoos, we would expect to see a higher frequency of sympatric speciation among highly virulent cuckoos that are under selection to mimic host young than among other parasitic and nonparasitic cuckoo species. To test this, we used a process-based simulation model to compare the geographic modes of speciation in highly virulent *Chrysococcyx* or *Chalcites* cuckoos [hereafter referred to as *Chrysococcyx*/*Chalcites*; the only clade in which mimicry of host nestlings has evolved in response to rejection of cuckoo nestlings by hosts (12–14, 23, 24)] with other parasitic and nonparasitic cuckoos in the family Cuculidae (20). We found the greatest support for the predominant role of sympatric speciation or a mixed model of speciation, which includes a degree of sympatric speciation, in three nested clades of

parasitic cuckoos. The support for sympatric speciation increased when considering the most-nested *Chrysococcyx*/*Chalcites* clade independently (Fig. 2C). The support for sympatric speciation in virulent cuckoos, particularly those of the *Chrysococcyx*/*Chalcites* clade, is stronger than has been seen in any other bird clades investigated in previous comparative studies (25, 26), including for finches in the family Viduidae (25), which are one of the most likely candidates for sympatric speciation among birds (27). This suggests that support for sympatric speciation is specifically compelling for the *Chrysococcyx*/*Chalcites* clade of cuckoos. The support for sympatric speciation also stands in contrast to the nonparasitic clades *Coccyzus* and *Coua*, in which we found the greatest support for speciation by isolation (allopatric or dispersal modes), and *Centropus*, which shows the greatest support for a predominantly parapatric mode of speciation (Fig. 2C).

Microevolutionary evidence: Focusing in on bronze-cuckoos

To understand the microevolutionary processes driving these macroevolutionary patterns, we investigated coevolutionary diversification in bronze-cuckoos, *Chalcites* spp. (sometimes placed within the *Chrysococcyx* genus), using

behavioral, phenotypic, and genetic data. These cuckoos impose heavy costs on their hosts and have evaded host defenses at the egg stage (28–30). However, hosts reject cuckoo nestlings, an action which has selected for mimicry of host young by cuckoo nestlings (12–14, 23, 24). We focused on two closely related species, the shining-bronze cuckoo *C. lucidus* and the little bronze-cuckoo *C. minutillus*, both of which are host specialists that primarily exploit *Gerygone* spp. of the family Acanthizidae across their range (the Australian subspecies of *C. lucidus* exploits other *acanthizid* hosts) (31). *C. lucidus* comprises four subspecies that breed in Australia, New Caledonia, New Zealand, the Solomon Islands, and Vanuatu (32). *C. minutillus* comprises 13 subspecies, more than any other brood-parasitic cuckoo (31). In Australia, three morphs are recognized based on subtle morphological differences: a "*minutillus*" form that breeds across northern Australia; a "*russatus*" form, with a distribution that overlaps that of "*minutillus*" in northeastern Queensland; and a "*barnardi*" form that breeds in southeastern Queensland and northern New South Wales (33, 34). The taxonomy of these morphs is contentious (20, 33, 34), and the factors that promote and maintain divergence, particularly in areas of sympatry, are unknown (34).
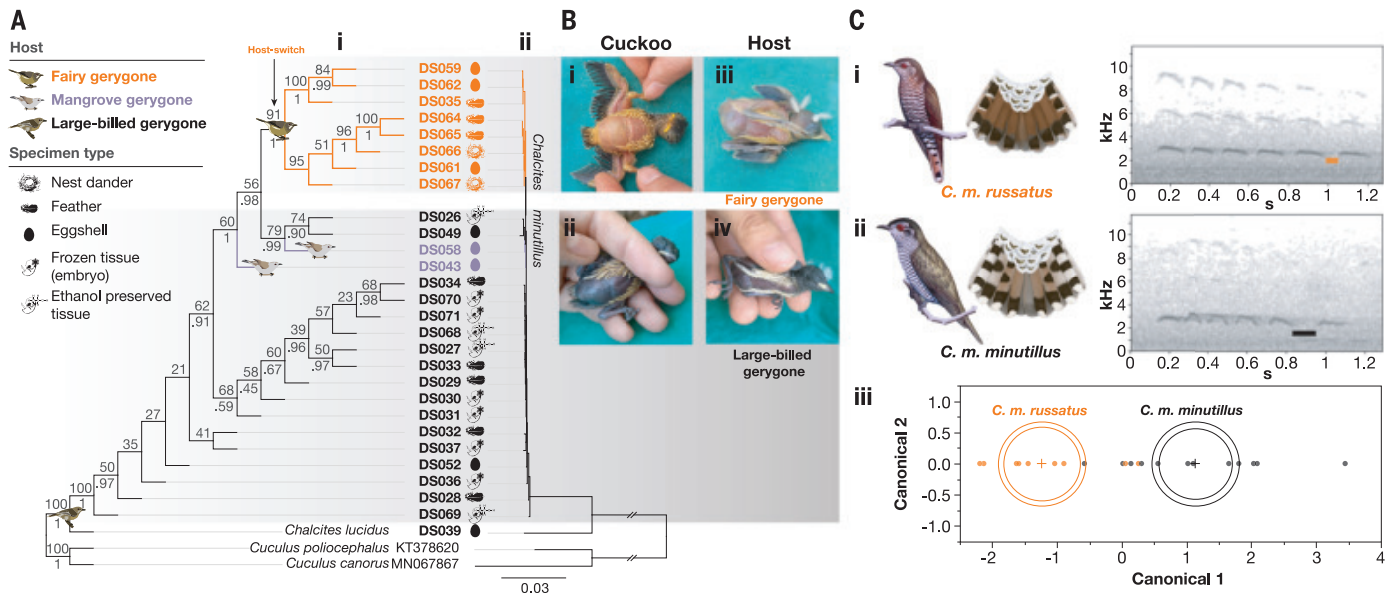
Fig. 3. Little bronze-cuckoos that exploit fairy gerygone hosts are phenotypically and genotypically divergent, showing incipient speciation driven by host specificity. (**A**) (i) Maximum-likelihood whole-mitochondrial phylogenetic tree of 27 little bronze-cuckoo specimens colored according to host preference [mt sequence alignment available at (58)]. Bootstrap support (%) values are indicated above, and Bayesian posterior probabilities are indicated below the node of the cladogram (missing values indicate the topology was not supported). (ii) The phylogram (branch length = nucleotide substitutions per site) is depicted to the right. (**B**) Phenotypic differences between the nestlings of the (i) *russatus* and (ii) *minutillus* morphs. *Russatus* nestlings (N = 5) have pale skin resembling (iii) fairy gerygone nestlings (N = 5 broods), whereas *minutillus* nestlings (N = 180) have dark skin resembling (iv) large-billed gerygone nestlings (N = 123 broods). (**C**) Phenotypic differences between adults of the (i) *russatus* and (ii) *minutillus* morphs. The *russatus* morph shows more rufous plumage than the *minutillus* morph (33) [illustrations: tails, Julian Teh, Commonwealth Scientific and Industrial Research Organisation; adults, J. Davies (33)]. The spectrograms show adult male advertising calls, and the bars indicate the longer pause before the final note in *minutillus* than *russatus*. (iii) Canonical plot showing multivariate mean (indicated by +) of call variables for *minutillus* and *russatus*. The circle corresponds to the 95% confidence limit for the mean. Groups that are significantly different have nonintersecting circles (discriminant function analysis; Wilk's l = 0.39, exact $F_{4,18}$ = 6.91, P = 0.002).

Evidence of local adaptation to hosts, selected by host rejection of cuckoo chicks

We investigated empirically whether coevolution with hosts underpins speciation in bronze-cuckoos. Rejection of cuckoo nestlings by hosts (23, 24) has selected for mimicry of host nestlings by cuckoos (12); the nestlings of bronze-cuckoo species mimic the skin, down, and flange color (12, 13) and begging calls (14, 35) of their respective hosts. We have previously demonstrated that mimicry is driven by coevolution with hosts because host rejection can be triggered by experimental alteration of mimicked traits in both parasite and host young (36). We found that average trait values (skin and flange color and morphology of down feathers) of nestling cuckoos are correlated with average trait values of host nestlings (12). With transplant experiments, we also showed that shining bronze-cuckoos suffer a fitness cost when reared by a secondary host rather than the primary host with which they have coevolved; 100% of nestlings were rejected by the secondary host, which they do not mimic (23).

We show an even finer scale of coevolution; selection for mimicry of host nestlings does not only lead to divergent cuckoo nestling morphology among species, but also between sympatric morphs within the same species. In northeast Queensland, the *russatus* and *minutillus* forms occur in sympatry, but it was previously unknown which hosts they exploit or whether their nestlings are morphologically distinct (37). We reveal divergent morphology between nestling little bronze-cuckoos reared by the two different hosts. The previously undescribed nestlings of both fairy gerygone (*Gerygone palpebrosa*) hosts and little bronze-cuckoos that were reared by fairy gerygones each have pale skin and a yellow gape flange (Fig. 3B). By contrast, sympatric little bronze-cuckoos reared by large-billed gerygones (*Gerygone magnirostris*) have dark skin and a white flange resembling those of large-billed gerygone nestlings (Fig. 3B) [and to a lesser extent, those of their secondary host, mangrove gerygones (*Gerygone levigaster*)]. The color differences between light and dark morph bronze-cuckoo nestlings have previously been shown by reflectance spectrophotometry and visual modeling to be detectable through a bird's eye (12, 38). Consistent with our finding that *minutillus* nestlings mimic large-billed gerygone nestlings, whereas *russatus* nestlings mimic fairy gerygone nestlings, the distributions of the two cuckoo morphs mirror those of the hosts they mimic; the wider range of the *minutillus* morph

corresponds closely with the range of large-billed gerygone hosts, whereas the narrower range of the *russatus* morph matches that of fairy gerygones (37) (Fig. 4).

Genetic divergence between populations corresponds to host use

To test whether these two morphs might represent the early stages of sympatric speciation, we took a molecular genetic approach (20). Evidence to address this question has been lacking because previous genetic analysis of little bronze-cuckoos has been done on adult birds (37) and is thus blind to the host preference of the individual. We targeted the period of the life cycle when host use can unequivocally be ascribed by sampling little bronze-cuckoo eggs and nestlings in host nests in the field (20). Such analyses have been hindered previously by the difficulties of locating sufficient numbers of parasitized host nests. We added to our field samples by using parasitized clutches of eggs held at the Australian National Wildlife Collection, CSIRO Australia (20), capitalizing on new techniques for DNA extraction from historical eggshells (39, 40). By harnessing 61 years of collecting effort, we report that genetic divergence in little bronze-cuckoos corresponds to host preference (total
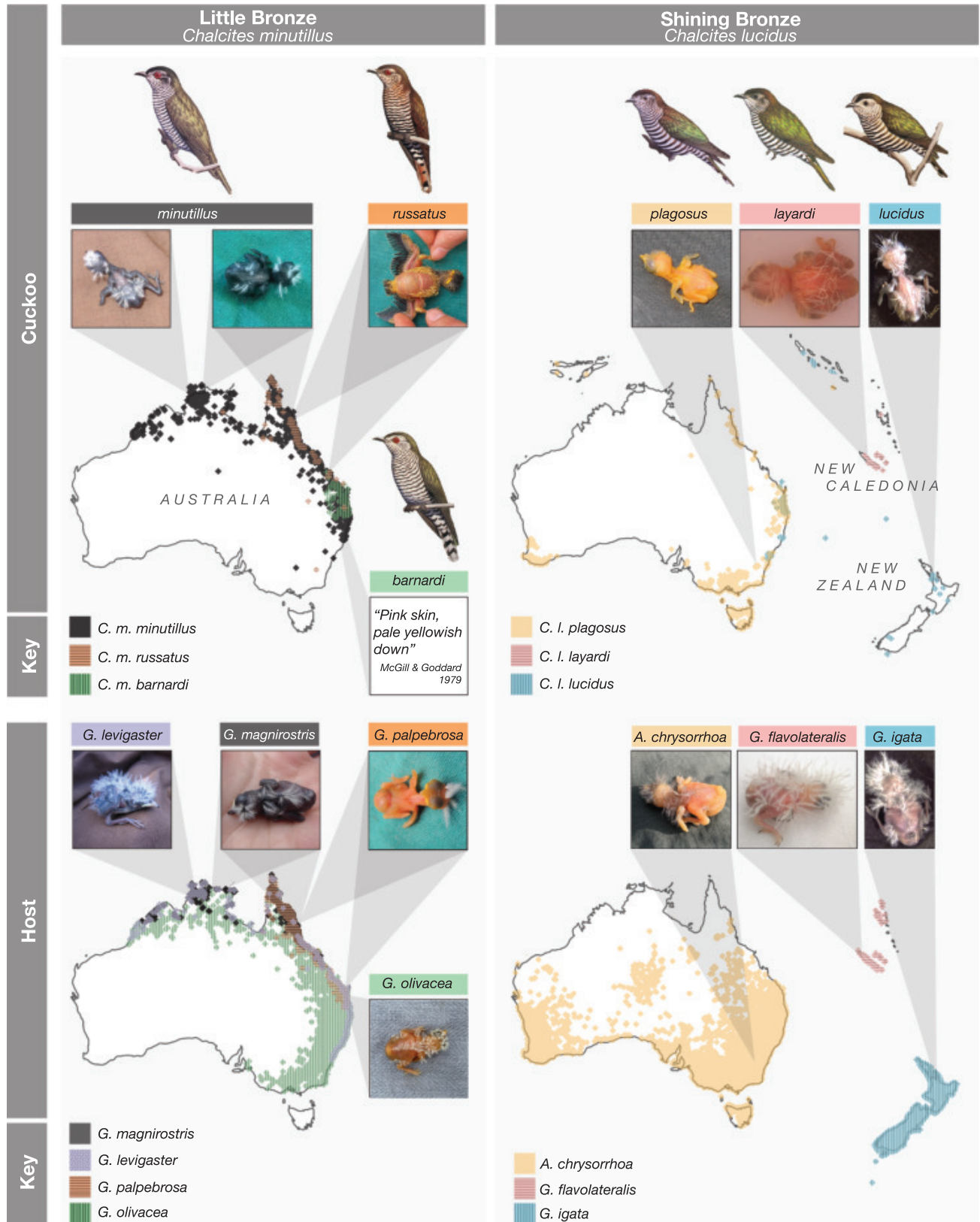
Fig. 4. Little bronze-cuckoo *C. minutillus* and shining bronze-cuckoo *C. lucidus* nestlings mimic the color of their respective host nestlings across their geographic range within Australia, New Caledonia, and New Zealand. Note that *C. lucidus lucidus* breeds only in New Zealand. Images: Adults are courtesy of J. Davies (*33*); nestlings *C. lucidus layardi* and *g. flavolateralis* are courtesy of A. Attisano, Polish Academy of Sciences (*12, 13*); *C. l. lucidus* and *G. igata* are courtesy of R. Thorogood, University of Helsinki, (*12, 13*); *G. olivacea* are courtesy of C. Taylor, University of Melbourne; other nestlings are courtesy of N.E.L. and H.-J.N. Description of *C. minutillus barnardi* nestlings from (*63*). The R v.4.0.3 package "ggplot2" was used to map subspecies distributions obtained from the Atlas of Living Australia (*64–66*) and eBird (*67*) (some islands were omitted for clarity).

in situ samples N = 27). Using a hybridization capture approach (hyRAD) (20), we surveyed 8167 restriction site–associated DNA (RAD) loci for 24,889 single-nucleotide polymorphisms (SNPs) (20). Sufficient orthologous SNPs were unable to be recovered across individuals with known host preference owing to the low nuclear DNA content in historic eggshells, so nuclear analyses were restricted to adult specimens for which host preference was unknown (20). However, both maximum likelihood and Bayesian phylogenetic inference of whole mitochondrial genomes reconstructed from off-target reads show that cuckoos parasitizing fairy gerygones form a monophyletic clade with high support (91% bootstrap support, posterior probability 1) (Fig. 3A). Individuals in this clade are more closely related to one another, regardless of geographic distance, than they are to sympatric little bronze-cuckoos laid in large-billed gerygone nests (Fig. 3A and fig. S6). This result is evidence of host specialization and, given that the multiple complex mimetic traits that are expressed in both male and female nestlings are unlikely to be solely maternally inherited (7, 15–17), it is consistent with assortative mating of little bronze-cuckoos reared by different host species.

Divergent adult plumage and vocalizations and genetic evidence for assortative mating

Furthermore, we included samples from 25 vouchered adult little bronze-cuckoo specimens in the mitochondrial analysis with the goal of linking adult plumage morphs to host specialization behavior (20). All vouchered adult *russatus* morphs had mitochondrial genomes most similar to those of cuckoo nestlings raised in fairy gerygone nests (fig. S11). This is the first unequivocal evidence linking adult plumage to host preference and nestling morphology, again consistent with assortative mating of little bronze-cuckoos reared by different host species. Similarly, most of the *minutillus* morphs clustered alongside cuckoo nestlings raised in large-billed or mangrove gerygone nests (fig. S11). The shallow nature of the mitochondrial phylogenetic tree and the weak nuclear differentiation of vouchered adult plumage morphs (fig. S9) indicate that genetic divergence driven by host preference is recent, ongoing, and does not yet constitute a complete reproductive barrier (Fixation Index $F_{ST} < 0.01$; table S2). Gene flow will reshuffle adaptive variation through recombination; as such, we may not observe genome-wide divergence during incipient speciation, especially at neutral or random loci, because adaptive variation may be restricted to a few key genes under selection. Assortative mating between different coevolutionary trait classes (i.e., individuals that produce black nestlings pair assortatively, as do individuals that produce pale nestlings) contributes to evidence that coevolving traits influence mating success (4).

What cues might facilitate assortative mating? Male and female cuckoos imprint on their host species and favor the breeding grounds of their host (41). Thus, *minutillus* individuals will favor the riverine habitat of large-billed gerygones, whereas *russatus* individuals will favor the rainforest-edge habitat of fairy gerygones. Such preliminary assortative mating may then be reinforced by premating isolation mechanisms such as vocalizations and plumage (42). These traits play vital roles in mate choice and species recognition in birds (43). We compared the calls of the *russatus* morph and the *minutillus* morph in sympatry and found that they differed subtly (20); calls of the *minutillus* morph were characterized by a significantly longer pause before the final note than that of the *russatus* morph (Fig. 3C). Similarly, male European cuckoo *Cuculus canorus* calls differed more between nearby populations that exploited different hosts than between distant populations that parasitized the same host (44). Plumage may also play a role in species recognition and mate choice (43), and the two morphs differ in some plumage traits (33) (Fig. 3C). Correlated evolution of coevolved traits (nestling skin color) and reproductive traits (calls or plumage) is suggestive of an influence of coevolving traits on mating success (4).

Coevolutionary diversification across the range of the brood parasites

Following this evidence of coevolutionary diversification in bronze-cuckoos, we would expect to find that subspecies of bronze-cuckoos will track divergent host nestling morphologies across their geographic range. This is indeed the case; nestling phenotypes of subspecies of the little bronze-cuckoo and the shining bronze-cuckoo in Australia, New Caledonia, and New Zealand (45) differ from one another in traits such as skin color, flange color, and the morphology of down feathers and bear a striking resemblance to the nestlings of their respective hosts (Fig. 4) (12, 13, 24, 46, 47). In contrast to the pronounced morphological differences between nestling bronze-cuckoos of different subspecies, the adults show only subtle plumage differences and all exhibit iridescent green dorsal plumage with barred white underparts (Fig. 4) (33). The correlation between a reproductive trait (plumage) and a coevolved trait (nestling skin color) across taxa contributes to evidence that coevolving traits influence mating success (4).

Discussion

We provide five sources of evidence of coevolutionary diversification in bronze-cuckoos at both macro- and microevolutionary scales (Fig. 1C and table S3) following the framework of Althoff *et al.* (4): (i) Current, ongoing coevolution; (ii) divergent selection on coevolving traits; (iii) coevolving traits influence mating success; (iv) selection limits gene flow among differentiated coevolved phenotypes; and (v) genetic or phenotypic diversification. Thus, we provide rare empirical evidence linking microevolutionary processes (i.e., processes driving genetic divergence between populations) with macroevolutionary patterns (i.e., speciation rates and processes) (3, 4).

Our study provides evidence that coevolutionary interactions between brood parasites and their hosts can drive speciation of the parasites, even in sympatry. This contrasts with a different mode of sympatric speciation that occurs in a less virulent brood parasite (27). In brood-parasitic *Vidua* finches, like bronze-cuckoos, nestlings show specialist mimicry of host young (48). However, unlike bronze-cuckoos, *Vidua* nestlings are reared alongside host nestlings and impose few costs on their hosts (49). Correspondingly, hosts have not evolved rejection of nonmimetic young (49). Instead, mimicry appears to have arisen through selection for nestling traits that exploit the preexisting provisioning rules of host parents (49, 50). Assortative mating occurs because both male and female *Vidua* finches imprint on their host (males mimic host songs and females use songs to choose a mate and a host nest to parasitize), providing a mechanism for reproductive isolation when a new host is colonized (27).

Our results, like those of the *Vidua* study (27), show speciation on only one side of the coevolutionary interaction, suggesting a process of speciation through host shift (51). However, the striking diversity of nestling morphologies among gerygones (Fig. 4)—in contrast to other nestling passerines, which are typically "uniformly drab" (52)—raises the possibility of cospeciation between bronze-cuckoos and their hosts. Mimicry of host nestlings by cuckoos may have selected for diversification of host nestling morphologies, as this would facilitate identification of parasite nestlings. Cospeciation between bronze-cuckoos and gerygones would be consistent with findings that gerygones have undergone more rapid and recent speciation than closely related taxa (53). Analogous diversification of host signatures has been documented in egg colors of brood parasite hosts (54) and cuticular hydrocarbon signatures of the ant *Formica fusca*, a host of socially parasitic ants (55).

Together, our results provide strong evidence that host defenses drive host specialization in highly virulent cuckoos, which in turn initiates speciation. An understanding of the processes of coevolutionary diversification is important, now more than ever, as anthropogenic climate change both disrupts existing tightly coupled interspecific relationships and generates new interactions (56). New parasite-host interactions could arise frequently and rapidly, accelerating rates of speciation. Understanding and modeling interspecies evolutionary

dynamics will be critical for obtaining accurate models of environmental change and for prioritizing conservation efforts.

REFERENCES AND NOTES

1. J. N. Thompson, *Am. Nat.* **173**, 125–140 (2009).
2. J. N. Thompson, *The Coevolutionary Process* (Univ. of Chicago Press, 1994).
3. A. A. Agrawal, X. Zhang, *Evolution* **75**, 1594–1606 (2021).
4. D. M. Althoff, K. A. Segraves, M. T. J. Johnson, *Trends Ecol. Evol.* **29**, 82–89 (2014).
5. N. Janz, *Annu. Rev. Ecol. Evol. Syst.* **42**, 71–89 (2011).
6. T. Suchan, N. Alvarez, *Entomol. Exp. Appl.* **157**, 98–112 (2015).
7. N. B. Davies, *Cuckoos, Cowbirds and other Cheats* (T & A D Poyser, 2000).
8. M. Broom, G. D. Ruxton, R. M. Kilner, *Behav. Ecol.* **19**, 22–34 (2008).
9. M. R. Servedio, M. E. Hauber, *J. Evol. Biol.* **19**, 1585–1594 (2006).
10. H. L. Gibbs *et al.*, *Nature* **407**, 183–186 (2000).
11. F. Fossøy *et al.*, *Nat. Commun.* **7**, 10272 (2016).
12. N. E. Langmore *et al.*, *Proc. Biol. Sci.* **278**, 2455–2463 (2011).
13. A. Attisano *et al.*, *J. Anim. Ecol.* **92**, 30–43 (2023).
14. H.-J. Noh, R. Gloag, A. V. Leitão, N. E. Langmore, *Curr. Zool.* **67**, 665–674 (2021).
15. P. Davoodi, A. Ehsani, R. Vaez Torshizi, A. A. Masoudi, *Anim. Genet.* **53**, 80–93 (2022).
16. T. A. McGrath, M. D. Shalter, W. M. Schleidt, P. Sarvella, *Nature* **237**, 47–48 (1972).
17. W. Forstmeier, C. Burger, K. Temnow, S. Derégnaucourt, *Evolution* **63**, 2114–2130 (2009).
18. S. L. Nuismer, S. P. Otto, F. Blanquart, *Ecol. Lett.* **11**, 937–946 (2008).
19. O. Maliet, H. Morlon, *Syst. Biol.* **71**, 353–366 (2022).
20. Materials and methods are available as supplementary materials.
21. O. Krüger, M. D. Sorenson, N. B. Davies, *Proc. Biol. Sci.* **276**, 3871–3879 (2009).
22. O. Krüger, M. Kolss, *J. Evol. Biol.* **26**, 2447–2457 (2013).
23. N. E. Langmore, S. Hunt, R. M. Kilner, *Nature* **422**, 157–160 (2003).
24. N. J. Sato, K. Tokue, R. A. Noske, O. K. Mikami, K. Ueda, *Biol. Lett.* **6**, 67–69 (2010).
25. A. Skeels, M. Cardillo, *Am. Nat.* **193**, 240–255 (2019).
26. A. B. Phillimore *et al.*, *Am. Nat.* **171**, 646–657 (2008).
27. M. D. Sorenson, K. M. Sefc, R. B. Payne, *Nature* **424**, 928–931 (2003).
28. R. Gloag, L.-A. Keller, N. E. Langmore, *Proc. Biol. Sci.* **281**, 20141014 (2014).
29. N. E. Langmore, R. M. Kilner, *Behav. Ecol. Sociobiol.* **63**, 1127–1131 (2009).
30. N. E. Langmore *et al.*, *Behav. Ecol.* **16**, 686–692 (2005).
31. S. M. Billerman, B. K. Keeney, P. G. Rodewald, T. S. Schulenberg, Eds., *Birds of the World* (Cornell Laboratory of Ornithology, 2022).
32. R. B. Payne, *The Cuckoos* (Oxford Univ. Press, 2005).
33. P. J. E. Higgins, *Handbook of Australian, New Zealand and Antarctic Birds. Volume 4: Parrots to Dollarbird* (Oxford Univ. Press, 1999).
34. S. A. Parker, *Zool. Verh.* **187**, 3–58 (1981).
35. N. E. Langmore, G. Maurer, G. J. Adcock, R. M. Kilner, *Evolution* **62**, 1689–1699 (2008).
36. H.-J. Noh, R. Gloag, N. E. Langmore, *Proc. Biol. Sci.* **285**, 20180726 (2018).
37. L. Joseph, T. Zeriga, G. Adcock, N. E. Langmore, *Emu* **111**, 113–119 (2011).
38. A. Attisano *et al.*, *Sci. Rep.* **8**, 10359 (2018).
39. C. Carøe *et al.*, *Methods Ecol. Evol.* **9**, 410–419 (2017).
40. M. T. Gansauge *et al.*, *Nucleic Acids Res.* **45**, e79 (2017).
41. J.-W. Lee, H.-K. Moon, H.-J. Noh, M.-S. Kim, J.-C. Yoo, *Behav. Ecol.* **32**, 248–256 (2021).
42. J. W. Smith, C. W. Benkman, *Am. Nat.* **169**, 455–465 (2007).
43. M. Andersson, in *Monographs in Behavior and Ecology*, J. R. Krebs, T. Clutton-Brock, Eds., (Princeton Univ. Press, 1994).
44. T. I. Fuisz, S. R. de Kort, *Proc. Biol. Sci.* **274**, 2093–2097 (2007).
45. M. D. Sorenson, R. B. Payne, in *The Cuckoos*, R. B. Payne, Ed. (Oxford Univ. Press, 2005), pp. 68–94.
46. N. J. Sato *et al.*, *Curr. Biol.* **25**, R1164–R1165 (2015).
47. K. Tokue, K. Ueda, *Ibis* **152**, 835–839 (2010).
48. G. A. Jamie *et al.*, *Evolution* **74**, 2526–2538 (2020).
49. J. G. Schuetz, *Evolution* **59**, 2017–2024 (2005).
50. M. E. Hauber, R. M. Kilner, *Behav. Ecol. Sociobiol.* **61**, 497–503 (2007).
51. D. M. de Vienne *et al.*, *New Phytol.* **198**, 347–385 (2013).
52. R. M. Kilner in *Bird Coloration, Volume 2: Function and Evolution*, G. E. Hill, K. J. McGraw, Eds. (Harvard Univ. Press, 2006).
53. A. S. Nyári, L. Joseph, *PLOS ONE* **7**, e31840 (2012).
54. C. N. Spottiswoode, M. Stevens, *Am. Nat.* **179**, 633–648 (2012).
55. S. J. Martin, H. Helanterä, F. P. Drijfhout, *Proc. Biol. Sci.* **278**, 496–503 (2011).
56. D. R. Brooks, E. P. Hoberg, *Trends Parasitol.* **23**, 571–574 (2007).
57. Gekkonid, langmore-2023-cuckoo-evolution, Github (2023); https://github.com/gekkonid/langmore-2023-cuckoo-coevolution.
58. A. Grealy *et al.*, Coevolution with hosts underpins speciation in brood parasitic cuckoos, Dryad (2023); https://doi.org/10.5061/dryad.x95x69ppf.
59. M. de L. Brooke, N. B. Davies, *Nature* **335**, 630–632 (1988).
60. N. B. Davies, J. A. Welbergen, *Science* **324**, 1318–1320 (2009).
61. R. Thorogood, N. B. Davies, *Science* **337**, 578–580 (2012).
62. W. Jetz, G. H. Thomas, J. B. Joy, K. Hartmann, A. O. Mooers, *Nature* **491**, 444–448 (2012).
63. I. G. McGill, M. T. Goddard, *Aust. Birds* **14**, 23–24 (1979).
64. Atlas of Living Australia, Minutillus-records-2023-05-08 (2023); https://bie.ala.org.au/species/https://biodiversity.org.au/afd/taxa/10c7b87a-b13b-4960-b33a-10f143854494.
65. Atlas of Living Australia, Russatus-records-2023-05-08 (2023); https://bie.ala.org.au/species/https://biodiversity.org.au/afd/taxa/cc3aeeba-ee48-4e48-a00a-7f980d76b882.
66. Atlas of Living Australia, Barnardi-records-2023-05-08 (2023); https://bie.ala.org.au/species/https://biodiversity.org.au/afd/taxa/0cb848d7-5bb6-4a81-9a9b-53a50dd1faa6.
67. eBird Basic Dataset, version EBD_relMar-2023 (Cornell Laboratory of Ornithology, 2023).

SUPPLEMENTARY MATERIALS

science.org/doi/10.1126/science.adj3210
Materials and Methods
Supplementary Text
Figs. S1 to S11
Tables S1 and S2
References (*68–120*)
Data S1

my IDP **Science Careers**
INDIVIDUAL DEVELOPMENT PLAN

Features in myIDP include:

- Exercises to help you examine your skills, interests, and values.

- 20 career paths with a prediction of which ones best fit your skills and interests.

- A tool for setting strategic goals with optional reminders to keep you on track.

- Articles and resources to guide you through the process.

- Options to save materials online and print them for further review and discussion.

- A certificate of completion for users that finish myIDP.

Start planning your future today!
myIDP.sciencecareers.org

In partnership with:

FASEB
Federation of American Societies
for Experimental Biology

University of
Massachusetts
UMASS. Medical School

UCSF
University of California
San Francisco

UIC

BURROUGHS
WELLCOME
FUND

Finding the big picture

"**D**o you remember why we proceeded with this study?" my Ph.D. supervisor asked. "What was the goal of these experiments?" I had painstakingly conducted 4 months of work, thawing soil, extracting microbial genomic DNA, quantifying hydrocarbons, and washing endless piles of glassware. But faced with these seemingly straightforward questions, I was speechless. Amid the daily grind and technical details, I had lost sight of how my work fit with the research hypothesis and the overall system we were investigating. Seeing my puzzled expression, my supervisor stepped in, helping me retrace the steps that led to these experiments. And he left me with a closing thought: "Always think big picture, Anirban."

This wasn't the first time I had lost track of my research goals. In earlier endeavors, including my master's degree and research internships, I had focused on running as many experiments, performing as many meta-analyses, and generating as many results as I could. I welcomed details and grew accustomed to getting lost in them. When I was uncertain about next steps, I would go to my mentors for help. They would often ask me why I had conducted certain experiments and whether I had a clear understanding of the project goal. In most cases I replied yes, not realizing this wasn't, in fact, the case. When I felt lost, I instead assumed my problem was lack of technical expertise.

"My detail-loving approach alone would no longer cut it."

But my Ph.D. supervisor's comment helped me realize my detail-loving approach alone would no longer cut it. I could not continue to delve into the depths without also considering how they connected with the big-picture goal. I was going to need to learn to develop the skills I had previously leaned on others for.

I realized that one solution might be as simple as slowing down a bit. I started taking periodic breaks from running experiments to reflect on the "so what" of the studies I was conducting. Previously I would have seen this as a waste of precious time I could have spent collecting data. But I was coming to see it was a crucial part of the research process.

I also learned tremendously from two postdocs, who helped me balance top-down and bottom-up thinking by connecting experiment planning and data analysis with overall study objectives. They helped me develop the habit of always asking ahead of time how a specific experiment or analysis would help answer the hypothesis. This led to more structured, focused thinking about subsequent steps.

Adopting big-picture thinking also improved my writing. I was always good at writing individual sections of a manuscript but struggled to connect the key results and discussion to the introduction. My supervisor and our postdocs helped me develop strategic big-picture questions to guide manuscript development, such as "What is the story arc in the introduction and how does it align with the project goal?" "Why would a reader be interested in my findings?" and "Why did I do this work in the first place?"

With time, I began to complement my love of details with an ability to evaluate the how and why of research tasks and the relevance of my work beyond the experiments, data, and analyses. I was still getting lost in the details, but I was now able to understand why. I could also articulate the story behind my research. By the time I reached the final phase of my doctorate, I was consistently asking myself how the studies I was considering were relevant to my hypotheses. I spent as much time and energy planning experiments as doing them—and I was amazed at what a difference it made.

I've since completed my Ph.D. and moved on to work in industry, where the art of structured thinking, clarification, and remembering the overall goal is also incredibly valuable. I have realized that big-picture thinking is one of the many adaptable, universal skills one can bring from a Ph.D. And I'm grateful my mentors and managers pushed me to develop it. ∎

Anirban Kundu is a senior sustainability consultant at Anthesis Consulting. Send your career story to SciCareerEditor@aaas.org.

ILLUSTRATION: ROBERT NEUBECKER

JOIN US
for the last AAAS Pacific Division Annual Meeting

June 17-20, 2024
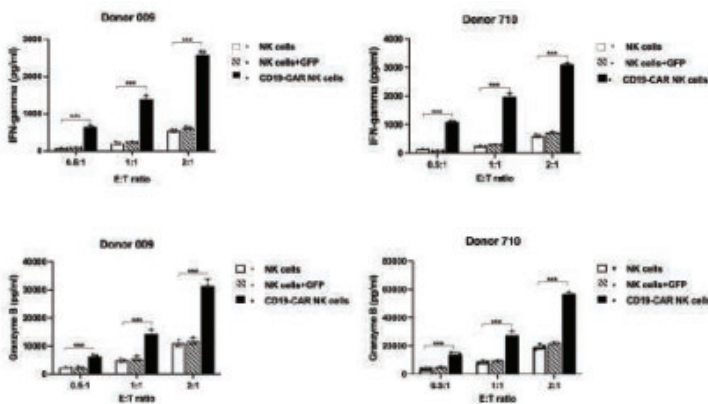University of San Diego

Register at **aaaspd.org**